ZnO(core)/TiO2(shell) composites : influence of TiO2 microstructure, N-doping and decoration with Au nanoparticles on photocatalytic and photoelectrochemical activity

Maciej Kwiatkowski

DOCTORAL DISSERTATION

under international joint-supervision

UNIVERSITÉ BOURGOGNE FRANCHE-COMPTÉ,
Dijon
École Doctorale Carnot-Pasteur

UNIWERSYTET WARSZAWSKI,
Warszawa
Wydział Chemii

In Partial Fulfillment of the Requirements for the Degree

Docteur	Doktor Nauk Chemicznych
Chimie Physique	Chemia Fizyczna

ZnO(core)/TiO_2(shell) composites: influence of TiO_2 microstructure, N-doping and decoration with Au nanoparticles on photocatalytic and photoelectrochemical activity

By

Maciej KWIATKOWSKI

Thesis Supervisors:

Prof. Dr. hab. Magdalena SKOMPSKA, University of Warsaw, Poland
Dr. hab. Igor BEZVERKHYY, Chargé de recherche CNRS, Université de Bourgogne Franche–Comté, France

Warsaw, 28 September 2017

Composition of the Jury

Paweł KRYSIŃSKI	Professor	Poland	Chairman
Nicolas KELLER	Directeur de recherches CNRS	France	Thesis Reviewer
Anna LISOWSKA-OLEKSIAK	Professor	Poland	Thesis Reviewer
Igor BEZVERKHYY	Chargé de recherche CNRS	France	Thesis Supervisor
Magdalena SKOMPSKA	Professor	Poland	Thesis Supervisor
Gilles BERHAULT	Chargé de recherche CNRS	France	Examiner
Krzysztof MAKSYMIUK	Professor	Poland	Jury Member
Grzegorz LITWINIENKO	Professor	Poland	Jury Member

Thesis title in French (Titre de thèse en français):

Composites ZnO(coeur)/TiO_2(coquille): influence de la microstructure de TiO_2, du dopage par azote et de la décoration avec des nanoparticules d'or sur l'activité photocatalytique et photoélectrochimique

Thesis title in Polish (Tytuł rozprawy po polsku):

Układy hybrydowe "ZnO(rdzeń)/TiO_2(powłoka): wpływ mikrostruktury TiO_2, domieszkowania azotem i obecności nanocząstek Au na aktywność fotokatalityczną i fotoelektrochemiczną układu

Table of contents

Acknowledgements

I would like to deliver my deepest gratitude to my supervisors, Prof Dr. Magdalena Skompska and Dr. Igor Bezverkhyy, for their dedication, encouragement and outstanding scientific support during the whole doctoral program.

Special thanks to Prof Dr. Krystyna Jackowska, Prof Dr. Jean-Pierre Bellat, Dr. Aurelie Lagorce for insightful scientific suggestions, discussions, and support.

Also, special thanks for professional assistance during measurements to Dr. Rémi Chassagnon for Transmission Electron Microscopy (TEM), Dr. Frédéric Herbst for Scanning Electron Microscopy (SEM), Dr. Olivier Heintz for X-ray photoelectron spectroscopy (XPS), Mr Nicolas Geoffroy for X-ray Diffraction Analysis, as well as to Mr Christian Paulin for his excellent technical support.

Thanks to my friends and co-workers for helping hands, comradeship and nice atmosphere.

Thanks to the University of Warsaw, the Université de Bourgogne Franche-Comté, as well as to the French Government and the French Embassy in Poland for providing me this opportunity to participate in a 'co-tutelle' doctoral program.

This work was partially supported by National Science Centre (Poland) within the project: DEC 2012/07/B/ST5/02431.

Dedicated to my family

Abstract

Efficient use of renewable energies is one of the most difficult technological challenges facing humanity. Among all renewable energy sources, the sunlight is considered as the most abundant and accessible one. To convert it into usable and controllable form, the modern technology relies on generation of electron-hole pairs in semiconductors upon light absorption. The obtained separated charge carriers possess extra energy brought by the converted sunlight which can be further utilized in various ways. Currently, the most common approach consists in its direct transformation into electricity in p-n junctions. Alternatively, the electrons and holes can be used to perform chemical reactions. The electrons can be transferred to reduce various organic compounds or inorganic species, while simultaneously the holes can play the role of oxidizer by subtracting the electrons from the other substances. Through these reactions it would be possible to accumulate the solar energy in chemical species allowing thus to alleviate the intermittence of the sunlight. Unfortunately, the existing materials do not easily cross the laboratory level to realize this approach on industrial scale. That is why the development of new semiconductor photocatalysts, which harvest and convert efficiently the visible part of solar spectrum, is of paramount importance.

For many years the most often studied photocatalytic materials have been ZnO and TiO_2. However, it has been recently shown that composites based on ZnO and TiO_2 possess even more promising properties than many other semiconductors in various photocatalytic applications. Despite many works reporting high photoactivity of these composites in different applications, the detailed information about the structure–properties correlation is lacking. In order to fill this gap we decided to focus our attention to study the influence of microstructure of ZnO/TiO_2 composites on their properties in photocatalytic degradation of organic pollutants, and in application in half-reaction of 'solar fuel' generation, namely photoassisted water electro-oxidation. To realize such study the composites should satisfy the requirements of a high surface area and good electric conductivity. We chose therefore the design based on ZnO nanorods supported on ITO (Indium Tin Oxide)-coated glass electrode. The ZnO nanorods (NRs) were then covered with a layer of TiO_2 under different deposition conditions. The composition and microstructure of the obtained ZnO(core)/TiO_2(shell) composites were modified in the aim to elucidate how these parameters influence their photocatalytic activity. Consequently, the efforts were made to impart visible light activity to the elaborated

ZnO/TiO_2 composites by modifying titanium dioxide layers with nitrogen and decoration with Au nanoparticles.

The thesis consists of three parts: *Bibliography*, *Experimental* and *Results and Discussion*.

First part of the present PhD thesis, *Bibliography*, is dedicated to the analysis of literature concerning fundamental properties of semiconductor materials, solid/electrolyte interface as well as principles of photocatalysis and photoelectrochemical water oxidation. Also, the photocatalytic properties of ZnO and TiO_2, and those of their composites are reviewed in this section. Furthermore, methods for improvement visible-light absorption are also described, i.e. N-doping and surface plasmonic effects due to the noble metal nanoparticles (Au NPs) deposited on semiconductors.

The second part, *Experimental*, covers the preparation procedures and characterization techniques used in the work. First, the details are given for electrochemical seeding of ITO support, hydrothermal growth of ZnO nanorods, sol-gel deposition of TiO_2 (and N-doped TiO_2), and photodeposition of Au NPs. Second, the characterization techniques used in realization of this project are described: SEM (Scanning Electron Microscopy), HAADF-STEM and HR-TEM (High Angle Annular Dark Field Scanning Electron Transmission Microscopy and High Resolution Transmission Electron Microscopy), XRD (X-ray Diffraction Analysis), XPS (X-ray Photoelectron Spectroscopy), EDS 'or EDX' (Energy Dispersive Spectroscopy) analyses connected with electron microscopy techniques, UV-vis Spectroscopy and DRS (Diffuse Reflectance UV-vis Spectroscopy, TGA-DSC (Thermogravimetry Differential Scanning Calorimetry Analysis), TOC (Total Organic Carbon) analysis, RT-PL (Room Temperature Photoluminescence Spectroscopy), electrochemical techniques including: LSV (Linear Sweep Voltammetry), CV (Cyclic Voltammetry), chronoamperometry, chronopotentiometry, as well as the set-ups elaborated by the author for the purpose of photocatalytic and photoelectrochemical measurements.

The main results of the PhD thesis are presented in the third part, *Results and Discussion*, consisting of four chapters.

In the first chapter (*Chapter 4.1*), the results of the studies on electrochemical seeding of ITO-electrode in $Zn(CH_3COO)_2$ solution are presented. The length and width of ZnO nanorods grown by hydrothermal method from $Zn(NO_3)_2$ aqueous solution on Zn/ZnO-seeded ITO substrate were shown to depend strongly on initial Zn^{2+} concentration and the synthesis duration. The arrays of well-separated ZnO 'obelisk-like' nanorods of width varied from 100 nm at tips to ~ 300 nm at bottom and average length of 1.9 μm were prepared under optimized conditions, and used as starting point for further fabrication of (core)ZnO/TiO_2(shell) composites.

In the second chapter (*Chapter 4.2*), a simple and low-cost sol-gel method was developed in order to form TiO_2 thin layers on ZnO nanorods by hydrolysis of titanium(IV) butoxide. The results of studies lead to elaboration of two most distinctive variants of sol-gel procedure that allow to deposit TiO_2 layers of controlled thicknesses and different morphology (rugged or compact). The rugged TiO_2 layers were obtained after 6 hours of one step sol-gel synthesis followed by calcination of the sample at 450 ^oC, ensuring formation of anatase-TiO_2, whereas the uniform coating of 25 nm – 40 nm thickness was obtained *via* three successive 30 min-synthesis with the intermediate calcination of the sample after each deposition cycle. The composite containing the rugged TiO_2 layer was shown to possess significantly higher activity in model pollutant (methylene blue, MB) degradation and in photoassisted H_2O electro-oxidation under 400 nm monochromatic light irradiation. This improved photoactivity was correlated with the composite microstructure and attributed to a higher porosity and better accessibility of ZnO/TiO_2 interface region through the rugged TiO_2 layer by the reagents. The TiO_2 (shell) layers of similar morphology were also prepared by atomic layer (ALD) and chemical vapor deposition (CVD) techniques and it was shown that the composites fabricated by us with the use of simple sol-gel procedure yield comparable (or even higher) photoactivity. Finally, it was confirmed by total organic carbon (TOC) analysis that the ZnO/TiO_2 composites elaborated in this work are also active in decomposition of the pollutants in a dumb hill leachate solution (waste water) under 400 nm monochromatic irradiation.

In *Chapter 4.3* it is shown that the ZnO/TiO_2 interface plays a key role in enhancement of photodecomposition of MB under 400 nm illumination. The increase of photocatalytic activity was attributed to the shift of absorption edge of ZnO/TiO_2 towards visible light in comparison to that of the ZnO(core)-etched TiO_2. Further enhancement of photocatalytic activity of ZnO/TiO_2 was achieved through its additional calcination at 450 °C for 3 h. This simple treatment brings 40% increase in the rate of MB decomposition and a two-fold rise of the photocurrent in H_2O oxidation. Measurements of open circuit potential (V_{OC}) showed that the improved properties of additionally calcined ZnO/TiO_2 composites stem from the decrease of electron-hole recombination rate. STEM (Scanning Transmission Electron Microscopy) studies showed that the additional calcination resulted in formation of voids at the ZnO/TiO_2 interface. EDX (Energy Dispersive X-ray) analysis and XPS (X-ray Photoelectron Spectroscopy) results proved that formation of voids is accompanied by the outward diffusion of Zn ions into TiO_2 layer and allowed to conclude about the existence of the Kirkendall effect at ZnO/TiO_2 interface. Occurrence of this effect observed for the first time at unusually moderate temperature (450 °C) was shown and attributed to a highly defective nature of the surface layer of the ZnO nanorods.

In the last chapter (*Chapter 4.4*), the composites consisting of ITO-supported ZnO nanorods covered with nitrogen-doped titanium dioxide, $TiO_2(N)$, shell were decorated with gold nanoparticles (Au NPs) in order to improve their photocatalytic activity under visible light. The photocatalytic properties of ZnO/TiO_2/Au and $ZnO/TiO_2(N)$/Au ternary composites were studied under illumination with Xe lamp equipped with a 400 nm cut-off filter. It was found that low Au NPs loading (0.37% at.) resulted in 60% enhancement of photocatalytic decolorization of MB under visible light with respect to the Au-free sample owing to plasmonic effects. Also, a simultaneous N-doping and Au NPs-decoration allows to multiply by three the photocurrent in photoelectrochemical water oxidation at the potential of 0.8 V *vs*. Ag/AgCl. It was also demonstrated that the Au-decorated composites possess a strong electrocatalytic activity in reduction O_2 to active oxygen species (*via* formation of $O_2^{\bullet -}$ radicals) under a small negative bias (–0.25 V *vs.* Ag/AgCl) in dark. Illumination of the polarized sample with visible light was shown to enhance this process resulting in rapid decomposition a model pollutant (MB) even in the presence of Na_2SO_4. This approach allows to completely overcome a problem of inhibition of the photocatalytic process by dissolved inorganic salts on non-

polarized catalysts, thus meeting the aim of promising material for photoelectrocatalytic remediation of waste water, often containing a significant amount of inorganic ions.

Streszczenie (abstract in Polish)

Opracowanie technologii umożliwiających efektywne wykorzystanie odnawialnych źródeł energii należy do największych wyzwań stojących przed ludzkością. Energia słoneczna jest najławiej dostępnym i niewyczerpywalnym źródłem energii. Jej przetworzenie w formę przemysłowo użyteczną odbywa się poprzez wytworzenie par elektron-dziura w oświetlonym półprzewodniku, a nastepnie ich wykorzystanie w odpowiedni sposób. Najlepiej znane i najczęściej praktykowane jest bezpośrednie przekształcenie tych nośników w energię elektryczną dzięki zastosowaniu pólprzewodnikowego złącza p-n. Alternatywnym sposobem jest wykorzystanie wygenerowanych par elektron-dziura w fotokatalitycznych reakcjach chemicznych. Elektron może wziąć udział w reakcji redukcji, natomiast dziura w utlenieniu różnych zwiazków organicznych lub nieorganicznych na granicy faz półprzewodnik/roztwór. Dzięki tym reakcjom można gromadzić energię słoneczną w postaci związków chemicznych i w ten sposób łagodzić problem okresowej jej dostępności. Niestety, stosowane obecnie półprzewodniki ze względu na pewne ograniczenia nie dają jeszcze możliwości zastosowania tej technologii na skalę przemysłową i dlatego istnieje potrzeba opracowania nowych materiałów lub układów hybrydowych.

Przez wiele lat materiałami najczęściej stosowanymi w fotokatalizie był tlenek cynku (ZnO) i dwutlenek tytanu (TiO_2), jednakże oba te materiały charakteryzuja się stosunkowo dużą szybkością rekombinacji fotowygenerowanych nośników ładunku i dużą energią pasma zabronionego, co w konsekwencji przekłada się na małą wydajność przetwarzania energii słonecznej docierającej do powierzchni Ziemi. Ostatnio wykazano, że kompozyty ZnO/TiO_2 posiadają korzystniejsze właściwości fotokatalityczne niż każdy z tych materiałów osobno. Pomimo wielu doniesień litaraturowych potwierdzających wysoką fotoaktywność tych układów w różnych zastosowaniach, wciąż jednak brakuje danych dotyczacych zależności między ich strukturą i właściwościami. Aby wypełnić tę lukę, w ramach niniejszego projektu doktorskiego podjęto systematyczne badania nad wpływem mikrostruktury kompozytów ZnO/TiO_2 typu rdzeń-powłoka na ich aktywność w procesach fotodegradacji modelowych zanieczyszczeń organicznych i fotoelektrochemicznego utleniania wody. Stosowane do tego typu badań kompozyty powinny posiadać dużą powierzchnię właściwą i wykazywać dobre przewodnictwo elektryczne. Dlatego w pracy skoncentrowano się na układach bazujących na nanodrutach ZnO wytworzonych na elektrodzie ITO (szkle

pokrytym cienką warstwą tlenku indowo-cynowego). Nanodruty zostały następnie pokryte cienką warstwą TiO_2, stosując różne warunki jego osadzania. Skład i mikrostruktura uzyskanych kopozytów ZnO(rdzeń)/ TiO_2(powłoka) były modyfikowane w celu określenia wpływu tych parametrów na właściwości fotokatalityczne układu. Następnie, zastosowane zostały metody uaktywnienia kompozytu w świetle widzialnym, poprzez zdomieszkowanie TiO_2 azotem oraz osadzenie na powierzchni katalizatora nanocząstek Au.

Niniejsza rozprawa składa się z trzech częsci: *Bibliography, Experimental* i *Results and Discussion.*

Pierwsza część, *Bibliography*, stanowi przegląd literatury dotyczącej tematu rozprawy, najważniejszych właściwości półprzewodników, granicy faz półprzewodnik/roztwór oraz zjawisk i procesów związanych z fotokatalizą i fotoelektrochemicznym utlenianiem wody. W części tej opisane zostały również fizykochemiczne i fotokatalityczne właściwości ZnO i TiO_2 oraz układów kompozytowych. Przedstawione zostały również metody zwiększenia absorpcji promieniowania w zakresie światła widzialnego, takie jak domieszkowanie TiO_2 azotem oraz wykorzystanie efektu plazmonowego nanocząstek metali szlachetnych (np. Au) osadzonych na powierzchni półprzewodników.

W drugiej części, zatytułowanej *Experimental*, opisane zostały procedury opracowane do syntezy układów ZnO/TiO_2 oraz metody stosowane w pracy do ich charakterystyki. Podane zostały szczegółowe informacje dotyczące elektrochemicznego zasiewania podłoża ITO, hydrotermalnego wzrostu nanodrutów ZnO, syntezy TiO_2 metodą zol-żel i jego domieszkowania azotem oraz procedury fotoosadzania nanocząstek Au. Ponadto krótko opisane zostały metody pomiarowe stosowane w trakcie realizacji badań: SEM (skanningowa mikroskopia elektronowa), HAADF-STEM (skanningowa transmisyjna mikroskopia elektronowa z obrazowaniem za pomocą elektronów rozproszonych pod dużymi kątami), XRD (rentgenowska analiza dyfrakcyjna promieniowania X), XPS (spektroskopia fotoelektronów w zakresie promieniowania X), EDS ‘lub EDX’ (rentgenowska spektroskopia energodyspersyjna) analiza połączona z technikami mikroskopii elektronowej, spektroskopia absorpcyjno-emisyjna UV-vis, DRS (spektroskopia odbicia dyfuzyjnego w zakresie UV-vis), TGA-DSC (analiza termograwimetryczna połączona z skanningową kalorymetrią różnicową), TOC (analiza

zawartości całkowitego węgla organicznego), RT-PL (spektroskopia fotoluminescencyjna w warunkach temperatury pokojowej), techniki elektrochemiczne: m.in. LSV (woltamperometria z liniową zmianą potencjału), CV (cykliczna woltamperomeria), chronoamperometria, chronopotencjometria, oraz autorski zestaw składający się z diody (LED) wysokiej mocy, emitującej monochromatyczne światło o długości fali 365 nm lub 400 nm, wykorzystany do oświetlania układów w badaniach fotokatalitycznych i fotoelektrokatalitycznych

Najważniejsze wyniki uzyskane w trakcie realizacji pracy zostały przedstawione i przedyskutowane w trzeciej części pracy, zatytułowanej *Results and Discussion,* składającej się z trzech rozdziałów.

W pierwszym rozdziale (*Chapter 4.1*) przedstawione zostały wyniki badań dotyczących elektrochemicznego zasiewania elektrody ITO cienką warstwą Zn/ZnO, w roztworze $Zn(CH_3COO)_2$. Stanowiła ona podłoże dla nanodrutów ZnO, których długość i średnica kontrolowane były poprzez zmianę stężenia jonów Zn^{2+} i czas trwania syntezy hydrotermalnej. Po optymalizacji parametrów syntezy, na zasianym podłożu ITO uzyskiwane były w sposób powtarzalny warstwy nanodrutów, dobrze od siebie odseparowanych, w kształcie „obelisków" o średnicy ok. 100 nm u wierzchołka i 300 nm u podstawy oraz długości ok. 1.9 μm.

Drugi rozdział (*Chapter 4.2*) dotyczy metody pokrywania powierzchni nanodrutów ZnO cienką warstwą TiO_2 poprzez hydrolizę butanolanu tytanu (IV). W rezultacie zaproponowano dwa warianty syntezy zol-żel, prowadzące do uzyskania warstw o różnej morfologii, chropowatej i zwartej. Warstwa chropowata była uzyskiwana w trakcie jednoetapowej, 6-godzinnej syntezy, po zakończeniu której próbka była wygrzewana w temperaturze 450 ^oC w celu przekształcenia bezpostaciowego TiO_2 w formę anatazu. Pokrycie ZnO zwartą warstwą TiO_2 o grubości 25 nm – 40 nm uzyskiwano w wyniku trzech nastepujących po sobie 30-minutowych syntez, z wygrzewaniem próbki między kolejnymi cyklami osadzania. Pierwszy z tych kompozytów wykazywał znacząco wyższą aktywność zarówno w procesie fotodegradacji modelowego zanieczyszczenia organicznego (błękitu metylwnowego, w skrócie MB), jak i fotoelektrochemicznego utleniania wody, przy naświetlaniu próbki światłem monochromatycznym o długości fali 400 nm. Wspomniana zwiększona fotoaktywność została skorelowana z mikrostrukturą kompozytu i wyjaśniona większą porowatością warstwy TiO_2, a w konsekwencji lepszą

dostepnością granicy faz ZnO/TiO_2 dla reagentów. Dla porównania, powłoki TiO_2 o podobnej morfologii zostały również osadzone na nanodrutach ZnO metodami ALD (osadzania wartw atomowych) i CVD (chemicznego osadzania z fazy gazowej) i okazało się, że kompozyty przygotowane przy użyciu opisanej powyżej prostej metody zol-żel wykazują porównywalną (a nawet wyższą) fotoaktywność. Ponadto wykazano i potwierdzono metodą pomiaru całkowitego węgla organicznego (TOC), że opracowane kompozyty ZnO/TiO_2 są aktywne w fotokatalitycznym rozkładzie zanieczyszczeń organicznych zawartych w próbach wody pochodzacej z terenów z miejskich wysypisk śmieci.

W rozdziale trzecim (*Chapter 4.3*) wykazano, że kluczową rolę w zwiększeniu aktywności fotokatalitycznej opracowanych kompozytów w świetle monochromatycznym (λ = 400 nm), odgrywa granica faz ZnO/TiO_2. Efekt ten został przypisany przesunięciu granicy absorpcji światła przez ten układ w kierunku fal dłuższych w stosunku do zakresu promieniowania absorbowanego przez warstwę TiO_2 pozostałą po wytrawieniu rdzenia ZnO. Dalszy wzrost aktywności fotoktalitycznej ZnO/TiO_2 osiagnięto po dodatkowym wygrzaniu kompozytu przez 3 h w temperaturze 450 ^oC. Dzięki tej prostej procedurze uzyskano 40% wzrost szybkości fotorozkładu MB i dwukrotny wzrost fotopradów w reakcji utleniania wody. Wyniki pomiaru zmian potencjału obwodu otwartego (V_{oc}) dowiodły, że przyczyną poprawy właściwości fotokatalitycznych układu ZnO/TiO_2 po dodatkowej kalcynacji jest zmiejszenie szybkości rekombinacji fotowygenerowanych nośników ładunku. Badania z zastosowaniem skaningowego transmisyjnego mikroskopu elektronowego (STEM) wykazały, że dodatkowa kalcynacja układu prowadzi do wytworzenia „luk" na granicy faz ZnO i TiO_2. Analiza składu pierwiastkowego metodą rentgenowską (EDX) i metodą spektroskopii fotoelektronów (XPS) dowiodła, że procesowi temu towarzyszy dyfuzja jonów Zn do warstwy TiO_2. Wyniki te pozwoliły na sformułowanie wniosku o wystąpieniu efektu Kirkendalla na granicy faz ZnO/TiO_2. Zaobserwowanie tego efektu po raz pierwszy w tak niskiej temperaturze (450 ^oC) było możliwe dzięki dużej ilości defektów strukturalnych na powierzchni ZnO.

Ostatni rozdział (*Chapter 4.4*) dotyczy kompozytów $ITO/ZnO/TiO_2$ dodatkowo zmodyfikowanych poprzez zdomieszkowanie warstwy TiO_2 azotem ($TiO_2(N)$) i osadzenie na niej nanoczastek Au w celu zwiekszenia ich fotoaktywności tych układów w zakresie światła widzialnego. Właściwości fotokatalityczne kompozytów

ZnO/TiO_2/Au i ZnO/TiO_2(N)/Au były badane po ich oświetleniu lampą ksenonową z filtrem odcinającym wszystkie długości fali światła poniżej 400 nm. Stwierdzono, że po osadzeniu nawet niewielkiej ilości nanoczastek Au (0.37 % at.) na ZnO/TiO_2, dzięki efektowi plazmonowemu uzyskuje się 60 % wzrost szybkości fotodekoloryzacji MB w świetle widzialnym, natomiast zastosowanie kompozytu ZnO/TiO_2(N)/Au pozwoliło na trzykrotny wzrost fotoprądu w procesie utlenienia wody przy potencjale 0.8 V względem elektrody Ag/AgCl. Wykazano również, że kompozyty z osadzonym złotem posiadaja silne właściwości elektrokatalityczne w reakcji redukcji tlenu do aktywnych form tlenu (poprzez tworzenie rodników nadtlenowych $O_2^{\bullet -}$), przy stosunkowo niewielkim potencjale ujemnej polaryzacji (–0.25 V). Oświetlenie spolaryzowanej próbki światłem widzialnym spowodowało wzmocnienie tego procesu, w wyniku czego nastąpił wzrost szybkości fotorozkładu MB, nawet w obecnosci Na_2SO_4. To rozwiazanie pozwoliło przezwyciężyć problem inhibicji procesu fotokatalitycznego przez obecność w roztworze anionów soli nieorganicznych. Dzieki temu opracowane w niniejszej rozprawie układy stanowią bardzo atrakcyjny materiał fotokatalityczny, który może zostać zastosowany do oczyszczania ścieków zawierajacych często znaczne ilości jonów soli nieorganicznych.

Résumé de la thèse (abstract in French)

L'utilisation efficace des énergies renouvelables est l'un des défis technologiques les plus difficiles auxquels l'humanité est confrontée. Parmi toutes les sources d'énergie renouvelables, la lumière du soleil est considérée comme la plus abondante et accessible. Pour la convertir en une forme utilisable la technologie moderne repose sur la génération de paires électron-trou dans les semi-conducteurs lors de l'absorption de la lumière. Les porteurs de charge séparés obtenus possèdent une énergie supplémentaire apportée par la lumière du soleil qui peut être utilisée de différentes façons. À l'heure actuelle, l'approche la plus utilisée consiste en sa transformation directe en électricité dans les jonctions p-n. Alternativement, les électrons et les trous peuvent être utilisés pour effectuer des réactions chimiques. Les électrons peuvent être transférés pour réduire divers composés organiques ou des espèces inorganiques, alors que les trous peuvent jouer le rôle d'oxydant en soustrayant les électrons des autres composés. Grâce à ces réactions, il serait possible d'accumuler l'énergie solaire dans des espèces chimiques permettant ainsi d'atténuer les difficultés liées à l'intermittence de la lumière du soleil. Malheureusement, les matériaux existants ne franchissent pas facilement le niveau de laboratoire pour réaliser cette approche à l'échelle industrielle. C'est pourquoi le développement de nouveaux photocatalyseurs à base de semi-conducteurs, qui récoltent et convertissent efficacement la lumière solaire, est d'une importance primordiale.

Pendant de nombreuses années, les matériaux photocatalytiques les plus souvent étudiés ont été ZnO et TiO_2. Cependant, on a récemment montré que les composites basés sur ZnO et TiO_2 possèdent des propriétés encore plus prometteuses que de nombreux autres semi-conducteurs dans diverses applications photocatalytiques. Malgré de nombreux travaux décrivant une grande activité photocatalytique de ces composites dans différentes applications, les informations détaillées sur la corrélation structure-propriétés font défaut. Afin de combler cette lacune, nous avons décidé de concentrer notre attention sur l'étude de l'influence de la microstructure des composites ZnO/TiO_2 sur leurs propriétés dans la dégradation photocatalytique des polluants organiques, et dans la demi-réaction de la génération de «combustible solaire», à savoir oxydation électrochimique photoassistée de l'eau. Pour réaliser une telle étude, les composites doivent satisfaire aux exigences d'une surface élevée et d'une bonne conductivité électrique. Nous choisissons donc la conception basée sur les nanobâtonnets de ZnO supportés sur l'électrode en verre revêtue d'ITO (Indium Tin Oxide). Les nanobâtonnets

de ZnO (NR) ont ensuite été recouverts d'une couche de TiO_2 dans différentes conditions. La composition et la microstructure des composites ZnO(coeur)/ TiO_2(coquille) obtenus ont été modifiées dans le but d'élucider comment ces paramètres influencent leur activité photocatalytique. Par conséquent, les efforts ont été fournis pour conférer une activité dans le domaine de visible aux composites ZnO/TiO_2 élaborés en modifiant les couches de dioxyde de titane avec dopage par de l'azote et la décoration avec des nanoparticules Au.

La thèse comprend trois parties: *la Bibliographie*, *Expérimentale* et *Résultats et Discussion*.

La première partie de la présente thèse, *Bibliographie*, est consacrée à l'analyse de la littérature sur les propriétés fondamentales des matériaux semi-conducteurs, l'interface solide-électrolyte ainsi que les principes de la photocatalyse et de l'oxydation photoélectrochimique de l'eau. En outre, les propriétés photocatalytiques de ZnO et TiO_2, et celles de leurs composites sont examinées dans cette section. Aussi, des procédés pour améliorer l'absorption de la lumière visible sont également décrits, c'est-à-dire les effets de dopage par azote et de plasmon de surface dû à la présence de nanoparticules de métaux nobles (Au NPs) déposées sur la surface des semi-conducteurs.

La partie *Expérimentale*, couvre les procédures de préparation et les techniques de caractérisation utilisées dans le travail. Tout d'abord, les détails sont donnés pour l'ensemencement électrochimique du support ITO, la croissance hydrothermale des nanobâtonnets de ZnO, le dépôt sol-gel de TiO_2 (et de TiO_2 dopé à l'azote) et la photodéposition des nanoparticules d'or. Deuxièmement, les techniques de caractérisation sont présentées : MEB (microscopie électronique à balayage), TEM (microscopie électronique en transmission), STEM-HAADF (microscopie électronique en transmission par balayage avec un détecteur angulaire de grand angle), EDS (spectroscopie de dispersion de rayons X), XPS (spectroscopie photoélectronique par rayons X), DRX (diffraction des rayons X), ATG-DSC (analyse thermogravimétrique et calorimétrie différentielle), TOC (analyse du carbone total), spectroscopie UV-visible (en solution ou en phase solide), spectroscopie de photoluminescence, LSV (voltampérométrie par balayage), CV (voltampérométrie cyclique). Dans cette partie nous décrivons aussi des dispositifs pour les mesures de l'activité photocatalytique construits dans le cadre de cette thèse.

Les principaux résultats de la thèse sont présentés dans la troisième partie, *Résultats et Discussion*, composée de quatre chapitres.

Dans le premier chapitre (*Chapitre 4.1*), les résultats des études sur l'ensemencement électrochimique de l'électrode ITO dans la solution $Zn(CH_3COO)_2$ sont présentés. Nous avons montré que la longueur et la largeur des nanobâtonnets de ZnO préparés par voie hydrothermale à partir de la solution aqueuse de $Zn(NO_3)_2$ sur le substrat ITO ensemencé de Zn/ZnO dépendent fortement de la concentration initiale de Zn^{2+} et de la durée de synthèse. Les massifs de nanobâtonnets de ZnO, bien séparés, de type "obélisque" dont la largeur varie de 100 nm dans la partie supérieur jusqu'à ~ 300 nm à la base et d'une longueur moyenne de 1,9 μm ont été préparés dans des conditions optimisées et utilisés comme point de départ pour la fabrication de composites ZnO(cœur)/TiO_2(coquille).

Dans le deuxième chapitre (*Chapitre 4.2*), une méthode sol-gel simple et peu coûteuse a été développée afin d'obtenir des couches minces de TiO_2 sur des nanobâtonnets de ZnO par hydrolyse du butoxyde de titane (IV). Nous avons pu ainsi trouver les conditions réactionnelles qui permettent de déposer par méthode sol-gel des couches de TiO_2 d'épaisseur contrôlée et de morphologies différentes (discontinue ou compacte). La couche de TiO_2 discontinue a été obtenue après 6 h de la réaction sol-gel suivie d'une calcination de l'échantillon à 450°C, assurant la formation d'anatase. Le revêtement compact et uniforme d'une épaisseur de 25 nm à 40 nm a été obtenu après trois étapes de 30 min avec la calcination de l'échantillon après chaque étape. Nous avons montré que le composite contenant la couche de TiO_2 discontinue possède une activité beaucoup plus élevée dans la dégradation d'un polluant modèle (bleu de méthylène, MB) et dans l'oxydation électrochimique photoassistée de l'eau sous illumination monochromatique de 400 nm. Cette photoactivité améliorée a été corrélée avec la microstructure de composite et attribuée à une porosité plus élevée et une meilleure accessibilité pour les réactifs de l'interface ZnO/TiO_2 dans le cas de la couche discontinue. Les couches de TiO_2 de morphologie similaire ont également été préparées par déposition atomique en phase liquide (ALD) et par déposition chimique en phase vapeur (CVD). Il a été démontré que les composites fabriqués par nous avec un procédé sol-gel simple sont comparables (voir supérieurs) en termes d'activité photocatalytique. Enfin, il a été confirmé par l'analyse totale du carbone organique (TOC) que les composites ZnO/TiO_2 élaborés dans ce travail sont également actifs dans la

décomposition des polluants dans les eaux usées réelles sous illumination monochromatique de 400 nm.

Dans le *Chapitre 4.3*, nous montrons que l'interface ZnO/TiO_2 joue un rôle clé dans l'amélioration de la photodégradation de MB sous illumination de 400 nm. L'augmentation de l'activité photocatalytique a été attribuée à l'extension de l'absorption optique de ZnO/TiO_2 vers le domaine de la lumière visible ce qui n'est pas le cas pour TiO_2 non associé avec le cœur de ZnO. Une amélioration supplémentaire de l'activité photocatalytique de ZnO/TiO_2 a été obtenue grâce à sa calcination supplémentaire à 450 °C pendant 3 h. Ce traitement simple augmente de 40% la vitesse de décomposition du MB et multiplie par deux le photocourant dans l'oxydation de H_2O. Les mesures du potentiel de circuit ouvert ont montré que les propriétés améliorées des composites ZnO/TiO_2 calcinés proviennent de la diminution de la vitesse de recombinaison électron-trou. HAADF-STEM a montré que la calcination supplémentaire a entraîné la formation de cavités à l'interface ZnO/TiO_2. Les analyses EDX et XPS ont révélé que la formation des cavités s'accompagne de la diffusion externe des ions Zn dans la couche de TiO_2 et a permis ainsi d'établir l'existence de l'effet Kirkendall à l'interface ZnO/TiO_2. L'apparition de cet effet observé pour la première fois à une température modérée (450 °C) a été attribuée à une concentration importante de défauts dans la couche superficielle des nanobâtonnets de ZnO.

Dans le dernier chapitre (*Chapitre 4.4*), les composites constitués de nanobâtonnets de ZnO supportés sur ITO et recouverts de dioxyde de titane dopé à l'azote, $TiO_2(N)$, ont été décorés de nanoparticules d'or (Au NP) afin d'améliorer leur activité photocatalytique sous lumière visible. Les propriétés photocatalytiques des composites ternaires $ZnO/TiO_2/Au$ et $ZnO/TiO_2(N)/Au$ ont été étudiées sous illumination de lampe Xe équipé d'un filtre pour le rayonnement en dessous de 400 nm. Nous avons constaté que même une faible teneur en or (0,37% en poids) entraîne une amélioration de la décoloration photocatalytique de MB sous lumière visible de 60% par rapport à l'échantillon exempt d'or en raison de l'effet plasmonique. En outre, une utilisation simultanée de dopage par l'azote et de la décoration par Au NP permet de multiplier par trois le photocourant de l'oxydation photoélectrochimique de l'eau à 0,8 V (Ag/AgCl). Il a également été démontré que les composites décorés de nanoparticules d'or possèdent en absence d'illumination une forte activité électrocatalytique dans la réduction O_2 en des espèces d'oxygène actives en photocatalyse (via la formation de radicaux) sous un petit biais

négatif (–0.25 V contre Ag/AgCl). L'illumination de l'échantillon polarisé avec de la lumière visible a permis encore d'améliorer ce processus, ce qui a provoqué une décomposition rapide du MB même en présence de Na_2SO_4. Cette approche permet donc de surmonter le problème d'inhibition du processus photocatalytique sur des catalyseurs non polarisés par des sels inorganiques dissous. Elle présente ainsi une voie prometteuse vers une nouvelle technologie de purification photoélectrocatalytique des eaux usées, contenant souvent des quantités importantes de sels inorganiques.

List of abbreviations and acronyms

The symbols listed below follow the recommendations of the International Union of Pure and Applied Chemistry (IUPAC)

A	electron acceptor
$A^{\bullet-}$	anion radical
AM1.5	air mass optical filter
(a.u.)	arbitrary units
CB	conduction band
D	electron donor
$D^{\bullet+}$	cation radical
E_{CB}	energy of the bottom of conduction band (eV)
E_{VB}	energy of the top of valence band (eV)
e	elementary charge (1.602×10^{-19} C)
e^-	electron
e_r^-	reactive photogenerated electron
e_{tr}^-	trapped photogenerated electron
E_F	Fermi level energy (eV)
E_q	energy of band gap (eV)
EDS/EDX	energy dispersive spectroscopy
E_{fb}	energy of flat band
$E^s_{F,n}$	quasi-Fermi level for electrons
$E^s_{F,p}$	quasi-Fermi level for holes
F	Faraday constant ($F = eN_A$) ($9.648 \cdot 10^4$ C mol^{-1})
h	Planck constant ($6.626 \cdot 10^{-34}$ J s)
h^+	holes
h_r^+	reactive photogenerated holes
h_{tr}^+	trapped photogenerated holes
i	current (A)
ITO	indium tin oxide covered glass substrate
j	current density (A cm^{-2})
k_{tr}	rate constant for charge transfer across the semiconductor/solution interface
k_{rec}	rate constant for e^-/h^+ recombination
L	minority carrier diffusion length
λ	wavelength (nm)
MB	methylene blue
MO	methyl orange
N_A	Avogadro number ($6.022 \cdot 10^{23}$ mol^{-1})
NHE	normal hydrogen electrode
NR(s)	nanorod(s)
NP(s)	nanoparticle(s)
NT(s)	nanotube(s)
PC	photocatalysis
PEC	photoelectrochemical
RhB	rhodamine B
R	Universal gas constant (8.3144 J mol^{-1} K^{-1})
SC(s)	semiconductor(s)
SEM	scanning electron microscopy/microscope
STEM	scanning transmission electron microscopy
τ_n	lifetime of the electrons
τ	current decay time constant
t	time
TEM	Transmission electron microscopy/microscope
W_{SC}	depletion layer thickness
VB	valence band
ν	frequency (Hz)
V_a	working electrode potential
V_{OC}	open circuit potential (V)
XRD	X-ray diffraction
XPS	X-ray photoelectron spectroscopy
Δφ	potential drop across the space-charge layer

1. Introduction

Among many fascinating properties of semiconductors one of the most important is their capacity to absorb UV-vis light with formation of electron-hole pairs if the light energy exceeds the band gap of the semiconductor (*Figure 1*). Thus obtained separated charge carriers possess extra energy brought by light which can be used in different ways. Currently the most important use of this energy is the direct production of electricity in p-n junctions created in photovoltaic (PV) materials. This technology represents the main use of the solar light with 177 GW installed global capacity (in 2014) with 90% of it being produced with planar structures based on silicon in mono- or polycrystalline forms [1].

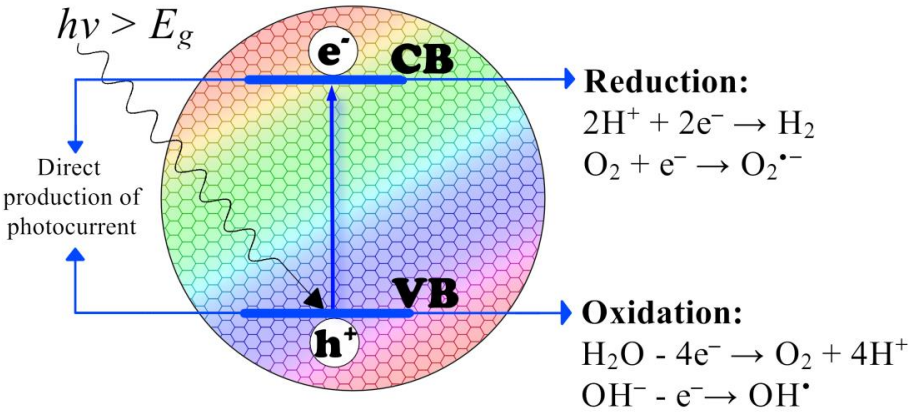

Figure 1 Scheme of photocatalytic action on a metal oxide semiconductor, such as TiO_2.

The electrons and holes produced upon light absorption can also be used for performing chemical reactions. The electrons arriving at the surface of semiconductor particles can be transferred to various organic or inorganic species resulting in their reduction. The holes can play the role of oxidizer by subtracting the electrons from the species localized on the particle surface. The electrochemical potential of the produced charge carriers is determined by the position of the valence band (VB) and conduction band (CB) and may thus be adjusted by choosing an appropriate material. This flexibility permits to perform various transformations using the electrons and holes produced in semiconductor after the light absorption. In the present manuscript we will be concerned with two types of reactions.

First of them is the photoassisted water splitting in which the electrons are used to reduce protons to molecular hydrogen while the holes oxidize water molecules producing

oxygen (*Figure 1*). This reaction, frequently referred to as 'artificial photosynthesis', is of paramount importance since it allows to produce a valuable fuel (H_2) from abundant resource (H_2O) using free energy (solar light). This process can also help to alleviate the main drawback of solar energy – its intermittent character.

In the second type of reactions the photogenerated electrons and holes are involved in formation of very reactive radicals $O_2^{\bullet -}$ and $^{\bullet}OH$, respectively. These radicals are powerful in decomposition of various organic compounds, known as toxic pollutants, with one or many double bonds. Photocatalytic water purification is one of the most important challenges in the environmental protection because, in contrast to many conventional methods, may lead to a complete mineralization of polluting molecules.

To accomplish the reaction of water splitting without any bias (so called 'photocatalytic water splitting') the electronic structure of the semiconductor should fulfill several conditions. The edge of the conduction band should be more negative than the potential of H^+ reduction (–0.41 V *vs.* NHE at pH 7). To oxidize the water molecules the holes must have the potential more positive than that of H_2O/O_2 redox couple (0.82 *vs.* NHE at pH 7). Given these values the band gap of the semiconductor must be at least 1.23 eV [2]. The few materials which satisfy these conditions and can operate under visible light (CdS, GaP) are unfortunately not stable under illumination [3]. Some ternary oxide semiconductors which possess the necessary configuration of CB and VB (e.g. $SrTiO_3$ or $NaTaO_3$) have the band gap > 3.2 eV which allows to use only UV light (λ < 400 nm) constituting 4% of the solar spectrum [4]. In order to overcome this problem the use of two different materials was proposed to realize separately anodic and cathodic reactions. These two materials are electrically connected to form the so called photoelectrochemical cell (PEC, *Figure 2*).

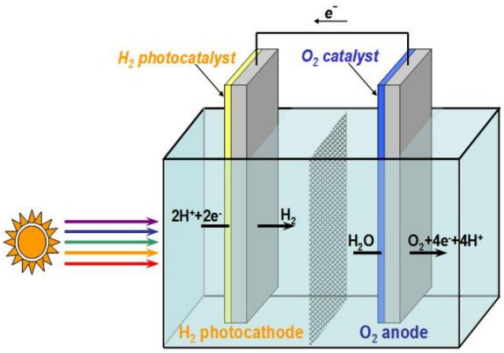

Figure 2 Scheme of photoelectrochemical cell (PEC) for water splitting application.

This approach allows to match better the properties of the materials with the conditions needed for each reaction. Indeed, while the proton reduction proceeds relatively rapidly on the surface of noble metals, water oxidation is a sluggish four-electron reaction which limits the overall process [2]. That is why a significant effort has been devoted to the search of semiconducting materials capable to realize water oxidation which allowed to identify some promising materials: TiO_2, Fe_2O_3, WO_3, $BiVO_4$ [3].

In the case of pollution abatement the reduction and oxidation reactions may occur on the surface of the same band gap material. According to thermodynamics, the photogenerated electrons and holes are powerful in photodegradation process if the bottom of conduction band is located above the reduction potential of O_2 to $O_2^{\bullet -}$ (–0.28 V *vs.* NHE at pH 7) while the top of the valence band is below the oxidation potentials of OH^- or H_2O to $^{\bullet}OH$ radical (2.27 V *vs.* NHE at pH 7 [5]). These thermodynamic requirements are fulfilled by semiconductors with large band gap energy. Additionally, the material for photocatalytic water purification must be stable in a wide pH range, non-toxic, easily processable and of low cost. Given all these requirements TiO_2 has appeared as the most popular material for this application.

Despite the attractiveness of titanium dioxide both as anode for photoassisted water splitting and water purification, it possesses two major drawbacks. As mentioned above its band gap allows to use only a small fraction of the sunlight. The second serious shortcoming of TiO_2 is a high rate of recombination of photogenerated charge carriers leading to low photonic efficiency. The onset of TiO_2 absorption may be to some extent shifted toward the visible light through non-metal doping [6] or deposition of plasmonic metal nanoparticles [7]. To enhance the electron−hole separation and diminish the recombination rate several methods have been proposed in the literature: modification of TiO_2 with metal particles (Pt, Au, Pd) [8,9] or its association with another semiconductor (WO_3, Cu_2O, Fe_2O_3, CdS) having different position of CB or/and VB [10,11]. Recently it has been shown that using nanostructured composites involving 1D nanostructures (nanorods or nanotubes) brings additional advantages in addressing these issues mostly due to better light absorption and shorter diffusion length in such systems [12].

The composites based on ZnO and TiO_2 have been shown to possess promising properties in various photocatalytic applications despite the similarity of the band gap structures of these two oxides (see the references in the *Bibliography* part). A high hole

mobility in ZnO (205 $cm^2\ V^{-1}\ s^{-1}$, [13]) or formation of mid-gap states [14] have been proposed as the origin of this enhancement. However, the details of the involved mechanism are still unknown.

In order to obtain the material applicable both in organics degradation and water splitting a high surface area and good electric conductivity are needed. We chose therefore the design based on ZnO nanorods supported on ITO-covered glass support. The ZnO nanorods were then covered by a layer of titanium dioxide under different conditions. The composition and microstructure of the obtained composites were varied in the aim to elucidate how these parameters influence their catalytic activity. Additionally, we tried to impart visible light activity to the composites using methods known for pure titanium dioxide: the TiO_2 layer was doped with nitrogen and decorated with gold nanoparticles.

Based on a complementary experience of Warsaw and Dijon teams in synthesis and characterization of nanostructured materials we decided to prepare and study in detail the influence of preparation parameters on the photocatalytic properties of ZnO/TiO_2 nanostructured composites.

First part of the dissertation, *Bibliography*, is dedicated to the analysis of literature concerning fundamentals of semiconductor materials, solid/electrolyte interface as well as principles of photocatalysis and photoelectrochemical water oxidation. Also, properties of ZnO, TiO_2, and their composites as ZnO/TiO_2 in the field applied photocatalysis are reviewed and covered in this section. Furthermore, methods for improvement toward visible light absorption are also described, i.e. N-doping and surface plasmonic effects due to the noble metal nanoparticles deposited on semiconductors (Au NPs).

The second part, *Experimental*, covers details of electrochemical seeding of ITO-catalyst support, hydrothermal growth of ZnO nanorods, sol-gel TiO_2 (and N-doped TiO_2) preparation and deposition onto ZnO, and photodeposition methods of Au NPs. Also, the methods and techniques used in this work are described, as well as the set-ups elaborated for the purpose of this work, i.e. irradiation LED devices.

In the third part, the main results, discussion, and conclusions are given. This part consists of four chapters: *Chapter 4.1* deals with preparation of ITO-catalyst supports

and optimization of hydrothermal growth of ZnO, *Chapter 4.2* concerns preparation of ZnO/TiO_2 core/shell composites by sol-gel method, their detailed characterization, and photocatalytic and photoelectrochemical properties. Also, comparison to other deposition techniques (ALD, CVD) is given. The *Chapter 4.3* reveals the origin of enhancement nature of the ZnO/TiO_2 interface on photocatalytic and photoelectrochemical properties. Final *Chapter 4.4* describes preparation, characterization of N-doped TiO_2 and ZnO/TiO_2/Au ternary composites for improved photoactivity under visible light.

The results from this work allow to correlate ZnO/TiO_2 composites architecture, i.e. shape, size, and morphology, as well as N-doping TiO_2 and Au-decoration, with optical properties, photocatalytic, and photoelectrochemical activity under monochromatic (400 nm) and/or visible light irradiation.

The obtained results have been published in the following papers:

(1) K. Zarębska, M. Kwiatkowski, M. Gniadek, M. Skompska, *Electrodeposition of $Zn(OH)_2$, ZnO thin filmsand nanosheet-like Zn seed layers and influence of their morphology on the growth of ZnO nanorods*, **Electrochimica Acta** 98 (2013) 255 – 262

(2) M. Kwiatkowski, I. Bezverkhyy, M. Skompska, *ZnO nanorods covered with a TiO_2 layer: simple sol–gel preparation, and optical, photocatalytic and photoelectrochemical properties*, **Journal of Materials Chemistry A** 3 (2015) 12748

(3) M. Kwiatkowski, R. Chassagnon, O. Heintz, N. Geoffroy, M. Skompska, I. Bezverkhyy, *Improvement of photocatalytic and photoelectrochemical activity of ZnO/TiO_2 core/shell system through additional calcination: Insight into the mechanism*, **Applied Catalysis B: Environmental** 204 (2017) 200 – 208

(4) M. Kwiatkowski, R. Chassagnon, N. Geoffroy, F. Herbst, O. Heintz, I. Bezverkhyy, M. Skompska, *Enhancement of visible light photoelectrocatalytic activity of ZnO (core)/TiO_2(shell) composite by N-doping and decorating with Au^0 Nanoparticles*, **Electrochimica Acta** 246 (2017) 213 – 225

2. Bibliography

2.1. General properties of semiconductors

2.1.1 Electronic structure

Electronic band structure theory of solid-state mater classifies a material as metal, semiconductor or insulator depending on value of its band gap (E_g). Accumulation of atoms in solid mater results in formation of 'energy bands': electron-occupied valence (VB) and electron-free conduction (CB). In metals electron-unoccupied CB coincides with electron-occupied VB (*Figure 3A*). The charge carriers can in this case move freely from VB to CB without energy activation, providing therefore a good electric conductivity. In case of insulators the forbidden zone (energy gap) is large, E_g > 6 eV, and so the electric conductivity is completely suppressed. In case of semiconductors (E_g ~ 1 – 6 eV) an external thermal energy activation or absorption of light (*hv*) is necessary to excite and transfer electrons from VB to CB (*Figure 3B*). Also, contrary to metals, the electric conductivity of SCs increases at elevated temperatures [15].

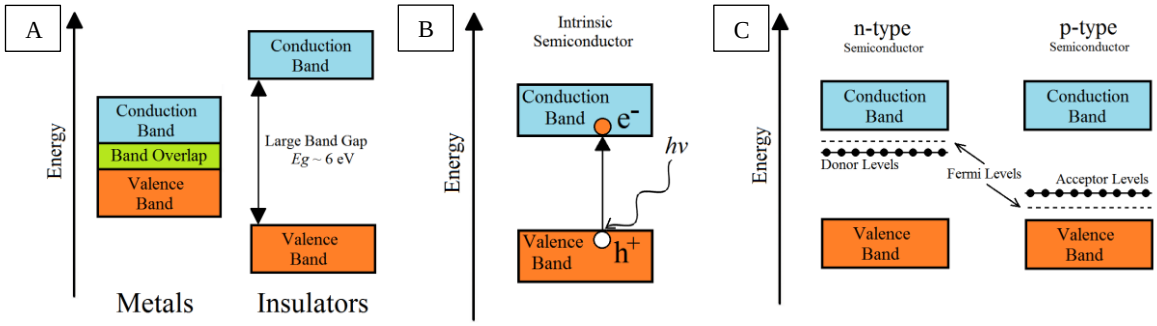

Figure 3 Band structures of metals and insulators (A), electron-hole photogeneration in intrinsic (undoped and defect free) semiconductor (B), and band structure of n-type and p-type semiconductors (C).

As consequence of electron (e^-) transition from VB to CB, in the VB a hole (h^+) is left. However, a real metal oxide semiconductor crystal possesses structural defects and/or impurities, which result in appearance of donor or acceptor energy levels, close to the edges of CB or VB, respectively (*Figure 3C*). In general, electron band-to-band transitions are much stronger than these involving additional energy levels due to their low population. A semiconductor (SC) that is of an n-type holds additional energy levels occupied by electrons, whereas the one with extra empty energy levels located closer to VB, which can be occupied by the electrons from VB is of a p-type. Such situations lead to the shift of Fermi level (E_F) energy from the middle band gap position typical for

intrinsic semiconductor to CB for n-type SC or to VB in p-type SC. Fermi level can be either described as energy level at which probability of an electronic state being occupied is 0.5 or in terms of thermodynamics it corresponds to the electrochemical potential of electron in solids. In this context it is worth to mention that TiO_2, similarly to ZnO, is an n-type SC [16]. In general, the fate of a pair of separated charge carriers can be dualistic, either they migrate to the surface of semiconductor and take part in redox reactions (e_r^-, h_r^+: reactive electron and hole), or recombine to release energy in the form of light emission ($h\nu_1$) or thermal dissipation (*Figure 4A*). Acceptor and donor levels may serve as trapping levels for electrons and holes. Trapped charge carriers (e_{tr}^-, h_{tr}^+) may be deactivated therein and not participate in any surface reaction, ultimately recombining and releasing energy by locally heating crystal structure or by emission of light of a lower energy than the energy of light absorbed ($h\nu_2$).

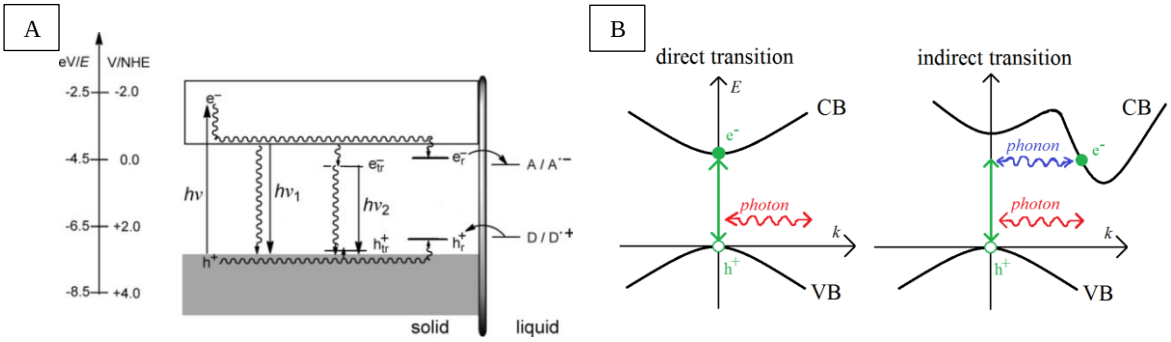

Figure 4 (Photo)electron-hole pair possible utilization in a reaction at solid/liquid interface or its radiative ($h\nu_1$, $h\nu_2$) recombination (A) [17], direct and indirect electron transitions in a semiconductor (B).

Also, two different types of electron transitions characterize semiconductors (*Figure 4B*). In a simplified energy description, electron transition can proceed when the minimum of CB is located at the same value of wave vector (***k***) as the maximum of VB and such transition is called 'direct'. On the other hand, when these positions maxima are displaced, the 'indirect' transition occurs. While the quantum momentum is conserved in direct transition and only photon energy is needed for such, the indirect transition requires additionally absorbed phonon to obey the laws of momentum transition to larger ***k*** value. According to the literature, the probability of electron transition in a case of indirect SC is lower by almost two orders of magnitude than in direct SC [18]. An example of SC of direct transition occurrence is ZnO, whereas TiO_2 exhibits indirect behavior.

Rapid recombination of photogenerated electrons and holes is a key issue in many semiconductors, such as TiO_2, hampering efficient utilization of the charges. The charge carrier generation lasts 10^{-6} ns [19], and the trapped charge carriers lifetimes are enlisted in the *Figure 5*.

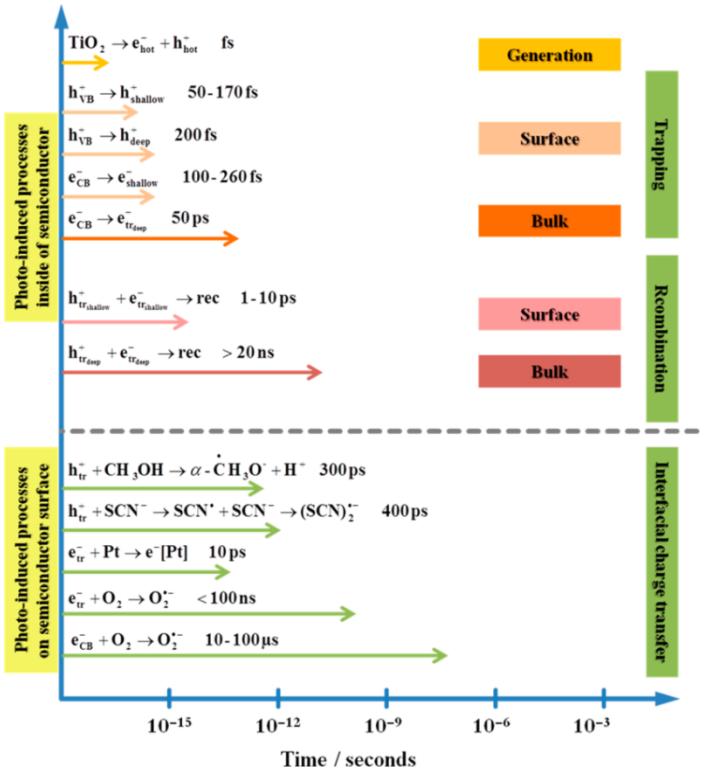

Figure 5 Time scale of different electron-involved processes occurring in semiconductor/electrolyte system [20].

2.1.2. Nanomaterials – the advantage over the bulk

A material with at least one linear dimension lower than 100 nm can be defined as a nanomaterial. An enormous attention is attracted mostly due to their dramatically different properties in a comparison to bulk-scale counterparts. Among many unique features of nanomaterials, one in particular should be mentioned here. Nanomaterials are characterized with a large surface area and in this sense high surface energy ($U_{surface}$) is a consequence of as such, expressed by:

$$U_{surface} = \gamma\, 6 \frac{M}{\rho} \frac{1}{d} \tag{1}$$

where ρ is a material density, M is molar weight, d is particle diameter, whereas γ is specific surface energy. According to the eq. 1, surface energy increases inversely proportional to the size of particle. As consequence, the thermodynamic driving force to minimize the surface energy is strong and has many consequences, such as determination

of a shape of growing particle (long rods or flat plates). With a simple assumption of a tetragonal particle with sides 'a' and 'b' have related surface energies 'γ_a' and 'γ_b', so the surface energy is given by:

$$U_{surface} = 4\,\gamma_a ab + 2\,\gamma_b a^2 \tag{2}$$

Assuming constant volume, and giving minimum surface energy ($\frac{\partial U_{surface}}{\partial a} = 0$), one arrives:

$$\frac{\gamma_a}{\gamma_b} = \frac{a}{b} \tag{3}$$

then if $\gamma_a > \gamma_b$, nanoparticles grow and/or agglomerate in the form of rods, whereas for the condition $\gamma_a < \gamma_b$ a plate-shape dominates. Surface energy, and so the particle shape and size, strongly influence a phase transformation temperature i.e. anatase/rutile TiO_2. It is worth to mention that different planes possess different surface energy, which can contribute to overall photoactivity of the material [21], i.e. (001) planes of anatase TiO_2 exhibits low photocatalytic activity [22], whereas the same (001) planes of rutile TiO_2 happens to be highly reactive [23]. Majima *et al.* [24] reported that the energetically stable {101} crystal face ($U_{surface}$ = 0.44 J m^{-2}) showed a higher photocatalytic activity than the {001} face with a higher surface energy ($U_{surface}$ = 0.90 J m^{-2}). Also the group of Manivannan *et al.* [25] found that the TiO_2 {101} face is highly reactive surface for the reduction of molecular O_2 molecules to $O_2^{\bullet-}$. Preparation methods, such as sol-gel, result in formation of uniformly shaped particles ($\gamma_a \approx \gamma_b$), often with sharp edges after calcination. Since, in sharp crystals the {101} faces dominate, the photoelectron charge transfer to acceptor-electrolyte is promoted, thus reducing the electron-hole recombination [26]. Similar conclusion was drawn from studies of low-energy {101} and high-energy {001} TiO_2 crystal facets by Roy *et al.* [27], who reported enhanced photocatalytic degradation on methyl orange (MO) by synthesized material with appropriate ratio of these facets. Therefore, it is also important to design carefully and prepare a nanomaterial, taking into account shape, size, faces, and polycrystallinity. Moreover, it should be mentioned that excess of the surface energy, caused by surface deformations is responsible for formation of electrical potential barrier at the solid/electrolyte interface [28], which is also important for electrochemical properties. Relation of semiconductor E_g with the size of nanoparticles can be presented in the simplified form as follows [29]:

$$E_g = E_g^* + \frac{\alpha}{d^2} \quad (4)$$

where E_g^* is the band gap energy of bulk material, d is diameter of a nanoparticle, and α is quantity proportional factor. This relation shows that the band gap of SC nanomaterials decreases with increased particle size. Also, it should be mentioned that in the nanosized materials the effective diffusion length of photogenerated charge carriers to the surface is shortened providing therefore their more efficient utilization.

Among all 1D nanostructures, nanorods and nanotubes are the most attractive for electrode preparation since the effective working surface area increases significantly. Columnar nanostructure arrays show better electron drift mobility than non-hierarchical, random networks of porous film (i.e. for TiO_2 films: array (A): $5.6 \cdot 10^{-6}$ cm^2 V^{-1} s^{-1}, porous network (B): $6.6 \cdot 10^{-7}$ cm^2 V^{-1} s^{-1}, *Figure 6*). In this sense, higher electron drift mobility yields better electrochemical responses [30].

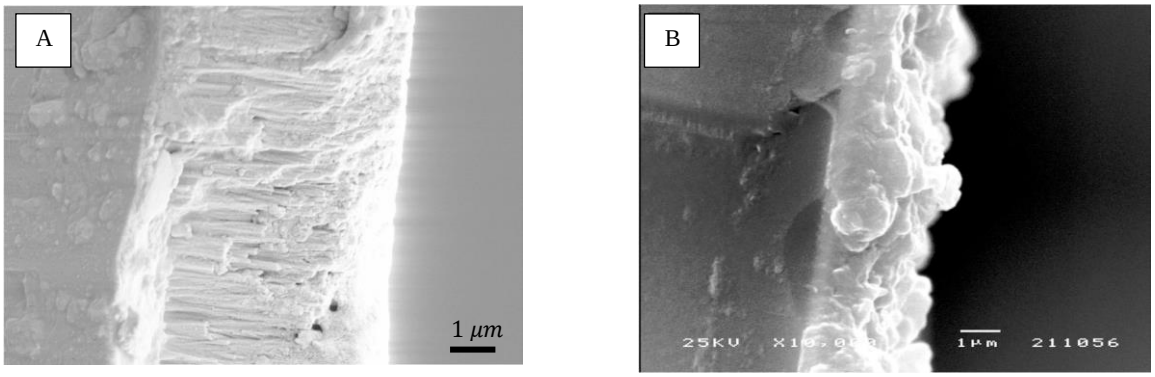

Figure 6 SEM cross-section images of array (A), and porous network TiO_2 (B) [30].

2.1.3. Optical properties

The 'optical band gap' of a semiconductor may be determined from UV-vis absorption spectrum with the use of Lambert-Beer law:

$$I_{tr} = I_0 \cdot exp[-\alpha d] \quad (5)$$

where I_0 is light intensity before, whereas I_{tr} after passing through a thin film of thickness d, and α is absorption coefficient of the solid material. Here, it should be noted that the equation 5 can be used in the case of flat material surface without light intensity loses because of scattering and reflection. Also, α depends on the energy of light, and its value should be specified for the given wavelength. The intensity of light decreases after passing throughout the material and the distance at which 63% of initial light intensity

remains, is called absorption length or optical penetration depth, expressed explicitly as α^{-1}, and it depends on irradiation light wavelength [31]. For rutile TiO_2 the value of α^{-1} changes from 10 nm at 300 nm *via* 1 μm for 380 nm [32], and to about ~ 40 μm for light irradiation of 400 nm wavelength [33]. The absorption coefficient is correlated with the optical band gap energy according to the Tauc equation [34,35,36]:

$$(ahv)^{1/n} = \alpha_0(hv - E_g) \tag{6}$$

where α_0 is material constant (10^5 – 10^6 cm^{-1} eV^{-1}), n is a type of electron transition given for indirect (n = 2) and direct (n = ½) semiconductor, recalling that TiO_2 is indirect, and ZnO is direct SC. Plotting $(ahv)^{1/n}$ *vs.* energy of incident light (hv) and extrapolating straight line to zero value, one can determine the optical band gap value (*Figure 7*).

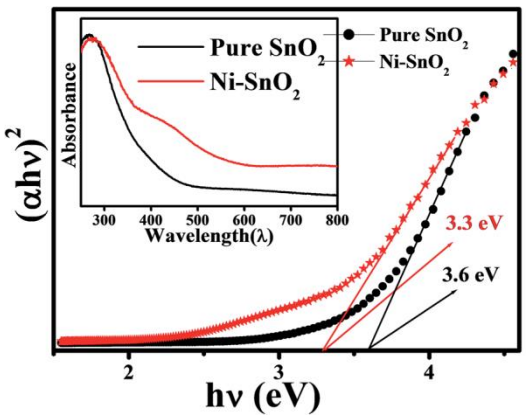

Figure 7 Determination of optical band gap values of pure SnO_2 (black circles), and Ni-doped SnO_2 (red stars) counterpart from their absorption spectra (inset) [37].

The absorption coefficient (α), according to the Urbach rule [38], depends on temperature and photon energy, accordingly to the equation:

$$\alpha(hv, T) = \alpha_0 \cdot exp\left[\frac{\sigma(hv - E_0)}{kT}\right] \tag{7}$$

where E_0 is optical energy coordinate of the convergence point and σ is steepness parameter of absorption edge defined as [39]:

$$\sigma(T) = \sigma_0 \frac{2k_BT}{\hbar\omega} \tanh\left(\frac{\hbar\omega}{2k_BT}\right) \tag{8}$$

where σ_0 is a temperature independent constant which represents the phonon energy associated with the so-called 'Urbach absorption tail'. According to equation 7, the

absorption coefficient increases exponentially in the range of absorption edge. While approaching to it, the density of states of VB and CB, related to population of their surface states, manifests in stepwise increase of α, which explains the Urbach absorption 'tail'. This means that more pronounced absorption should be observed when approaching the band gap value of SC.

As it was discussed above, the materials possess structural defects manifesting in step decreasing values of $(\alpha h\nu)^{1/n}$. Such weak absorption shoulders are proportional to the density of defect states in the material. In this sense, a less defective crystal has more perpendicular inclination of absorbance (*Figure 7*). Also, due to low concentration of defect states the intensity of such transition is much weaker than the band-to-band transition. Consequently, absorption of the material at lower energies, i.e. towards visible light can be improved by introducing more defect states. This can be done by doping a material or increasing concentration of oxygen vacancies in metal oxides. The other possibility is to use plasmonic metal nanoparticles.

2.1.4. Semiconductor/solution interface and related phenomena

Theory of the charge transfer at the semiconductor/solution interface has been described by the Marcus-Gerischer model [40,41,42].

There are two principle reasons of differences in the charge transfer process at the semiconductor/solution and metal/solution interface. One is much lower concentration of the mobile charge carriers in semiconductor leading to different structure of a double layer (*Figure 8A, B*) and in consequence different kinetic limitations, and the second one is involvement of two kinds of the charge carriers (electron and holes) in the interfacial reactions at semiconductor/solution interface [43]. After immersion of n-type semiconductor in the solution containing a redox couple (in dark), the electrons flow from one phase to another to reach the equilibration of Fermi energy levels of the both phases (E_F and $E_{F,\mathrm{redox}}$, respectively). This leads to redistribution of charge carriers within the near-interface region in the semiconductor of 10 nm – 1000 nm thickness (called as space-charge layer) and eventually to the 'band bending' and potential drop $\Delta\varphi_{SC}$ across the space-charge layer (*Figure 8B and D*). When the E_F of n-type semiconductor before equilibration lies above $E_{F,\mathrm{redox}}$, the electrons from donor levels of semiconductor flow towards the electrolyte, leading to development of positively charged space charge layer (depletion layer) in the semiconductor and causing upward

band bending. At the same time, the counterbalance negative charges are accumulated from electrolyte solution side and the potential drop $\Delta\varphi_H$ is formed in the Helmholtz layer of thickness 0.4 nm – 0.6 nm *(Figure 8B)*. However, because of lower charge density in the space charge layer of semiconductor than that in the Helmholtz layer, the potential drop ($\Delta\varphi_{SC}$) in the semiconductor is the main factor determining the total capacitance of the interface. In contrast the Helmholtz layer cannot be neglected at the metal/solution interface because of very high electron density in metal with respect to the charge density (ions) in the solution (*Figure 8A*).

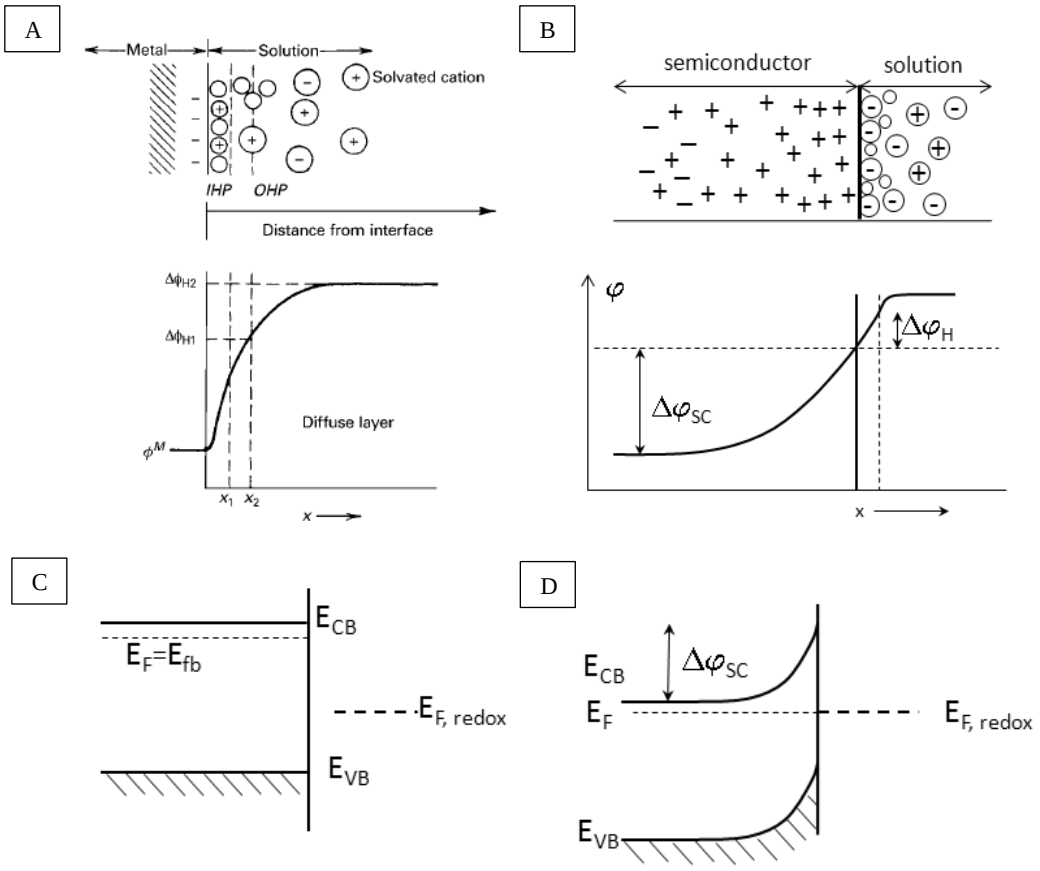

Figure 8 Comparison of the charge and potential distribution at the metal/solution (A) and n-type semiconductor/solution (B) interface. N-type semiconductor before (C) and after (D) contact with a redox couple in solution in dark.

In case when there is no excess charge on the semiconductor side of the interface, the Fermi level energy is called as flat band energy, $E_{fb} = E_F$.

Band bending in a semiconductor can be also induced by applying an external bias potential (V_a) to SC. Application of anodic polarization resembles n-type SC band

bending; however when V_a is equal to E_{fb} (*vs.* NHE), then the band bending is not observed and the space-charge layer is not developed.

Under illumination the generated charge carriers are separated between CB and VB, so their energies are different from the dark equilibrated state, and can be described by equation:

$$E_F^S = E_F + kTln(\frac{\Delta q^s}{q_0}) \quad (9)$$

where E_F is the energy of Fermi level in dark, Δq^s denotes concentration difference of charge carriers under steady-state illumination period and at the dark thermal equilibrium (q_0) [44]. Thus, under illumination, E_F splits into two quasi-Fermi levels, one for electrons ($E_{F,n}^S$) and second for holes ($E_{F,p}^S$) (*Figure 9*).

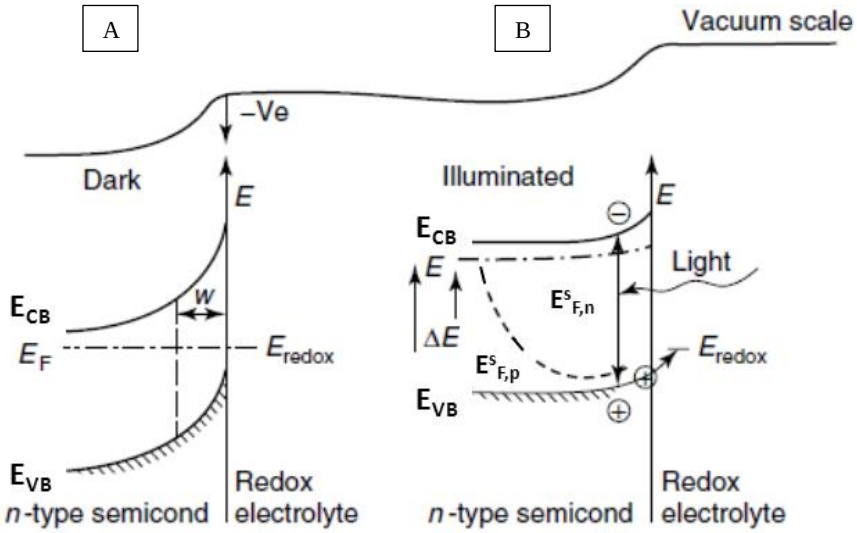

Figure 9 N-type semiconductor/electrolyte interface in dark (A) and under illumination (B) [45].

Majority charge carriers in n-type SC are electrons and quasi-Fermi level will be always close to E_{fb}. Therefore, the difference between E_{fb} and E_{CB} can be smaller than 0.1 eV ($E_F \approx E_{F,n}^S$) [46], while quasi-Fermi level of holes ($E_{F,p}^S$) is strongly different from that of the Fermi level (E_F).

For the reaction to happen the standard redox potentials of the solution species should be located within the SC band gap. However, the oxidation and reduction potentials of donor/acceptor species may differ from the standard redox potential even by 0.5 eV due to contribution of reorganization energy caused by a solvent [47]. Since the exact

energies of reorganization and quasi-Fermi levels cannot be precisely estimated, in practice the equilibrium redox potential values and CB/VB positions are used for thermodynamic predictions of process occurrence.

Application of external potential separates and makes drift the charge carriers, i.e. the electrons are moved *via* external circuit to the counter electrode and the holes are transferred to the semiconductor surface. Recombination thus is hindered. Thermodynamically it is favorable for electrons to lower their energy and holes move in opposite direction (upwards) in energy scale.

The maximum photovoltage can be calculated accordingly to:

$$V_{\text{ph}} = E_{F,\text{redox}} - E^{s}_{F,n} \tag{10}$$

Under anodic polarization and in dark the weak 'thermal' current, however negligible, can be recorded (*Figure 10A, line a*).While in illuminated state, e^{-}/h^{+} pairs are generated and by the force of electrical field those charges are driven in the circuit constituting photocurrent (*Figure 10A, line c*). With an increase of negative applied potential over the value of V_{fb}, the electrons from semiconductor Fermi level are transferred to the electron acceptor in the solution (A) and cathodic current increases. In this range the photocurrent is close to dark current because illumination does not change noticeably the population of the majority charge carriers (*Figure 10A, lines b and d).*

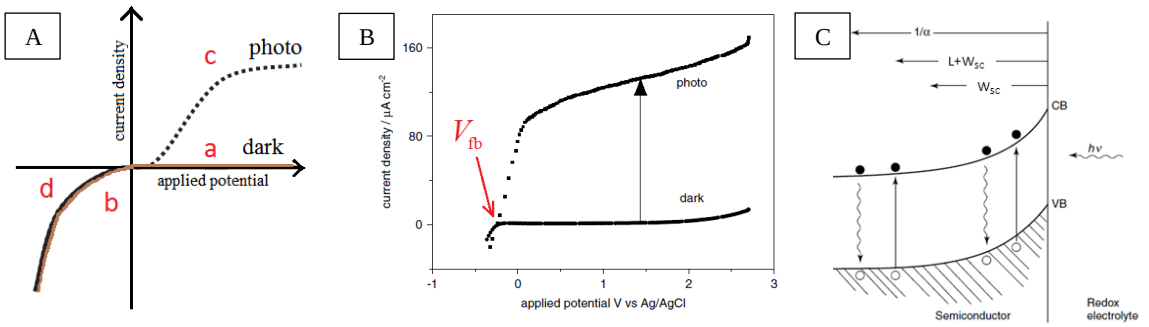

Figure 10 Ideal current-potential characteristic for n-type semiconductor in dark (a, b) and under illumination (c, d) (A) [48]. Linear sweep voltammogram (LSV) for Ti/TiO_2 in 0.1 mol dm^{-3} Na_2SO_4, in the dark and under illumination. Sweep rate 10 mV s^{-1}, pH 5.6 [49]. Model of the n-type semiconductor/electrolyte boundary under illumination with indication of characteristic regions defined as depletion layer width (W_{sc}), minority carriers diffusion length (L) and light penetration depth ($1/\alpha$) [50] (C).

The obtained photocurrent density (j_{ph}) is a difference between the current density under illumination (j_{ill}) and in dark (j_{dark}):

$$j_{ph} = j_{ill} - j_{dark} \tag{11}$$

The photocurrent is a sum of contributions from the charge carriers created in the space charge region and transported to the surface by electric field and those produced out of depletion layer and transported by diffusion field. In the simplest case, without recombination, the total photocurrent for monochromatic light derived from Gärtner model [51] is given by equation:

$$j_{ph} = eI_o\left[1 - \frac{\exp(-\alpha W_{sc})}{1+\alpha L}\right] \tag{12}$$

where I_o is incident light intensity at the surface, α is the absorption coefficient, W_{sc} is a depletion layer thickness and L is the minority carrier diffusion length (*Figure 10C*).

The value of L is a function of the life time of minority charge carriers (τ) and diffusion coefficient (D):

$$L = \sqrt{D\tau} \tag{13}$$

The dependence of the photocurrent on potential may be derived using the relationship between W_{sc} and potential difference ($V_a - V_{fb}$) [51]:

$$W_{sc} = \left(\frac{2\varepsilon\varepsilon_o(V_a - V_{fb})}{eN_D}\right)^{1/2} \tag{14}$$

where N_D is the donor density, ε is the dielectric constant of the semiconductor.

When the absorption coefficient or the thickness of the space charge is very large ($\alpha W_{sc} \gg 1$), then $j_{ph} = eI_o$, i.e. all created charge carriers contribute to the photocurrent and the photocurrent reaches the saturation value (*Figure 10A, line c).*

Ideally, point of zero photocurrent under illumination refers to situation when working electrode potential V_a is equal to V_{fb} (potential of a flat band), in other words onset of photocurrent corresponds to V_{fb} (*Figure 10B*). It is also worth to note that the value of V_{fb} determined from photocurrent measurement is dependent on solution pH, and in case of TiO_2 it fulfills the equation [52]:

$$V_{fb} = -0.40 - 0.06\ \text{pH}\ (\textit{vs. NHE}) \tag{15}$$

However, due to presence of defects such as surface states, a zero point photocurrent can vary. Such current-voltage relationship can be observed for crystallites of 3 nm – 30 nm size, despite the fact that space-charge layer is not formed [53,54,55]. This can be observed only when such particles form aggregates in the form of thick porous films or networks.

Thus, the photocurrent value shows the effectiveness of photogeneration of charge carriers. Also, when j_{ph} value is greater than zero it means that the electrode plays the role of photoanode, whereas if $j_{ph} < 0$ the electrode is photocathode.

As presented above, photocurrent can be measured under constant illumination with linear change of applied bias (i.e. linear sweep voltammetry, LSV), but also under constant bias with dark and illuminated periods (transients, *Figure 11)*. In the initial seconds of light on/off transitions the characteristic spikes followed by exponential current decays within a few seconds to the steady-state values are observed. They originate from electron recombination with free or surface-trapped holes [56]. After the spike during the light 'on' period the current value stabilizes ($j(\infty)$) if the rate of arrival of holes is balanced by recombination and the charge transfer at the semiconductor/solution interface [57]. When the light is switched off, the production of holes is interrupted and the electrons move back towards the surface to recombine with the remaining holes resulting in the spike in opposite direction.

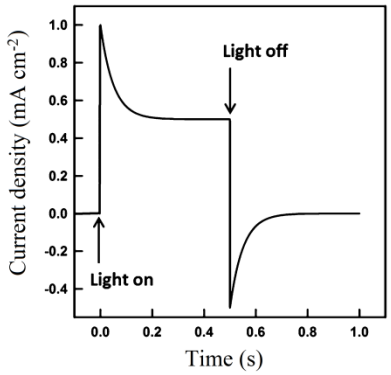

Figure 11 Chronoamperometric response of n-type semiconductor electrode during light 'on' and 'off' periods, adapted from [58].

The intensity of the spikes depends on the rate of charge carrier recombination. In order to estimate the ratio of the rate constants for charge transfer across the semiconductor/solution interface (k_{tr}) and for e^-/h^+ recombination (k_{rec}), the photocurrent

transients *j(t)* can be analyzed according to the model proposed by Peter [57]. As reported, the decay time constant (τ) is determined by $(k_{tr} + k_{rec})^{-1}$:

$$\tau = (k_{tr} + k_{rec})^{-1} \tag{16}$$

while the value of τ can be derived from the normalized photocurrent decay :

$$\frac{j(t)-j(\infty)}{j(0)-j(\infty)} = e^{-t/\tau} \tag{17}$$

where *j(0)* and *j(∞)* are the current densities at $t = 0$ and at steady-state (∞), respectively.

The values of decay time constants can be obtained by fitting the exponential function to the experimental data. Then, the ratio of k_{tr}/k_{rec} determined from the equation for steady-state current:

$$\frac{j(\infty)}{j(0)} = \frac{k_{tr}}{k_{tr}+k_{rec}} \tag{18}$$

allows to conclude whether the charge transfer dominates over the recombination ($(k_{tr}/k_{rec}) > 1$) or situation is opposite ($(k_{tr}/k_{rec}) < 1$).

Photopotential of the electrode can be determined when no bias is applied to the photoelectrode according to the eq. [59]:

$$V_{ph} = |V_{OC,ill} - V_{OC,0}| \tag{19}$$

where, $V_{OC,ill}$ and $V_{OC,0}$ are the open-circuit potentials (OCP) under illumination and in dark, respectively. In practice, $V_{OC,ill}$ for n-type semiconductors is more negative under illumination than in dark ($V_{OC,ill} < V_{OC,0}$). Similarly to photocurrent transient measurements, OCP is recorded in light on/off periods.

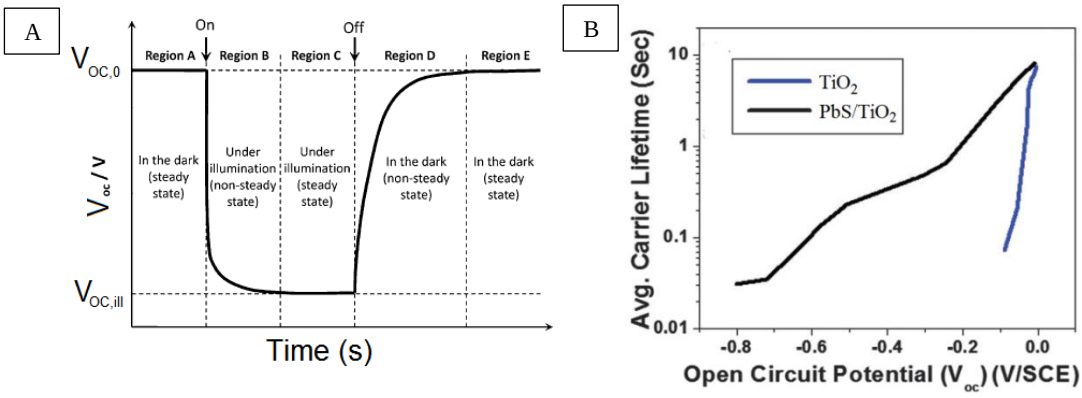

Figure 12 Model OCP behavior of n-type semiconductor (A) [60], and dependence of average carrier lifetime vs. OCP for thin TiO_2 and PbS modified TiO_2 films (B) [61].

In common OCP behavior (chronopotentiometry) for n-type electrode (i.e. TiO_2) one can distinguish several regions (A – E in *Figure 12A*). Once the potential of the electrode in dark is stabilized in terms of half-reaction kinetics (Region A) the light can be turned on and immediate drop of photopotential is observed due to photogeneration and separation of the charge carriers (Region B). When charge generation and consumption are equilibrated the photopotential stabilizes (Region C). At this point light can be turned off and the photopotential decays (V_{OC}) by slow relaxation (Region D) to initial value, reaching finally steady state in dark (Region E). For semiconductor electrodes such as ZnO, and TiO_2 the results of V_{OC} decay can be used to estimate electron lifetime (τ_e), [62] accordingly to the eq.:[63]

$$\tau_e = -\frac{kT}{e}\left(\frac{dV_{OC}}{dt}\right)^{-1} \tag{20}$$

where k is the Boltzmann constant, e is the elementary charge and T is the temperature expressed in Kelvins, and t is decay time. Such approach allows to estimate the overall lifetime of trapped and free electrons upon their photogeneration in semiconductors (*Figure 12B*), and as visible the lifetime may be strongly influenced by its composition.

2.1.5. Photoelectrochemical water oxidation

Photo-assisted water oxidation is a half-reaction of water splitting. Such process however, cannot proceeds on neither ZnO nor TiO_2 without application of external bias potential because H^+/H_2 redox potential is above the Fermi level energy of the semiconductor (*Figure 13*).

Therefore, the three electrode system is needed equipped with a photoanode (i.e. n-type SC), Pt cathode and the reference electrode (for example Ag/AgCl). Water is oxidized by holes, whereas the electrons photogenerated in photoanode flow to Pt cathode where hydrogen is then generated, according to reaction scheme:

$$2h^+ + H_2O \rightarrow ½\ O_2 + 2H^+ \qquad \text{: at photoanode} \qquad (21)$$

$$2H^+ + 2e^- \rightarrow H_2 \qquad \text{: at cathode} \qquad (22)$$

Photoanode composed of TiO_2 exhibits maximal photovoltage of 0.7 V – 0.9 V [64], which is too small for water splitting without bias.

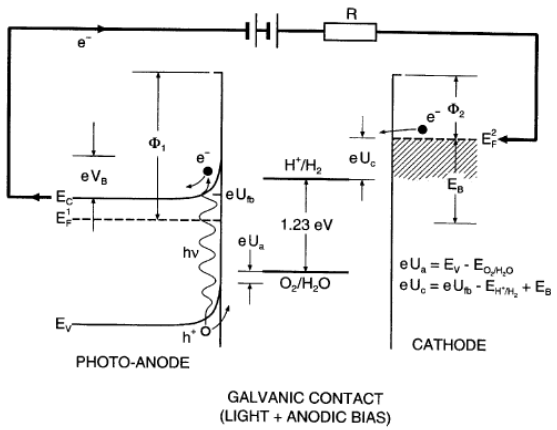

Figure 13 Scheme of n-type semiconductor photoanode and metal cathode in photoelectrochemical cell under light illumination and anodic bias [65].

The overall water splitting reaction:

$$H_2O \rightarrow H_2 + ½\ O_2 \qquad (23)$$

is an endothermic reaction with standard free enthalpy of 236.8 kJ mol^{-1}. Half-reactions of oxidation and reduction are:

$$\text{reduction: } 2H_2O + 2e^- \rightarrow\ H_2 + 2OH^- \quad E^0_{red} = -0.41 \text{ V } \textit{vs.} \text{ NHE at pH 7} \qquad (24)$$

$$\text{oxidation: } O_2 + 4e^- + 4H^+ \rightarrow 2H_2O \quad E^0_{ox} = 0.82 \text{ V } \textit{vs.} \text{ NHE at pH 7} \qquad (25)$$

and the summary energetic process can be correlated with standard free energy accordingly:

$$E = (E^0_{red} - E^0_{ox})e = \Delta G^0_{H2O} / 2N_A = h\nu = 1.23 \text{ eV} \qquad (26)$$

Contrary to photocatalytic degradation of organic pollutants where the light is 'utilized' to accelerate spontaneous processes, the water oxidation might be considered as light

energy ‘storage’ since the process is not spontaneous under ambient conditions. In other words, water splitting has $\Delta G^0 > 0$, which is so-called uphill electron transfer process, while photocatalysis $\Delta G^0 < 0$ is a downhill electron transfer process.

To carry the water splitting reaction on TiO_2 photoanode the overpotential is required. The O_2/H_2O reaction typically requires an additional 0.275 V (U_a, *Figure 13*) anodic overpotential, while H^+/H_2 half-reaction requires an additional 0.05 V (U_c, *Figure 13*) cathodic overpotential to realize the reaction at a reasonable rate [65].

ΔG^0 for water splitting is 2.46 eV per H_2O molecule. Two pairs of e^-/h^+ decompose 1 molecule of H_2O so the energy required for one electron is 1.23 eV. From this point of view a good candidate for water splitting can be i.e. GaAs with E_g of 1.4 eV. However, it is prone to photocorrosion in aqueous media [66]. Also, taking into account the ΔG^0 value, the excess of energy is needed to overcome kinetic limitations of this reaction, and so the E_g should be therefore $\geq$ 2 eV [65]. To conclude, some general demands for effective semiconductor working as photo-anode can be specified:
(1) band gap should be of approx. 1.9 eV (it is a compromise of small band gap which promotes absorption of wide range of light spectrum, however not too small to overcome kinetic limitations),
(2) CB should be more negative than reduction potential of water ($E_{CB} < E_{red\ H2O}$),
(3) VB should be more positive than oxidation potential of water ($E_{VB} > E_{ox\ H2O}$),
(4) electron transfer via SC/electrolyte interface should be fast,
(5) photocorrosion should be eliminated.

Either water oxidation or water reduction can be conducted or these reactions are sacrificial oxidation and sacrificial reduction, since reductant and oxidant are consumed in the processes. Despite recent results on determination of the mechanism of water oxidation, still discussion in literature is continued. Thus ones consider that surface states at semiconductor/solution interface serve as intermediate place for O_2 evolution, the others postulate that surface $^{\bullet}OH$ radicals in $(TiOH)^+$ may serve as an initial stage of the process involving h^+. Contrary to that, it was also reported that O_2 evolution may lead to formation of surface OH radicals. Moreover, the others showed that h^+ can be trapped in the lattice of O atoms without formation of OH radicals [20, and references therein].

2.1.6. Heterogeneous photocatalysis

Heterogeneous photocatalysis is currently one of the most attractive among other advanced oxidation methods for remediation of the environment, especially air and water purification (*Figure 14A*). Its advantage arises from a unique combination of opportunities that biological or chemical methods solely cannot offer nor achieve expected effect of degradation of pollutants. The method was enlisted as one of the advanced oxidation processes (AOP), with advantages of relatively cheap photocatalytic materials which do not require additional chemical substances to work, free of chemical wastes and the processes proceeds in ambient temperature. Oxidative degradation of organic pollutants initially was being achieved with 'old' methods that are based on formation of reactive ozone (O_3). AOP are the methods that generate other oxidizing agents such as hydroxyl radicals ($^{\bullet}OH$), which are more reactive than 'reference' O_3, by far of a few or several orders of magnitude (*Figure 14B*).

A

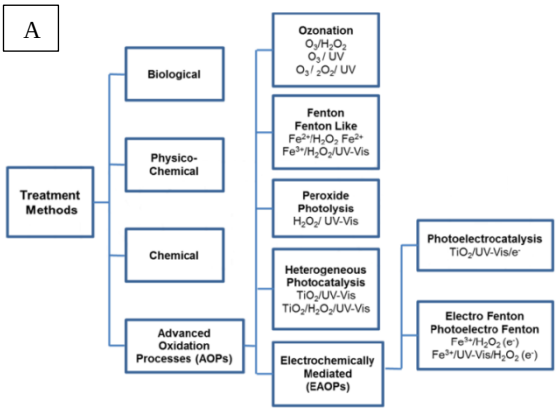

B

Compound	Reaction rate constant k (dm^3 $mole^{-1}$ s^{-1})	
	O_3	$^{\bullet}OH$
Phenols	10^3	10^9 to 10^{10}
N-containing organics	10 to 10^2	10^8 to 10^{10}
Aromatics	1 to 10^2	10^8 to 10^{10}
Ketones	1	10^9 to 10^{10}
Alcohols	10^{-2} to 1	10^8 to 10^9
Alkenes	10^{-2}	10^6 to 10^9

Figure 14 Methods and techniques used for water remediation (A) [67], comparison of the rate constants of decomposition reactions with the use of reactive ozone (O_3) and hydroxyl radicals ($^{\bullet}OH$) (B) [68].

Photogenerated hydroxyl radicals can degrade organic pollutant compound in either one or two ways: by abstraction of hydrogen atom to form water (i.e. from alkenes or alcohols, *Figure 15A*) and/or can be added to aromatic compounds initiating its decomposition chain reactions (*Figure 15B*) [70].

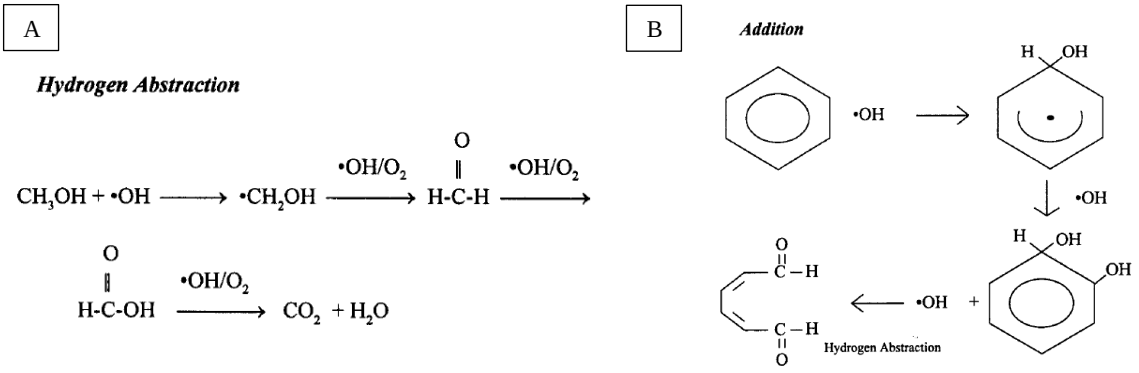

Figure 15 Degradation mechanisms of: an alcohol via hydrogen abstraction (A), and an aromatic compound via addition reaction (B) by photogenerated hydroxyl radicals (˙OH) [71].

Therefore, the heterogeneous photocatalysis attracts a great attention since it still requires further improvement and understanding as 'relatively' recent and need-to-develop method and technique. There are few models to describe quantitatively the effectiveness of heterogeneous photocatalytic process. One of the classical kinetic models for heterogeneous photocatalytic degradation process is the Langmuir-Hinshelwood model, which is based on classical equilibrium coverage θ_e on uniform surface, represented by equation:

$$\theta_e = \frac{K_a c}{1+K_a c} \tag{27}$$

where K_a is adsorption equilibrium constant, and c is reactant concentration, and the rate of degradation can be expressed as:

$$k_r\,\theta_e = rate = -\frac{dc}{dt} = \frac{k_r K_a c}{1+K_a c} \tag{28}$$

where, t is time of irradiation, k_r is reaction constant. Assumptions to the model are:

(1) at equilibrium state the population of adsorption sites is constant,
(2) only one reactant occupies one adsorption site,
(3) reactant molecules do not interact between themselves,
(4) the adsorption is reversible,
(5) rate of adsorption is higher than any subsequent reactions,
(6) energy of adsorption is the same at each adsorption site.

For initial concentrations c_0 lower that 10^{-3} M, the equation is simplified by the assumption $K_a\,c << 1$:

$$-\ln\left(\frac{c}{c_0}\right) = k_r K_a t = k_{app} t \tag{29}$$

where, k_{app} is apparent first-order rate constant (*Figure 16A*). Such model can be applied in MB decomposition and quantitative comparison of photocatalytic activity of catalysts can be based on the determined k_{app} values.

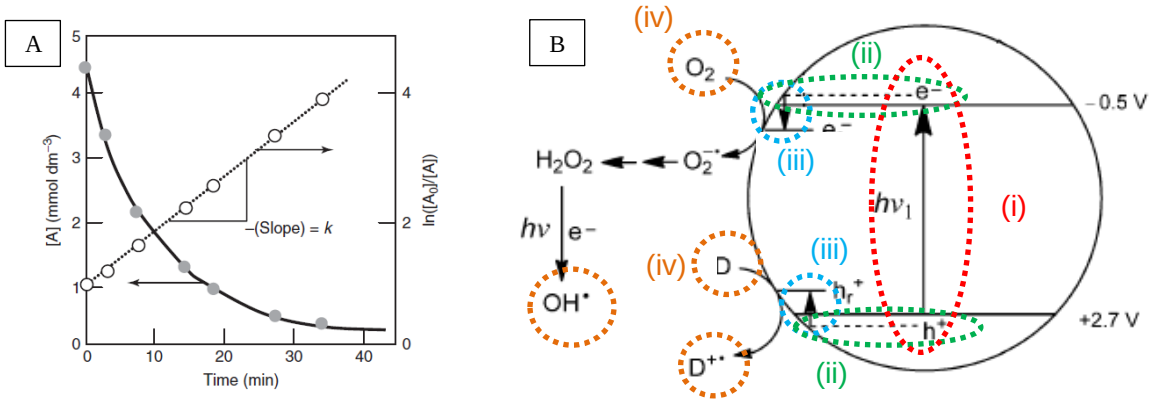

Figure 16 Determination of apparent first-order kinetic rate constant based on Langmuir-Hinshelwood model (A), and photocatalytic stages of the process associated with energy level scheme of semiconductor (B) [69].

In general, each heterogeneous SC photocatalytic process can be divided into four main stages, indicated in *Figure 16B*:

(i) absorption of light and separation of charge carriers in SC (red circle),

(ii) diffusion of e^-/h^+ to the surface of photocatalyst (green circles),

(iii) charge transfer across photocatalyst/(acceptor/donor) interface (blue circles),

(iv) substrate-to-product transformation chain reactions (orange circles).

Each individual stage has limitations and overcoming them can finally lead to improvement of photoactivity. Upon light absorption by semiconductor, chain reactions involving different species are initiated. Two pathways can be distinguished, regarding initiation by photogenerated holes and electrons, accordingly [70,71]:

Holes:

$$TiO_2 + h\nu \rightarrow TiO_2\,(e^- + h^+) \tag{30}$$

$$TiO_2(h^+) + RX_{ad} \rightarrow TiO_2 + RX_{ad}^{\bullet+} \tag{31}$$

$$TiO_2(h^+) + H_2O_{ad} \rightarrow TiO_2 + {}^{\bullet}OH_{ad} + H^+ \tag{32}$$

$$TiO_2(h^+) + {}^-OH_{ad} \rightarrow TiO_2 + {}^{\bullet}OH_{ad} \tag{33}$$

Electrons:

$$TiO_2(e^-) + O_2 \rightarrow TiO_2 + O_2^{\bullet -} \quad (34)$$

$$O_2^{\bullet -} + H^+ \rightarrow HO_2^{\bullet} \quad (35)$$

$$O_2^{\bullet -} + HO_2^{\bullet} \rightarrow {}^{\bullet}OH + O_2 + H_2O_2 \quad (36)$$

$$2HO_2^{\bullet} \rightarrow O_2 + H_2O_2 \quad (37)$$

$$TiO_2(e^-) + H_2O_2 \rightarrow TiO_2 + OH^- + {}^{\bullet}OH \quad (38)$$

$${}^{\bullet}OH + {}^{\bullet}OH \rightarrow H_2O_2 \quad (39)$$

$$H_2O_2 + {}^{\bullet}OH \rightarrow H_2O + HO_2^{\bullet} \quad (40)$$

There is also possibility for reaction to occur:

$$H_2O_2 + TiO_2(e^-) + H^+ \rightarrow {}^{\bullet}OH + H_2O \quad (41)$$

$$O_2^{\bullet -} + h^+ \rightarrow {}^1O_2 \quad (42)$$

Reactions (32) and (33) generate highly reactive hydroxyl radicals (${}^{\bullet}OH_{ad}$), which are mainly responsible for degradation of adsorbed organic pollutants at SC surface. Other highly active species $O_2^{\bullet -}$ and 'free' ${}^{\bullet}OH$ are also involved in this process.

Photocatalytic anti-bacterial properties of TiO_2 have been also reported [72], however for bacteria disinfection are mainly responsible 'free' ${}^{\bullet}OH$ radicals generated in electron-pathway. Hydroperoxyl radicals ($HO_2^{\bullet}$) possess less oxidative power than hydroxyl radicals (${}^{\bullet}OH$, ${}^{\bullet}OH_{ad}$). Therefore, reactions (39) and (40) are undesirable. Also, it should be noted that in reaction (42) short living singlet molecular oxygen can be formed, which also a catalytic reactive species [73,74]. To conclude, the key photocatalytically active species are $O_2^{\bullet -}$, ${}^{\bullet}OH_{ad}$, ${}^{\bullet}OH$.

The oxidative and reduction power of radicals is due to their potential, which depends on pH of the solution, as presented in *Figure 17B*, and in general became more negative with increasing pH [75]. The same trend is observed for flat band potentials of semiconductors. As shown in *Figures 17A* and *17B*, due to strong oxidative power of photogenerated holes they are primary species in degradation of the organic pollutants.

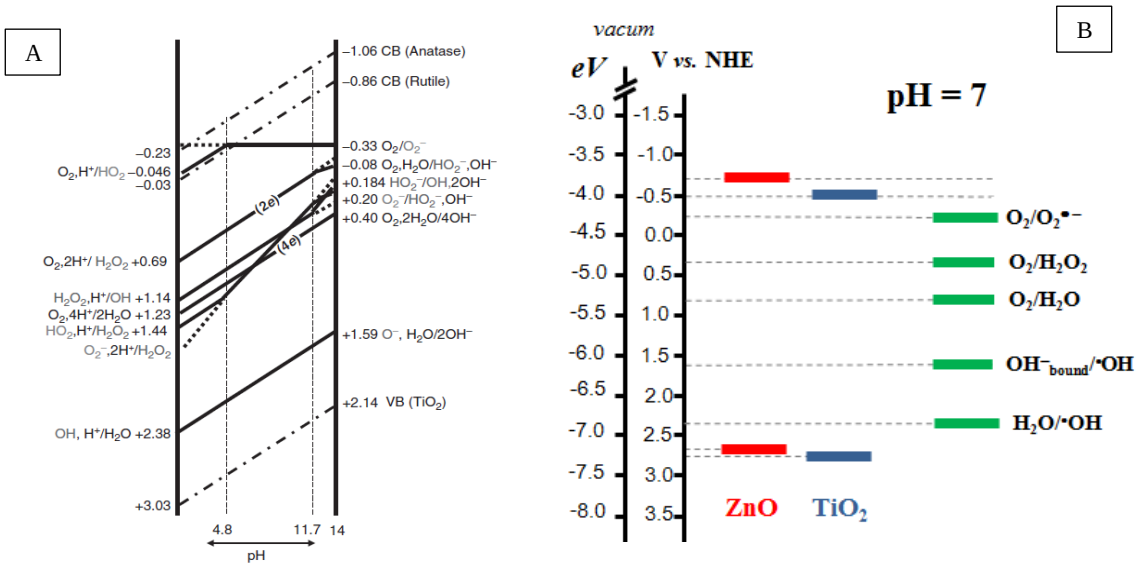

Figure 17 Redox potential dependence on pH (A) [75], and energy positions for ZnO and TiO_2 anatase calculated for pH 7 (B).

As seen on the schemes, CB position of ZnO and TiO_2 are only slightly more negative than $O_2/O_2^{\bullet-}$ redox couple potential allowing photogenerated electrons to be transferred from near-CB and CB energy levels to O_2. At the same time, the photogenerated holes are supplied by an electron donor i.e. H_2O whose redox potential are more negative than near-VB and VB energy level positions. Not all photogenerated electron-hole pairs are participating in the reactions, even if energetically it is favorable. This is due to the size of particles and the charge carrier diffusion distance to the surface of SC/reaction center before they recombine, and in general it is a few – several nanometers [76].

2.1.7. Dye adsorption on semiconductors

Adsorption of dye molecules is an important phenomenon in surface heterogeneous photocatalysis. This may influence the Fermi energy level of a SC, which depends on nature of adsorbed species and solvents, i.e. E_F of TiO_2 in acetonitrile is shifted by about 0.4 eV towards cathodic range in a comparison to that in water [77]. In general a high adsorption of organic pollutants on SC's surface should yield a higher photocatalytic decomposition rate [78], and electron-hole recombination is hindered by reduction of adsorbed oxygen to superoxide radical [79]. Adsorption centers, most often are not selective, and therefore a photocatalytic degradation rate of organic pollutants might be inhibited by concurrent surface-adsorbed cations [80].

2.1.8. Pollution abatement

Photocatalytic degradation of organic pollutants can be monitored with adequate technics and methods. For model dye pollutants, i.e. MB, methyl orange (MO), or Rhodamine B (RhB), photo bleaching can be monitored at the wavelength of maximum absorption peak (λ_{max}) in visible range, MB: 664 nm, MO: 463 nm, RhB: 555 nm. For colorless compounds, such as phenol, photodegradation is observed in UV range, λ_{max} = 272 nm.

Apart from spectrophotometric evaluation, other methods are also in use, such as high-performance liquid chromatography (HPLC) [81], which gives information on the intermediate species formed during decomposition of initial compound. Other also widely used is total organic carbon (TOC) removal monitoring, which provides information on mineralization of organic compound into CO_2. The latter method is more pertinent, since waste water remediation aims to remove organics, putting a fewer accent on the exact composition of the sample. Due to difficulties of complex systems, harsh pH, presence of dissolved inorganic salts, remediation of water requires active photocatalyst, i.e. N-ZnO [82], Ni-TiO_2 [83], Cu/N-TiO_2 [84], intensive UV light irradiation (250 W UV-A [85]), elevated temperatures, and frequently additional external energy in the form of electrical bias (i.e. E_{cell} = 2.0 V [86]). Therefore, it is of a crucial need to develop highly active, stable photocatalyst, which is effective under visible light and possibly without external bias potential.

In order to unify and standardize evaluation of photocatalytic activity of semiconductor catalyst the International Standardization directive was established [87], as well as similar suggestions have been proposed in literature in the field of photocatalysis [88,89].

2.1.9. Model pollutant photocatalytic degradation

Some dyes like methylene blue (MB), methyl orange (MO), or Rhodamine B (RhB) are widely used as probe molecules for determination of photocatalytic activity of catalysts and in the present work MB was chosen for this purpose. Decolorization of MB follows the apparent first-order kinetics which is convenient for determination of decolorization rate constants for catalyst and their possible quantitative comparison. MB UV-vis spectrum covers a region of negligible absorption within 350 nm – 500 nm, whereas two peak located around 614 nm and 664 nm can be seen (*Figure 18A*). The former can be ascribed to dimer form of MB, whereas the latter peak is ascribed to electron transition in

the monomer (*Figure 18B*). According to the literature, in 10 μM aqueous solution of MB only 7% is in dimer form [90].

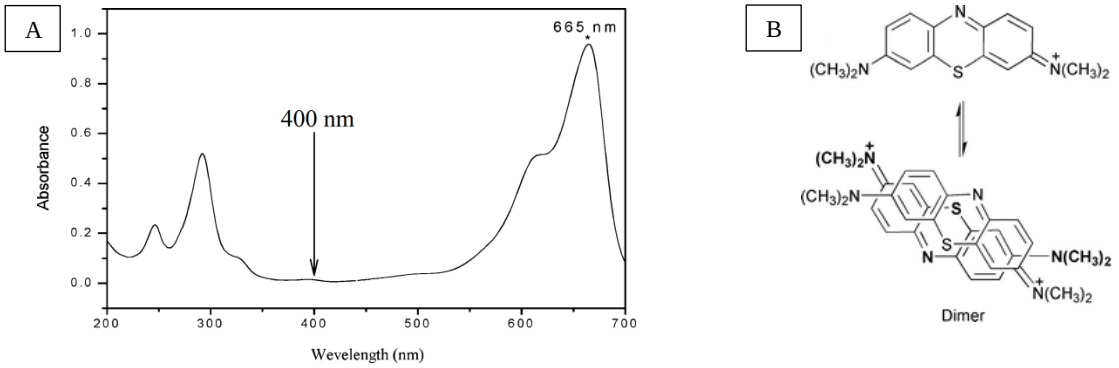

Figure 18 UV-vis absorption spectrum of methylene blue (MB) in aqueous solution (A) [91], and chemical structure of MB monomer and dimer (B) [92].

Therefore, determination of photocatalytic activity of a catalyst in MB decomposition under irradiation with light of 350 nm – 500 nm is not influenced by the dye self-decolorization. However, under visible light MB photobleaches reversibly in the presence of catalyst and sacrificial electron donor (SED) in deaereated solutions. The product of such reaction, colorless leuco-MB (LMB), is unstable in time, and finally returns to initial MB form.

However, in case when molecular oxygen is present in MB solution, the dye undergoes irreversible process, known as photosensitization-autoxidation. In such case, the electrons from dye excited state (MB*) are transferred to CB of semiconductor ($E^0_{MB^{\cdot+}/MB^*} = 0.71$ V), and then to O_2 leading to formation of $O_2^{\bullet-}$, leaving the oxidized form of dye ($MB^{\bullet+}$). The electrons injected to SC may lead to formation of hydroxyl radicals ($^{\bullet}OH$) and those to degradation the dye.

Under visible light the semiconductor of the wide band gap does not play a role of photocatalyst, since it is not a generation source of e^-/h^+, but only a medium for injection of electrons to its surface reactive centers.

Considering MB photodegradation by photoactive material upon its illumination with the light of sufficient energy, the photogenerated electrons are transferred from CB of semiconductor to dissolved oxygen (O_2), to form superoxide radicals ($O_2^{\bullet-}$). On the other hand, the holes participate in a formation of another radical species $^{\bullet}OH$ from H_2O and/or OH^-. Both radicals ($O_2^{\bullet-}$ and $^{\bullet}OH$) can afterwards induce a chain reaction leading

to oxidation of organic compounds [93]. However, because of a rather small difference between the reduction potential of oxygen to superoxide radical ($O_2^{\bullet-}$; –0.28 V *vs.* NHE) and the potentials of the lower edges of conduction bands of TiO_2 (about –0.5 V *vs.* NHE at pH 7) [11,94] and ZnO (about –0.63 V *vs.* NHE) [95], the reducing power of conduction band electrons of these semiconductors is rather low and decolorization of MB more likely occurs via oxidation by holes from the valence band. Methylene blue dissolved in DI water exists in cationic form. Thus, its adsorption on semiconductors depends on pH of the solution and the isoelectric point (IEP) of TiO_2 [96]:

$$pH_{solution} < IEP, \text{ then: } TiOH + H^+ \leftrightarrow TiOH_2^+ \quad (43)$$

$$pH_{solution} > IEP, \text{ then: } TiOH + OH^- \leftrightarrow TiO^- + H_2O \quad (44)$$

MB adsorption/desorption on TiO_2 surface should reach equilibrium within 1 h [97]. However according to ISO procedure [87] one should maintain the catalyst in a contact with MB solution for 24 h before photocatalytic tests. Photodegradation mechanism of MB proceeds *via* first initial stage of N=C bond breaking, which is responsible for observed decolorization, and then *via* sequence of reactions to final simple inorganic compounds as presented in *Figure 19.*

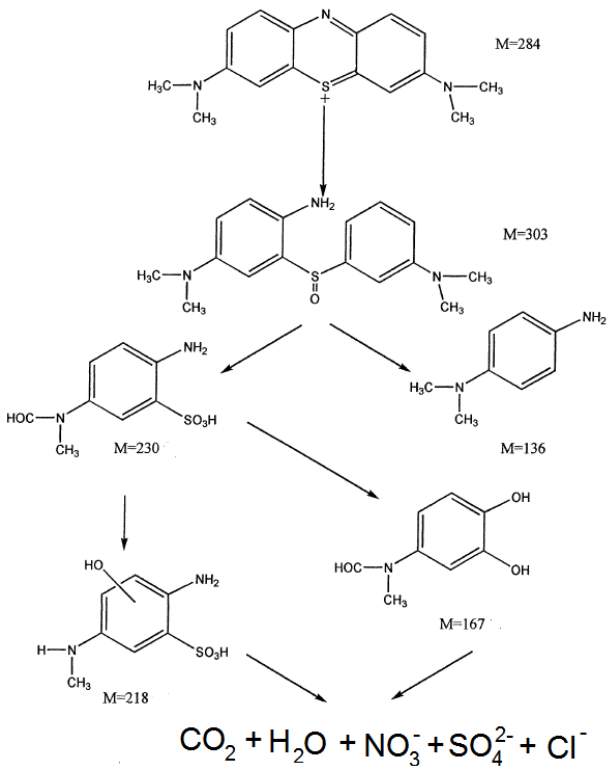

Figure 19 Photodegradation mechanism pathway of methylene blue (MB) [97].

2.1.10. Zinc Oxide: properties

ZnO crystals exist in three forms: cubic rocksalt, zinc blende, or wurzite type (*Figure 20A*). Under normal conditions the thermodynamically stable form of ZnO is wurzite of hexagonal structure with lattice parameters a = 3.25 Å and c = 5.2 Å, and can be obtained in the form of large crystals [98].

Due to the wide band gap of ~ 3.37 eV (at room temperature) [99] and high exciton binding energy of 60 meV, ZnO possess efficient exciton emission [100,101]. Also in ZnO, a high electron mobility of 205 – 400 $cm^2\ V^{-1}\ s^{-1}$ is observed [102], which is higher than that in TiO_2: $10^{-5}\ cm^2\ V^{-1}\ s^{-1}$ [103,104]. One of the major drawbacks of ZnO is its chemical dissolution in acidic and strong basic aqueous solutions (pH > 13).

ZnO nanostructures can be prepared by various methods including: (1) CVD or metal-organic CVD [105], (2) hydrothermal growth [106], (3) electrodeposition [107], or (4) sol-gel [108]. The hydrothermal synthesis is often used leading to formation of ZnO nanorods, and a simplified growth mechanism for such process is depicted in *Figure 20B* [109]. In short, during such wet-chemical synthesis ZnO is formed by building-up from small crystal-by-crystal (seed) growth, preferentially along (001) crystal planes, which is more polarized (by Zn^{2+} and O^{2-} terminal species) then (100) sides of the crystal structure. Such preferential growth is also governed by lowering the high surface energy of (001) planes (as discussed in *Bibliography*, paragraph 2.1.2). The hydrothermal synthesis conditions influence appearance of structural defects (*Figure 21*), i.e. rapid growth at high temperatures or instead of thermal heating microwave heating is used.

Therefore, unlike in case of many other semiconductors, the optical, electronic, and photocatalytic properties of ZnO are consequence of surface and native defects (i.e. vacancies, interstitials, and antisites) [110,111]. The defect ionization energies vary from ~ 0.05 to 2.8 eV [112].

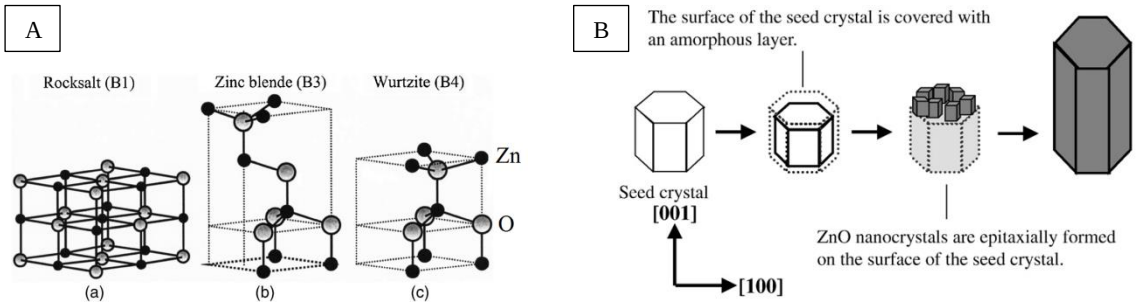

Figure 20 (A) ZnO crystal structure of rocksalt (a), zinc blende (b), and wurzite (c) [113]. A scheme depicting stages of hydrothermal growth mechanism of ZnO nanorods (B) [115].

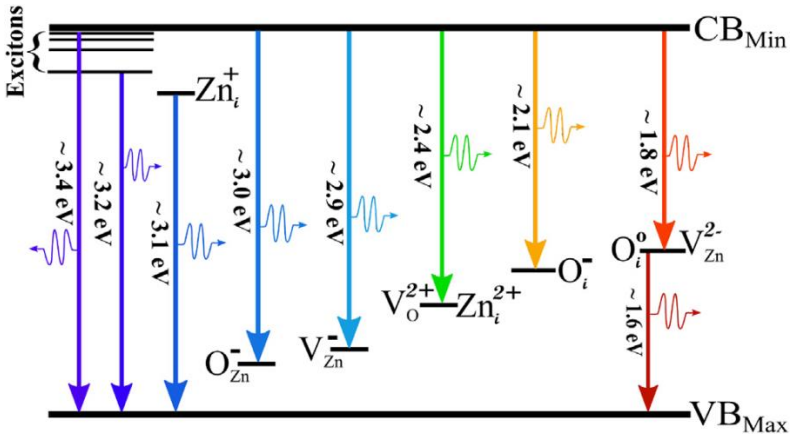

Figure 21 Schematic diagrams of native defect energy levels in ZnO [114]. Notation used: i stands for interstitial site, Zn: zinc, O: oxygen and V is vacancy.

ZnO nanoparticles have been used in various applications such as gas: sensor [115], H_2 storage [116], optical devices [117], (dye-sensitized) solar cells [118] and photocatalysis [119]. Photogenerated electron-hole pairs in ZnO can also be used in polymerization reactions [120], including the Photo-Kolbe reaction [121]. Also, ZnO nanoparticles can be found in cosmetics as a strong UV-blocking component of sunscreen creams [122]. ZnO is one of the most used semiconductors in optoelectronic devices [123]. Moreover, because of this deep green emission (585 nm) the material found its successful application in LED [124] and laser [125] devices.

2.1.11. Titanium Dioxide: properties

TiO_2 exists in nature in three polymorph forms including brookite, anatase, and rutile (*Figure 22*). Among all forms of TiO_2, the most attractive one is metastable anatase, as it generally exhibits higher photocatalytic activity than the others [126]. Brookite can be described as oxygen-deficient form of TiO_2 and similarly to anatase it is less thermodynamically stable than rutile in normal conditions. Those metastable forms of TiO_2 can be transformed into rutile at high temperatures (600 ^{o}C – 800 ^{o}C) [127,128]. However, the exact transformation temperature strongly depends on many parameters i.e. size of particles, preparation conditions, or presence of structural defects [129]. Despite the fact that the mobility of charge carriers is the highest in rutile due to better crystallinity, anatase exhibits more effective use of charge carriers in the reactions since it possesses more defect sites such as oxygen vacancies, which serves as active reaction centers. TiO_2 anatase is an example of n-type semiconductor with possession of dominant native defects (often oxygen vacancies), which can be formed its preparation

[130]. Band gap energy (E_g) in TiO_2 anatase, brookite, and rutile are ~ 3.2 eV, ~ 3.1 eV, and ~ 3.0 eV, respectively [131,132]. While the VB energy level is the same for all forms of TiO_2 (E_{VB} = 2.64 V at pH 7) [133], the position of CB is different for each form. Optical absorption is affected by different electron transition process; which in case of anatase is indirect, while direct in rutile.

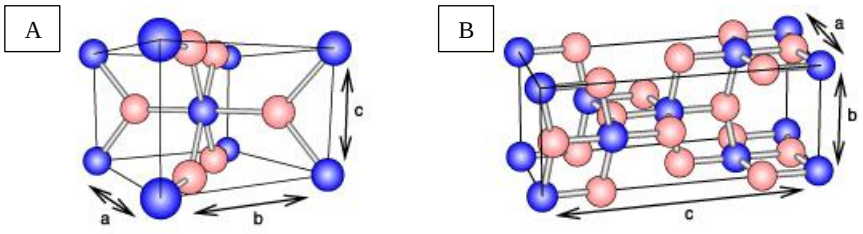

Figure 22 Ball-stick representation of periodic structures of rutile (A) and anatase (B) TiO_2 [134], blue represents Ti, whereas red stands for O ions. Rutile cell distances are a = b = 4.49 Å, c = 3.01 Å, for anatase TiO_2: a =b = 3.77 Å, c = 9.56 Å.

Because of the high refractive index (anatase: 2.45, rutile: 2.70 [135]) and non-toxicity, TiO_2 is used as an outdoor paint component, which also serves as a photocatalytic self-cleaning surface [136,137]. Other popular application fields of TiO_2 include gas sensors [138], optics [139], or ceramics [140]. TiO_2 is chemically stable in a wide range of pH: 1 – 14, and therefore may be used in harsh conditions, and so the most promising field of its application is photocatalytic degradation of organic pollutants [141]. However, TiO_2 suffers from fast recombination of charge carriers [142], and light absorption limited to UV range (E_g ~ 3.0 – 3.2 eV).

Table 1 Basic crystal properties of ZnO and TiO_2.

	ZnO wurzite	TiO_2 anatase
crystal system	Hexagonal [143]	Tetragonal
electron Hall mobility at 300 K ($cm^2\ V\ s^{-1}$)	200	4 – 20 [144]
hole Hall mobility at 300 K ($cm^2\ V\ s^{-1}$)	5 – 180	$2 \cdot 10^{-3}$
E_g	~ 3.3 [145]	~ 3.1
E_{CB}	–0.63	–0.5
E_{VB}	~ 2.5	~ 2.7

2.1.12. Doping of TiO_2

In order to extend the range of light absorption by TiO_2 to visible, a doping by either metals or non-metals was widely used. This may result in appearance of new midgap energy states and in some cases like N-doping in band gap decrease (*Figure 23*). Incorporation of different cations or anions into crystallographic structure of metal oxide, in most cases, also increases its photocatalytic activity [146,147,148,149,150].

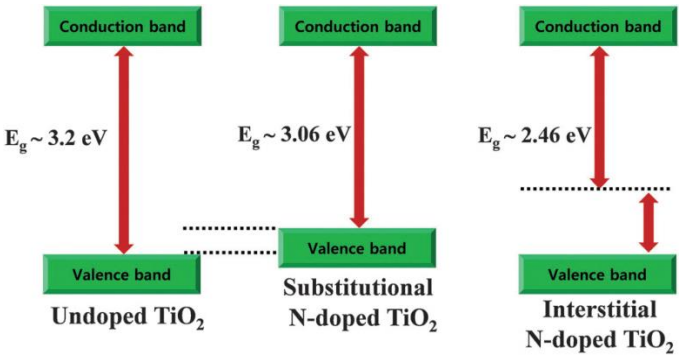

Figure 23 Band structure of TiO_2 undoped TiO_2 and influence of N-doping on band gap energy value (E_g) [151].

TiO_2 can be doped with metal cations such as Cr^{3+} [152,153], Cu^{2+} [154], Ni^{3+} [155], Fe^{3+} [156], $V^{4+/5+}$ [157], Nd^{3+} [158], Co^{2+} [159], and/or with non-metal anions, i.e. N [160,161], S [162], I [163,164], F [165], P [166], or B [167,168]. Among all anionic dopants, nitrogen seems to be the most popular, since the absorption of visible light is higher for N-doped TiO_2 than for other dopants i.e. S-doped TiO_2, and finally leads to better photocatalytic activity of the modified semiconductor [169]. Co-doping with two different anions is also possible and the doped material exhibits higher activity than each single anion-doped SC, i.e. N-,S-doped TiO_2 [170]. Mixed simultaneous co-doping (cationic and anionic) also promotes higher activity, i.e. Ce-,N-doped TiO_2 [171], Ni-,N-doped TiO_2 [172], or Nb-,N-doped TiO_2 [173]. The crucial factor that influences photoactivity is the level of doping; either too low or too high is undesirable. Doping level of TiO_2 is usually around or less than 1%, and in case of N-doping it was found that approx. 0.25% is the optimal value to achieve the highest catalytic activity, $TiO_{1.9925}N_{0.0075}$ [174].

Though N-doping of TiO_2 always results in the increase of absorption towards visible light but it does not lead in parallel to systematic enhancement of photocatalytic activity [175,176]. In case of photo-electrolysis of water on N-doped TiO_2 electrodes a

key issue is the photocurrent stability [177]. Combination of experimental (XPS) and theoretical (density of states (DOS) calculations) studies allows to understand the nature, role of N-doping and shed some new light on importance of doping methods [178].

N-doping can be achieved by different methods and techniques, most popular are: (1) liquid phase method (sol-gel) [179,180]. In such approach, nitrogen is incorporated into TiO_2 lattice during its precipitation. Prior to this, TiO_2 precursor, such as titanium(IV) propoxide is dissolved in alcohol medium in the presence of a nitrogen precursor. Examples of nitrogen precursor are inorganic salts NH_4Cl [181], urea [182], or $NH_{3(aq.)}$ [183]. (2) Annealing of TiO_2 at elevated temperatures (500 ^oC – 700 ^oC) in a flow of inert gas containing nitrogen precursor, i.e. ammonia [184], guanidine hydrochloride [185]. Other methods include: (3) electrochemical N-doping under constant potential in a solution containing nitrogen precursor, such as triethylamine, urea [186,187], (4) hydrothermal synthesis methods [188,189], (5) nitrogen incorporation in a plasma conditions at 400 ^oC [190].

All methods incorporate nitrogen in substitutional and interstitial sites (*Figure 24A*, and *24B*). According to the literature, for N1s core binding energy within the range of 396 eV – 398 eV corresponds to nitrogen incorporated into metal oxide structure as N–Ti–N, therefore substituting oxygen. Also, the nitrogen state was defined as either anion [191] or atom [192]. Binding energies of about 400 eV are assigned to Ti–O–N or Ti–N–O linkage, characteristic of interstitial N atoms [193,194]. Also, N1s peaks of about 402 eV were ascribed to chemisorbed N_2 or adsorbed organic species [195]. Substitutional nitrogen introduces N2p energy levels little above VB of TiO_2 (0.14 eV), while interstitial energy levels are located higher (0.73 eV above TiO_2 VB) [196,197,198]. Substitutional is a negative oxidation state, interstitial is positive.

Studies show that the increased absorption of visible light is indeed due to appearance of new ‘nitrogen-related’ energy levels but also due to additional oxygen vacancies energy levels formed in a SC [199], according to the reaction scheme:

$$TiO_{2-2x}N_{2x} \rightarrow TiO_{2-3x}N_{2x} + xV_O + \tfrac{1}{2}xO_2 \qquad (45)$$

As postulated, oxygen vacancies increase the light absorption in visible range and the role of nitrogen incorporation is also prevention of reoxidation of formed oxygen vacancies, and this may lead to the increase of material photoactivity [200]. However, N-

doping may not always results in increase of photoactivity despite the fact of increased light absorption. An explanation of lowering photoactivity was postulated, based of EPR results [201], taking into account formation of two kinds of nitrogen-related states above VB of TiO_2: paramagnetic ($N_b^{\bullet}$) and diamagnetic (N_b^{-}). The reactions with oxygen at each state are different and can be presented as follows:

$$N_b^{-} + O_2 \rightarrow N_b^{\bullet\text{”}} + O_2^{\bullet-} \quad (46)$$

$$N_b^{\bullet} + O_2 \rightarrow N_b^{+} + O_2^{\bullet-} \quad (47)$$

where, $O_2^{\bullet-}$ is paramagnetic superoxide radical, $N_b^{\bullet\text{”}}$, N_b^{+} are oxidized paramagnetic centers, and N_b^{-} is diamagnetic energy state. Holes can be only localized at $N_b^{\bullet}$ or N_b^{+} centers which explain their low reactivity due to strongly suppressed mobility.

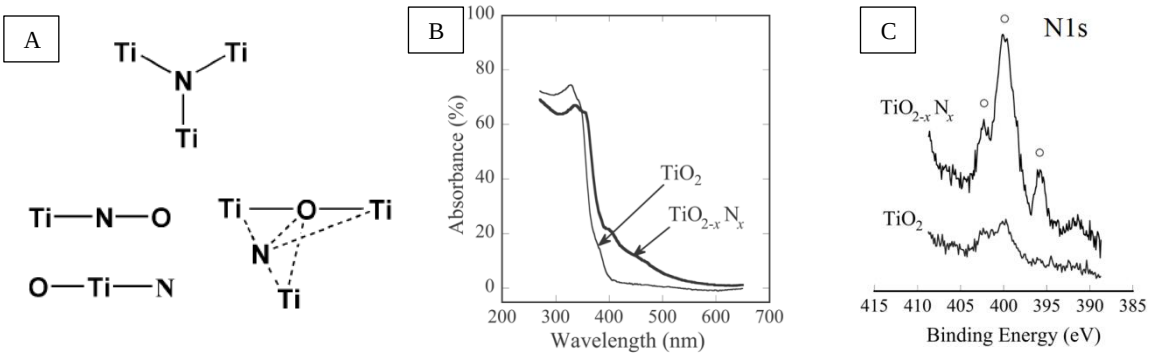

Figure 24 Titanium and nitrogen bonding in substiutional (A), and interstitial (B) positions [202]. UV-vis absorbance spectra (C), and XPS spectra (D) of bare and N-doped TiO_2 [203].

2.1.13. Plasmonic effects of noble metal NPs

2.1.13.1. Plasmonic metals in visible range

Interaction of light with conducting electrons in solids results under certain conditions in appearance of collective oscillation of valence electrons which is referred to as surface plasmon resonance (SPR) (*Figure 25A*). If such oscillation is excited in the particle whose size is smaller than the length of light, the phenomenon is called localized surface plasmon resonance (LSPR). The frequency range at which LSPR phenomenon occurs depends on the chemical nature of the particle. While in the oxides like RuO_2 or ITO the resonance frequency is located in the IR range, in Ag, Au and Cu the LSPR can be excited by visible light.

LSPR can be used to enhance the light conversion by a semiconductor by associating it with a metal nanostructure. Three different mechanisms have been proposed to explain the increase of photocatalytic activity [204]:

(1) Hot carrier injection

(2) Plasmon-induced resonance energy transfer (PIRET)

(3) Light rapping enhancement

Below we present in more detail these three mechanisms along with the conditions in which they are realized.

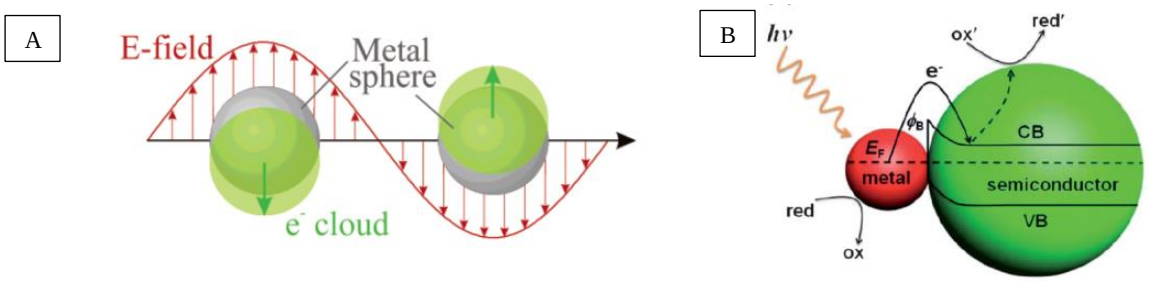

Figure 25 Scheme depicting plasmon oscillation of electron 'cloud' in a metal sphere particle (A) [205]. Noble metal (Me) nanoparticle (red) and n-type SC (green) energy diagram level showing formation of Schottky barrier φ_B at Me/SC interface and plasmonic electron transfer from Me to CB of SC [206].

2.1.13.2. Mechanism of action of plasmonic NP:

1) Hot electron injection

Regarding aspect of band positions in SC and energy levels of metal NPs, the Fermi level for noble metals is located approx. at 0 V *vs.* NHE, in case of Au it is slightly more positive ($E_{F,Au}$ = 0.45 V). The energy of plasmonic resonance varies from 1.0 eV to 4.0 eV; therefore, electron transfer from noble nanoparticles to CB of SC is possible. Association of a SC and Me NPs causing Fermi level energies of Me NPs and SC to equalize and formation of Schottky (φ_B) energy barrier at SC/Me interface (*Figure 25B*).

Once formed LSPR exists for about 30 fs. After this time the plasmon dephases i.e. the electron oscillations lose their collective nature. In small particles (< 15 nm) this process results in formation of so-called hot electrons having excess of energy corresponding to the plasmon frequency (560 nm or 2.2 eV in the case of Au NPs). Given that the difference between $E_{F,Au}$ and E_{C,TiO_2} is about 1 eV, the hot electrons are able to overcome

the Schottky barrier and can be injected into the conducting band of TiO_2 (*Figure 26*). These electrons can then be involved in the photocatalytic reactions.

For example, a degradation of organic pollutants can be presented as follows [207]:

$$Ag_{NPs} + h\nu \rightarrow Ag_{NPs}^* \quad (48)$$

$$Ag_{NPs}^* + TiO_2 \rightarrow Ag_{NPs}^{\bullet+} + TiO_2(e^-) \quad (49)$$

$$TiO_2(e^-) + O_2 \rightarrow TiO_2 + O_2^{\bullet-} \quad (50)$$

$$Ag_{NPs}^{\bullet+} + Cl^- \rightarrow Ag_{NPs} + Cl^0 \quad (51)$$

Apart from formation of previously described photocatalytic reactivity of $O_2^{\bullet-}$, also Cl^0 can cause degradation of organic pollutant.

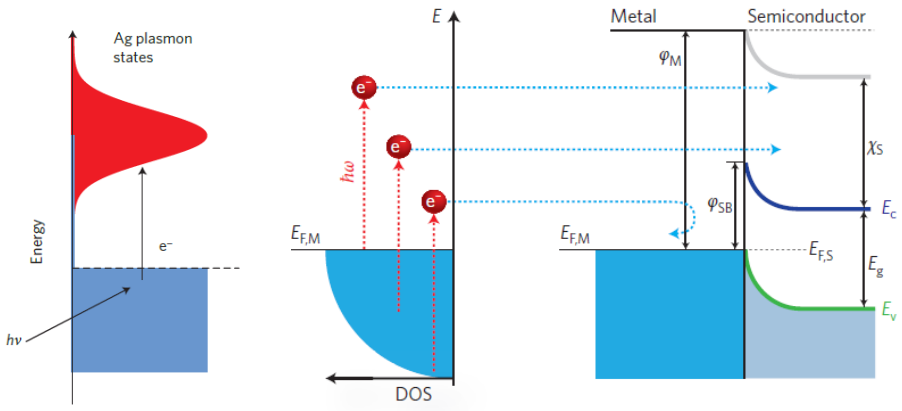

Figure 26 Scheme depicting hot electron transfer from plasmonic nanoparticle with excited electron above Fermi level of metal ($E_{F,M}$). Only these electrons whose energy can overcome Schottky barrier ($\varphi_{SB} = \varphi_M - \chi_S$), where φ_M is work function of a metal, χ_S is electron affinity of the semiconductor, can be transferred to semiconductor [208].

2) Plasmon induced resonance energy transfer (PIRET)

Due to LSPR the electric field around the nanostructure is strongly amplified (up to 10^6 times) creating so-called hot spots. The energy of this field can be transferred to SC particle through a resonant non-radiative transfer which results in increase of the rate of electron-hole generation. This phenomenon occurs only if the light absorption of SC overlaps with the plasmonic band of the metal. For this reason, for Au NPs (plasmon resonance at ~ 560 nm) the PIRET is observed only when they are associated with N-doped TiO_2 but not with pure TiO_2 which does not absorb light in visible range (see

below). Another important condition for optimal PIRET is the distance between the metal NP and SC. Even if the effect is observed for the metal particles in direct contact with the surface of SC, the enhancement is stronger when two counterparts are separated by 5 nm – 7 nm of a dielectric layer (*Figure 27*).

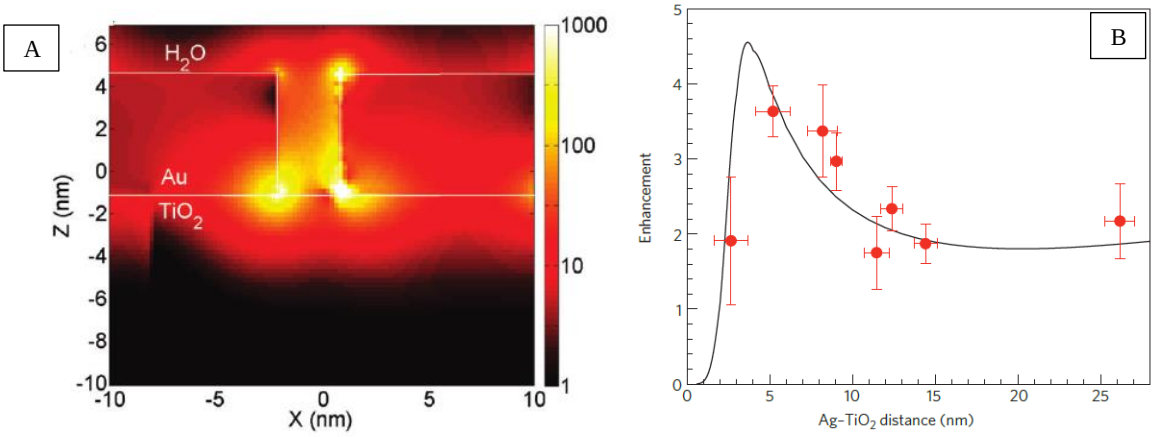

Figure 27 Local field intensity enhancement of two proximate particles of Au/TiO_2 (A) and the enhancement dependence of light utilization on Me NPs and semiconductor distance (B) [209].

3) Light trapping enhancement

Photocatalytic activity of a metal-SC composite can be also enhanced by light scattering on large plasmonic particles (> 30 nm) i.e. on Ag nanocubes (of edge length 118 ± 25 nm), which induce additional absorption of light by increasing the light path through the material [210] (*Figure 28*). The light in such composite material undergoes multi-reflection like in an ensemble of mirrors that ultimately increase the overall light absorption.

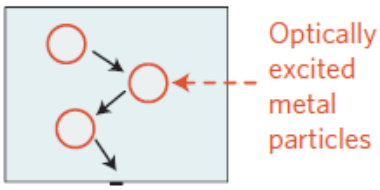

Figure 28 Light scattering on large (> 30 nm) plasmonic nanoparticles – absorption enhancement through increasing light penetration path [211].

2.1.13.3. Preparation of Au nanoparticles on semiconductor surface

Noble metal nanoparticles can be prepared and deposited on semiconductor surface by the following methods:

1) Precipitation-deposition; i.e. Au aqueous precursor solution with Au^{3+} ($AuCl_4^-$) with adjusted pH by i.e. NaOH, $NH_3 \cdot H_2O$. Then, TiO_2 is suspended or immersed in the

solution, after some time taken out and dried in air. Then, in hydrogen atmosphere at 200 – 400 ^{o}C are annealed to form metallic gold Au^0 [212,213].

2) Photoreduction method; in such approach semiconductor (i.e. TiO_2, ZnO, α-Fe_2O_3, WO_3, etc.) is irradiated by UV light in noble metal precursor solution. Electrons photogenerated in SC take part in reduction of i.e. Au-precursor (i.e. $Au(OH)_xCl_{4-x}]^-$, pH adjusted from $AuCl_4^-$) and simultaneously are deposited on the surface [214,215,216].

3) Other methods including chemical reduction of gold precursor i.e. $HAuCl_4$ aqueous solution with addition of $NaBH_4$ in a presence of SC support material [217], physical vapor deposition [218], or ion exchange [219] i.e. as following in reaction scheme:

$$BiOBr + Ag^+ \rightarrow AgBr + BiO^+ \quad (52)$$

2.1.13.4. Examples of plasmonic metal nanoparticles/TiO_2 composites

Noble metal nanoparticles can work specifically better in degradation of selected compounds, i.e. methanol, or nitrobenzene [220], whereas for dichloropropionic acid (DCA) cause the decrease of degradation rate [221]. Photocatalytic performances regarding utilization of SC/Me NPs in degradation of organic pollutants are summarized in Table 2, while examples in photoelectrochemical application, such as water oxidation, are presented in Table 3. Also the most interesting examples in photoelectrochemical applications are described in more detail below.

Linic and Ingram [222] demonstrated preparation of N-TiO_2, Ag/N-TiO_2, and Au/N-TiO_2 photoanodes for water splitting under visible light irradiation. Ag cube-like particles had edge length of 118 ± 25 nm, while spherical Au particles were 24.5 ± 4.5 nm in diameter and both were prepared by polyol synthesis procedure. It was shown that Au-, and Ag-loaded catalysts exhibited plasmonic peaks approx. at 530 nm and 650 nm for Au, and 410 nm and 590 nm for Ag (*Figure 29A*).

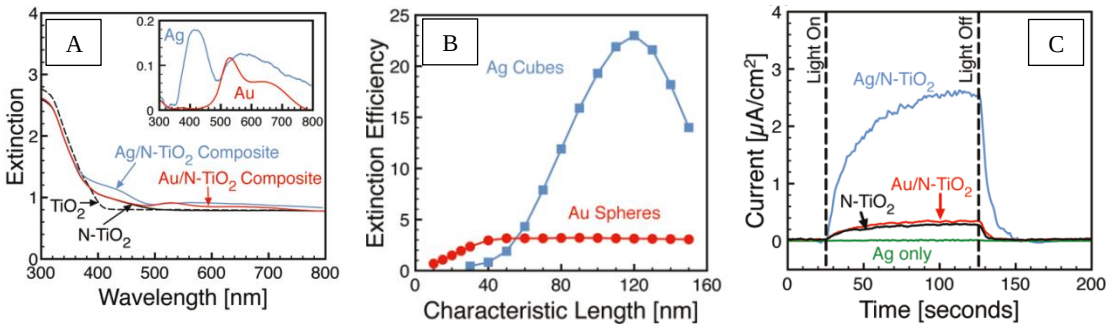

Figure 29 Optical properties of TiO_2, N-TiO_2, Au/N-TiO_2, and Ag/N-TiO_2 composites (A), extinction efficiency as function of Ag-cube edge length or Au-sphere radius within the 400 nm – 500 nm wavelength range (B), photocurrent response of photoelectrodes under 400 – 900 nm irradiation (C) [219].

It was found that the energy of Au surface plasmon resonance (SPR) was not high enough to form e^-/h^+ pairs by radiative energy transfer. In case of Ag (inset *Figure 29A*) the improved formation of e^-/h^+ in N-TiO_2 was due to strong light scattering on Ag nanocubes. However, it was found that extinction efficiency depends on the size and shape of the particle (*Figure 29C*). Also local electromagnetic field enhancement was observed on Ag resulting in higher formation of e^-/h^+ in close-contact N-TiO_2, ultimately resulting in improving water splitting efficiency (*Figure 29B).*

Cronin *et al.* [223] reported preparation of TiO_2 nanotube (NT) electrode by anodization of 0.01 cm thick Ti foil with pore diameter of ~ 40 nm, and a further covered with 5 nm Au thin layer by electron beam evaporation. The samples were employed in photocatalytic water splitting under 663 nm visible) monochromatic light irradiations. It was found that photocurrent observed for Au/TiO_2 (0.3 μA) was strongly enhanced (by factor of 66) in a comparison with bare TiO_2 (4.5 nA, *Figure 30A*). Also photocurrent enhancement ratio was shown to be the highest in visible range with the maximum of about 7 located at around 650 nm excitation wavelength (*Figure 30B*).The observed photocatalytic improvement was assigned to the presence of plasmonic Au NPs which exhibited strong local electromagnetic field enhancement and short minority carrier diffusion length in TiO_2.

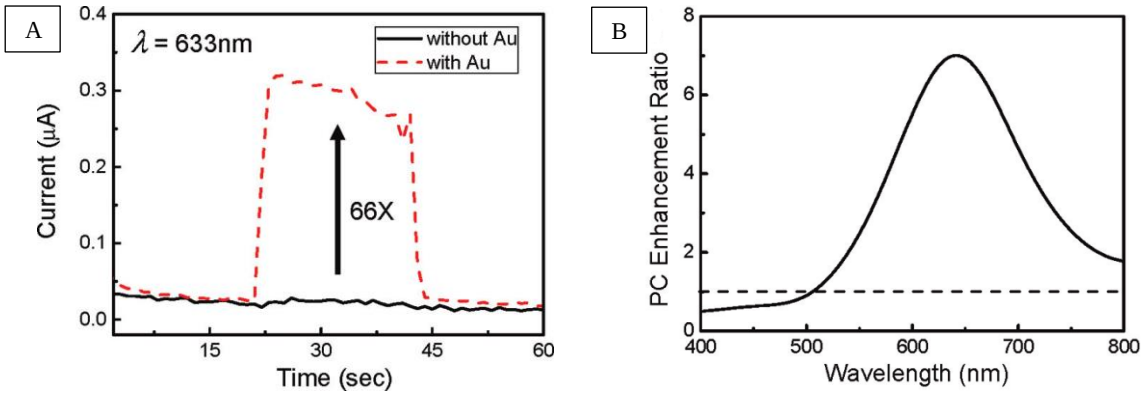

Figure 30 (A) Photocurrent transient obtained on TiO_2 nanotube (NT) electrode (black solid line), and for the same electrode after deposition of 5 nm Au layer (red dashed line). (B) Photocurrent (PC) enhancement ratio spectrum obtained from comparison of results on Au/TiO_2(NT) and bare TiO_2(NT) [222].

Rosseler *et al.* [224] reported hydrogen production from photoelectrochemical water splitting on Pt- or Au-TiO_2(anatase/rutile) composites performed in pure water as a hydrogen source, and methanol as a sacrificial additive agent under solar light irradiation. Prepared TiO_2 with 1:1 anatase to rutile ratio was controlled by addition of polyoxyethelene(10)cetyl ether (Brij56) to be also compared with P25 commercial catalyst. It was shown that non-decorated TiO_2 exhibits negligible water splitting efficiency, while in contrast a small decoration of TiO_2 with Pt (wt. 2%) or Au (wt. 2%) significantly enhanced H_2 production from water splitting, showing also higher efficiency with Au than with Pt (*Figure 31*). The higher efficiency for Au/TiO_2 than for Pt/TiO_2 was ascribed to almost much higher reversible reaction of water splitting on Pt than on Au, and nature and concentration noble metal NPs on SC and the contact between them.

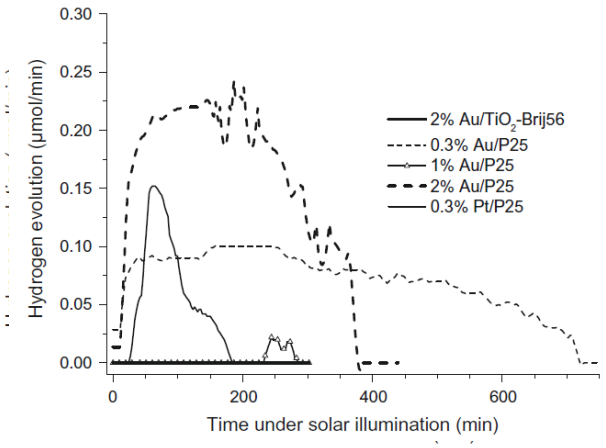

Figure 31 Hydrogen evolution on Au/TiO_2 and Pt/TiO_2 photocatalysts in photoelectrochemical water splitting with different metal/TiO_2 weight ratios [223].

Table 2 Photocatalytic degradation of organic pollutants on plasmonic Me NPs/TiO_2 composites.

Type of composition	Preparation method of noble NPs	Photocatalytic test	Irradiation Type	Ref.
Ag/TiO_2	Ag on TiO_2 was heated in N_2 at 800 °C to form Ag NPs	MB decomposition increased by a factor of 7 with comparison to TiO_2	10 W black-fluorescent lamp (peak emission 380 nm)	[225]
$Au/TiO_2/SiO_2$	Turkevich method	MB solution after 2.5 h complete decolorization on SiO_2/TiO_2/Au, 20% decolorize on SiO_2/TiO_2	Xe lamp with 420 nm cut-off filter, 450 W (visible light)	[226]
Ag/TiO_2	Ag NPs were synthesized via the citrate reduction method	MB decolorization on Ag/TiO_2 enhancement factors over bare TiO_2 with: a) Ag-nanowires by 2.1; b) Ag-spheres by 2.4; c) Ag-nanocubes by 3.8	100 W light source with λ of 365 nm (fwhm of 4 nm)	[227]
Ag/TiO_2	Ag-ion-loaded TiO_2, and then reduced with $NaBH_4$	MB decolorization under UV light: TiO_2: k = 0.0186 min^{-1}; Ag/TiO_2: k = 0.0723 min^{-1}; and under visible light: TiO_2 k = 0.007 min^{-1}; Ag/TiO_2 k = 0.029 min^{-1}	150 W xenon lamp with 400 nm UV cut-off filter and 36 W UV lamp	[228]
Au/TiO_2	Au NPs photodeposition from $HAuCl_4$	2-propanol oxidation (5 vol %) Au/TiO_2 activity 0.5 μmol h^{-1}; TiO_2 0.04 μmol h^{-1}	visible light irradiation λ > 450 nm	[229]
Au/TiO_2 Ag/TiO_2 Pt/TiO_2	Ti^{3+}-ion-assisted UV-reduced TiO_2, additions: $HAuCl_4$, $AgNO_3$, or H_2PtCl_6	Benzene oxidation, for 180 min, yields: Au/TiO_2 ~ 60%; Pt/TiO_2 ~ 30%; Ag/TiO_2: negligible	300 W Xe lamp with UV cut-off filter, visible light (λ > 400 nm)	[230]
Au/TiO_2	Sol-gel: titanium(IV) butoxide and tetrachloroauric acid - $HAuCl_4$	MB decolorization (165 mL aqueous, 12 mg /L): pseudo-first-order kinetic constant (k, min^{-1}): pure TiO_2: 0.0144 ; 0.5% wt. Au/TiO_2 : 0.052	110 W high-pressure sodium lamp, visible light of 400 – 800 nm	[231]
Au/TiO_2 Pd/TiO_2 Pt/TiO_2	Me@TiO_2 core/shell, hydrothermal treatment of TiF_4 with $HAuCl_4$, or H_2PtCl_6, or $PdCl_2$	Rhodamine B (RhB) decolorization, apparent first-order constant (k, h^{-1}): Au/TiO_2: 0.83; Pd/TiO_2: 2.29; Pt/TiO_2 : 0.96 ; P25 : 0.72	300 W xenon lamp cut off filter for visible light, λ > 400 nm	[232]

Table 3 Photoelectrochemical activity of Me NPs/TiO_2 composite electrodes.

Type of composition	Preparation method	Photoelectrocatalytic test	Irradiation Type	Photoelectrochemical activity	Ref.
Au/TiO_2	Optical transparent electrodes coated with TiO_2 (2.5 cm^2) ~ 10 μm thick layer immersed in toluene 9 mM Au colloid	0.05 M NaOH *vs.* SCE	150 W xenon lamp, UV irradiation, λ > 300 nm	Photocurrent under constant potential : +0.75 V : Au/TiO_2 : ~ 0.42 mA; TiO_2 : ~ 0.09 mA –0.95 V : Au/TiO_2 : ~ 0.37 mA; TiO_2 : ~ 0.04 mA	[233]
Au/TiO_2 $Pt\text{-}Au/TiO_2$	One-pot photodeposition synthesis under λ = 365 nm and 310 nm on P25 TiO_2 from $HAuCl_4$, H_2PtCl_6	0.5 M KOH 0 V *vs.* Ag/AgCl	UV (400 W Hg vapor lamp, 240 mW cm^{-2}), solar simulator 300 W with AM1.5 (100 mW cm^{-2})	Photocurrent under UV : Pt-Au/TiO_2: ~ 70 μA cm^{-2}; Pt/TiO_2: ~ 38 μA cm^{-2} Au/TiO_2: ~ 20 μA cm^{-2}; TiO_2: ~ 13 μA cm^{-2} Photocurrent under AM1.5 : Pt-Au/TiO_2: ~ 2.2 μA cm^{-2}; Pt/TiO_2: ~ 0.3 μA cm^{-2} Au/TiO_2: ~ 1.5 μA cm^{-2}; TiO_2: none	[234]
Au/TiO_2	TiO_2 nanotubes (NT) prepared by anodization of Ti foil, Au by pulse electrodeposition	PC: 0.1 M Na_2SO_4 under 0.6 V *vs.* SCE, and also PEC: degradation of MO	300 W Xe lamp with ultraviolet filter (λ > 420 nm)	Photocurrent: Au/TiO_2 : 7 μA cm^{-2} ; TiO_2 : 1 μA cm^{-2}, MO photoelectrodegradation: Au/TiO_2 : 0.156 h^{-1} ; TiO_2 : 0.008 h^{-1}	[235]

2.2. Properties of semiconductor-based composites

2.2.1. Shape engineering

The advantages of composite material over its bare components might be the increased light absorption in the visible range, and also more effective charge separation due to the presence of the interface. Among many morphological combinations of components, some general types can be distinguished, such as simple blends, one material decorated with another, or core/shell structure (*Figure 32*). In the first type randomly shaped and sized particles are freely mixed together without well-defined interface; however the simplicity of preparation of such composites is their strong advantage. The second type, also a powder, the composite loaded particles is more sophisticated than the previous example and requires more effort to prepare. In such case, one material is deposited on another one with specific intention of architecture or morphology. The core/shell materials possess developed interfacial contact between two components, which may result in maximizing enhancement effects. Therefore, for the purposes of desired application one can attempt to optimize composition morphology and architecture to achieve the required properties.

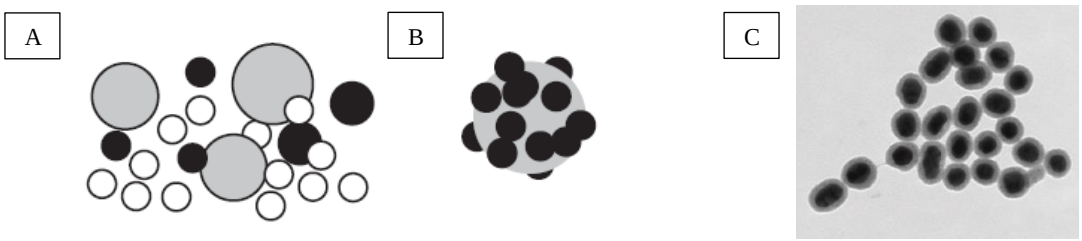

Figure 32 Possible combinations of two materials: a simple mixture (A), loading (B), core/shell (C) [236].

2.2.2. Band gap alignment

In general, one can consider three types of heterojunctions in the composites consisted of two different semiconductors (SC_x/SC_y), taking into account arrangement of their valence and conduction bands. In the first type (I), E_{CB} of SC_1 is located below E_{CB} of SC_2 and therefore, the photoexcited electrons may be transferred from CB of SC_2 to CB of SC_1, towards less negative potential energy, while the holes are injected in opposite direction from VB of SC_1 to VB of SC_2, (*Figure 33A*). For heterojunction of type II, where CB of SC_3 is below CB of SC_1, the electrons are moved from SC_1 to SC_3, and holes in opposite direction (*Figure 33B*). Type III heterojunction consists of SC_1/SC_4,

where CB and VB of SC_4 are located inside the band gap of SC_1, and owing to this, the electron and hole are both transferred from SC_1 to SC_4 (*Figure 33C*).

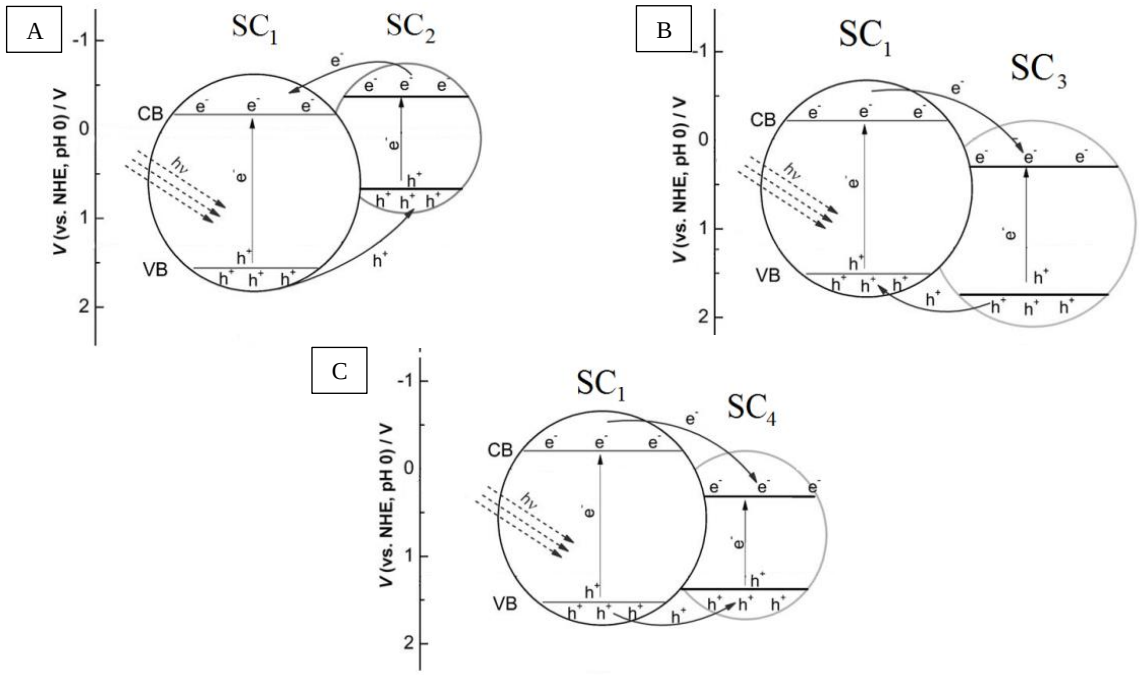

Figure 33 Schemes depicting possible heterojunction configurations in SC_1/SC_2 type I (A), SC_1/SC_3 type II (B), and SC_1/SC_4 type III (C),adapted from [237].

According to the literature, ZnO/TiO_2 composite can be ascribed to the type I, if TiO_2 is designated as SC_1 and ZnO as SC_2. There are also many other configurations available, and prominent examples are summarized in Table 4. Among them, some configurations are more popular than the others. For example TiO_2/CdS, belongs also to the type I, and often applied in H_2 production under visible light [238,239,240] due suitable energy bandgap of CdS (2.4 eV) and efficient charge carriers separation at the semiconductors interface. Recently, also a great attention has been dedicated to configurations involving graphene, i.e. TiO_2/graphene [241] also applied in H_2 generation, despite its unclear yet designation type [242].

Apart from SC_x/SC_y heterojunction composites, a commercial TiO_2 powder, known as P25 Degussa; consisted of physical mixture of rutile (20% wt.) and anatase (80% wt.), is a prominent example of so-called intercrystalline phase junction photocatalyst. In this type of composite both materials are of the same SC nature kind (i.e. TiO_2), but owing to differences in CB positions of different phases (anatase and rutile) the charge recombination is hindered [243]. CB positioning difference is very small

(i.e. anatase/rutile TiO_2 is about 0.2 eV) but high enough to improve the electron transfer from anatase to rutile (which is well crystallized – less defective), or the electrons migrate from well crystallized (less defective) rutile to the surface states in more defective anatase. Due to these effects, higher photocatalytic activities are observed for P25 than for each separated material [244,245], and for different weight ratios of anatase/rutile. Similarly to P25, the difference between the band energy alignment of ZnO and TiO_2-anatase is not significant. However, association of these two oxides (ZnO, TiO_2) has been shown to possess very promising photocatalytic properties in various applications, as in the case of widely used commercial P25.

Table 4 Examples of different types of SC_x/SC_y with different VB and CB positioning used in photocatalytic and photoelectrocatalytic applications.

Composite	Type (when SC_1 is TiO_2)	Ref.		Composite	Type (when SC_1 is ZnO)	Ref.
TiO_2/CdS	I	[246, 247]		ZnO/CdS	I	[248]
TiO_2/ZnO	I	[249,250]		ZnO/SnO_2	II	[251]
TiO_2/CeO_2	I	[252]		ZnO/CuO	III	[253]
TiO_2/Bi_2O_3	I	[254]		ZnO/CeO_2	II	[255]
TiO_2/SnO_2	II	[256]		ZnO/ZrO_x	Reverse III	[257]
TiO_2/WO_3	III	[258,259,260]		ZnO/ZnS	II	[261]
TiO_2/ZrO_2	Reverse III	[262,263]				
TiO_2/CuO	III	[264]				

2.2.3. ZnO/TiO_2 composites

In this chapter the properties of ZnO/TiO_2 composites will be described. Due to a large number of publications on this subject our description cannot be exhaustive. Instead, we tried to analyze the most representative works and formulate the general trends concerning the photocatalytic and photoelectrochemical properties of this type of composites.

The first section of this chapter (2.2.3.1) deals with non-supported composites in which the microstructure of the composites is not always precisely known. Then, the nanostructured and supported composites are described (2.2.3.2) in which one of the oxides is present in the form of nanorods or nanotubes. The section 2.2.3.3 is devoted to the materials based on supported ZnO nanorods decorated with TiO_2 nanoparticles whose structure is similar to that of materials studied in the present thesis. Finally, in section 2.2.3.4 several examples of ZnO(core)/TiO_2(shell) composites doped with nitrogen and/or decorated with Au NPs will be described.

2.2.3.1. Non-supported ZnO/TiO_2 composites

The examples of the works describing the photocatalytic properties of various unsupported ZnO/TiO_2 composites are given in Table 5. Because of unsupported nature of these materials the photoelectrochemical properties were not studied and only their photocatalytic activities were measured. Analysis of this data shows that despite a widely varying preparation conditions almost in all cases the combination of ZnO and TiO_2 allows to obtain a gain in catalytic activity in degradation of organic species of different nature under UV light. Despite the fact that in some cases the increase is not very significant, these studies show that ZnO/TiO_2 combination is definitely worth being studied in detail.

To better understand the factors influencing the performance of such materials and to gain insight in the mechanism of this enhancement one needs to work with the composites having well-defined microstructure. Growing these materials on conducting support like ITO or FTO allows also to study them by electrochemical methods. That is why many attempts to synthesize such supported composites with well-defined microstructure and to characterize their properties have been done.

Table 5 Photocatalytic properties of ZnO/TiO_2 non-supported composites

Type of ZnO/TiO_2 composition	Preparation method	Photocatalytic test	Irradiation type	Decolorization, degradation, or absorbance decrease:	Ref.
Powder: spherical shape	homogenous hydrolysis from $Zn(CH_3COO)_2$ and $Ti\{O(C_4H_9)\}_4$	MO decolorization, catalyst loading 2.5 g dm^{-3}	125 W high pressure Hg lamp λ = 365 nm	MO decolorization after 20 min: ZnO/TiO_2: ~ 88%; ZnO: ~ 50%; TiO_2: ~ 75%	[265]
Powder: highest activity for wt. ratio 1:4; $ZnO:TiO_2$	solid-state dispersion	4-chlorophenol (25 mg dm^{-3}), catalyst loading 100 mg /50 ml	16 W UV-B lamp λ: 303 nm – 578 nm	4-chlorophenol degradation degree after 75 min): ZnO/TiO_2: ~ 100%; ZnO ~ 75%; TiO_2 ~ 84%	[266]
Nanofibers: best results for ZnO/TiO_2 (wt. %) 84.2/15.8	electrospinning with $Zn(CH_3COO)_2$ and $Ti\{OCH(CH_3)_2\}_4$	Probe compounds: 8 ppm RhB, and 20 ppm phenol	12 W (RhB decolor.), 24 W (phenol degrad.) UV lamp, λ = 365 nm	Degree of RhB decolorization after 24 min: ZnO/TiO_2: ~100%; TiO_2: ~ 65% Degree of phenol degradation after 20 h: ZnO/TiO_2: ~ 75%; TiO_2: ~ 60%	[267]
Powder: ZnO/TiO_2 flowers/deposit	ZnO hydrothermally prepared mixed with P25	MB (10 ppm 25 ml), 20 mg catalyst loading	UV irradiation λ = 365 nm	MB decolorization after 180 min: ZnO/TiO_2: ~ 70%; ZnO: ~ 48%; TiO_2 (P25): ~ 65%	[268]
Powder: Nanostructured hollow mixed spheres	coating of functionalized polystyrene beads with ZnO and TiO_2	Rhodamine 6G: 10^{-5} M, 70 ml, catalyst loading: 60 mg	High pressure Hg (Xe) lamp, UV-vis irradiation	Rhodamine 6G complete decolorization after: 20 min (ZnO/TiO_2); 75 min (ZnO); 100 min (TiO_2)	[269]
Powder: ZnO/TiO_2 in the form of frame network	phase selective growth of ZnO (5 mg) on TiO_2 anatase (5 mg) faces	MO (10 mg dm^{-3}, 50 mL), process carried out in 10 ^oC, catalyst loading 10 mg	300 W Xe lamp λ: 220 nm – 420 nm	MO decolorization after 30 min: ZnO/TiO_2 (frame network): ~85% ZnO/TiO_2 (mixed particles): ~ 53%	[270]
Powder: TiO_2(anatase)/ZnO from 10% molar Zn^{2+} concentration	TiO_2 prepared by hydrolysis of $TiCl_3$, ZnO formed by impregnation method from $Zn(NO_3)_2$	4-nitrophenol (20 mg/L), 0.5 L, catalyst loading 1 g/L	25 W Hg lamp, photon flux 13.5 mW cm^{-2}	zero-order rate constant: ZnO/TiO_2: 56 $\cdot 10^6$ M h^{-1} TiO_2: 52 $\cdot 10^6$ M h^{-1} ZnO: 18 $\cdot 10^6$ M h^{-1}	[271]
Powder: ZnO/TiO_2 (non-supported NRs)/NPs)	hydrothermal ZnO mixed with sodium titanate and kept for 24 h at 180 ^oC	MB (20 ppm, 200 ml), catalyst loading 80 mg	500 W high pressure Hg lamp λ = 368 nm	Pseudo-first order constant values (min^{-1}): ZnO/TiO_2: k = 0.138; ZnO NRs: k = 0.029	[272]

2.2.3.2 Nanostructured supported ZnO/TiO_2 composites

The photocatalytic and photoelectrochemical properties of supported composites which do not contain ZnO nanorods are presented in Table 6. Mostly these types of composites consist of TiO_2 nanotubes or nanorods grown on conducting support and decorated with ZnO nanoparticles. As mentioned before, such arrangement allows to measure the photocurrent in photoassisted water oxidation. The corresponding values are also given in Table 6.

A well-defined structure of these supported composites presented in this Table allowed to apply the electrochemical methods to characterize some features of the mechanism allowing higher performance of the composites in comparison with pure ZnO and TiO_2.

2.2.3.3 Supported ZnO nanorod (core)/TiO_2(shell) composites

Table 7 summarizes the properties of the composites consisting of supported ZnO nanorods covered with TiO_2 nanoparticles.

Wang *et al.* [273] prepared film of all-nanoparticle ZnO/TiO_2 composite by layer-by-layer deposited on FTO. It was shown that the improved photocurrent transient response of ZnO/TiO_2 (~ 5 μA cm^{-2}) with respect to that of TiO_2 counterpart (~ 0.75 μA cm^{-2}) was due to the presence and good connection ZnO/TiO_2 heterojunction. It was also observed by electrochemical impedance spectroscopy (EIS) that the composite possessed lower charge transfer resistance than the bare TiO_2. It was explained and concluded that better charge separation in ZnO/TiO_2 was because of the presence of ZnO in ZnO/TiO_2, which (according to cited literature) should show lower recombination rate and faster electron transport in ZnO than in TiO_2.

Ozer *et al.* [274] fabricated the branched hierarchical ZnO/TiO_2 nanostructures by combined hydrothermal (ZnO) and electrospinning (TiO_2) methods. Different preparation parameters resulted in tuning of ZnO/TiO_2 surface area and morphology roughness. It has been demonstrated by electrochemical impedance spectroscopy (EIS) that the electron transfer was enhanced by formation of branched hierarchical structures. Also, it was highlighted that the presence of ZnO/TiO_2 heterojunction interface plays an important role in effective exciton dissociation.

Hernández *et al.* [275] have prepared 1D (core)ZnO/TiO_2(shell) composites on FTO glass electrode. ZnO was grown hydrothermally on FTO-seeded substrate, while

TiO_2 was prepared by a sol-gel method. The composite was used in photoelectrochemical water splitting under solar light irradiation and the effectiveness was two and four times higher than those of ZnO and TiO_2 counterparts (*Figure 34*). TiO_2 deposition was done at different duration time, 5 and 10 min. Deposition of TiO_2 on ZnO resulted in a slight band gap narrowing with respect to the latter material, i.e. from 3.31 eV for ZnO to about 3.24 eV for ZnO/TiO_2. This was attributed to high scattering effects caused by high crystallinity in absence of oxygen vacancies. According to the authors the higher photocurrents observed for ZnO/TiO_2 composites were due to more efficient charge transfer at SC/electrolyte interface, and faster electron transport from active layer to FTO. However, the authors presented different reasons of origin of the effects. They postulated that TiO_2 particles effectively passivate recombination surface sites in ZnO, hindering recombination of the charge carriers. They also pointed out faster electron transfer in ZnO than in TiO_2 due to formation of heterojunction. Moreover, the improved properties were explained by higher active surface area due to the TiO_2 deposition.

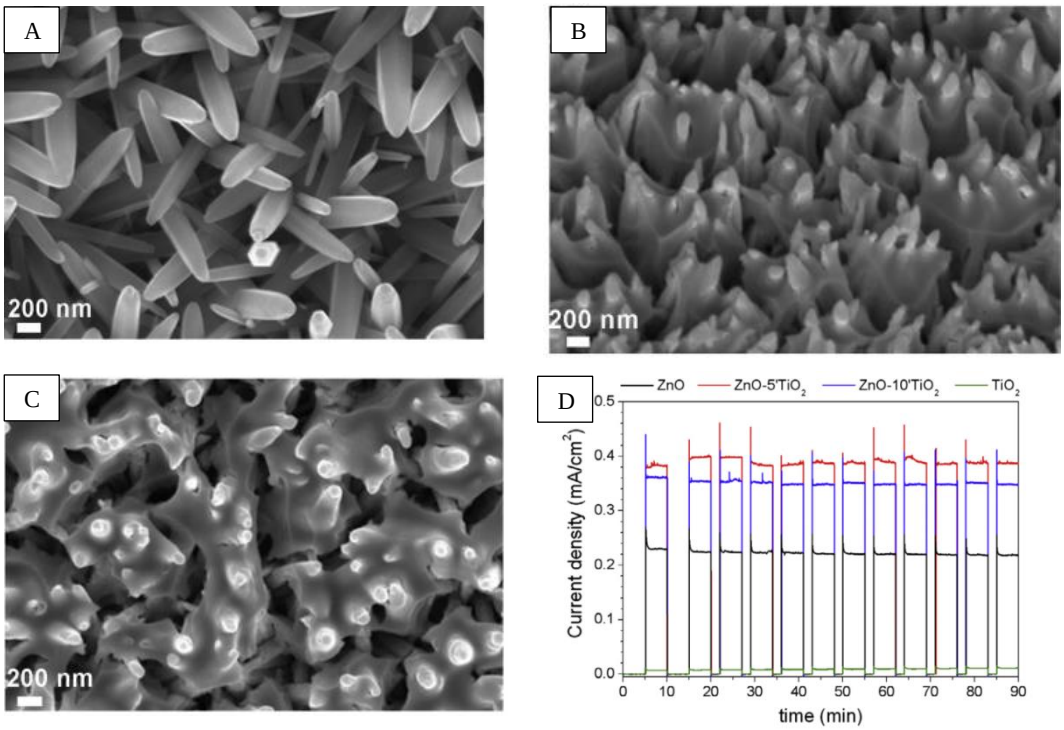

Figure 34 SEM images of bare ZnO (A), and core/shell ZnO/TiO_2 composites with TiO_2 layer prepared after 5 min (B), and 10 min (C) of impregnation. Photocurrent transients of the respective photoanodes under solar light (450 W Xe lamp) irradiation at 0.2 V vs. Ag/AgCl (D) [274].

Basak and Panigrahi [276] studied photocurrent response of ZnO/TiO_2 core/shell electrodes under 325 nm laser light irradiation (He–Cd laser) for three thicknesses of

TiO_2 layers, deposited on ZnO nanorods by spin-coating with different number of coatings (1, 3, and 5). It was shown that the core/shell composite with three coatings exhibited the highest photocurrent under 325 nm UV-laser pulses (*Figure 35*). The photocurrent enhancement was ascribed to effective charge separation due to the difference (~ 0.2 eV) of CB positions of ZnO and TiO_2. It was also concluded that further increase of the number of coatings photogenerated electrons could be trapped by adsorbed oxygen at TiO_2 resulting in lowering the photocurrent.

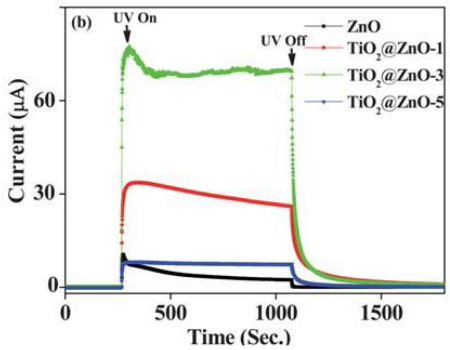

Figure 35 Transient current under dark and illuminated periods for corresponding ZnO and ZnO/TiO_2 composites [275].

Table 6 Photoactivity of supported ZnO/TiO_2 composites (all architectures except ZnO(nanorods)/TiO_2).

Type of ZnO/TiO_2 composite	Preparation method	Photocatalytic (PC) test or photoelectrocatalytic (PEC) test	Irradiation type	Photocatalytic or photoelectrochemical activity	Ref.
TiO_2 nanotubes (NT) with ZnO	TiO_2(NT): anodization of Ti foil, ZnO electrochemical deposition	PC: MB decolorization (5 mg/L)	12 W UV light λ = 365 nm	MB decolorization after 150 min: TiO_2/ZnO: ~ 80%; TiO_2: ~ 57%	[277]
TiO_2/ZnO (nanorods)/ (shell)	FTO/TiO_2 hydrothermal synth., ZnO by atomic later deposition (ALD)	PEC: 0.1 M NaOH, N_2 purged solution, also cyclic voltammetry (CV) 50 mV s^{-1}	300 W Xe lamp (AM 1.5 filter) $\lambda > 300$ nm 100 mW cm^{-2}	Water splitting: photocurrent at 0.4 V: TiO_2: negligible; TiO_2/ZnO: ~130 µA cm^{-2}	[278]
TiO_2/ZnO (nanorods)/ (shell)	FTO/TiO_2 hydrothermal synth., covered with ZnO shell	PEC: Water splitting 1 M Na_2SO_4	500 W Xe lamp, solar light, 100 mW cm^{-2}	LSV and transient photocurrent under constant 0.7 V (*vs.* RHE): TiO_2/ZnO : 0.65 mA cm^{-2}; TiO_2: 0.15 mA cm^{-2}	[279]
ZnO/TiO_2 (NPs/NPs)	Layer-by-layer deposition on FTO	1 mM $NaNO_3$, applied potential: +0.4 V *vs.* Ag/AgCl	4 W UV lamp 1.2 mW cm^{-2}, λ: 365 nm	ZnO/TiO_2 (~ 5 µA cm^{-2}) TiO_2 counterpart (~ 0.75 µA cm^{-2}	[280]
TiO_2/ZnO (nanotubes)/(shell)	TiO_2 by anodization Ti foil, ZnO by impregnation	PC: degradation of RhB PEC: water oxidation in 0.1 M Na_2SO_4	300 W Xe lamp λ = 365 ± 15 nm	PC: RhB degradation: TiO_2/ZnO ~ 78%; TiO_2: ~ 63%; ZnO film ~ 16% PEC: water oxidation: ZnO/TiO_2 ~ 2.5 ·10^{-4} A cm^{-2}; TiO_2 ~ 1.5 ·10^{-4} A cm^{-2}	[281]

Table 7 Photoactivity of supported ZnO(nanorods)/TiO_2 composites.

Type of ZnO/TiO_2 composition	Preparation method	Photocatalytic (PC) test or Photoelectrocatalytic (PEC) test	Irradiation type	Photocatalytic or Photoelectrochemical activity	Ref.
ZnO/TiO_2	ZnO hydrothermal growth, TiO_2 prepared from ethanol suspension	PC: 20 ppm or 10 ppm Orange II solution, volume of 150 ml	for UV 18 W BLB T8 lamp, λ: 315 – 400 nm, for visible, linear lamp 500 W, 9700 Lm	Orange II decolorization (after 210 min) under UV: ZnO/TiO_2: ~ 53%; ZnO: ~ 28% under visible: ZnO/TiO_2: ~ 72%; ZnO: ~ 35%	[282]
ZnO/TiO_2	film was prepared on quartz substrate by pulse laser deposition	PC: MO or MB (20 mg/L)	500 W high-pressure mercury lamp for visible light	Decolorization without catalyst (after 10 h): MO: ~ 6.8%; MB: ~ 5.9% with: ZnO: MO: ~ 19%; MB: ~ 8.7% TiO_2: MO: ~ 25.5%; MB: ~ 12.3% ZnO/TiO_2: MO: ~ 32.9%, MB: ~18.6%	[283]
ZnO/TiO_2 nanorods/nanobelts	TiO_2 *via* hydrothermal synth., ZnO *via* solution dipping technique	PEC: photoassisted water oxidation, 0.5 M Na_2SO_4, under 0.5 V *vs.* Ag/AgCl	Xe lamp, irradiance intensity ~ 120 mW cm^{-2}	Photocurrent: ZnO (NRs): ~ 0.25 mA cm^{-2}; TiO_2/ZnO: ~ 1.80 mA cm^{-2}	[284]
ZnO/TIO$_2$ NRs/'nano-brush'	ZnO *via* hydrothermally, TiO_2 magnetron sputtering	PC: Bromo-Pyrogallol red (Br-PGR) 0.02 mg/L	25 W mercury tube lamp UV λ: 254 nm	Decolorization of Br-PGR after 210 min: ZnO/TiO_2: 81%; TiO_2 film: 32%	[285]

2.2.4 N-doped and/or Au-nanoparticle decorated ZnO/TiO_2 composites

Sato with co-workers [286] applied highly oriented ZnO/$TiO_{2-x}N_y$ composite in photocatalytic decomposition of NO_x gas under visible and/or UV light. ZnO nanorods deposited on a glass substrate by hydrothermal method were etched with NH_3 and cetyltrimethyl ammonium bromide solution to form ZnO nanotubes. Then, the nanotubes were spin-coated with N-doped TiO_2 prepared by solvothermal reaction from $TiCl_3$ and hexamethylenetetramine (HMT) as nitrogen doping precursor. A red-shift of absorption edge of ZnO/$TiO_{2-x}N_y$ samples with respect to that of bare ZnO (*Figure 36A*) was ascribed to the contribution of heterojunction. Photocatalytic activity of the samples were studies in conversion NO_x gas under irradiation of the wavelength $\lambda > 510$ nm, $\lambda > 400$ nm, and $\lambda > 290$ nm by using 450 W high-pressure mercury lamp with appropriate light filters (*Figure 36B*). The increased photoactivity of ZnO(nanotube)/$TiO_{2-x}N_y$ composite under $\lambda > 400$ nm and $\lambda > 290$ nm was ascribed to unique surface features of the well-aligned nanotube structure and promoted charge separation at the ZnO/TiO_2 interface.

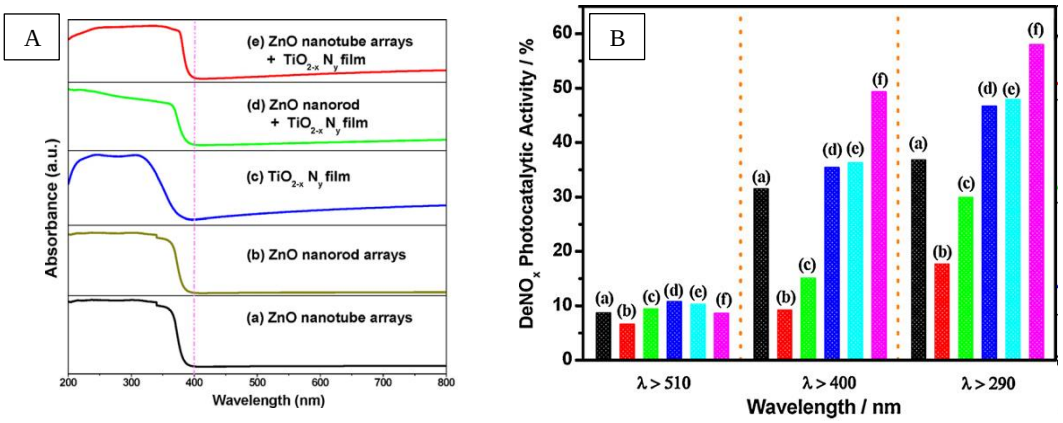

Figure 36 Optical properties of ZnO, and ZnO/$TiO_{2-x}N_y$ composites (A), and photocatalytic degradation of NO_x under $\lambda > 510$ nm, $\lambda > 400$ nm, and $\lambda > 290$ nm light irradiations on: (a) TiO_2 (P25) powder, (b) ZnO nanorod arrays on the glass substrate, (c) ZnO nanotube arrays on the glass substrate, (d) $TiO_{2-x}N_y$ film on the glass substrate, (e) ZnO nanorod arrays/$TiO_{2-x}N_y$ composite on the glass substrate, and (f) ZnO nanotube arrays/$TiO_{2-x}N_y$ composite on the glass substrate [285].

To the best of our knowledge, there are only a few reports on ternary ZnO/TiO_2/Au composites. Recently, Kumar *et al.* [287] have reported preparation of ZnO/TiO_2/Au (ZTA) for photocatalytic degradation of organic pollutants. The ZnO nanorods were covered with TiO_2 by sol-gel method and decorated with Au nanoparticles synthesized by citrate-caped method (*Figure 37A*). The photocatalytic

properties were investigated in photodegradation of $2.5 \cdot 10^{-5}$ M MB (methylene blue), CR (Congo red), and MG (malachite green) dyes mixture of 1:1:1 molar ratio (*Figure 37B and 37C*) under irradiation with light of the wavelength 365 nm, visible > 420 nm, and UV-vis with tungsten halogen lamp. The photocatalyst, in the form of powder (10 mg) was loaded in 25 ml of pollutant mixture solution. The photocatalytic decolorization of the solution was ascribed to formation of super oxide radicals from dissolved molecular oxygen.

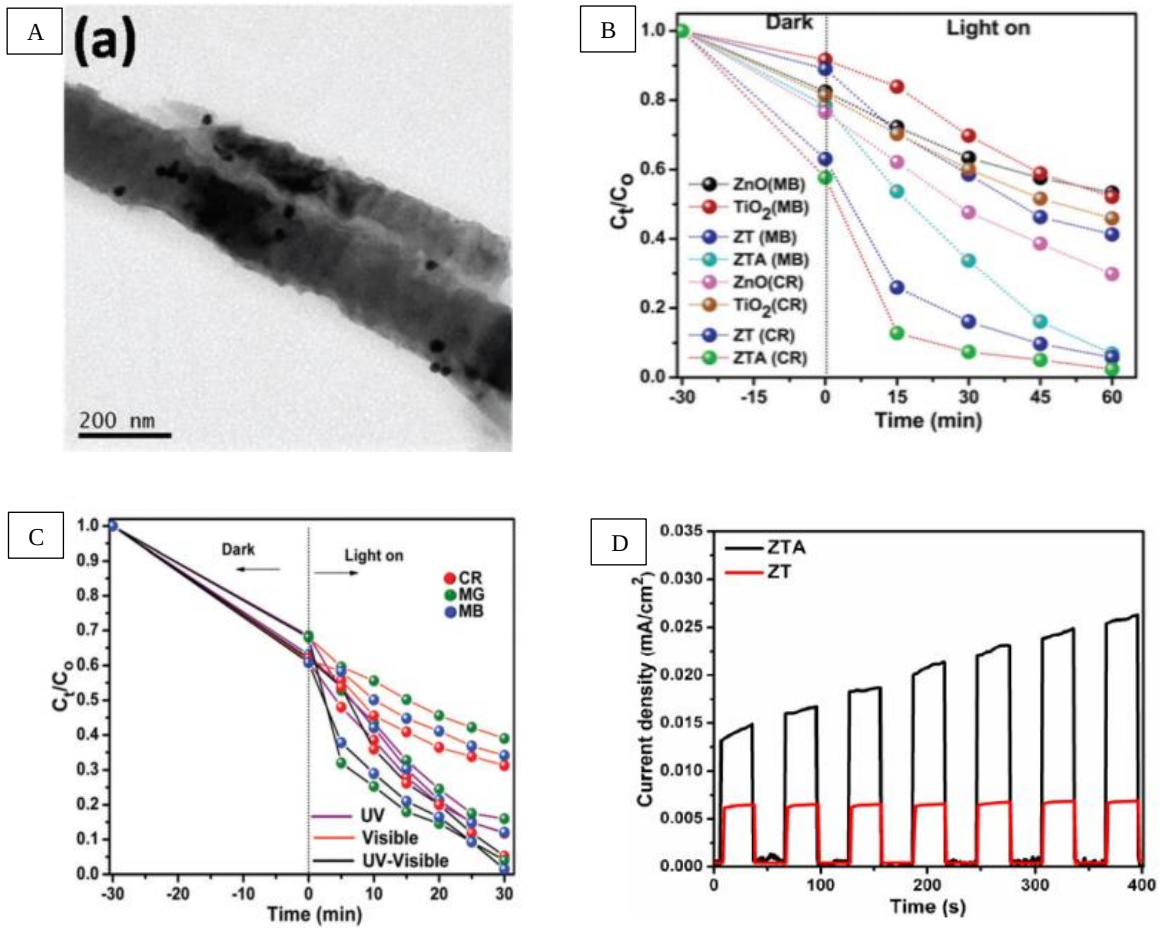

Figure 37 TEM image of ZnO/TiO_2/Au ternary composite (A). Photocatalytic decolorization of methylene blue (MB), and Congo red (CR) under solar (UV-vis) light irradiation for ZnO, TiO_2, ZnO/TiO_2, (ZT), and ZnO/TiO_2/Au (ZTA) catalysts (B). Photodecolorization of dye pollutants under UV, visible, and solar light in the presence of ZnO/TiO_2/Au ternary composite (C). Water photooxidation under zero bias voltage (vs. Ag/AgCl) for ZTA and ZT under visible light irradiation [287].

Different charge transfer mechanisms have been proposed, depending on irradiation wavelength: under UV a transfer of electrons from ZnO and TiO_2 to Au co-catalyst, decolorization under visible light was ascribed to LSPR of Au since ZnO and TiO_2 were

not photoactivated, and finally both effects were taken into account under solar light (UV-vis). For water photo-oxidation at zero bias voltage the highest photocurrents were recorded under visible light for ZnO/TiO_2/Au due to plasmonic effect (*Figure 37D*). However, the transient currents were less stable than those for ZnO/TiO_2.

Shao *et al.* [288] reported preparation of ZnO/TiO_2 nanofibers decorated with Au nanoparticles for photocatalytic degradation of methyl orange (MO) and 4-nitrophenol (4-NP) under UV light (313 nm). Deposition of Au was achieved by addition of $HAuCl_4$ solution to ZnO/TiO_2 suspension. Gold loading (10.53 wt. %, with Au NPs grain size ranging from 15.6 nm to 26.5 nm) resulted in development of a plasmonic peak at 540 nm (*Figure 38A*). Although the band gap energy of ZnO/TiO_2 (3.17 eV) was only slightly lowered with respect to E_g of ZnO (3.26 eV) and TiO_2 (3.23 eV), both composites (with and without Au NPs) demonstrated improved efficiency in photodegradation of MO and 4-NP (*Figure 38B* and *38C*, respectively). This enhancement was ascribed to several effects: efficient separation of charge carriers at ZnO/Au and TiO_2/Au interface due to formation of Schottky barrier, as well as to inhibition of recombination at the ZnO/TiO_2 interface. This was confirmed by photoluminescence (PL) emission spectra.

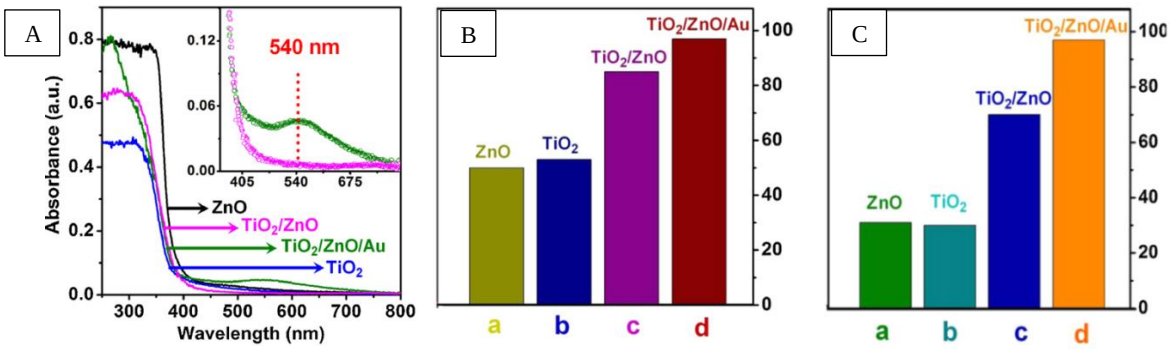

Figure 38 Optical properties of ZnO, TiO_2, ZnO/TiO_2 nanofibers, and ZnO/TiO_2/Au (A). Inset A: plasmonic peak position of Au in the ternary composite. Percentage of methyl orange (B) and 4-nitrophenol (C) degradation after 30 min irradiation with UV light with the use of mono-, binary and ternary photocatalysts [288].

Fouad *et al.* [289] studied ZnO/Au and TiO_2/Au powder composites, where Au NPs were prepared by a Turkevich method based on chemical reduction of Au precursor by citrate nitrate [290]. Photocatalytic activity of the catalysts was determined in degradation of malathion under UV, and sun light irradiation. Percentage of pollutant degradation after 1 h under sun light was 5, 6, 62, 67 for ZnO, TiO_2, ZnO/Au, and

TiO_2/Au, respectively, and correspondingly 60, 68, 79, and 81 under UV irradiation. Degradation under UV was also confirmed by HPLC measurements. The observed differences between UV and sun light degradation efficiencies were ascribed to higher intensity of UV light that excites directly semiconductors, the presence of Au co-catalyst with active reaction centers for electrons, improved charge separation at Au/SC interface and formation of active oxygen. More effective degradation (by order of magnitude) under sun light in case of Au-containing in a comparison to their Au-free counterparts was ascribed to the plasmonic effects of Au.

2.2.5. Conclusions and the aim of thesis

Enhancement of photocatalytic properties of ZnO/TiO_2 composites with respect to photoactivity of non-coupled materials is well documented in the literature. In general, this improvement has been ascribed to several reasons, such as more efficient electron-hole separation, lower recombination rate of photogenerated charge carriers as well as higher surface area due to porosity of TiO_2 shell. However, these explanations have been often provided without strong support by the kinetic parameters of the interfacial charge transfer processes because most of composites were used in the form suspensions in the solution, excluding application of electrochemical techniques. There are only a few reports on ZnO/TiO_2 composites deposited on the conducting substrates but investigations of a dynamics of electron-hole recombination process in these systems are still missing. Little attention is also devoted to the influence of morphology of the core-shell composite and microstructural properties of the ZnO/TiO_2 interface on photocatalytic performance of the system.

Therefore, the aim of this PhD project was to provide the systematic studies of the ZnO/TiO_2 composites in the form of core/shell nanostructures deposited on the conducting substrate to establish the clear correlation between synthesis conditions of the system, morphology and photocatalytic activity in photodecolorization of methylene blue and water photoelectrochemical oxidation. A particular interest will be focused on the role of the boundary between ZnO and TiO_2 in efficient separation of the photogenerated charge carriers. The dynamics of the electron-hole recombination process and charge transfer at the composite/solution interface will be studied by means of electrochemical methods.

The studies will be also addressed to improvement of the photocatalytic performance of the composites in the visible light by modification of TiO_2 shell by doping with nitrogen and deposition of noble metal nanoparticles on the composite surface. The synergetic effect of these two approaches, postulated for TiO_2, has not explored in the literature as yet with respect to ZnO/TiO_2 composite. Another novelty will be application of small cathodic bias to utilize the active oxygen species formed during oxygen electroreduction on Au-decorated composites in photocatalytic decolorization of MB.

3. Experimental

3.1. Chemical reagents and materials

Chemicals (provided by Sigma-Aldrich and ROTH) and substrates used in this work for synthesis of composites, their modifications and photocatalytic tests:

gold(III) chloride hydrate (~52% Au basis),	$HAuCl_4 \cdot \sim 2H_2O$
zinc nitrate hexahydrate (≥ 99%),	$Zn(NO_3)_2 \cdot 6H_2O$
titanium(IV) butoxide (97%),	$Ti(OCH_2CH_2CH_2CH_3)_4$
2-propanol (isopropanol) (≥ 99.9%),	C_3H_8O
zinc acetate dihydrate (≥ 99.5%),	$Zn(CH_3COO)_2 \cdot 2H_2O$
hydrochloric acid 36%,	$HCl_{(aq.)}$
sodium hydroxide,	NaOH
sodium sulfate,	Na_2SO_4
potassium chloride,	KCl
ammonium hydroxide solution (≥ 23%) ,	$NH_4OH_{(aq.)}$
ammonium chloride	NH_4Cl
methylene blue (≥ 95%),	$C_{16}H_{18}N_3SCl$

Aqueous solution were prepared with the use of deionized water (DI) (Millipore, 18 MΩ cm) was used. Indium tin oxide (ITO) conducting glass support of a sheet resistance 20 $\Omega \square^{-1}$ was purchased from Prazisions Glass & Optik GmbH (Germany).

3.2. Synthesis

The ZnO/TiO_2 core/shell composites were prepared in a sequence of consecutive stages described below.

3.2.1 ITO Pre-treatment and electrochemical seeding (preparation stage 1)

In all experiments the glass plates covered with indium tin oxide (ITO) were used as substrates for all ZnO/TiO_2 composites and their further modifications (N-doping, and Au-decoration). It is composed of Sn doped In_2O_3, as $In_{2-x}Sn_xO_{3-2x}$ (or In_2O_3/SnO_2, usually 9:1 by weight). All details, has been recently summarized in an interesting review concerning preparation, physical and chemical properties of transparent conductive oxides electrodes [291].

The ITO substrates of the size approx. 1.5 cm^2 × 3 cm^2 (the surface covered with catalysts was about 1 cm^2 – 1.5 cm^2) were ultrasonically cleaned and degreased with

acetone and then immersed for 10 s in 3 M NaOH, rinsed with distilled H_2O, etched for 15 s in concentrated H_2SO_4 and finally rinsed again thoroughly with distilled (DI) water. According to the literature [292], etching of ITO in acid peels off an 'initial' layer and exposes a 'fresh' surface which is more active due to higher surface energy. Moreover, the etching increases the density of hydroxyl groups on the ITO surface and in consequence density of the nucleation centers for nucleation-growth process.

In order to deposit a uniform layer of ZnO nanorods on ITO, the substrate should be 'seeded' with a thin layer of ZnO, playing the role of nucleation centers in the synthesis stage. Electrochemical deposition of the seed layers was performed in a three-electrode, single compartment electrochemical cell with ITO working electrode, a Pt counter electrode and aqueous $Ag/AgCl/Cl^-$ (3 M KCl) reference electrode (denoted further in the text as Ag/AgCl). The process was carried out in an aqueous solutions of 0.1 M $Zn(CH_3COO)_2$ by potentiostatic method at polarization potential of –1.2 V *vs.* Ag/AgCl using AUTOLAB PGSTAT 30 (Ecochemie, The Netherlands). In effect the ITO was covered with Zn nanoplates and nanoblocks (more details and SEM images of the obtained seed layers are presented *Chapter 4.1*). Then, the plates were annealed in air at 300 °C for 1 h to transform the superficial layer of Zn into ZnO.

3.2.2. ZnO hydrothermal synthesis (preparation stage 2)

ZnO nanorods were prepared on seeded ITO surface *via* hydrothermal synthesis from optimized conditions: 0.04 M $Zn(NO_3)_2$ aqueous solution at fixed pH 10.6 (adjusted by addition of $NH_{3(aq.)}$), in tightly closed Teflon® reactor (presented in *Figure 39A*) at 80 ^oC [293]. After 2.5 h, the reactor was quickly cooled down to ambient temperature under cold water stream. Such quenching treatment should results in improved crystallinity of ZnO [294]. The samples were washed thoroughly with deionized water and calcined at 300 ^oC for 1 h (hereafter, ZnO-plates). The hydrothermal synthesis of ZnO in the presence of $NH_{3(aq.)}$ can be summarized in equations 53 – 55:

$$Zn^{2+} + 4NH_3 \leftrightarrow Zn(NH_3)_4^{2+} \quad (53)$$

$$NH_3 + H_2O \leftrightarrow NH_4^+ + OH^- \quad (54)$$

$$Zn(NH_3)_4^{2+} + 2OH^- \xrightarrow{\text{temp.}} ZnO + 4NH_3 + H_2O \quad (55)$$

In such pH conditions the growth is promoted by high concentration of $Zn(NH)_4^{2+}$ as presented in *Figure 39B.*

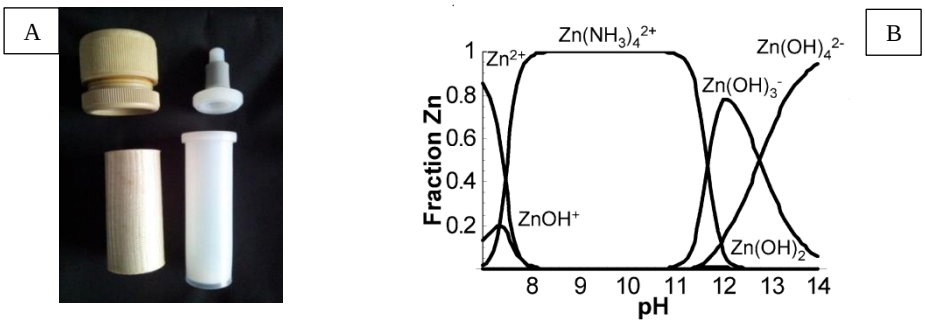

Figure 39 Photo of hydrothermal reactors used in synthesis (A) and zinc species fractions in the hydrothermal synthesis solution as function of pH (B) [295].

3.2.3. TiO_2 sol-gel deposition (preparation stage 3)

ZnO-plates were placed upside-down in 2-propanol containing TiO_2 precursor, titanium(IV) butoxide (*TIB*) in a volume ratio 100 : 1, in an open glass reactor at ambient temperature. After 15 min of conditioning, a portion of water was slowly introduced (H_2O : *TIB* molar ratio of was 4 : 1) in order to initiate hydrolysis of *TIB* followed by condensation/precipitation according to the reaction schemes:

$$Ti(OC_4H_9)_4 + 4H_2O \rightarrow Ti(OH)_4 + 4C_4H_9OH \qquad \text{(hydrolysis)} \qquad (56)$$

$$Ti(OH)_4 \rightarrow TiO_2 \cdot xH_2O + (2 - x)H_2O \qquad \text{(condensation/precipitation)} \qquad (57)$$

TiO_2 nanoparticles were formed both on ZnO nanorods surface and in the bulk of the solution. In order to prevent deposition of large particle clusters on the surface the samples were placed upside-down using a Teflon ring as a support. Precipitation/deposition was carried out for 6 h and then, the sample was taken out from the solution, washed by soaking in ethanol. For further convenience, such procedure has been ascribed as 'one deposition cycle' or shortly '***1c***'. The second type of ZnO/TiO_2 samples was also prepared by modified sol-gel procedure: the TiO_2 deposition on ZnO was performed in three consecutive 30 min cycles ('***3c***').

Some ZnO/TiO_2 samples (***3c***) were additionally calcined at 450 ^oC for 3 h for (denoted as, ***3c-Cal***) and the results of studies on them are presented in *Chapter 4.3*. In some experiments ***3c*** and ***3c-Cal*** samples were immersed in HCl aqueous solution of pH 3 for 20 h in order to remove ZnO cores to obtain finally '***3c-HCl***' and '***3c-Cal-HCl***', named respectively.

3.2.4. N-doping of TiO_2 (modification of preparation stage 3)

Doping of ZnO/TiO_2 composites with nitrogen was accomplished during the sol-gel synthesis of TiO_2, by addition of NH_4Cl to the solution of *TIB* in isopropanol in such amount to reach the molar ratio 1 : 10 of NH_4Cl to the TiO_2 in the bulk of the solution. Taking into account the fact that water added to isopropanol to hydrolyze titanium(IV) butoxide is also involved in hydration of NH_4^+ and Cl^- ions, the volume of water injected to the reactor mixture was tripled with respect to that added in the 'standard' procedure described above. Moreover, the synthesis time was shortened to 30 min. Next, the samples were calcined at 450 ^oC for 1 h as in the case of pristine (non-doped) ZnO/TiO_2 composites. This modified sol-gel procedure was repeated three times and therefore, the obtained core/shell systems with N-doped TiO_2 layer; ZnO/TiO_2(N), are denoted as '***3c(N)***'.

3.2.5. TiO_2 prepared by ALD and CVD techniques

In case of CVD technique, TiO_2 layers are deposited from the top target source placed above ITO/ZnO sample, whereas in ALD the sample is placed in sprayed atmosphere of the precursor. Deposition in case of CVD is continuous one stage and was carried out from the solution of titanium(IV) isopropoxide for 400 s at 450 ^oC, while in ALD deposition at ~ 280 ^oC using multiple cycles. Since, the temperature could not provoke formation of well-crystallized TiO_2, contrary to CVD; in this case sample was further calcined at 450 ^oC for 1 h. Each deposition cycle was initialed by injection of sprayed water into the chamber where a sample and sprayed titanium precursor were placed.

The synthesis was performed by Dr. Ludovic Avril from the SIOM team of ICB laboratory from Université de Bourgogne Franche–Comté.

3.2.6. Au-nanoparticle photodeposition (preparation stage 4)

Decoration of ZnO/TiO_2 composites of the similar morphology of the shell layer (***1c*** and ***3c(N)***) with Au nanoparticles was achieved by a photodeposition method. Since the amphoteric ZnO dissolves in acids, a simple procedure reported in the literature [296] with the use of $HAuCl_4$ as gold precursor was modified to reach, non-corrosive conditions. Thus, the pH of aqueous solution obtained by dissolution of 0.083 g $HAuCl_4 \cdot xH_2O$ in 50 ml DI water, was adjusted to ~ 6.7 with 1 M NaOH, so that $[Au(Cl)_x(OH)_{4-x}]^-$ complex ions were formed. Then, ***1c*** and ***3c(N)*** samples were immersed into the solution and irradiated for 20 s each with 365 nm monochromatic light

from LED illumination device (140 mW cm^{-2}). Under UV irradiation, the photoexcited electrons generated in ZnO/TiO_2 composite reduce gold ionic precursor and Au nanoparticles are deposited on the semiconductor surface. Finally, the samples were washed with DI water and calcined at 400 ^oC for 2 h. The obtained Au-promoted ZnO/TiO_2 and ZnO/TiO_2(N) composites, are hereafter named as '***1c-Au***' and '***3c(N)-Au***', respectively.

Table 8 Acronyms of the composite systems elaborated and studied in this work.

Acronym of sample	Composition	Description of composite
1c	ZnO/TiO_2	ZnO NRs covered with TiO_2 (sol-gel) 1 deposition cycle for 6 h, followed by calcination at 450 ^oC for 1 h
3c	ZnO/TiO_2	ZnO NRs covered with TiO_2 (sol-gel) 3 deposition cycles, each one for 30 min and followed by calcination at 450 ^oC for 1 h
'***ALD***'	ZnO/TiO_2	ZnO NRs covered with TiO_2 prepared by Atomic Layer Deposition technique
'***CVD***'	ZnO/TiO_2	ZnO NRs covered with TiO_2 prepared by Chemical Vapor Deposition technique
3c-Cal	$ZnO/Zn{:}TiO_2$	***3c*** sample treated by additional calcination at 450 ^oC for 3 h
3c-HCl	remained TiO_2^* (shell)	***3c*** sample treated by $HCl_{(aq.)}$ for 20 h pH 3 (ZnO-cores etched)
3c-Cal-HCl	remained $Zn{:}TiO_2^*$ (shell)	***3c-Cal*** sample treated by $HCl_{(aq.)}$ for 20 h pH 3 (ZnO-cores etched)
3c(N)	ZnO/TiO_2(N) N-doped TiO_2	TiO_2 (sol-gel) 3 deposition cycles, each one for 30 min with a presence of NH_4Cl and followed by calcination at 450 ^oC for 1 h
1c-Au	ZnO/TiO_2/Au	***1c*** sample with deposited Au NPs by photodeposition for 20 s under 365 nm irradiation and calcined at 400 ^oC for 2 h
3c(N)-Au	ZnO/TiO_2(N)/Au	***3c(N)*** sample with deposited Au NPs by photodeposition for 20 s under 365 nm irradiation and calcined at 400 ^oC for 2 h

3.3. Characterization methods

3.3.1. Electron microscopies (SEM, TEM) and elemental analysis of the samples (EDX)

Scanning electron microscopy (SEM) was used to examine the surface morphology of the samples. In general, electrons generated in a emitter impacts are accelerated by electromagnetic field and impacts the sample emitting various types of electrons depending on the penetration depth (*R*), which can be expressed by equation [297,298]:

$$R \approx \frac{27.6 \cdot A \cdot (E_0)^{1.67}}{\rho \cdot Z^{0.889}} \quad (58)$$

where, *A* is mass number (g mole^{-1}), E_0 is energy of accelerated electrons that impacts the sample (k*e*V), ρ is density of the material (g cm^{-3}), and *Z* is atomic number. After impacting the surface of material, the secondary electrons (SE) are formed depending on the penetration depth (see scheme *Figure 40A*: SE1, SE2, SE3). The electrons are also reflected from the sample by elastic scattering and these back-scattered electrons (BSE) vary in their amount and direction due to the composition and topography of the surface. All these electrons are collected by detectors, and since they possess different energies the signal of different resolution and contrast is recorded. The BSE electrons have energies greater than 50 eV, whereas SE poses energy lower than 50 eV. Brightness and contrast of SE is related to low energy that is electron flux and dose of beam. Small energies may result in accumulation of electrons (negative charging effect) if the sample is a poor electric conductor. Therefore, samples must be electrically conductive, and if not they undergo metallization by sputtering thin layers of Au (a few nm) or a layer of carbon (~ 13 nm). In case of BSE their emitted number is proportional to atomic number of the element in a sample. BSE that are emitted at low angle from a sample can be collected by a LABE detector, which is more sensitive to surface information (*Figures 40B* and *40C*). LABE and SE resolutions are comparable [299].

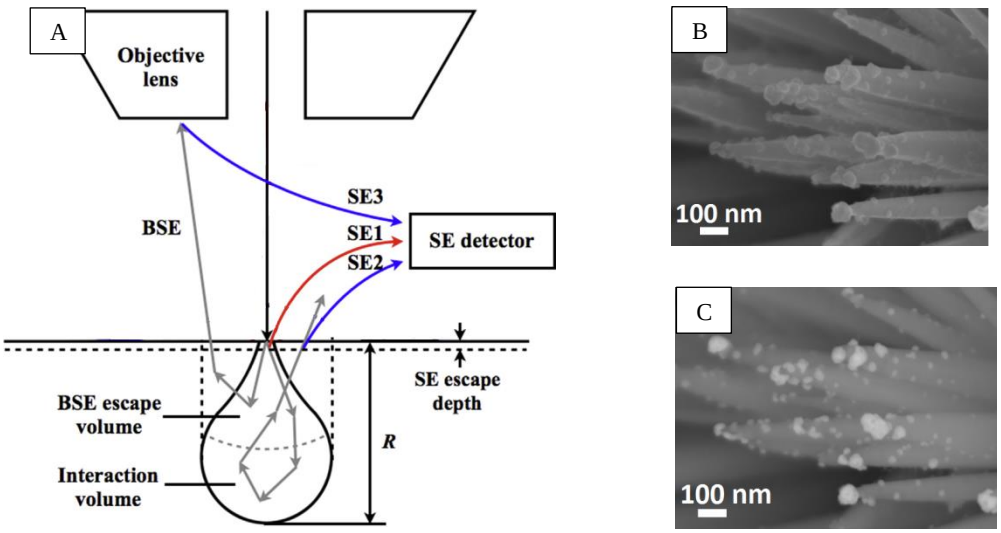

Figure 40 Scheme of electron beam interaction with a material, and subsequent generation of various electron types (A) [300]. SEM image of ZnO (Z_{Zn} = 30) nanorods decorated with Au (Z_{Au} = 79) nanoparticles in SE1 detection mode (B) and LABE mode (C), own results.

In this work the surface morphology was examined by scanning electron microscope (SEM, JEOL-7600F) equipped with EDS SDD Oxford that allowed EDX-SEM elemental analyses across 10 μm^2 area of the samples and a low-angle backscattered electron detector (LABE) [301].

Transmission electron microscopy (TEM) allows to observe internal structure of the samples, also with a high resolution mode (HR-TEM). Resolution of TEM images (δ) depends on electron acceleration beam voltage (V), accordingly to the equation:

$$\delta = \frac{0.61\,\lambda}{n \sin\alpha} = \frac{0.61\,h}{n \sin\alpha \sqrt{2 m_0 e V}} \tag{59}$$

where ($n \sin \alpha$) is numerical aperture, m_0 is the rest mass of electron, and e is the electron charge. Also, to observe thicker sample higher electron energy (eV) is necessary. Samples absorb and scatter the electrons and in general elastically scattered electrons are used for imaging.

Often TEM can operate in two modes: bright-field (BF) and dark-field (DF) imaging. The sample is placed in the line of optical axis of electron beam and detector. If electrons that passed through a sample and reached detector placed in line of initial beam, the image that is created is in BF mode. In case, when scattered electrons were

chosen for image creation the mode is called DF. The image contrast is a result of different absorption (BF) or scattering of incident electrons (DF) by different material nature (density) and thickness. The later one comes from incoherent elastic scattering, while the former one from coherent elastic scattering at Bragg angles [302]. In DF mode properly oriented electron beam towards a sample containing well crystallized particles results in bright contrast. Opposite to that BF imaging results a brighter contrast for material thinner and amorphous.

Useful and interesting possibilities are provided further by Scanning Transmission Electron Microscopy (STEM) that allow to scan the probe across the sample, due to additional scan coils to TEM, thus generating various scattered electron signals that after detection are plotted as a function of probe position [303].

Observations under high resolution regime allow to use angular detector, which collects inelastically scattered electrons. The observed difference in image contrast is due to different electron scattering, and this depends on atomic number Z, so-called Z-contrast. Most efficient contrast differences for elements are observed when transmitted electrons that left the specimen are collected at high angles with respect to the optic axis (high-angle annular dark field detection (HAADF). Such mode is one of possibilities for signal collection in STEM. Others includes: (1) bright field detection (STEM-BF) that allow to collect transmitted electrons leaving the specimen at low angles with respect to the optic axis, (2) EELS – electron energy loss spectroscopy, where the spectrum is plotted as function of number electrons that left the specimen with a loss of energy due to interaction *vs.* that lost energy. Also the (3) X-ray energy dispersion spectroscopy (EDX) is enabled during STEM observation that include mapping of elements, line scan and point analysis.

EDX was used to provide information of elemental composition, atomic distribution (mapping), and semi-quantitative analysis. In general, atoms emit characteristic X-rays, which can be related to Moseley's law:

$$v = \alpha(Z - \beta)^2 \tag{60}$$

where, v is the frequency of emitted X-ray line, α and β are line constants, and Z is atomic number of an element. Electrons emit lines accordingly to their donation of filling the vacancy in shell orbitals around the atom nucleus, i.e. Kα, Kβ, Lα. In EDS energy

dispersion spectra these lines correspond to the peak energy positions usually within the range of 1 keV to 20 keV. Area under the peak can give information about amount of the element in a sample.

In this work, internal microstructures were studied by means of high resolution (HR-TEM), while high-angle annular dark-field scanning electron microscopy (HAADF-STEM) was performed on JEOL JEM-2100F working at 200 kV. The samples prepared for TEM characterization were detached from the ITO support by scratching with prior dropping of ethanol on the surface. Then a drop (ethanol and removed samples) was placed at copper mesh grid.

3.3.2. Optical properties

In order to investigate optical absorption properties of the samples within the range of 350 – 700 nm, the Shimadzu UV-3600 spectrometer equipped with an integration sphere was used. The UV-vis spectra were used to determine the optical band gap energy, E_g, by means of the Tauc equation: [304]

$$\alpha h\nu = A(h\nu - E_g)^{1/n} \tag{61}$$

where $h\nu$ is the photon energy, A is the frequency-independent constant, and exponent n depends on the nature of transition in the semiconductor, i.e., n = ½ for allowed direct and n = 2 for allowed indirect transition. Regardless of some controversy, it has been found that ZnO is an n-type direct band gap semiconductor, [305] while anatase-TiO_2 is a material with the indirect transition [306,307,308]. Optical band gap energies were determined from the plot of $(\alpha h\nu)^{1/n}\ vs.\ h\nu$, from intersection of the tangent line with the horizontal axis.

Such spectral methodology approach has some limitations in a regard to the samples. The equation is applicable to layered films. In case of non-flat layered samples the scattered and reflected light should be also taken into considerations. Such problem is solved in spectrophotometers equipped with integration sphere attachment that allow to collect the reflected flux. Integration sphere attachment is coated from the inside usually with polytetrafluoroethylene (PTFE) or barium sulfate ($BaSO_4$) which diffuse reflectance is close to 1 [309], and geometry set-up configurations with sample being illuminated with diffused light 'illuminated geometry' (*Figure 41A*) or with light in-axis to the sample in angle < 10^o 'view geometry' (*Figure 41B*). In both cases baffles are placed

between the sample and 'illuminated' or 'view' geometry to avoid superposing the reflected light.

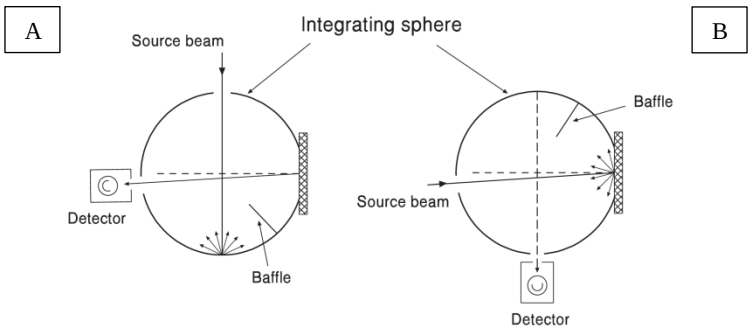

Figure 41 Geometric set-up configurations ('illuminated' and 'viewed', A and B, respectively) of integration sphere attachment used in optical band gap determination from UV-vis spectra [309].

Tauc theory is sufficient for optical band gap determination, and examples are found for bare materials [310], and also for composites [311]. In the shape of $(\alpha h\nu)^{1/n}$ *vs.* $h\nu$ one can observe inclination of the curve which can be correlated with the band-to-band transitions between CB and VB in the SC.

3.3.3. XRD

Crystallinity of the samples was studied using X-ray diffraction (XRD). The X-ray beam arrives at the sample's surface under an θ angle and are scattered to leave the sample at the same angle. By analysis of the peak width in XRD pattern, the crystal size can be determined using the Scherrer relationship:

$$L = \frac{K \cdot \lambda}{\beta \cdot cos\theta} \tag{62}$$

where L is an average particle size, K is the Sherrer constant (0.9) and β is peak width at half height. For thin layers deposited on the solid substrate the grazing-angle XRD (GAXRD) technique was used in order to obtain the information about the surface layer of the composites. GAXRD measurements were performed with diffractometer Bruker D8-A25 Discover equipped with a LYNXEYE XE detector.

3.3.4. XPS

X-ray Photoelectron spectroscopy (XPS) was applied in order to determinate atomic states and surface composition of samples by usage of apparatus PHI 5000Versaprobe

with mono-chromatic Al Kα1 X-Rays. In short, the analysis is based on energy exchange between photons from the beam with electrons in atoms of specimen. Then excited electron may escape from the atom and these emitted electrons possess certain kinetic energy accordingly to the equation [312,313]:

$$h\nu = E^{f} - E^{i} + E'_{k} \quad (63)$$

Where, $h\nu$ is energy of incident electron, E^{f} is the total energy of the final state of the ion, E^{i} is the initial state of the atom, and E'_{k} is photoelectron kinetic energy. All elements within a certain chemical compound, except hydrogen, emit characteristic core photoelectrons. For a certain element (atom) in a chemical compound the binding energies of atom's core level is different because of other surrounding atoms, which is a base for XPS analysis of the compound composition. Therefore qualitative analysis is based on peak position at certain binding energy of photoelectrons from these atoms (elements), while (relative) quantitative analysis is based on the calculation of the area under this peak. The analysis takes place under low pressure conditions, usually lower then 10^{-7} torr. The 95% of the signal collected is from less than 10 nm thick layer, making XPS analysis strongly surface adapted.

3.3.5. Photoluminescence

Once the material absorb the light enters an electronic excitation state. Then, a process of spontaneous emission of photon may occur in order to release absorbed energy by the material, called photoluminescence (PL). In such method a sample is illuminated with excitation wavelength and the emitted light is analyzed. The information provided by PL of solid surfaces concerns its nature and modification states [314], as well as the electronic energy levels present in a sample are the information that one can obtain by analyzing PL emission spectra. The photoluminescence (PL) emission spectra of the samples were recorded using Fluorolog-3 spectrofluorometer (Horiba Scientific) with a 400 nm excitation wavelength at room temperature.

3.3.6. TGA-DSC

Thermogravimetry (TGA) together with differential scanning calorimetry (DSC) analyses allow to measure the changes of material weight (TGA) and the simultaneous energy release or absorption in the form of heat (DSC), respectively, while the sample is being heated up, cooled down or kept in isothermal conditions [315]. With the usage of these combine techniques one can i.e. determine the temperature of solid material phase

transformation, which usually is connected by noticeable energy change with no weight mass change. The analyses in this work were performed with the use of a SENSYS Evo TGA-DSC, Setaram Instruments (France). Ramping of temperature was set at 5 ^{o}C min^{-1}. The technique provides information of thermal behavior of the sample. The mass of the sample was approx. 10 mg, placed inside platinum crucible under air or nitrogen flow with a flow rate of 20 cm^3 min^{-1}.

3.3.7. TOC

Total organic carbon (TOC) content in solution was determined by means of Analytik Jena AG TOC analyzer (multi N/C 3100). In such measurement, the solution were pre-treated by adding 25 µl of 4 M $HCl_{(aq.)}$ in order to remove carbonates. Next, solution was purged with a flow of oxygen. Then samples are burned out at the Pt catalyst at 800 ^{o}C, while the water from the solution is soaked by Peltier cooler. Detection is based on CO_2 analysis by infrared detector. Area under the peak of detected CO_2 is correlated with the amount of carbon in the analyzed solution.

The measurements were performed in co-operation with Mr. M. Sulwiński from the Faculty of Biology, University of Warsaw.

3.3.8. Linear sweep voltammetry, cyclic voltammetry, chronoamperometry

(Photo)electrochemical measurements were performed with the use of potentiostat Autolab (Metrohm B. V., The Netherlands) in three-electrode cell, with a composite sample as the working electrode (WE) (approx. 1 cm^2 geometrical working surface area), Ag/AgCl/Cl$^-$ (3 M KCl) as a reference electrode (RE), and Pt wire as a counter electrode (CE). To provide electrical conductivity in the solution an electrolyte should be present, i.e. Na_2SO_4 (in this studies 5 mM).

However, when redox reactions occur under certain potential, the Faradaic current is observed. In cyclic voltammetry (CV) and linear sweep voltammetry (LSV) an external potential applied to the WE is changed linearly in time with the scan rate υ, usually from the range 20 mV s^{-1} – 100 mV s^{-1}. In CV after reaching the final potential E_f, the polarization direction is reversed to arrive back to the initial value E_i, as illustrated in *Figure 42A*. When a redox reversible couple is present in the solution, in the cyclic voltammogram one can observe the formation of anodic oxidation peak at the potential E_{pa} and cathodic reduction peak at E_{pc} (*Figure 42B*). For ideally reversible redox couple the difference between the peaks potentials $\Delta E_p = E_{pa} - E_{pc}$ should be 59/n mV.

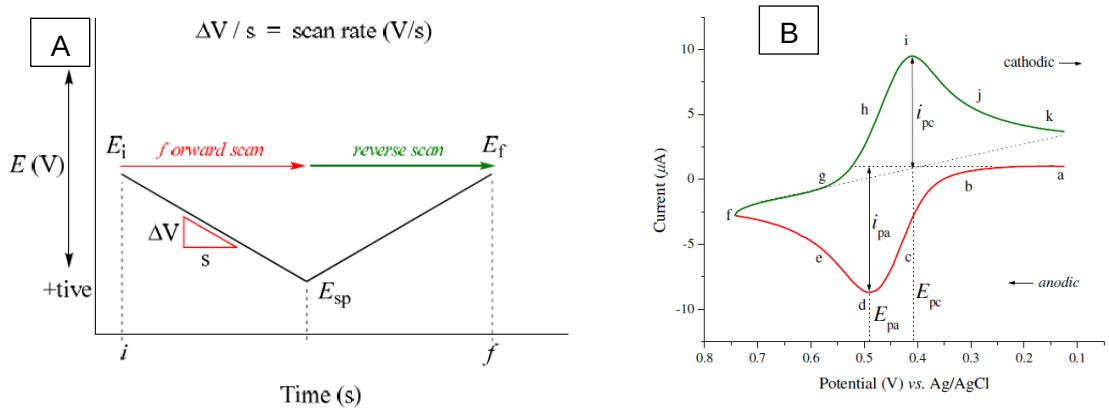

Figure 42 Potential change in time and a model reversible cyclic voltammogram for reversible redox couple [316].

The experiments were carried out either in aqueous solution of 5 mM Na_2SO_4 or in the same solution containing 10 μM MB. The linear sweep voltammograms (LSV) and cyclic voltammograms (CV) were obtained with the scan rate of 10 mV s^{-1}, while the current transients were recorded at constant potentials of –0.25 V or 0.8 V *vs.* Ag/AgCl. If needed, the solutions were deareated by purging with argon for 30 min.

Chronoamperometry is a technique where constant potential is applied to the working electrode and current flow is observed over time. Integration of surface below the $I(t)$ curve corresponds to the charge passed involved in the process. In such method the solution is not stirred so the transport of electroactive species to the electrode occurs only by diffusion. Therefore, the current is a function of time according to Cottrell equation:

$$I = n\mathrm{F}A\frac{\mathrm{D}^{\frac{1}{2}}c_0}{\pi^{\frac{1}{2}}t^{\frac{1}{2}}} \tag{64}$$

where, n is number of electrons involved in the process, F is Faraday's constant, A is geometrical working area of electrode, D is diffusion coefficient of electroactive species, c_0 is nominal concentration of electroactive substance in the bulk of solution, and t is time of applied bias. Also, worth to mention is that charging of double layer takes place within milliseconds.

3.3.9 Photocurrent and open circuit potential

The fundamentals of photocurrent and open circuit potential measurements were described in detail in previous paragraph 2.1.4. in *Bibliography* part. In this work the

photocurrent measurements were done with the use of Autolab, in three electrode cell, with elaborated ITO-based photocatalysts (i.e. ITO/ZnO, ITO/ZnO/TiO_2, ITO/ZnO/TiO_2/Au, etc.) as working electrode, a Pt wire as counter electrode and aqueous Ag/AgCl as a reference electrode, in 5 mM Na_2SO_4 aqueous solution. The working electrode surface area was approx. 1 cm^2. The V_{oc} experiments were carried out in deareated aqueous solution of 0.2 M KCl in phosphate buffer of pH 6.8.

3.3.10 Set-up for photocatalytic and photoelectrochemical measurements

Photocatalytic (PC) activity of the samples was tested by measurement of photodecolorization rate of model pollutant, methylene blue (MB), according to the International Standard Procedure [87]. The PC tests were performed in quartz cell containing 2.5 ml (all experiments described in *Chapters 4.2 and 4.3*) and 5 ml (all tests in *Chapter 4.4*) of 10 μM MB aqueous solutions under either LED 400 nm irradiation or visible light irradiation of 160 mW cm^{-2} intensity generated by an arc xenon lamp (450 W arc xenon lamp (Oriel)) equipped with a 400 nm cut-off filter. In order to perform tests with monochromatic light, an originally designed light emitting diode-based device was assembled (see the scheme and a photo in *Figure 4A*, and *43C*). The core of the device relies on a high power emitter (400 nm) with a narrow relative spectral power distribution. LEDs were provided by LED Engin (USA). In case, when tests were performed using visible light the distance was adjusted to keep the same intensity. The optical light irradiance of the LEDs was measured with the use of an IL1700 International Light (USA) radiometer. The LED illumination device allowed to maintain a constant temperature of 24.6 ^oC in aqueous solutions in the cuvette at a distance of 1 cm from the emitters (*Figure 43B*).

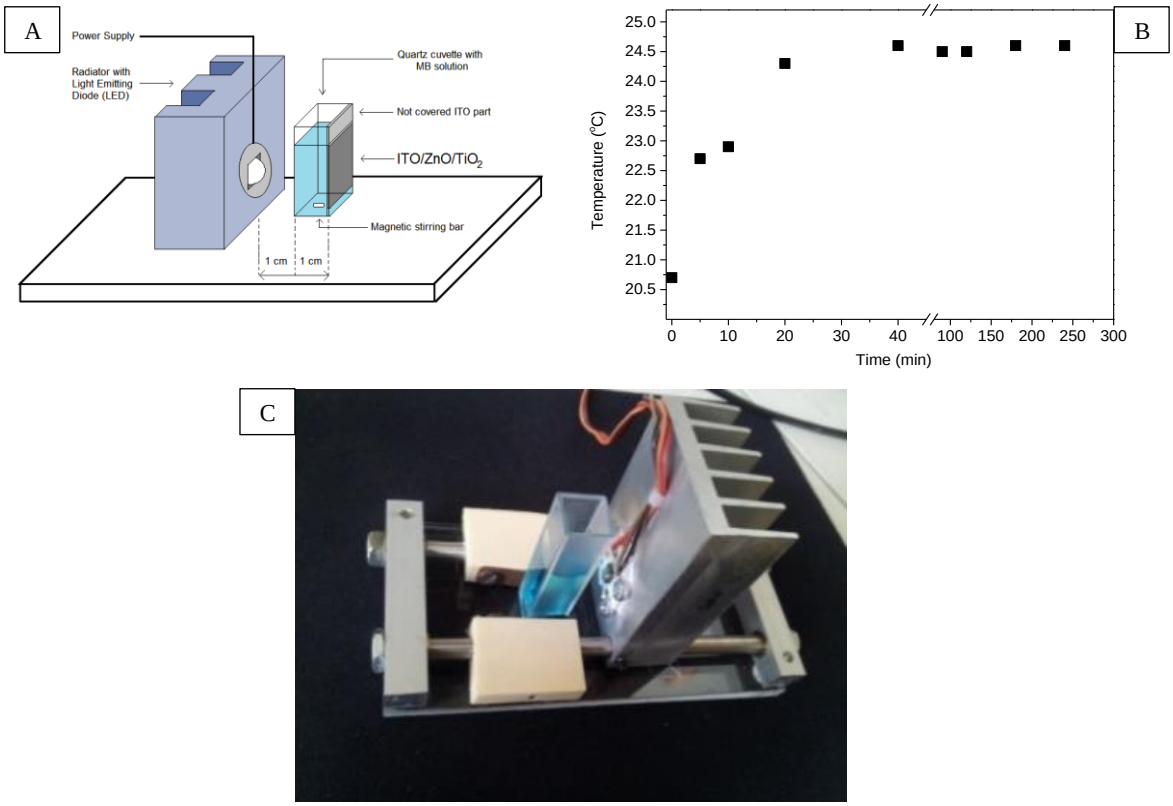

Figure 43 Scheme (A) and of originally designed LED device used in photocatalytic and photoelectrochemical tests. Temperature change over time of MB aqueous solution in a cuvette placed at fixed distance of 1 cm from LED emitter (B), and photo of the LED device (C) and the UV-vis spectrometer chamber (D); arrows the between figures C and D, symbolize the measurement approach.

The samples were placed on the rear wall of the cuvette at a distance of 2 cm from the LED light source. MB negligibly absorb light between 350 nm and 450 nm, and molar extinction coefficient of ε(664 nm) = 7402.8 m^2 mol^{-1} in aqueous solution of 10 μM, which corresponds to absorption $A'_{\lambda,664nm}$ = 0.74, while for 20 μM is $A''_{\lambda,664nm}$ = 1.48 [317]. According to the ISO directive a tested sample geometrical area should be between (100 ± 1) mm^2 and (1500 ± 15) mm^2. The absorption spectra of MB solution were recorded in interval periods no longer than 20 min (usually 10 min or 15 min). For this, the quartz cuvette (with all transparent walls) was placed directly in spectrometer chamber.

Prior to PC tests, the samples were conditioned in dark in 20 μM MB aqueous solutions for 24 h in order to avoid a concentration drop due to adsorption of MB during the main PC test. UV-vis spectra of MB solutions were collected using Shimadzu UV-3600 spectrometer and the change of MB concentration was determined from decrease of

absorption maximum at the wavelength of 664 nm. The MB decolorization on TiO_2 obeys first-order kinetics and therefore, apparent first-order rate constants ($\boldsymbol{k_{vis}}$) were determined from the linear slope of logarithm of concentration ratio (c/c_o) as a function of time. It is assumed that decolorization of MB on TiO_2 obeys a first-order rate equation:

$$\frac{c}{c_0} = e^{-kt} \tag{65}$$

Thus, the kinetic data obtained under illumination were analyzed by plotting the natural logarithm of concentration ratio (c/c_0) as a function of time, and an apparent first-order rate constants (k_{400}) were determined from the slope of this linear plot.

4. Results and Discussion

4.1 Growth of ZnO nanorods on ITO-covered plates

4.1.1. Preparation of ITO-plates seeded with nanocrystals

All ZnO/TiO_2-based catalysts for photocatalytic and (photo)electrochemical measurements were fabricated on ITO conductive glass plates. It is essential to provide good attachment of the catalyst to the substrate to avoid any weight losses during catalytic process and ensure good electrical contact between the catalyst and electrode surface to achieve satisfactory electrochemical properties. In this context, electrochemical seeding methods surpass commonly used physical adsorption techniques such as the 'doctor blade' or sputtering methods. Taking into account that the catalysts elaborated in this work are based on ZnO nanorods (subsequently covered with TiO_2 and decorated with Au nanoparticles), potentiostatic reduction of Zn^{2+} to metallic Zn-seed crystals, and their further superficial transformation into ZnO, satisfies the needs of proper surface immobilization and allow keeping good electric contact between Zn/ZnO seeds and ZnO nanorods grown epitaxially in the following stage by a hydrothermal method.

Zinc acetate is a precursor more often used for chemical seeding [318] or chemical bath deposition [319] of ZnO nanostructures than for an electrochemical seeding of the substrate. In aqueous solutions, $Zn(CH_3COO)_2$ undergoes partial hydrolysis according to the scheme:

$$Zn(CH_3COO)_2 + H_2O \rightarrow Zn(OH)^+ + 2CH_3COO^- + H^+ \qquad (66)$$

An additional source of OH^- ions is needed for the precipitation of $Zn(OH)_2$ and may be provided by electrochemical reduction of molecular oxygen present in the solution, according to the scheme:

$$O_2 + 2H_2O + 4\,e^- \rightarrow 4\,OH^- \quad E^0 = 0.4\ V\ \textit{vs.}\ NHE \qquad (67)$$

Before preparation of the seed layer on ITO by a potentiostatic method, preliminary experiments were performed by cyclic voltammetry in the potential range from –0.1 V to –1.2 V in the solution of 0.1 M $Zn(CH_3COO)_2$ in the presence of oxygen and in deareated solution. Such tests were necessary to determine the most suitable reduction potential of Zn^{2+} on the ITO electrode. The recorded voltammograms presented in *Figure 44A*, show that in the non-deareated solution the reduction current (black

curve – 1) starts to increase slowly at potentials more negative than –0.62 V *vs.* Ag/AgCl, which can be explained by above mentioned reduction of dissolved oxygen (reaction scheme 67). In contrast, in the deareated solution (red curve – 2) no current was observed until –1.1 V. In the range of potentials more negative than –1.1 V, reduction of Zn^{2+} and deposition of metallic Zn occurs ($E^{0}_{Zn^{2+}/Zn}$ = –0.76 V, Zn^{2+}/Zn (~ –1.0 V *vs.* Ag/AgCl). During the reverse scan the metallic Zn is reoxidized to Zn^{2+} ions giving rise to the anodic oxidation peak at about –0.9 V. The charge balance between the reduction and oxidation charges (curve 2, inset, *Figure 44A*) obtained in deaerated solution indicates that Zn deposition/dissolution process is the only process occurring on the electrode. In contrast, when the deposition was performed in non-dearated solution the charge involved in reoxidation was only 55% of the reduction charge (curve 1, inset, *Figure 44A*), i.e. a concurrent irreversible reaction to Zn^{2+}/Zn reduction occurred on the electrode in the cathodic range. There are two reasons of this imbalance: reduction of molecular oxygen dissolved in the solution and passivation of deposited Zn, which could be a result of formation of native amorphous zinc hydroxides. According to the literature, the critical value of pH at which an aqueous solution becomes supersaturated with $Zn(OH)_2$ at 25 ^{o}C should be 6.7 [320].

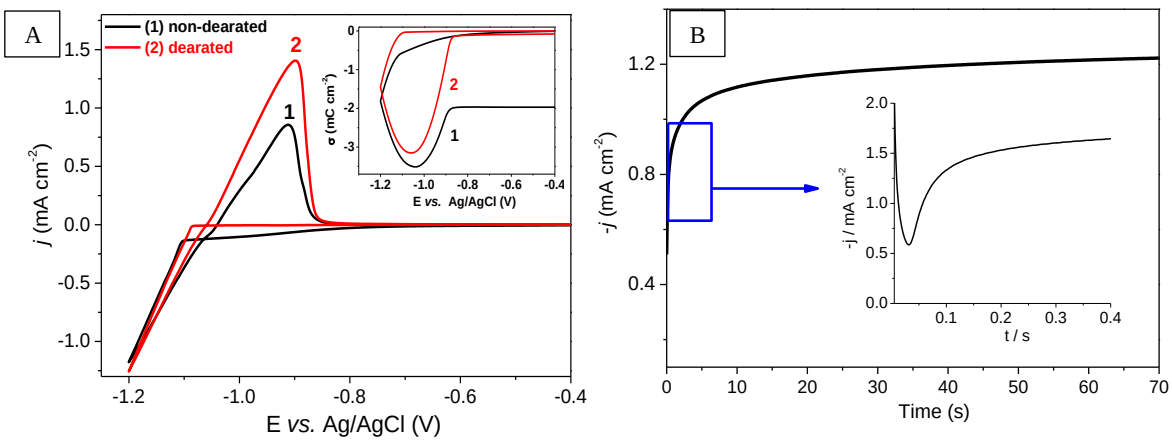

Figure 44 Cyclic voltammograms (CV) obtained on ITO electrodes vs. Ag/AgCl, in aqueous solution of 0.1 M $Zn(CH_3COO)_2$ at 25 ^{o}C and 40 mV s^{-1} scan rate (A) in non-dearated (black curve, 1) and dearated conditions (red curve, 2). Inset A: plot of charge densities vs. polarization potential obtained by integration of CV curves. Chronoamperometric curve obtained during polarization of ITO at potential of –1.2 V in the non-deareated aqueous solution of zinc acetate (B). Inset B: initial part of current-time profile at time scale from 0 to 0.4 s (B).

Since the pH of solution used for the electrodeposition was 6.2 the reduction of oxygen at the ITO electrode probably resulted in a local increase of pH above this threshold value, leading to precipitation of native amorphous zinc oxide. In order to keep the preparation procedure simple, the potentiostatic ITO seeding was limited to non-dearated solution conditions. *Figure 44B* presents a chronoamperometric curve obtained in this solution at polarization potential of −1.2 V. The overall shape of current transient is typical of the nucleation and growth process [321]. Namely, the current density after a short minimum, located at about 0.03 s, rises to the plateau and then increases very slowly but continuously in the longer time scale, as for kinetically controlled process. The morphology of the samples obtained after the passage of charge density of about 140 mC cm^{-2} is illustrated in *Figure 45A*. The Zn-nanosheet structures show dominantly vertical arrangements to the ITO substrate. The formation of plate-like Zn nanostructures by electrochemical methods or thermal metal–vapor depositions have been already reported in the literature [322,323] and the zinc plates obtained by these methods were much thicker (above 100 nm). In contrast, in this work the Zn nanosheets were only a few nm in possibly the thickest part (the darkest edges, *Figure 45B*), and had tendency to grow in multi-layered patterns. The formation of Zn nanosheet structures has been also reported for electrochemical deposition of $Zn/Zn_5(OH)_8Cl_2 \cdot H_2O$ [324] and for $Zn(OH)_2$ synthesized chemically in liquid-liquid biphasic (organic–aqueous) system containing hydrophobic long-chain carboxylate ions (as heptanoate, decanoate) in organic (xylene) phase [325].

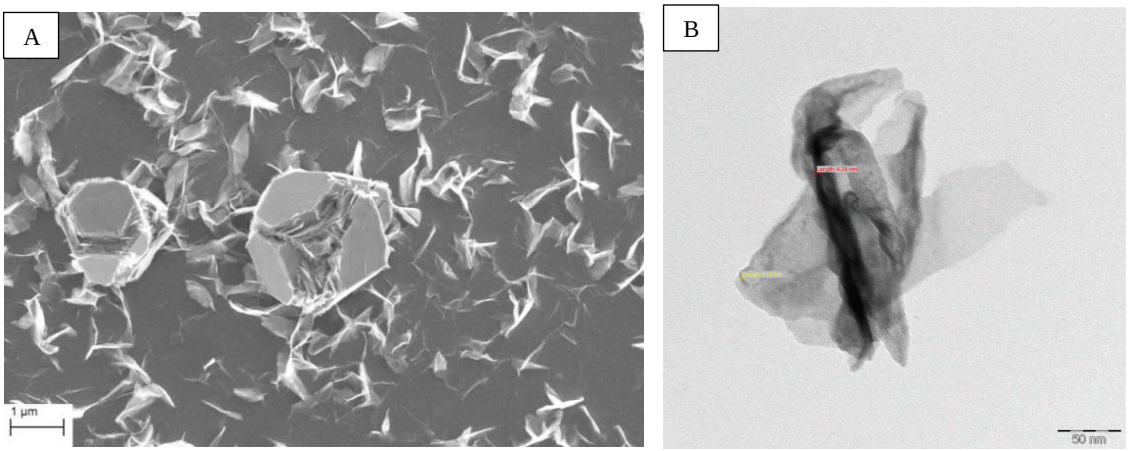

Figure 45 SEM image of Zn seeded ITO surface (A), and TEM image of representative Zn nanosheets deposited and physically removed from ITO surface (B).

The Zn nanosheets have been also synthesized by thermochemical reduction of ZnS in the atmosphere of N_2 in the presence of CO and H_2 [326] or by the hot filament metal-oxide vapor deposition (HFMOVD) technique [327] but their morphology was different from that presented in *Figure 45*.

The questions which arise concern the presence and mechanism of formation of large crystals observed alongside Zn-nanosheet structures. The answer to the first question may be found by analysis of SEM images of the samples at different stages of the crystal growth, presented in *Figure 46*. The samples were prepared at different deposition charge densities, from 70 to 280 mC cm^{-2}. As visible, the first step of the process consists in the formation of pentagonal or hexagonal templates probably by folding the adjacent nanosheets (*Figure 46A*) which are subsequently building up with the neighboring lamellar structures (*Figure 46B*). Then, these templates are filled in with other vertically aligned nanosheets (*Figure 46C*) which finally lead to the formation of crystals of a plate structure (*Figure 46D*).

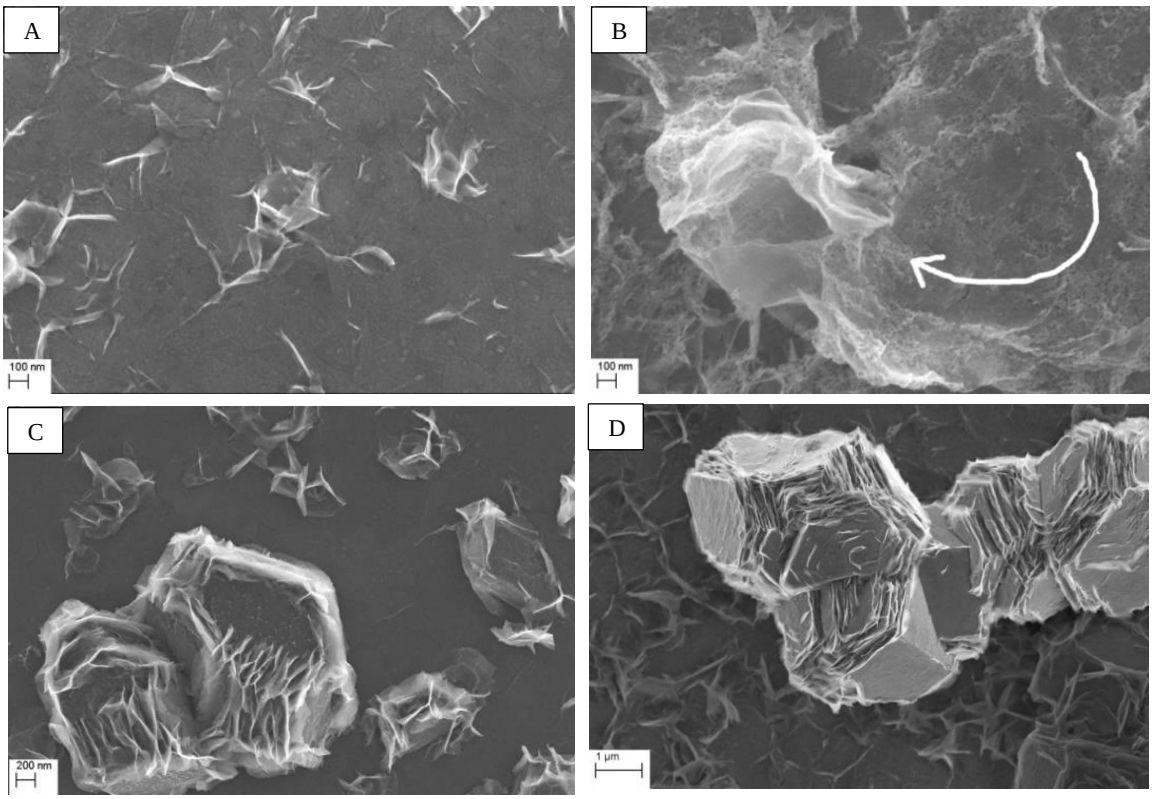

Figure 46 SEM images of Zn seed layers potentiostatically deposited on ITO electrode at constant potential of –1.2 V in the non-deaerated solution of 0.1 M $Zn(CH_3COO)_2$ at different progression stages of Zn crystal formation.

Therefore, the Zn nanosheets can occur less probably at the close neighboring to the well-developed crystals than in a further distance from them. So the crystals are likely to be formed from Zn smaller structures. In order to form the well-developed Zn-crystal seed layer it was found that at least the sufficient charge density ($\geq$ 70 mC cm^{-2}) should pass. On the other hand, high charge density ($\geq$ 280 mC cm^{-2}) results in formation of overgrown Zn crystals eventually leading to their fusion into big chain-crystal structures (*Figure 46D*). Therefore, the current density of about 140 mC cm^{-2} seems to be the most suitable in terms of preparation of ZnO nanorods in a next stage. Since metallic zinc undergoes passivation in air, the Zn crystals are covered with a thin native oxide monolayer (1 – 3 Å) [328]. As reported, $Zn(OH)_2$ transforms into ZnO within the temperature range from 70 ^oC to 140 ^oC [329], whereas $Zn(CH_3COO)_2$ into ZnO starts at 120 ^oC [330]. On the other hand, the calcination temperature should not exceed 450 ^oC. Above this temperature hexagonal metallic Zn crystals begin to transform into ZnO nanotubes in the form of external gauntlet to the internal Zn crystal initial embryo, as reported elsewhere [331,332].

In order to confirm the formation of ZnO on the surface of Zn, the samples before and after calcination were examined by XRD. In XRD pattern obtained for non-calcined sample (*Figure 47A*) one can observe only the signals corresponding to reflections from (002), (100), (101) and (102) planes of hexagonal Zn, respectively at 2θ : 36.4°, 39.0°, 43.4°, 54.5° (JCPDS 03-065-5558) and several peaks ascribed to the ITO substrate (labeled with asterisk). Calcination of the sample leads to the appearance of additional signals, most notably at $2\theta = 34.5^o$ corresponding to (002) lattice plane of ZnO wurzite (*Figure 47B*). This peak was not observed in the initial sample due to dominant amount of Zn over ZnO superficial native layers formed in effect of Zn-passivation during sample exposure to air.

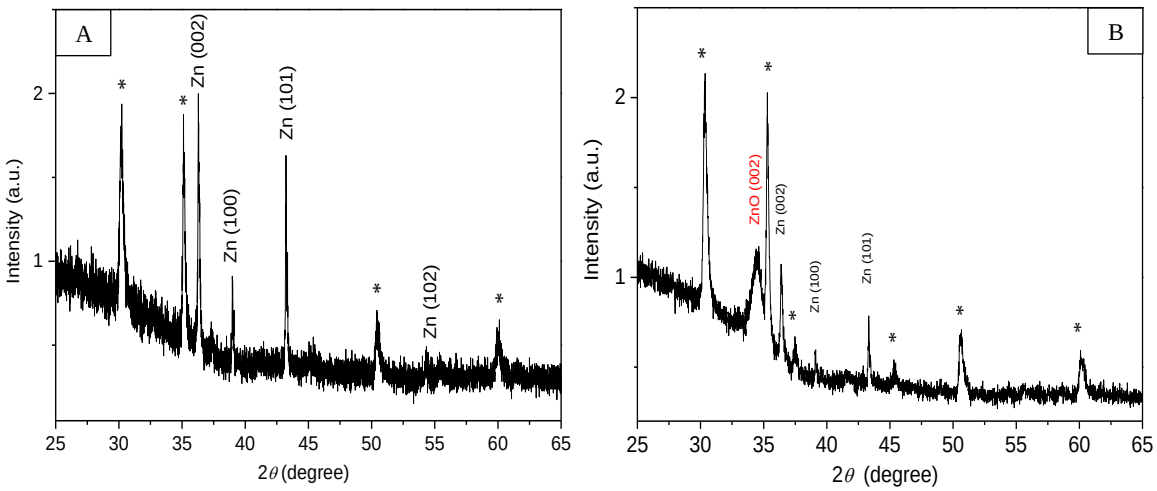

Figure 47 XRD patterns of the seed layer deposited in aqueous solution of 0.1 M $Zn(CH_3COO)_2$ at constant potential of –1.2 V before (A) and after calcination (B). Peaks labeled with asterisks correspond to ITO.

4.1.2. Hydrothermal growth of ZnO nanorods

ZnO nanostructures were fabricated via hydrothermal synthesis at 80 ^{o}C from aqueous solution containing $Zn(NO_3)_2$ with ammonia added to fix pH at 10.6. The synthesis products were 'star-like' ZnO structures formed in the bulk of solution (*Figure 48A*) and epitaxially grown 'obelisk-like' ZnO nanostructures on Zn/ZnO seeds (*Figure 48B*). It is worth to note that the seeding stage is essential for the immobilization of the ZnO nanostructures on the surface, since a simple rinsing with a stream of water removes all bulk-synthetized forms of ZnO structures from the plates.

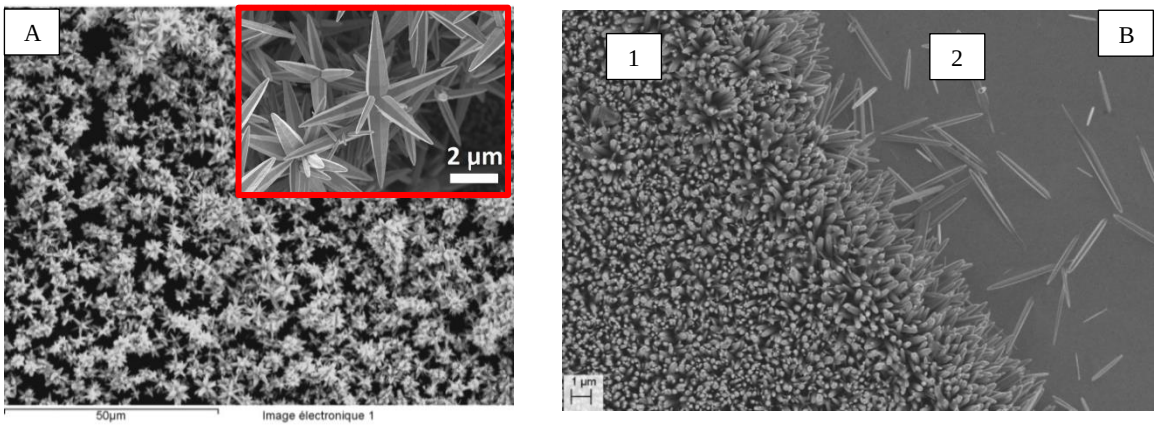

Figure 48 SEM images of ZnO 'star-like' structures formed in the bulk of solution (A), and SEM image of the edge between ZnO nanorods grown on Zn/ZnO seeded (1) and non-seeded (2) parts of the ITO plate (B).

The next task was to determine how the synthesis conditions, such as concentration of Zn^{2+} ions and reaction time influence on diameter and lengths of nanorods grown on

the seeded substrate. This is the key issue because the ZnO nanorods should be further covered with layers of TiO_2 and finally decorated with Au nanoparticles. Thus, the distances between the ZnO nanorods should be large enough for these further modifications. The exemplary results are compared in *Figure 49*. As shown in *Figure 49A*, when initial concentration of Zn^{2+} was 0.01 M, the nanorods were very thin and their tips had tendency to coalesce likely due to high surface energy. In contrast, the space between nanorods obtained at Zn^{2+} concentration 0.08 M is not sufficient for further modification (*Figure 49B*).

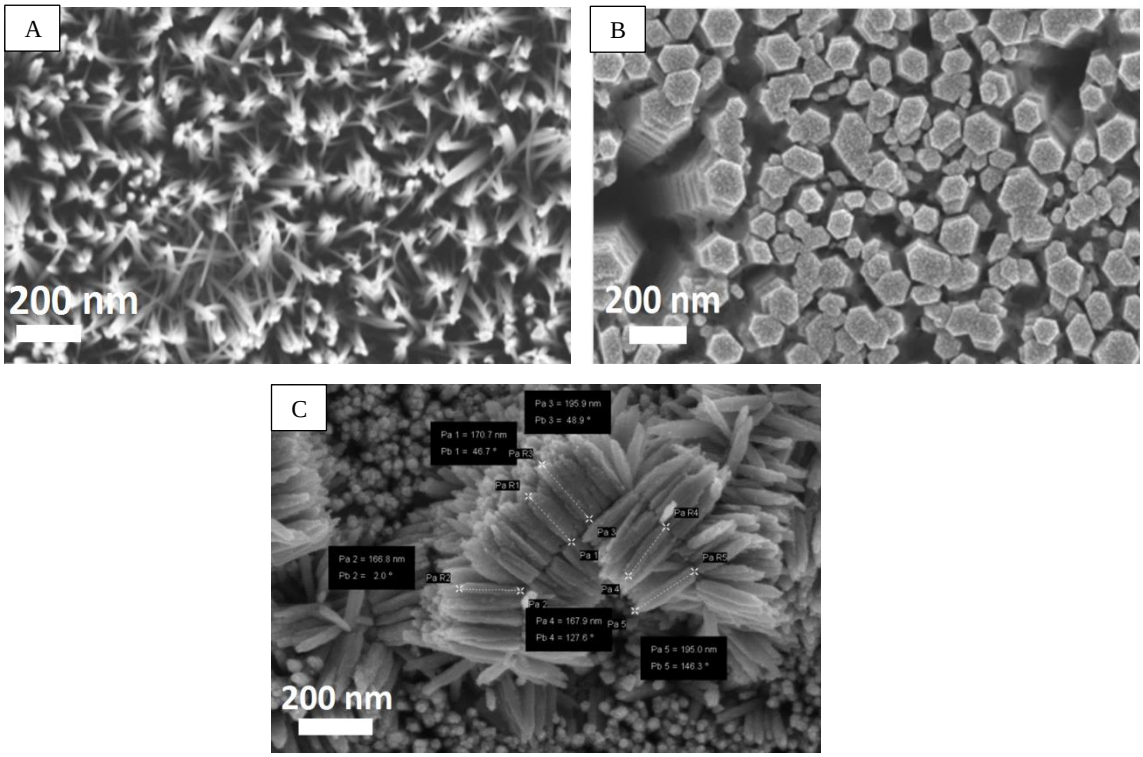

Figure 49 SEM images of ZnO nanorods grown from 0.01 M (A) and 0.08 M (B) initial zinc nitrate concentration after 2.5 h [333], ZnO nanorods grown from 0.02 M zinc nitrate solution after 1 h (C).

It was found that the optimal results were obtained after 2.5 h of hydrothermal synthesis from the solution of 0.04 M $Zn(NO_3)_2$. The average length of the nanorods after 2.5 h of synthesis was 1.9 μm, whereas the width varied from about 100 nm (at the top excluding sharp tip ending) to about 300 nm at the bottom of nanorods as they resembles 'obelisk-like' structures. The hexagonal ZnO nanorods with smooth sides (inset in *Figure 50A*) grown on the Zn/ZnO nanosheets structures were arranged in a uniform fashion (*Figure 50C*), whereas those grown on the Zn/ZnO crystals formed 'urchin-like' structures as illustrated in *Figures 50B* and *50D*. The XRD pattern of the sample shows dominant contribution of (002) ZnO plane at 2θ = 34.4^o which confirms high preferential

orientation and alignment of the ZnO structures. However, other weaker signals from ZnO can be noticed at 2θ: 36.3° of (101), 47.5° of (102), 56.6° of (110), 62.9° of (103), 68.0° of (112) planes. The presence of these signals in the XRD pattern can be assigned to different orientation of ZnO nanorods which grown on the side walls of the Zn/ZnO seeds. Other signals than ZnO, i.e. originating from Zn or ITO are negligible suggesting compact coverage of the support surface.

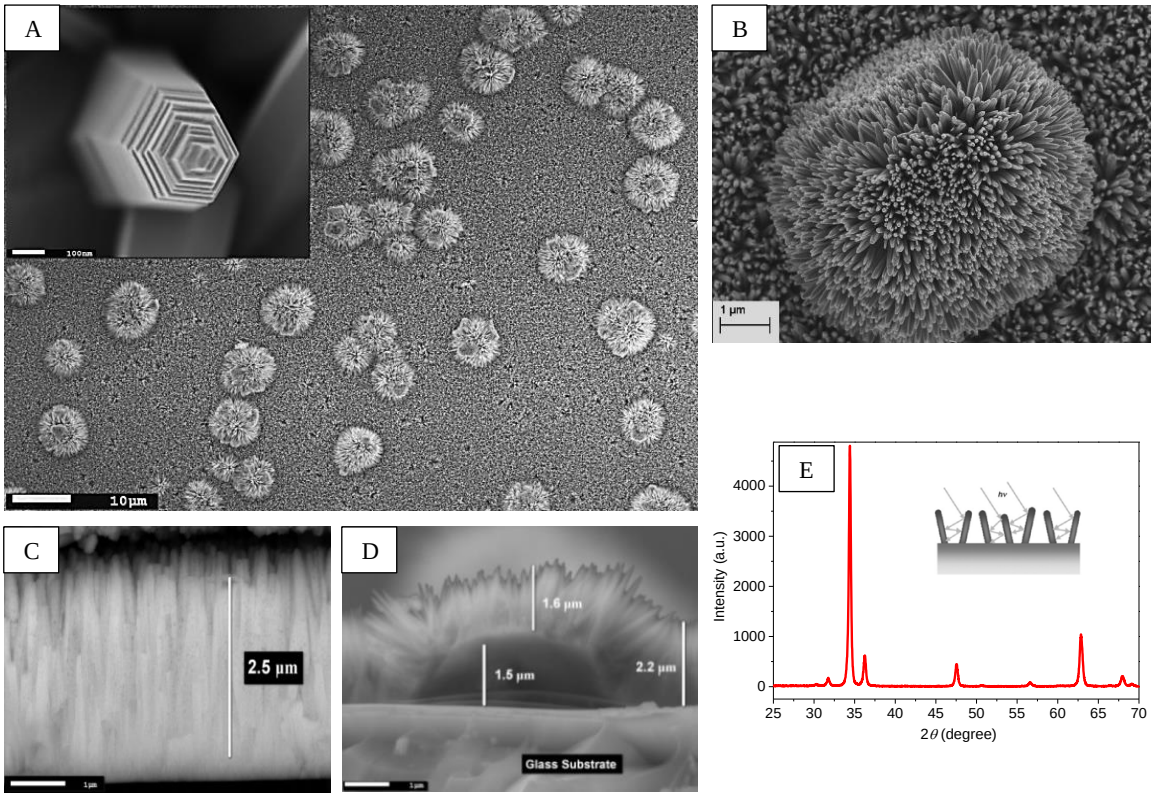

Figure 50 SEM images of ZnO nanorods obtained by hydrothermal method: top view of a large surface area (A) with a high-resolution micrograph of tip of a single ZnO nanorod (inset), urchin-like Zn/ZnO structure (B), and cross section views (B, C) seen in lower secondary and low-angle backscattered electron projection (LABE). XRD pattern of ZnO nanorods grown on Zn seeded ITO plate (E).

Since the urchin-like structures are formed randomly having also different size, the thickness of the resultant catalyst is not uniform. However, such urchin-like ZnO nanostructures may be advantageous for catalytic or sensor applications where large area of ZnO surface and easy access of the reagents to the nanorods are required. To our knowledge, only Cheng *et al.* [334] obtained similar electrode composed of urchin-like Zn/ZnO structures deposited on ITO by using complicated thermal vaporization techniques. It has been reported that urchin-like ITO/Zn/ZnO electrodes shown almost three times higher photocurrent than the electrodes of ZnO nanorods array in electro-

assisted water oxidation at 0.8 V (*vs.* SCE reference electrode) under xenon lamp light irradiation. The results presented above show that similar urchin-like Zn/ZnO nanorods can be obtained on Zn-seeded ITO by means of simple electrochemical/chemical methods, which allow for easy control of nanorods parameters.

4.1.3. Conclusions

The Zn/ZnO seed layers of different morphology (nanosheets and crystals) were electrochemically deposited (at the charge density ~ 140 mC cm^{-2}) at the potential of –1.2 V (*vs.* Ag/AgCl) on ITO electrodes from aqueous non-dearated solution of 0.1 M $Zn(CH_3COO)_2$. The obtained substrate was used for hydrothermal synthesis of 'obelisk-like' ZnO nanorods. The length and width of obtained ZnO nanorods depend strongly on Zn^{2+} concentration and synthesis duration. The arrays of well-separated ZnO nanorods of width varied from 100 nm at tips to ~ 300 nm at bottom and average length of 1.9 μm were prepared in optimized conditions: 2.5 h of growth in 0.04 M $Zn(NO_3)_2$ at pH 10.6 (fixed with ammonia) at 80°C.

ZnO nanorods were fabricated in the form of the uniform array on the regions of ITO layer seeded with Zn/ZnO nanosheets, whereas urchin-like ZnO structures were obtained on elemental Zn crystals. The optimization of synthesis conditions allowed to obtain Zn/ZnO(nanorods) well attached to ITO with a good electric contact with the substrate and highly developed surface. Such ITO/Zn/ZnO electrode may be used as the base for further modifications, to prepare core/shell ZnO/TiO_2 composites.

Figure 51a shows the simplified scheme of the elaborated procedure, whereas the SEM images presented in *Figure 51b* depicts the results obtained in the consecutive preparation stages of ITO/Zn/ZnO(nanorods) composites.

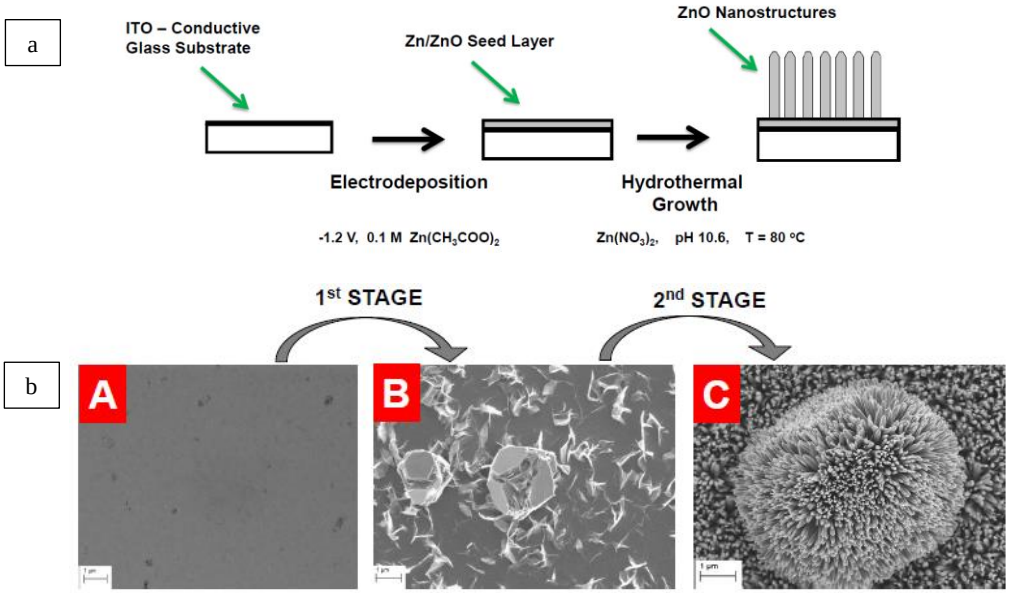

Figure 51 Scheme illustrating ITO/Zn/ZnO electrode preparation procedure (a) and SEM images collected during each fabrication stage (b).

4.2. Influence of the microstructure of TiO2 layer on the properties of ZnO/TiO_2 composites

4.2.1. Developing and characterization of core/shell ZnO/TiO_2 composites

As it was demonstrated in *Chapter 4.1*, the optimized synthesis conditions resulted in preparation of obelisk-like ZnO nanostructures with sharp tips and smooth side walls. These ZnO nanostructures served as a core material for coverage with TiO_2 shell. At first, it was intended to develop a simple, relatively rapid and reproducible procedure that can result in well-defined core/shell ZnO/TiO_2 composites with separated nanorods array. Therefore, in order to cover the ZnO nanorods with a thin layer of TiO_2, a sol-gel method was chosen. The attempts were undertaken to determine the influence of some procedure parameters on morphology of the resultant TiO_2 layer i.e. deposition time, molar and volume ratios of all synthesis precursors or even injection rate of water necessary to initiate the hydrolysis of titanium precursor. Titanium butoxide was chosen as an inexpensive TiO_2 precursor, while isopropanol was selected as a water-free reaction medium. The SEM images presented in (*Figure 52)* show morphology of samples prepared by sol-gel method when synthesis conditions were not well established. The ZnO nanorods visible in *Figure 52A* remained almost unmodified, while these in *Figure 52B* are covered with a thick TiO_2 layer, filling also the space between the nanorods. The jointed ZnO nanorod array and the TiO_2 layer resemble one dense integument that possesses characteristic cracks, visible in the SEM image, formed during calcination.

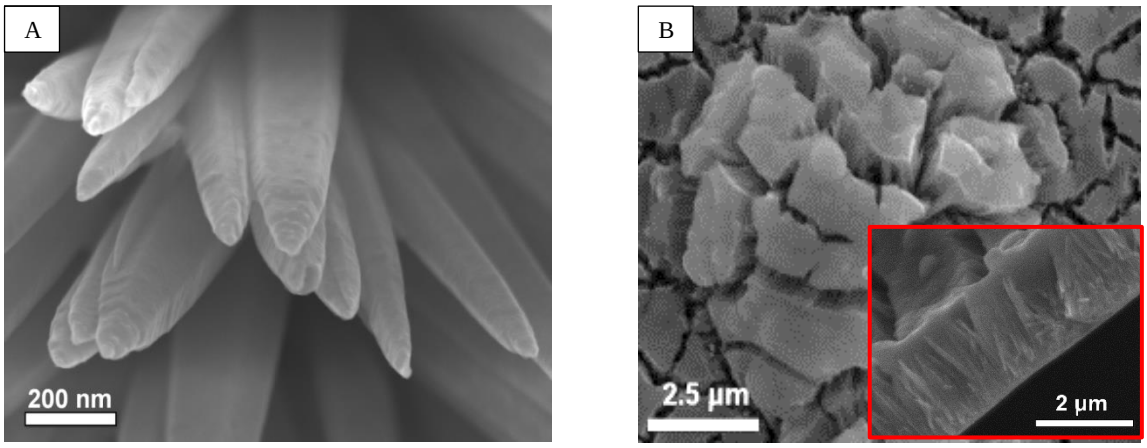

Figure 52 SEM images of ZnO nanorods with insufficient (A) and excessive (B) amount of TiO_2 deposited by sol-gel method. Inset B shows side view of the ZnO/TiO_2 array detached from the ITO-support.

Further investigations were carried out in order to optimize deposition procedure to cover the ZnO nanorods with thin layer of TiO_2. Ultimately, the optimization resulted in preparation of two different, most distinctive morphologies of TiO_2 layers. In the first case, precipitation/deposition of TiO_2 was carried out for 6 h in a one deposition cycle, and so the ZnO/TiO_2 composite was denoted as '***1c***'. The second type of ZnO/TiO_2 sample was prepared in three consecutive cycles, however, each the one lasting 30 min ('***3c***'); for more details of the preparation procedure, see section *'TiO_2 Sol-Gel Deposition'* in the *Experimental* part.

Since, as-deposited TiO_2 via sol-gel method is amorphous and in this form should have negligible photocatalytic properties [335], it was necessary to convert it into anatase by calcination. On the other hand, the temperature of calcination should be chosen with caution because it is an important factor influencing material properties. Taking into account complexity of designed ITO/ZnO/TiO_2 material one shall bear in mind the limitations of its components, i.e. 600 ^oC and above, can strongly reduce conductivity of indium tin oxide in ITO [336,337], which may finally result in lower electroactivity when the composite is used as an electrode. The materials prepared by sol-gel method are known to contain organic residues and the amorphous-to-anatase phase transformation temperature strongly depends on the size of TiO_2 nanoparticles and synthesis conditions. For this reason, TGA-DSC was used to determine the temperature at which these residues are completely eliminated and on the other hand, TiO_2 is transformed into anatase.

First, pure TiO_2 formed in bulk of the solution during $Ti(OC_4H_9)_4$ hydrolysis was characterized (*Figure 53A*). Analysis of the weight changes (red curve) and corresponding thermal effects (black curve) allowed to distinguish the following stages. The weight loss observed below 100 °C, accompanied by an endothermic broad peak, can be attributed to the dehydroxylation of the formed titanium (oxo)hydroxide. Further increase of the temperature to 200 ^oC – 300 °C results in an additional weight loss coinciding with a significant exothermic effect. This combination indicates clearly a burning out of the organic species occluded in the sample. The last process occurring at 400 °C results in a sharp heat release without any noticeable weight variation which allows to assign it to crystallization of anatase.

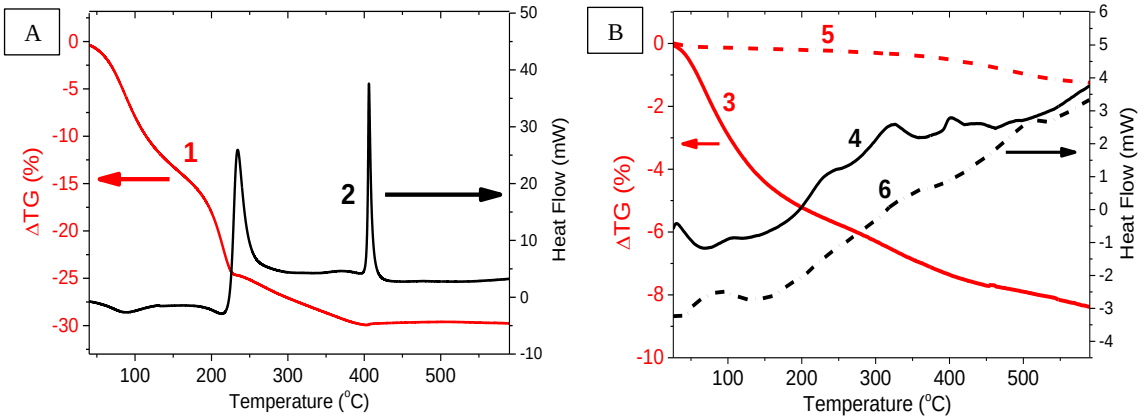

Figure 53 Thermogravimetric (TGA, red curves, 1, 3, 5) and differential scanning calorimetry (DSC, black curves 2, 4, 6) results for TiO_2 powder precipitated in the bulk of the deposition solution (solid lines, 53A) and for ZnO/TiO_2 composite detached from the support (solid lines, 53B). The dotted lines in Figure 53B correspond to the results obtained for bare ZnO nanorods. All measurements were performed under air flow.

The amount of the TiO_2 deposited on ZnO nanorods in a single sample was insufficient for correct TGA-DSC measurements. Therefore, the analysis was done on the material gathered from several identically prepared ***3c*** samples so the weight of collected material was sufficient (*ca.* 10 mg). The TGA-DSC profiles were also recorded for bare ZnO nanorods (*Figure 53B*, dotted curves) and this material was used as the reference one for the ZnO/TiO_2 system (*Figure 53B*, solid lines).The result obtained for bare ZnO is in accordance with general behavior of materials without phase transition. Although the peaks for ZnO/TiO_2 sample are less intense and broader than those for pure TiO_2 (*Figure 53A*), the same trends can be distinguished in the obtained TGA-DSC profiles. Below 100 °C the weight loss is endothermic and thus it can be attributed to the dehydroxylation of the amorphous titanium hydroxide. At higher temperatures the exothermic peaks are observed which are due to burning out of organic residues and crystallization of anatase phase. The broadening of the exothermic peaks in the case of ZnO/TiO_2 can be explained by its specific preparation procedure. Indeed, three layers produced in different steps can have slightly different thermal behavior stemming possibly from their varying arrangement relatively to ZnO nanorods. Such heterogeneity should naturally result in broader peaks than those for the non-supported solid prepared in a single step. The TGA-DSC data show that the calcination temperature of 450 °C is sufficient for burning out the organic residues. It follows also that at this temperature the deposited amorphous layer is transformed into anatase with a high rate as suggested by

the sharpness of the corresponding exothermic peak. This finding confirms that the chosen calcination time (1 h) allows a complete conversion of the amorphous titanium (oxo)hydroxide into a crystalline anatase. Also it should be noted that the initial layers formed on ZnO nanorods consisted of hydrated amorphous titanium dioxide in the form of titanium hydroxides, $TiO(OH)_2$ or $Ti(OH)_4$. After calcination of the samples at 450 °C for 1 h the surface of the nanorods became rough due to shrinking of deposit in effect of removal of water. For these reasons SEM images of both ***1c*** and ***3c*** composites after calcination were collected.

As it is shown in SEM image (*Figure 54A*) the ZnO surface at low magnification is not much changed in both ZnO/TiO_2 composites when compared to initial, raw ZnO samples (*Chapter 4.1*, *Figure 50*). However, at higher magnifications one can observe that the surface of ZnO nanorods has been significantly modified (*Figures 54B,* and *54C*). From comparison of the pictures taken at higher magnification it is evident that the surface of ZnO nanorods is covered with the layer of deposit. It is worth noting that in both cases the surface is free of TiO_2 particle aggregates or clusters.

Another fact should be also noted here – at higher magnifications it is visible that the surface of ***1c*** sample is more corrugated and rough (*Figure 54A*) than that of ***3c*** composite (*Figure 54C*). The SEM pictures presented in *Figure 54C* indicate that ZnO nanorods after three deposition cycles of TiO_2 are covered with a uniform, continuous and smooth coating. Application of low-angle backscattered electron detector (LABE) allowed distinguishing inner ZnO core (less transparent, brighter contrast) from the external TiO_2 shell especially closer to the edge of nanorod (more transparent, darker contrast) due to difference in atomic numbers of Zn and Ti (*Figure 54D*). Such detection was not possible for ***1c*** sample probably because of a thinner TiO_2 layer deposited on the nanorods.

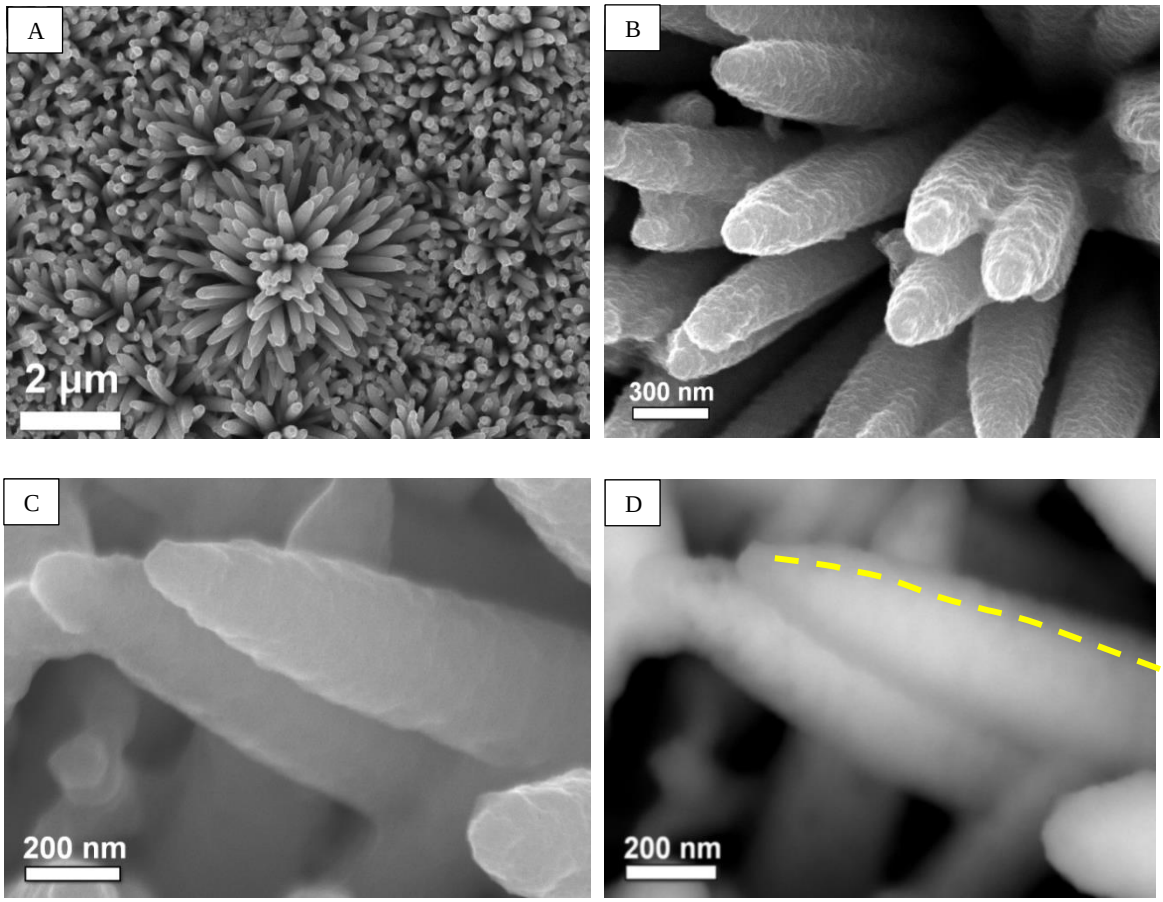

Figure 54 SEM images of ***3c*** *(A, C, D) and* ***1c*** *(B) ZnO/TiO_2 samples. Single nanorods observed at higher magnification using secondary electron imaging (SEI, C), and low-angle backscattering electron detection – LABE (D), yellow dashed line indicates the boundary between ZnO and TiO_2.*

More detailed study of the samples morphology was performed by TEM. A rough TiO_2 layer in ***1c*** sample is well visible in TEM images presented in *Figures 55A* and *55B*. It is also worth noting that in this case the TiO_2 layer is composed of nanoparticles of various shape and size (diameter in the range 3 nm – 8 nm, based on analysis of several TEM images of different ***1c*** nanorods). The micrographs presented in *Figures 55C* and *55D* clearly indicate that the three-cycle procedure led to formation of continuous TiO_2 layer of average thickness 25 nm – 40 nm.

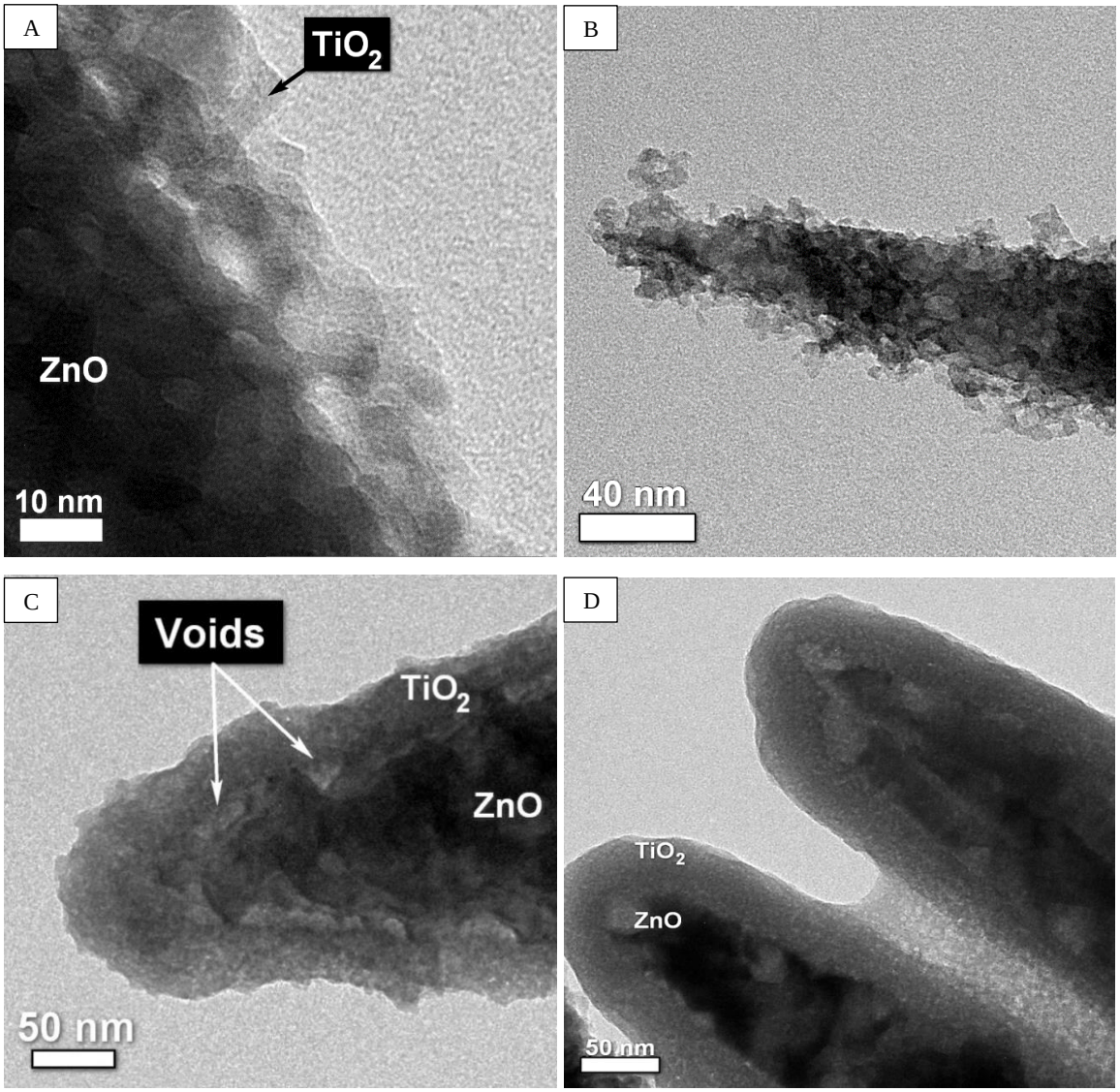

*Figure 55 TEM images of **1c** (A, B) and **3c** (C, D) ZnO/TiO_2 composites.*

Although the layer is composed of three thinner layers formed in separate deposition cycles, one cannot distinguish the frontiers between them. This means that nanoparticles formed in subsequent deposition cycles filled the gaps formed after calcination of the previous layer. It is also interesting to note that at high magnification one can see that the boundary between ZnO and TiO_2 is not smooth but some brighter pits are located in ZnO nanorods. These empty spaces could be formed according to the mechanism analogous to void formation in the Kirkendall effect [338], consisted in partial diffusion of elements during calcination. The detailed discussion of this phenomenon will be presented in *Chapter 4.3*. As to the procedure itself, we can conclude that it matched the prerequisite of a good reproducibility. The summary of the schemes of sol-gel deposition of TiO_2 on ZnO nanorods is presented in *Figure 56*.

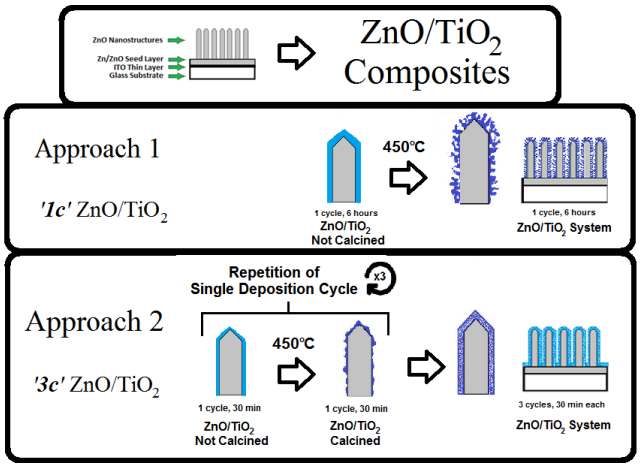

Figure 56 Schemes of the two approaches in preparation TiO_2 thin layers on ZnO nanorods: ***1c*** *(App. 1) and* ***3c*** *(App. 2).*

The spectroscopic tests (*Figure 57A*) proved that the decrease of methylene blue (MB) concentration in aqueous solutions, due to dye adsorption on the composites, was greater for ***1c*** sample than for ***3c*** one, whereas adsorption on ZnO was negligible. The mass of ZnO nanostructures measured with the sensitive microbalance was 1.15 mg per 1 cm^2 of seeded ITO substrate (geometrical size of the sample). The results of EDX analysis (Ti/Zn ratio) allow to estimate that the amount of TiO_2 deposited on ZnO nanorods in ***1c*** procedure was about 0.11 mg per 1 cm^2, while for ***3c*** was almost three times higher, 0.28 mg cm^{-2}.

The isoelectric point of TiO_2 may vary [339,340] therefore it was reasonable to determine it for TiO_2 nanoparticles obtained by sol-gel method used in this work for fabrication of ZnO/TiO_2 composite. Thus, the powder synthesized in the bulk of the solution was calcined at 450 ^oC for 1 h and suspended in aqueous solutions of different pH (adjusted with HCl or NaOH). As visible in *Figure 57B*, the isoelectric point determined from pH-dependence of zeta potential is about 4.3, i.e. at neutral pH the surface of TiO_2 nanoparticles is negatively charged. Since methylene blue is a cationic dye, one can expect its preferential adsorption on the surface of TiO_2-modified ZnO nanorods. This has been confirmed by UV-vis measurements of MB solution being in contact with ZnO/TiO_2 composites.

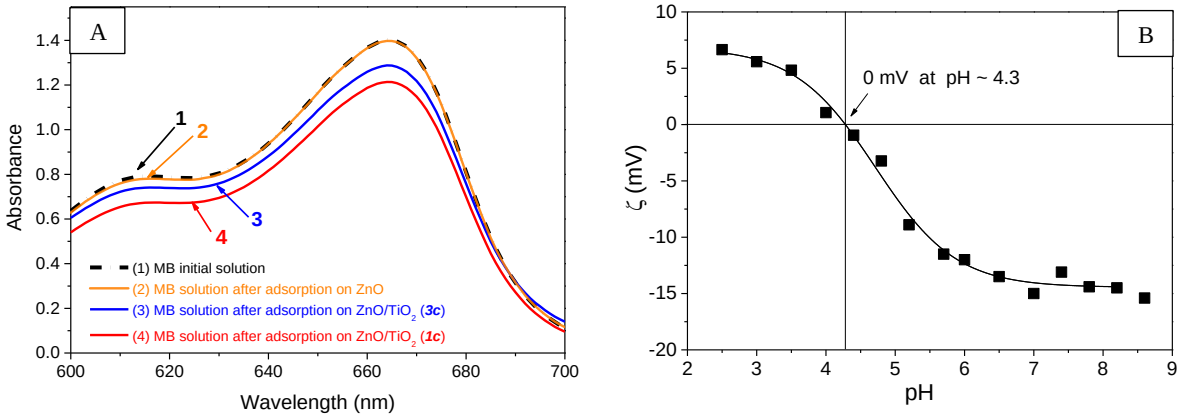

Figure 57 Absorption spectra of initial aqueous solution of 20 μM MB (curve 1) and after adsorption of MB for 24 h on ITO/ZnO (curve 2), ***3c*** *(curve, 3) and* ***1c*** *(curve, 4) (A) and zeta potential (ζ) of TiO_2 sol-gel prepared nanoparticles in a function of pH (B).*

The amount of MB molecules adsorbed on the ZnO/TiO_2 composites, estimated from absorption spectra, is $9 \cdot 10^{-8}$ mol per 1 mg of TiO_2 for ***1c*** sample and 3.5 times lower ($2.6 \cdot 10^{-8}$ mol per 1 mg of TiO_2) for ***3c*** sample. These results clearly demonstrate that TiO_2 layer obtained within ***1c*** synthesis procedure possess more developed surface than that formed *via* ***3c*** procedure which is consistent with TEM images presented above.

XRD characterization of the two discussed $ITO/ZnO/TiO_2$ composites and TiO_2 powder after calcination at 450 ^oC was performed to confirm a complete amorphous-to-anatase transformation upon calcination. The XRD patterns recorded for these materials are presented in *Figure 58A* together with ZnO and TiO_2-anatase reference patterns. The XRD pattern of TiO_2 powder calcined at 450 °C for 1 h fits to that of anatase-TiO_2 (ICDD Card No. 03-065-5714). The peaks observed at 2θ angle: 25.3°, 37.8°, 48.0°, 54.0°, 55.1°, 62.5°, 68.7°, 70.2°, 75.1°, 82.7°, correspond respectively to the planes: (101), (004), (200), (105), (211), (204), (116), (220), (215), (224). No other peaks were observed in TiO_2 powder suggesting formation of pure anatase phase. As to the XRD results of ITO supported samples, all recorded peaks are characteristic of ZnO Standard Pattern (ICDD Card. No. 00-036-1451). Among all ZnO-matched peaks in the samples, the two are particularly noticeable, due to their strong intensity, at 34.4^o and 62.9^o, suggesting strong preferential orientation of ZnO along crystallographic directions [002] and [103], respectively.

By the reason of such strong alignment of ZnO nanorods and very small amount of deposited TiO_2, the XRD patterns of ZnO/TiO_2 samples are mostly dominated by these two ZnO signals. Nevertheless, the most intense TiO_2 peak (101) can be still distinguished in the ***3c*** XRD pattern in which the TiO_2 deposited amount was expected to be the highest. The XRD results along with the TGA-DSC data confirmed thus the presence of TiO_2-anatase after calcination at 450 ^oC.

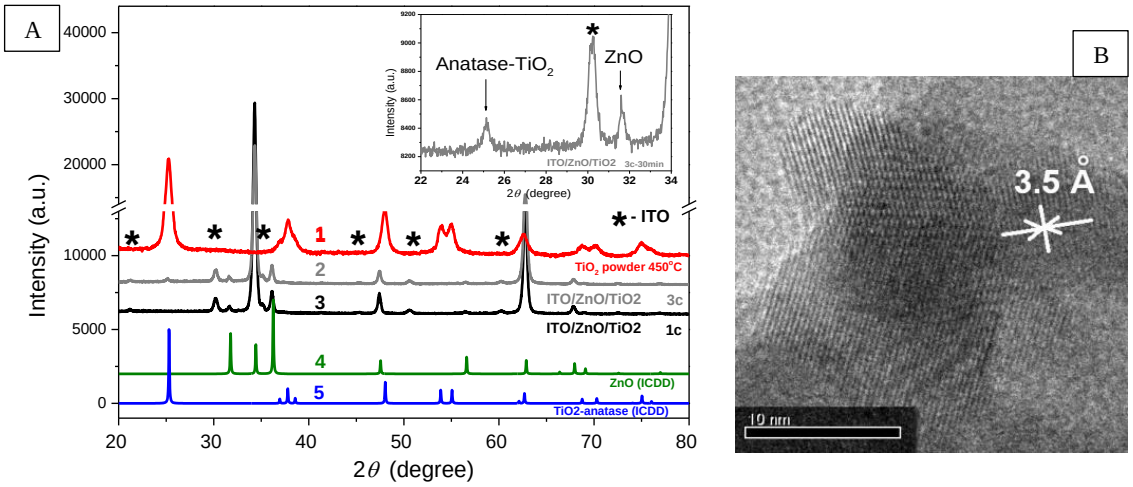

*Figure 58 XRD patterns of: TiO_2 powder obtained in the bulk of the solution by sol-gel method and calcined at 450 ^oC (red, line 1), **1c** (black, line 3) and **3c** (grey, line 2) ITO/ZnO/TiO_2 samples. Blue pattern (line 5) corresponds to the reference TiO_2-anatase, whereas green (line 4) to ZnO. Inset in the right top corner depicts anatase-TiO_2 peak position of (101) planes found in a **3c** sample (A). HR-TEM image of TiO_2 nanoparticles with indicated interplanar distance of 3.5 Å corresponding to the anatase-TiO_2 plane (101).*

Surface chemical composition of ZnO nanorods and ZnO/TiO_2 core/shell systems was determined by analysis of Ti2p, Zn2p and O1s peaks in XPS spectra presented in *Figure 59*. The positions of peaks of Zn $2p_{1/2}$ and $2p_{3/2}$ at 1021.4 eV and 1044 eV in the spectrum of ZnO nanorods are typical for Zn with oxygen surroundings [341,342]. The same conclusion can be drawn for Ti atoms as Ti $2p_{3/2}$ and Ti $2p_{1/2}$ peaks observed respectively at 458.5 eV and 464 eV, characteristic of Ti-O binding energies in TiO_2 nanoparticles [343,344]. The O1s peak in bare and TiO_2-covered ZnO nanorods has a complex structure with a pronounced shoulder. The position of the main component (530.2 eV) is typical for oxygen atoms in oxides [345,346]. The shoulder with the maximum at 532.8 eV can be attributed to the surface OH groups [347]. The OH groups detected on the surface of both samples after calcination (300 °C for bare ZnO nanorods or 450 °C for ZnO/TiO_2) cannot be due to incomplete dehydroxylation since according to

TGA-DSC it is completed below 200 °C (see *Figure 53*). Appearance of OH groups can thus be explained by the dissociative water adsorption on the surface of the samples during their exposure to the ambient air prior to recording of XPS spectra [348].

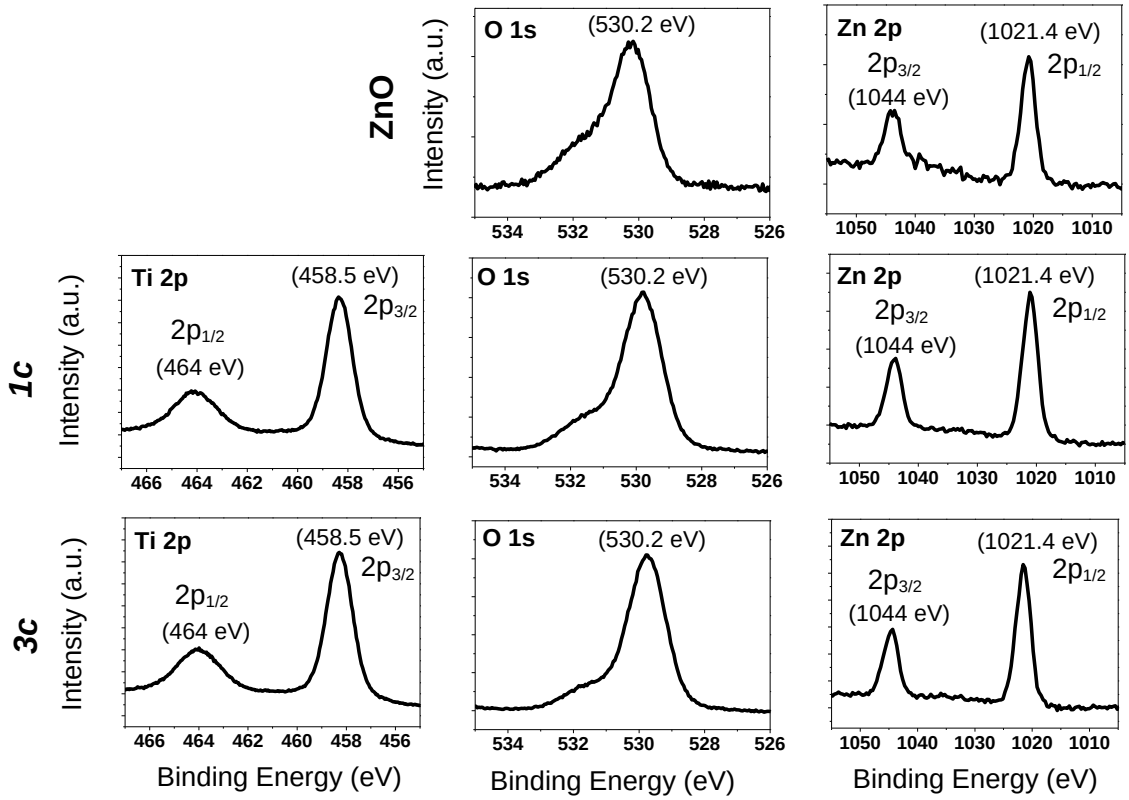

Figure 59 XPS spectra of pristine ZnO (top row), and ZnO/TiO_2 composites: ***1c*** *(middle row) and* ***3c*** *(bottom row).*

The results of the quantitative analysis of relative amount of Ti and Zn in different samples are presented in Table 9 along with EDX-SEM results. It follows from the EDX results that the increased number of sol-gel cycles (from one to three) allows to deposit higher amount of TiO_2, despite shortening of each cycle 6 h to 30 min. The total Ti/Zn ratio increased from 0.10 in ***1c*** samples to 0.27 in ***3c*** composites. In contrast, the XPS measurements deliver information about surface Ti/Zn ratio and allow to estimate the efficiency of the coverage of ZnO with TiO_2 layer. The data in Table 9 show that the trend is similar to that observed for the total amount of TiO_2. In this regard, the multiplication of cycle numbers brings a considerable increase of Ti/Zn ratio in the surface layer.

Table 9 Titanium-to-zinc ratios obtained from XPS, EDX-SEM measurements for composite systems and optical energy band gap values determined from UV-vis spectra. If not stated, the calcination was performed at 450 ^{o}C for 1 h.

Sample	Optical band gap energy E_g (eV)	XPS (atomic %) Zn	Ti	Ti / Zn ratio XPS	EDX
sol-gel TiO_2 powder	2.95 (n = 2)	–	–	–	–
ZnO calcined 300 ^{o}C 1 h	3.05 (n = ½)	–	–	–	–
1c (ZnO/TiO_2)	2.86 (n = 2) 2.93 (n = ½)	15	17	1.16	0.10
3c (ZnO/TiO_2)	2.78 (n = 2) 2.85 (n = ½)	10	20	2.00	0.27

Comparison of the XPS results with TEM observations allows to obtain additional information about textural properties of the TiO_2 layers. It is well known that a surface layer analyzed by XPS in inorganic materials is about several nanometers. Using QUASES-IMFP-TPP2M software (*available free at* http://www.quases.com/products/quases-imfp-tpp2m/) it is possible to estimate the thickness of coating-layer material that prevents from XPS detection of under-layer second material. The thickness of the coating material (J) can be estimated using the equation [349]:

$$I = I_0 exp \frac{-J}{Jcos\Delta\theta} \tag{68}$$

where, I is the intensity of the beam reaching detector, I_0 expresses the intensity of initial beam, and $\Delta\theta$ is the deviation of the angle from 45^{o}. The basic scheme of application of the equation is illustrated as inset in *Figure 60*.

The estimation for the flat ZnO surface covered with a continuous layer of crystalline TiO_2-anatase, showed that Zn atoms should not be seen in XPS if the thickness of TiO_2 layer exceeds 4 nm (*Figure 60*).

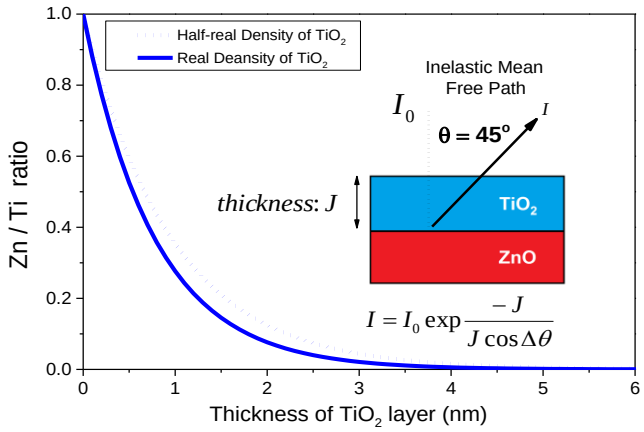

Figure 60 Theoretical Zn / Ti atomic ratio as a function of TiO_2 layer thickness deposited on ZnO, determined by calculations by means of QUASES-IMFP-TPP2M software. Inset: scheme on the right side of the curves illustrates the basis of the analysis concept (B).

The thickness of the shell formed in the ***3c*** sample (*ca.* 40 nm, see *Figure 55*) is however much larger than the calculated limit. Assuming that this TiO_2 shell is continuous, the presence of Zn signal in XPS spectra can be explained only if one admits that TiO_2 layer is porous. In this case, the effective density of the layer will be much lower than that of crystalline TiO_2 anatase and the photoelectrons emitted by Zn atoms will be able to reach the external surface of the particles. The presence of an intense signal of Zn in the XPS spectra of ZnO/TiO_2 is thus a clear indication that the produced TiO_2 anatase shell is porous.

In order, to characterize optical properties of the ZnO/TiO_2 composites, UV-vis absorbance spectra of the ***3c*** and ***1c*** samples are compared in *Figure 61* with the results obtained for bare ZnO nanorods and TiO_2 powder obtained *via* sol-gel method. As visible, the absorption edges for single oxides are at about 400 nm for ZnO or even slightly lower *ca.* 390 nm for TiO_2. In contrast, the composite ZnO/TiO_2 samples demonstrated noticeably red-shifted absorption onset (to ~ 450 nm). The spectra of the composites reveal also a pronounced low-energy absorption tail ('Urbach tail') increasing from about 550 nm, which may be a result of appearance of new interface energy states in the band gaps of ZnO and TiO_2. Since, these new interface levels can be localized closely to the conduction bands, excitation to them may be probable [19].

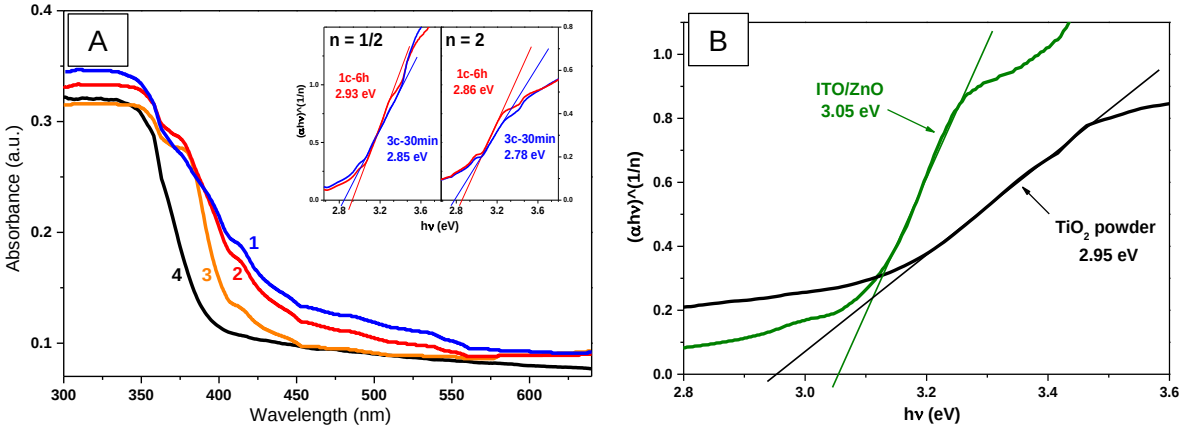

*Figure 61 Absorbance spectra of **3c** (blue curve, 1) and **1c** ZnO/TiO_2 systems (red curve, 2); the orange curve (3) to ZnO sample, whereas the black curve (4) corresponds to the spectrum of TiO_2 powder obtained by sol-gel method and calcined at 450 ^oC (A). Inset A represents the plots of $(\alpha h\nu)^{1/n}$ as a function of photon energy $(h\nu)$ for direct (n = ½) and indirect (n = 2) transitions in semiconductors. The $(\alpha h\nu)^{1/n}$ plots were calculated from the absorbance spectra. $(\alpha h\nu)^{1/n}$ as a function of photon energy (hν) for determination of optical energy band gaps of pristine ZnO and TiO_2 powder (B).*

Since the TiO_2 is an external layer thus, it was assumed in calculations and plotting that the exponent in the component materials is n = 2. However, concerning morphology and thickness of the TiO_2 layers one should compare both extremes (n = ½, n = 2) as it has been reasonably presented elsewhere for $ZnFe_2O_4/TiO_2$ composite systems [350]. As depicted in the inset in *Figure 61A*, the lowest value of optical energy band gap was found for ***3c*** ZnO/TiO_2 composite (~ 2.78 eV) and a little higher (~ 2.86 eV) was obtained for the ***1c*** ZnO/TiO_2 (Table 9). And yet, each system showed lower value of optical energy band gap than any particular separate bare material (ZnO (nanorods): 3.05 eV and TiO_2 (powder): 2.95 eV, *Figure 59B*). At this point it is also worth noting that zinc titanates of various Ti-to-Zn atomic ratios had their absorption edges in deep UV range (< 380 nm) and optical energy band gap values varied from 3.32 to 3.70 eV [351,352]. Thus, the optical behavior of the ZnO/TiO_2 systems can be ascribed to appearance at ZnO/TiO_2 interface of new states whose energy levels are localized inside the band gap. While formation of such states was previously postulated in ZnO/TiO_2 systems, their physical nature has not been elucidated up to date. In our case, the high concentration of the vacancies is evidenced by the formation of voids (*see Figure 55C*) which are in fact the clusters of such vacancies [353]. The energy levels corresponding to the vacancies in ZnO are localized inside the band gap [354] giving rise to sub-band gap

optical transitions in the visible range. Also in such energy states the electrons' lifetime can be effectively prolonged, hindering the recombination [355,356]. It would be therefore interesting to characterize the influence of these new interface energy states on photocatalytic efficiency, to do that the monochromatic irradiation (400 nm) emitted by LED was chosen.

4.2.2. Photocatalytic tests

In order to evaluate photocatalytic activity of the ZnO/TiO_2 composites, photodecolorization of a model pollutant (methylene blue, MB) was investigated according to the International Standard Organization procedure [87]. By choosing the monochromatic light of 400 nm wavelength photosensitization of MB was eliminated [357]. The mechanism of MB photodegradation by semiconductor materials in aqueous solutions can be explained by formation of oxidizing agents and proceeds through the initial stage which is decolorization (see *Bibliography paragraph 2.1.19* '*MB photocatalytic degradation*'). The decolorization rate of 10 μM MB aqueous solution under illumination with the LED of the wavelength 400 nm was determined from decrease of absorbance maximum intensity in UV-vis spectrum of the solution at the wavelength of 664 nm (*Figures 62A* and *62B*). In order to avoid the decrease of MB concentration in the test solution due to adsorption of the dye on TiO_2, all samples prior to exact photocatalytic measurements were held for 24 h in the 20 μM MB solution to attain an adsorption-desorption equilibrium. Together with the results obtained for illuminated samples, the data for 'dark' samples were collected as a reference. Also, to prove a complete mineralization of MB the total organic carbon (TOC) content was measured in the MB solutions before and after 120 min of illumination for ***3c*** and ***1c*** samples and the results were compared with decolorization percentage (*Figure 62D*).

According to the band gap values listed in Table 9, the photon energy corresponding to the wavelength 400 nm (3.1 eV) is high enough to excite the electrons from valence to conduction band of ZnO nanorods and ZnO/TiO_2 systems. However, the photocatalytic experiments shown that the performance of ZnO/TiO_2 systems is better than that of bare ZnO nanorods (*Figure 62B*).

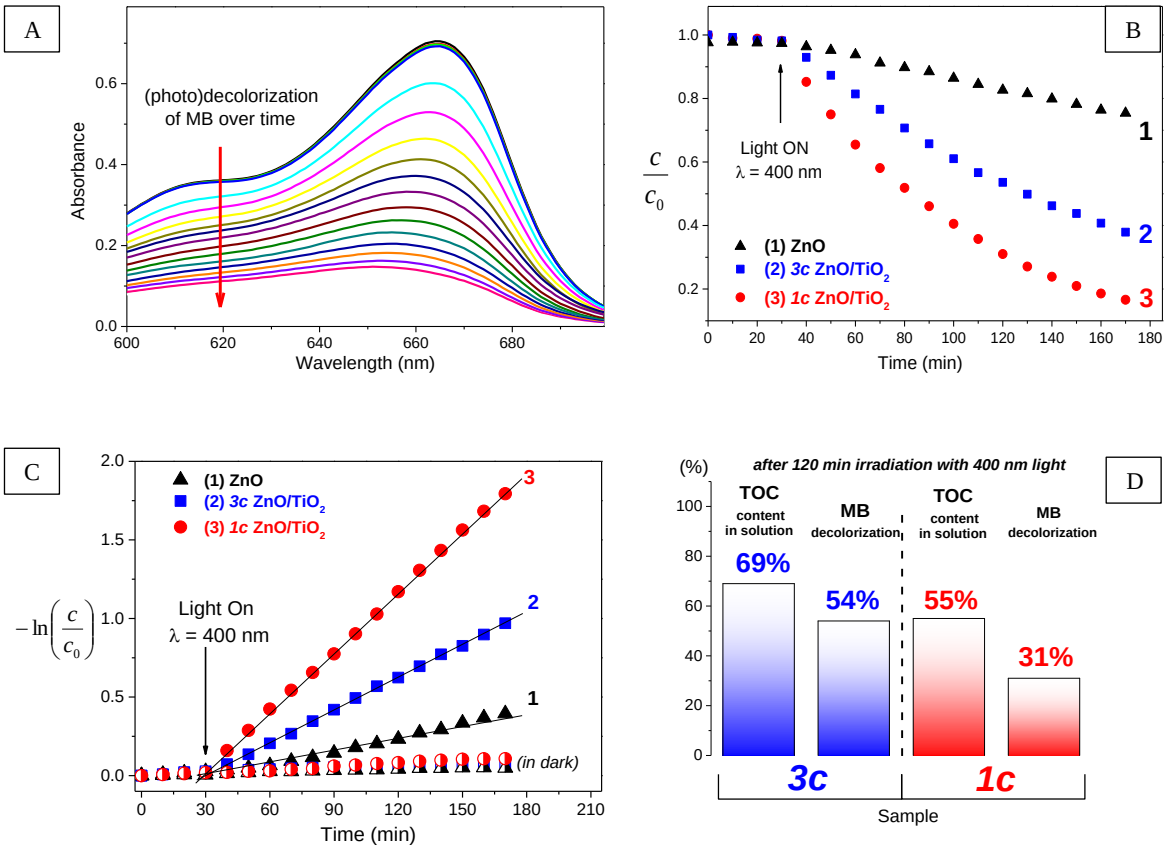

*Figure 62 (A) Evolution of absorption spectra of aqueous solution of MB during photocatalytic process on **1c** ZnO/TiO_2 composite under 400 nm irradiation. (B) Relative concentration changes (c/c_o) of MB determined from decrease of absorption peak at 664 nm during photocatalytic process with the use of ZnO (black triangles, 1), and ZnO/TiO_2 composites: **3c** (blue squares, 2) and **1c** (red circles, 3). (C) The linear plots of $-ln(c/c_o)$ vs. Time ($R^2 > 0.99$) used for determination of the apparent first-order rate constants of MB decolorization (k_{400}) from data in figure 62B (lines 1 – 3. The reference tests carried out in 'dark' conditions – ZnO (half-filled triangles), **3c** (half-filled squares), and **1c** (half-filled circles). (D) Comparison of total organic carbon (TOC) content in the solutions and MB photodecolorization efficiency after 120 min on **3c** and **1c** samples under 400 nm light irradiation.*

Moreover, the apparent first-order constant rate obtained for ***1c*** sample (k_{400} = 1.2 $\cdot 10^{-2}$ min^{-1}) is almost two times higher than that of ***3c*** sample (k_{400} = 0.7 $\cdot 10^{-2}$ min^{-1}) and even six times higher than that of the bare ZnO (k_{400} = 0.2 $\cdot 10^{-2}$ min^{-1}). A small value of the rate constant for ZnO is in accordance with very low absorbance at 400 nm observed in UV-vis spectrum of ZnO (*Figure 61*). Also, the activity of ***3c*** used without any calcinations at 450 ^{o}C was k_{400} = 0.4 $\cdot 10^{-2}$ min^{-1} (*not included in Figure 62*), which supports the importance of amorphous-to-anatase TiO_2 phase transformation.

Alongside MB decolorization tests, the total organic carbon (TOC) analyses were done for ***1c*** and ***3c*** samples (*Figure 62D*) in order to confirm degradation of the organic pollutant. According to the literature [97], MB photodegradation proceeds through chain reaction stages to final simple inorganic species such as NH_4^+, NO_3^-, SO_4^{2-}, CO_2. The TOC measurements of MB solutions before and after 120 min irradiation under 400 nm in the presence of the ZnO/TiO_2 composites showed that indeed MB is mineralized and organic carbon removal was greater for ***1c*** (45% removal) than for ***3c*** (31% removal). It is worth noting that in both cases the percentage of MB decolorization was higher than the TOC removal. Since the decolorization process is the first stage of a dye degradation, the differences are justified and consistent with the data reported also for other dye decomposition e.g. methyl orange (MO) [358].

The increase of absorbance in visible range after deposition of TiO_2 on ZnO may be a result of appearance of new interface energy levels as it was discussed in previous section. On the other hand, according to the literature, a lower edge of conduction band (CB) in ZnO lies a little above the CB of TiO_2 and therefore, the photogenerated electrons are transferred from CB of ZnO to CB of TiO_2, whereas the holes from VB of TiO_2 to VB of ZnO. Thus, the formation of ZnO/TiO_2 interface may lead not only to lowering excitation energy but also to better separation of charge carriers preventing fast charge carriers recombination.

In order to prove a significance of the hole-dependent dye decolorization mechanism rather than that via photoexcited electrons, the similar catalytic tests were performed with addition of methanol, known as an efficient scavenger of the photogenerated holes [359,360]. The results showed that photocatalytic activities of all samples decreased substantially (see comparison of the results in *Figure 62C*). The most notable drop of the rate constant value by factor 4 (from $1.2 \cdot 10^{-2}$ min^{-1} without to $0.30 \cdot 10^{-2}$ min^{-1} in the presence of methanol) was recorded for ***1c*** sample. The rate constants of the process performed with two other samples decreased twice, namely to $k_{MetOH} = 0.36 \cdot 10^{-2}$ min^{-1} for the ***3c*** sample and to $k_{MetOH} = 0.08 \cdot 10^{-2}$ min^{-1} for ZnO. These results support the assumption that MB decomposition mechanism can be associated mainly with the photogenerated holes and formation of $^{\bullet}OH$ radicals rather than with photoexcited electrons and $O_2^{\bullet-}$.

As it was presented in SEM and TEM micrographs (*Figures 54 and 55*) the TiO_2 layers in two composite samples differ significantly in morphology. The TiO_2 layer in ***1c***

sample is rugged and porous, while that in ***3c*** is smooth and compact. Therefore, the interface between ZnO and TiO_2 in ***1c*** is more easily accessible for reacting species (H_2O, O_2 and MB) in comparison to situation in ***3c***. Thus, it explains higher photocatalytic activity of ***1c*** sample. At this point; it is worth to recall that MB adsorption (during conditioning) was 3.5 times higher on ***1c*** than on ***3c***, which may also contribute to higher efficiency during photocatalytic test.

Table 10 Results of photocatalytic decolorization of MB (performed under irradiation 400 nm – LED, and xenon arc lamp with 400 nm cut-off filter)

Sample	Irradiation: LED k_{400} (10^{-2} min^{-1})	Irradiation: xenon lamp with filter < 400 nm k_{xenon} ($\cdot 10^{-2}$ min^{-1})	Irradiation: LED addition of methanol 3% v/v k_{400} ($\cdot 10^{-2}$ min^{-1})
ZnO	0.2	0.3	0.09
1c (ZnO/TiO_2)	1.2	0.8	0.30
3c (ZnO/TiO_2)	0.7	0.6	0.36

4.2.3. Photoelectrochemical tests

Photoelectrochemical properties of the composites were firstly studied in aqueous solutions, namely, in the reaction of water photo-oxidation expressed by the following equation:

$$2H_2O - 4e \rightarrow O_2 + 4H^+ \quad (69)$$

The mechanism of the process is still a subject of intensive studies and discussions in the literature [361]. Nonetheless, the anodic behavior of the semiconductor electrode in aqueous solution under illumination is often used as a test of photoelectrocatalytic properties of semiconductor materials. Therefore, ***1c*** and ***3c*** samples were studied at a constant positive potential of 0.8 V *vs*. Ag/AgCl in the solution of pH 6.8 containing 5 mM Na_2SO_4 in dark and under illumination with light of the wavelength 400 nm. As visible in *Figure 63*, in both cases the steady state photocurrent was achieved just after switching the light on but its value was almost six-times higher for the sample ***1c*** than that for ***3c*** electrode (0.75 mA cm^{-2} and 0.12 mA cm^{-2}, respectively). This difference may be ascribed to more extended surface area of TiO_2 deposited in ***1c*** procedure and probably higher amount of surface bound hydroxyl groups (Ti–OH) or/and surface bound water molecules ($Ti–OH_2$) which may be oxidized by the photogenerated holes.

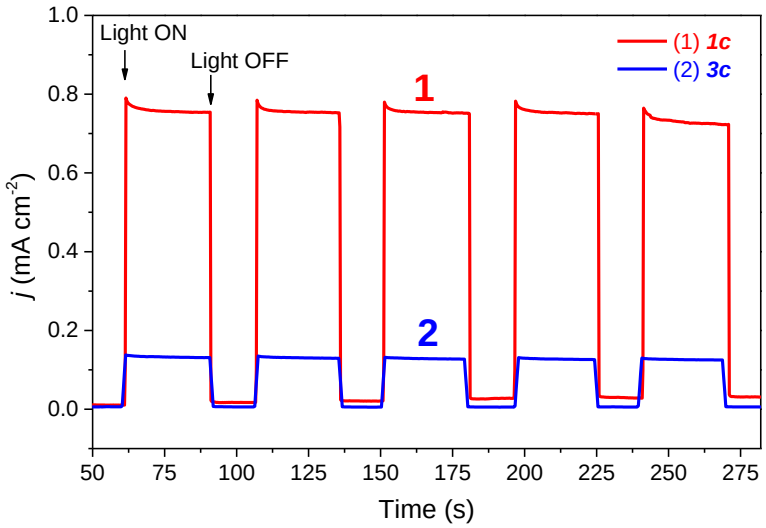

Figure 63 Chronoamperometric curves obtained on ***1c*** *ZnO/TiO_2 (curve 1, red), and* ***3c*** *ZnO/TiO_2 (curve 2, blue) composites in dark and under illumination, at constant potential of 0.8 V vs. Ag/AgCl in aqueous solution of 5 mM Na_2SO_4.*

In order to gain more insight into electrochemical behavior of the materials studied, ZnO nanorods and ZnO/TiO_2 systems deposited on ITO were tested by means of cyclic voltammetry in the solution of 0.1 M $LiClO_4$ containing ferrocene (Fc) as a redox probe. The measurements were performed in dark and under illumination. The cyclic voltammograms obtained in all systems studied are typical of n-type semiconductor in the redox electrolyte [362,363]. Namely, the dark oxidation currents at E > 0 V *vs.* Ag/AgCl are very small because of the very low population of the minority carriers (holes) at the semiconductor/solution interface. On the other hand, the reduction process with participation of the majority charge carriers (electrons) can proceed and cathodic current is dependent on the potential and concentration of electroactive species at the electrode. As visible in *Figure 64*, the cathodic and anodic dark currents obtained for $ITO/ZnO/TiO_2$ electrodes are noticeably higher than those recorded for bare ITO/ZnO. This may be ascribed to increase of the electrode/solution interfacial area after deposition of TiO_2. A slightly higher current density obtained for ***1c*** than that for ***3c*** ZnO/TiO_2 system (*c.f.* lines 1 in *Figures 64B* and *64C*) may be explained by more developed surface of TiO_2 as is illustrated in the TEM images in *Figure 55*. Upon illumination of the electrode the created electron-hole pairs are separated under the electric field. The holes are transferred towards the electrode surface and are involved in oxidation of ferrocene to ferrocenium cation leading to the increase of the height of oxidation wave. This process is energetically possible because the redox potential of Fc/Fc^+ redox couple

(0.36 V *vs.* Ag/AgCl), determined from mean potential between oxidation and reduction peaks in the cyclic voltammogram obtained on Pt electrode (see curve 4 in *Figure 65A*) is located within the band gap of TiO_2 and ZnO, relatively close to the lower edge of conduction band of TiO_2. The latter value for TiO_2 in acetonitrile solution is located at about 0 V *vs.* Ag/AgCl (in electrochemical scale), as estimated from the onset of oxidation current [364,365].

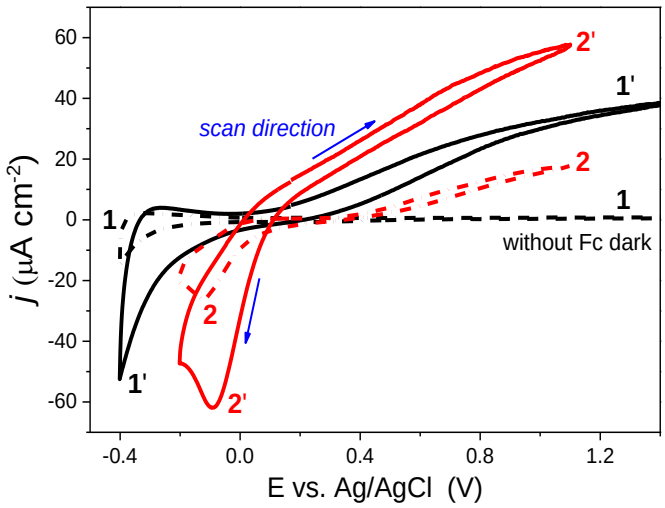

Figure 64 Cyclic voltammograms obtained on ***3c*** *ITO/ZnO/TiO_2 in dark (dashed lines), and under illumination (solid lines) in acetonitrile solution of 0.1 M $LiClO_4$ (curves 1 and 1') and the same solution containing 10^{-3} M Fc (curves 2 and 2').*

Comparison of the plots obtained for the three systems studied under illumination with xenon lamp shows that the oxidation current density is practically the same for ***1c*** and ***3c*** ITO/ZnO/TiO_2 electrodes (curves in *Figures 65B* and *65C*) and two times higher than that for bare ITO/ZnO (curve 3 in *Figure 65A*). This difference may be ascribed to larger surface area of TiO_2 with respect to ZnO or/and formation of the interface states at the ZnO/TiO_2 boundary, which may be involved in the charge transfer from the metal oxide to ferrocene. On the other hand, the presence of these surface states may also result in sub-band gap transition leading to photoelectrochemical activity of the system in visible range, which was confirmed after application of UV cut-off filter the wavelengths below 400 nm (curve 2 in *Figure 65*). The photoelectrochemical results obtained in anodic potential range are in conformity with photocatalytic data. It is also worth noting that in all cases the current density of the oxidation wave was practically independent on the scan rate (see inset in *Figure 65D*) probably due to relatively slow transport of the minority charge carriers (holes) to the semiconductor surface and/or slow rate of the

charge transfer process at the electrode/solution interface. Thus, the sample morphology and accessibility of the reagent to the interface have a small influence on the value of the anodic current.

In contrast, in the range of negative potentials the reduction peak is well developed and its location was dependent on the system studied, i.e. –0.1 V in the case of ITO/ZnO and ITO/ZnO/TiO_2 (***1c***) and more negative than –0.2 V for ITO/ZnO/TiO_2 (***3c***) electrode. This is probably a consequence of different resistance of the systems. One may expect that the layer of relatively compact layer of TiO_2 in ***3c*** sample may be a source of additional ohmic drop at the electrode/solution interface in comparison to that of ***1c*** electrode.

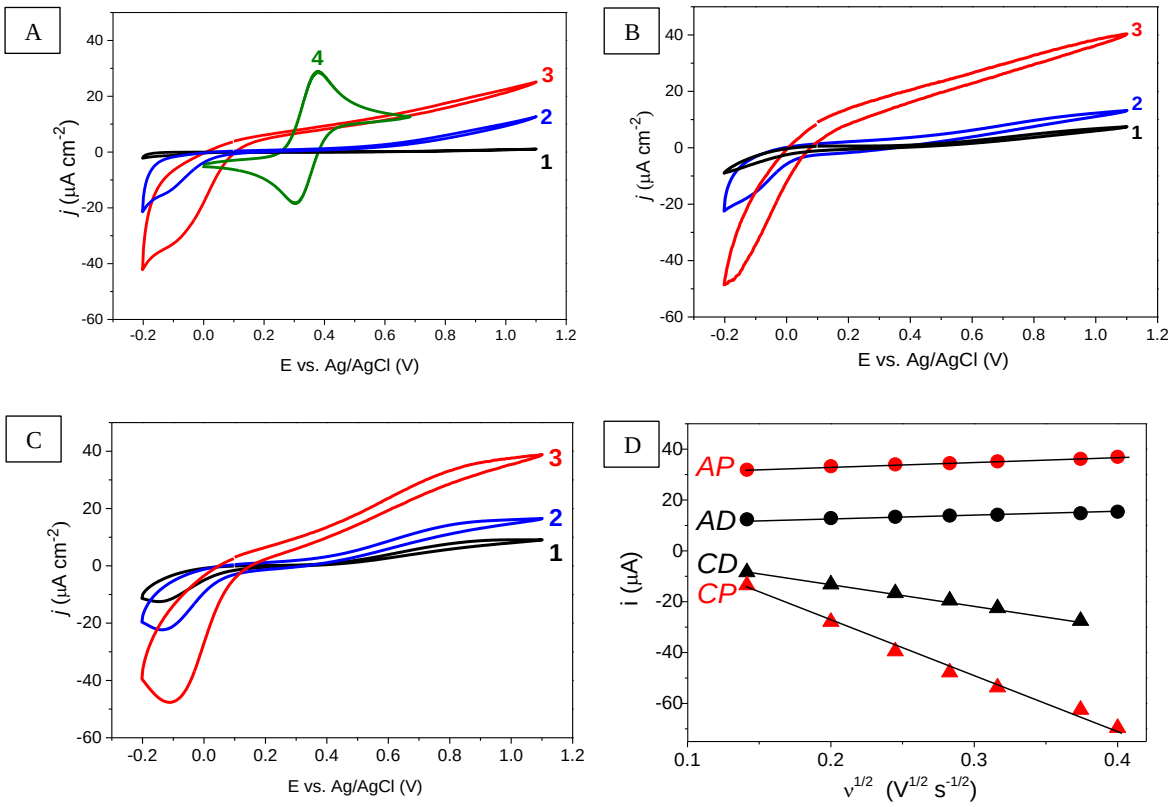

Figure 65 Comparison of the cyclic voltammograms obtained for ITO/ZnO (A), ***3c*** *ITO/ZnO/TiO_2 (B) and* ***1c*** *ITO/ZnO/TiO_2 (C) in dark (curves 1) and under illumination with xenon lamp with cut-off ≤ 400 nm filter (curves 2) and without filter (curves 3) in the solution of 1 mM Fc in 0.1 M $LiClO_4$/AN. Curve 4 in the plot (A) corresponds to the cyclic voltammogram obtained in the same solution on small Pt disc electrode. Figure 63D presents the dependences of the cathodic peak currents (▲– dark 'CD', ▲ – photo 'CP') and anodic currents (● – dark 'AD', ● – photo 'AP') at the potential of 1 V on the root of the scan rate for* ***1c*** *sample.*

It is also important to know that the intensity of the cathodic peak current is linearly dependent on the square root of the scan rate as for diffusion controlled process. This means that the reaction of ferrocenium ion reduction by photoexcited electrons (majority charge carriers) is relatively fast.To conclude, the photoelectrochemical tests showed that deposition of TiO_2 thin layers on ITO/ZnO nanostructured electrodes results in the increase of the photocurrent density for oxidation/reduction of ferrocene in acetonitrile, with respect to that on the bare ITO/ZnO, both in anodic and cathodic potential ranges. However, the value of the photocurrent is nearly the same for ***1c*** and ***3c*** samples. In contrast, a strong influence of the photocurrent density on the film morphology was observed for H_2O or OH^- oxidation in aqueous solution of Na_2SO_4. This is probably a result of improved adsorption of H_2O and OH^- groups on more developed surface area of ***1c*** sample than on the surface of more compact ***3c*** TiO_2 layer.

4.2.4. Photocatalytic tests with landfill leachate

The catalysts were tested so far in photocatalytic decolorization of a model dye pollutant. However, remediation of real waste water is a big challenge. Many difficulties and limitations for a photocatalyst to work efficiently in the solutions containing a mixture of organic and inorganic pollutants appear. Besides unknown composition of dissolved matter, there are more harsh conditions that may completely deactivate the catalyst, such as, irreversible adsorption of species which cannot be degraded (blocking effect), high or low value of pH, which can cause dissolution or passivation of a catalyst, or even high concentration of inorganic salts that can strongly inhibit the activity [366,367]. Two complementary methods that allow to track remediation of waste water from organic pollutants are spectroscopic observations of absorption at 254 nm, which in general is ascribed to π-π* transitions in aromatic (benzene-based) compounds, and the second is total organic carbon analysis.

The waste water leachate samples, as-received, were very concentrated and therefore they had to be diluted 25-times with DI water before the decolorization tests to avoid saturation of the UV-vis spectrometer's detector. The pH of diluted solution was 9. Prior to the tests, the catalysts were conditioned for 24 hours in diluted waste water solution to reach adsorption-desorption equilibrium. The typical result of a decolorization of landfill leachate solution under 400 nm irradiation is presented on *Figure 66A*.

The investigations were performed for ***1c***, ***3c*** and ZnO/TiO_2 composite with N-doped TiO_2 layer (***3c(N))***, prepared accordingly to the procedure described in the *Chapter 4.4*

(paragraph 4.1). The UV-vis spectrum of leachate solution is complex with broad shoulder around 270 nm, as presented on *Figure 66A*, showing its photocatalytic decolorization with usage of ***3c(N)***. Upon irradiation of the samples, a continuous decrease of absorption was observed and after 600 min the absorption above 350 nm practically decreased to zero while the shoulder remains at almost the same wavelength. The absorption in the UV can be attributed to $\pi \rightarrow \pi^*$ transitions in organic compounds with double C=C bonds, but it is impossible to identify the exact components of the leachate solution. Nonetheless, the photodecolorization tests were done with usage of other elaborated samples as well as for commercial catalyst P25 deposited on ITO. The latter one of the same mass (estimated by sensitive microbalance) as that of ZnO/TiO_2 catalyst was deposited by dispersing P25 powder in ethanol and dropwise placed on ITO surface, followed by calcination at 300 ^oC for 15 min. The relative changes of absorbance at the wavelength of 254 nm in a function of irradiation time with monochromatic light (400 nm) are presented in *Figure 66B*. It is important to know that the decolorization rate of the leachate solution with the use of all ZnO/TiO_2 samples was markedly higher than that with commercial P25 catalysts and the catalysts' activity increased in the order: ZnO < P25 < ***3c*** < ***1c*** < ***3c(N)***. The results of TOC analysis performed for all samples (*Figure 66C*) confirmed the same trend of activities. However as it is generally observed, the TOC removal was smaller than absorption decrease at 254 nm.

In order to determine the long term stability of the most efficient ***3c(N)*** catalyst, this sample was tested in three subsequent photocatalytic runs. However, for these tests waste water solution was not diluted with DI water before photocatalytic tests to provide 'real life' conditions. None diluted leachate solution saturates the UV-vis spectrometer detector, therefore in order to measure the absorption spectra of the solution, we followed the standard procedure of taking out a small portion (of about 0.1 ml from 2.5 ml total sample) of solution from the entire volume and was diluted 25-times. The results are presented in *Figure 66D*, and show almost identical decrease of absorption after the same time irradiation time intervals (2, 6, and 11 h). This proves that the ***3c(N)*** sample is stable in harsh, non-diluted, as-received the landfill leachate and can still remediate the solution with the same activity in consecutive photocatalytic runs.

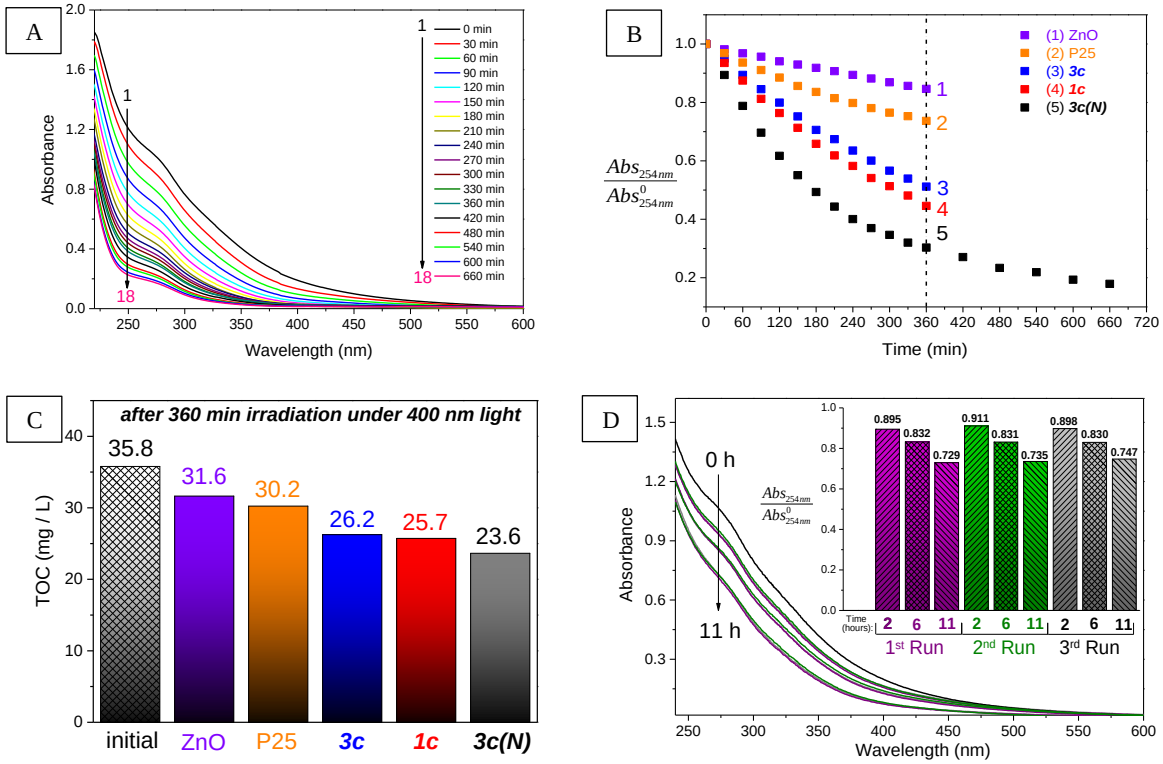

*Figure 66 UV-vis absorption of waste water leachate under irradiation of 400 nm monochromatic light and in presence of ZnO/TiO$_2$(N) composite – **3c(N)** photocatalyst (A), comparison of different photocatalyst activity in remediation of waste water solution (B), TOC removal from initial sample after 360 min of 400 nm irradiation in presence of the photocatalysts (C), evolution of absorption spectra of non-diluted waste water solution under illumination and presence of **3c(N)**. Inset D: absorption decrease at 254 nm with respect to initial value after 1st (pruple), 2nd (green), and 3rd (grey) photocatalytic run on **3c(N)** under 400 nm irradiation after 2, 6, and 11 hours.*

4.2.5. ZnO/TiO$_2$ composites with TiO$_2$ layers deposited by CVD and ALD techniques

The results presented and discussed in the previous chapters have shown that application of cheap and simple sol-gel method of TiO$_2$ synthesis allowed fabrication of core/shell ZnO/TiO$_2$ composites of satisfactory photocatalytic properties. However, TiO$_2$ may be deposited on ZnO nanorods also by means of other physico-chemical methods, such as Chemical Vapor Deposition (CVD) [368] and Atomic Layer Deposition (ALD) [369]. Therefore, for comparison, two other ZnO/TiO$_2$ composites with TiO$_2$ shells deposited by ALD and CVD methods were prepared and characterized by means of physicochemical techniques.

The deposition parameters in CVD and ALD were adjusted to achieve the thickness of TiO_2 layer similar to that obtained by of sol-gel synthesis. In such case, the comparison between all samples can be more reliable, even if some differences are inevitable. In both techniques TiO_2 layers were formed from the same starting precursor, titanium(IV) isopropoxide; The SEM images of the ZnO/TiO_2 '***CVD***' and '***ALD***' samples are compared in *Figure 67*.

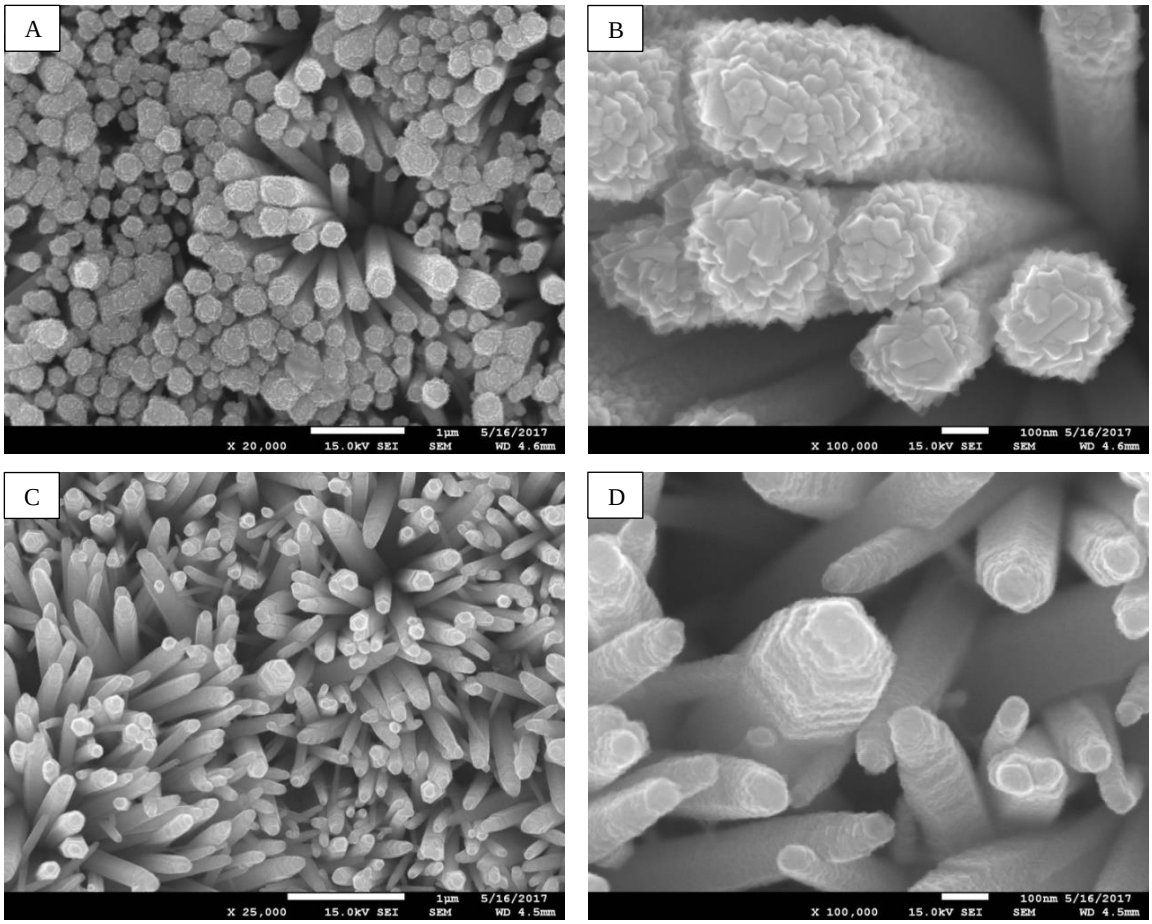

Figure 67 SEM images of ZnO/TiO_2 composites with prepared TiO_2 shells by CVD (A, B) and ALD (C, D) techniques.

As visible, in both cases the TiO_2 layer deposited on ZnO is relatively thin because the nanorods remained well separated, as it was in the case of the sol-gel prepared ZnO/TiO_2 composites. However, at close inspection one can notice that the ends of the nanorods covered with TiO_2 with the use of '***CVD***' are thicker and the layer is more rough (resembling a stock of 'fish scales') the than that deposited with '***ALD***' (*Figures 67B and 67D, respectively*). It is also interesting to note that the roughness of deposited TiO_2 surface layer seems to increase from bottom to top, *Figure 67B.* Such observation

confirms initial predictions of the more top-targeted deposition technique. In case of ALD-prepared TiO_2 shell the composite nanorods ZnO/TiO_2 seems to possess strong surface uniform roughness consisted of tiny deposited nanoparticle (*Figure 67D*). More details about morphology were revealed on HAADF-STEM and HR-TEM images of ZnO/TiO_2 composited with TiO_2 layers prepared by CVD (*Figure 68*) and ALD (*Figure 69*).

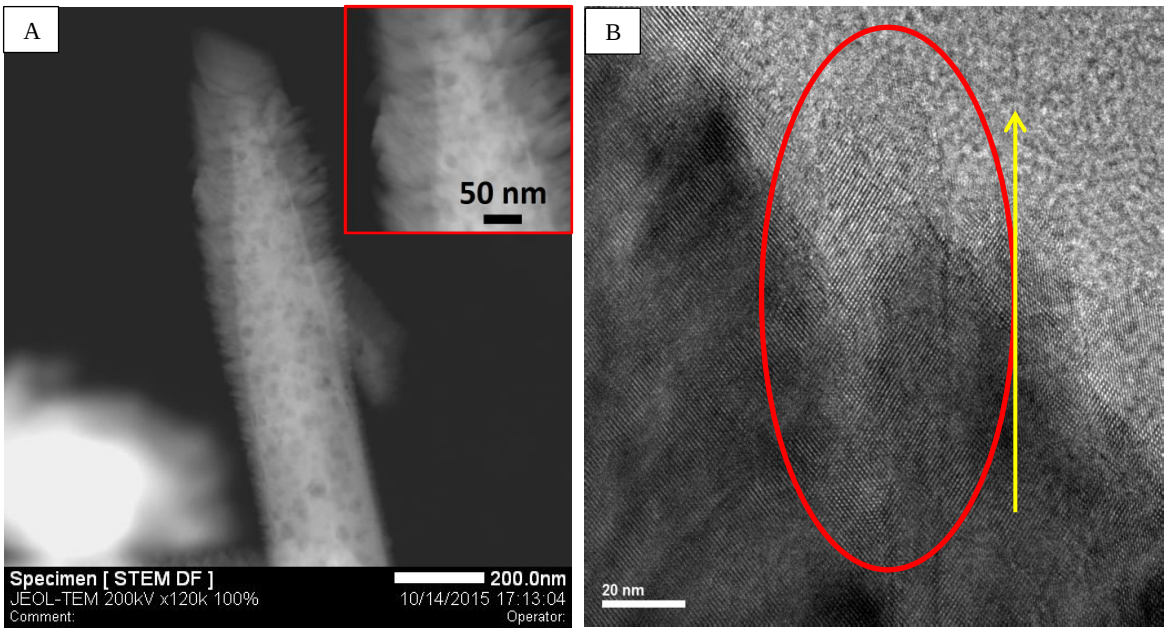

Figure 68 HAADF-STEM (A) and HR-TEM (B) images of ZnO/TiO_2 nanorods with TiO_2 layers prepared by CVD. Specific alignment of the TiO_2 deposited on ZnO is indicated with yellow arrow in red circle.

HAADF-STEM images of CVD-deposited TiO_2 show that the shell thickness is not uniform along ZnO nanorods, as it was initially suggested by SEM, and the whole composite nanorods resembles a shape of 'matches'. Moreover, TiO_2 shell consists of an array of TiO_2 needles on already existed ZnO nanorods array (array-on-array). The length of a single TiO_2 nanorod obviously varies along ZnO surface; however it does not exceed 150 nm on top of ZnO, whereas the diameter seems to be about 30 nm. Similar specific alignment of the TiO_2 nanorods deposited on also hydrothermally grown ZnO was reported by Gao *et al.* [370], however by different technique – magnetron sputtering. They also admitted that ZnO/TiO_2 interface is of a great importance for the special phase structure formation, and as such could relevantly impact photocatalytic properties of the material. As shown on the HR-TEM image (*Figure 68B*) the TiO_2 nanorods are well-crystallized and the interplanar distance was measured to be 3.5 Å, which corresponds to (101) plane of TiO_2 anatase. The electron microscopy pictures of the ZnO/TiO_2

composite with TiO_2 layer prepared by CVD showed that the system resembles the morphology of ***1c*** sample. HAADF-STEM and TEM images of the ZnO/TiO_2 composite with TiO_2 layer prepared by ALD technique are presented on *Figure 69A* and *69B*, respectively.

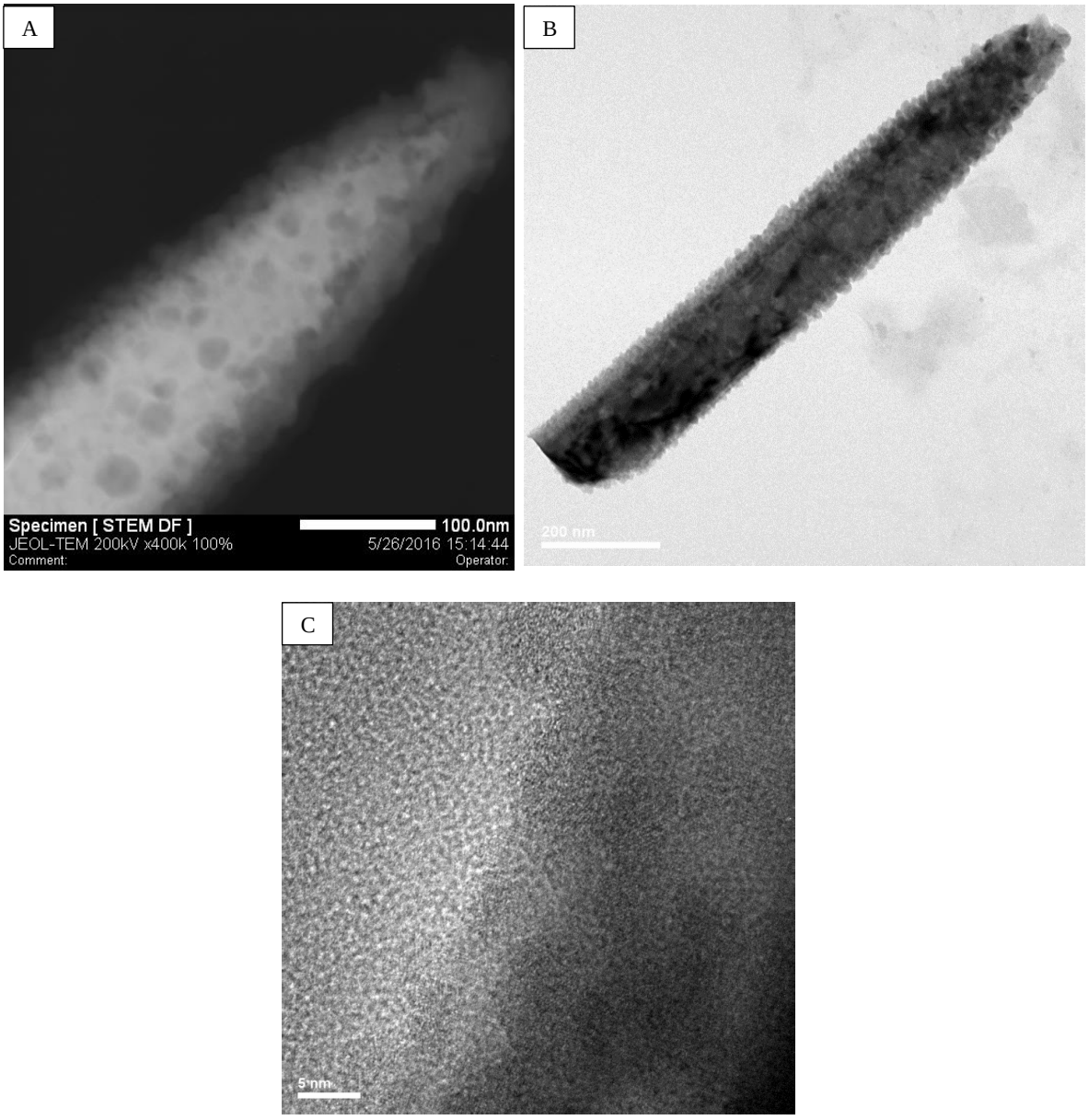

Figures 69 HAADF-STEM (A), TEM (B), HR-TEM (C) images of ZnO/TiO_2 nanorods with TiO_2 layers prepared by ALD technique.

As it is evidenced, the images the TiO_2 shell formed is uniform along the whole ZnO nanorod surface and appear to be composed of extremely small particles (smaller than 5 nm), whereas the thickness of the shell was about 30 nm. Such small particles that are forming continuous layer are a challenge for HR-TEM determination of interplanar

distances due to the overlapped particles. However, it was possible to notice in the images presented in *Figures 69C* some interplanar distances of 3.5 Å of well-crystallized TiO_2 anatase. The ALD preparation resulted, therefore, in a composite which appear like ***3c*** 'sol-gel' sample in two aspects: i) the continuity of TiO_2 shell and ii) the overall thickness of the layer. To conclude, one can observe that sol-gel samples: ***1c*** and ***3c*** have their similar counterparts prepared by CVD and ALD, respectively.

Optical properties of the '***CVD***' and '***ALD***' samples were measured within the range of 350 nm – 650 nm wavelengths and compared with bare ZnO and 'sol-gel' ZnO/TiO_2 composites (*Figure 70A*). The results showed that both '***ALD***' and '***CVD***' samples have almost identical absorption profile as the ***1c*** sample: the absorption 'Urbach tail' and onset edge. These results suggest similar contact between ZnO surface and TiO_2 particles for ***1c***, '***CVD***', and '***ALD***', whereas ***3c*** seems to possess higher amount ZnO and TiO_2 bounded as the absorption especially with 'Urbach tail' range is higher.

XRD patterns for '***CVD***' and '***ALD***' samples were also recorded in order to confirm the presence of anatase TiO_2 in the samples). As visible in *Figure 70B*, all peaks corresponding to ITO and ZnO are also present in both '***ALD***' and '***CVD***' spectra, as it was observed in the 'sol-gel' samples. The signals of TiO_2 anatase can be also detected, but only at $2\theta = 25.3^{o}$, (101) plane, due to the low amount of deposited material.

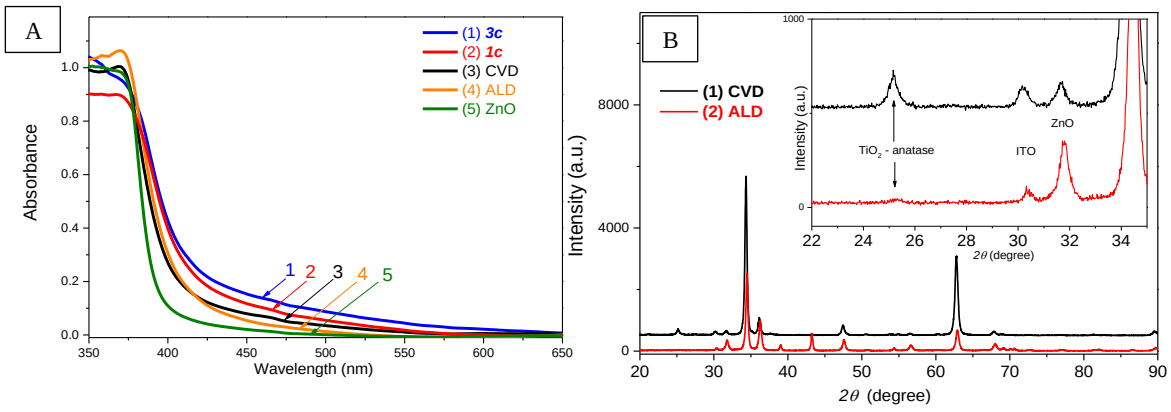

Figure 70 UV-vis spectra of ZnO/TiO_2 composites with TiO_2 shells prepared by CVD, and ALD with a comparison of bare ZnO, and the 'sol-gel 'ZnO/TiO_2 composites (A), XRD patterns of the 'CVD' and 'ALD' composite samples.

The photocatalytic properties of the '***CVD***' and '***ALD***' samples were tested in the same conditions as the samples ***1c*** and ***3c***, namely in 10 µM solution of MB under 400 nm monochromatic light irradiation. The results of the apparent first-order rate constants

(k_{400}) are listed in the Table 11. As presented, the most active sample was ***1c*** 'sol-gel' (k_{400} = 1.2 ·10^{-2} min^{-1}). However, slightly lower, but still comparative performance was recorded for ZnO/TiO_2 composite with TiO_2 layer prepared by ALD (k_{400} = 1.1 ·10^{-2} min^{-1}). On the other hand, both samples evidently decolorize MB better than the ***3c*** 'sol-gel' (k_{400} = 0.7 ·10^{-2} min^{-1}), and 'CVD' samples (k_{400} = 0.8 ·10^{-2} min^{-1}). The latter two samples showed also similar photocatalytic activities in MB decolorization.

*Table 11 Photocatalytic properties of ZnO/TiO_2 core/shell composites, with TiO_2 shell prepared by the sol-gel method (**1c** and **3c**), 'CVD', and 'ALD' techniques.*

ZnO/TiO_2 Sample	Decolorization of MB under 400 nm k_{400} (·10^{-2} min^{-1})	EDX Ti / Zn ratio
'***CVD***'	0.8	0.27
'***ALD***'	1.1	0.06
3c	0.7	0.27
1c	1.2	0.10

According to HAADF-STEM observations, ***1c*** and '***CVD***' samples should have better accessibility to the ZnO/TiO_2 interface than the ***3c*** and '***ALD***' samples. A difference between ***1c*** and '***CVD***' is seen in continuity of the TiO_2 layer along ZnO nanorods. While the former one is covered with a uniform, rugged TiO_2 layer, the latter has only deposit on the tips of ZnO. Therefore, the ***1c*** yields higher photoactivity than the '***CVD***' sample, because of better accessibility of ZnO/TiO_2 interface. On the other hand, the '***ALD***' sample showed also high photoactivity, despite the fact of continuity of the TiO_2 layer. This may suggest high porosity of TiO_2 layer in '***ALD***' sample.

4.2.6. Conclusions

In summary, the hybrid composite ZnO/TiO_2 systems were prepared by deposition of TiO_2 via simple sol-gel method on ZnO nanorods hydrothermally grown on ITO surface. Synthesis parameters such as deposition time or repetition of single sol-gel cycle, allowed to prepare either rugged TiO_2 layers or compact and continuous TiO_2 coatings. The rugged TiO_2 layers were obtained after 6 hours of one step sol-gel synthesis followed by calcination of the sample (***1c***), whereas the uniform coating of thickness of 25 nm – 40 nm was formed after three successive syntheses (cycles) with calcination of the sample after each cycle (***3c***). It was found that complete amorphous-to-anatase phase transition of TiO_2 nanoparticles deposited on ZnO occurs slightly below 450 °C, and organic residues were burnt-out entirely as was indicated by TGA-DSC results. The presence of TiO_2 anatase modification in the samples calcined at 450 °C was confirmed by XRD results.

The amount of TiO_2 deposited on ZnO nanorods may be increased either by the increase of deposition time in single sol-gel cycle or by application of three successive 30 min deposition cycles. Both ZnO/TiO_2 composite systems, showed substantial decrease of the optical band gap energy regardless of the assumed type of transition (direct or indirect) in comparison to the values for bare ZnO and TiO_2 materials. The stronger effect was found for ***3c*** samples in which the contact between ZnO and TiO_2 components was continuous.

The importance of such interface in relation to the optical properties was confirmed in photocatalytic and photoelectrochemical tests. The highest decomposition rate of MB in aqueous solution was achieved by ***1c*** ZnO/TiO_2 system showing 6-fold increase of photocatalytic activity in comparison with ITO/ZnO under irradiation with 400 nm light. Higher photocatalytic activity was observed for 1c sample than for ***3c*** both in MB degradation and in photoassisted water oxidation. This effect was attributed to a more open structure of TiO_2 shell in ***1c*** sample which allows better access of the reacting species from solution to the ZnO/TiO_2 interface.

The photoelectrochemical studies with the presence of ferrocene showed that higher current densities were observed for ITO/ZnO/TiO_2 composite electrodes than for ITO/ZnO sample in a broad potential range. These results confirm and emphasize the

significance of the TiO_2 layer morphology on photoelectrochemical properties of ZnO/TiO_2 core/shell systems.

The photocatalytic properties of ZnO/TiO_2 composites prepared by sol-gel method were compared with those of the materials produced by ALD and CVD. It was evidenced the developed sol-gel procedure of TiO_2 deposition on ZnO nanorods resulted in preparation of the composite catalyst of higher performance than the catalyst with TiO_2 layer prepared by CVD technique and comparable performance with ALD technique. Taking into account possibilities for preparation of the catalysts is seems more facile to use the sol-gel method, which can be easily implemented, whereas the use of ALD and CVD requires the specific apparatus, and often training to operate.

4.3. Influence of interface microstructure on the properties of ZnO/TiO_2 composites

4.3.1. Evidence for a key role of ZnO/TiO_2 interface in photocatalysis

In order to prove the importance of ZnO/TiO_2 interface in the photocatalytic decolorization of MB, comparative studies were performed on the ***3c*** sample and on the same sample after dissolution of ZnO core in $HCl_{(aq.)}$ at pH 3 for 20 h (hereafter designated as ***'3c-HCl'***), *Figure 71*.

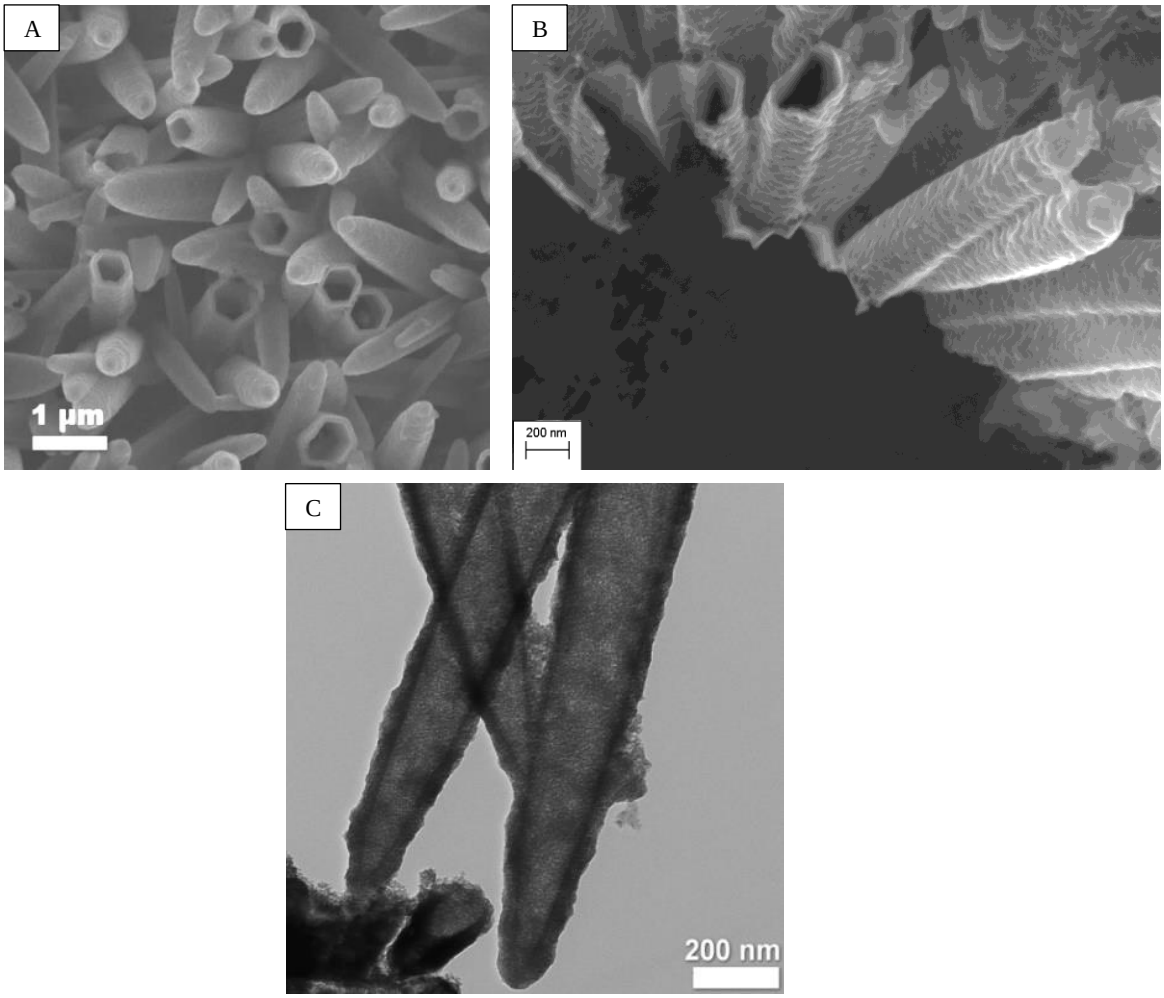

Figure 71 SEM (A, B) and TEM (C) images of hollow nanostructures obtained after removal of ZnO-core in $HCl_{(aq.)}$ from initial (core)ZnO/TiO_2(shell) composites.

The ***3c*** composite was chosen over other obtained ZnO/TiO_2 samples, as this material exhibits continuous and well-distinguished boundary between ZnO and TiO_2. Also, EDX-SEM analysis across 100 μm^2 area of samples after 20 h, 40 h, and 50 h of treatment in $HCl_{(aq.)}$ showed that the Ti:Zn ratio was almost the same in all cases (3.1, 3.3, and 3.3, respectively), confirming that 20 h of treatment was sufficiently long to

remove ZnO. The results presented in *Figure 72A* indicate that decolorization rate of MB significantly decreased when the ***3c*** sample was treated with $HCl_{(aq.)}$ (20 h) and the apparent rate constant of the process (k_{400}) decreased by a factor 6.4 with respect to that obtained for the non-treated ***3c*** sample. These results show that the presence of ZnO/TiO_2 interface plays indeed a crucial role in the photocatalytic process. In order to understand the origin of this effect the optical absorbance spectra of the samples were recorded (*Figure 72B*).

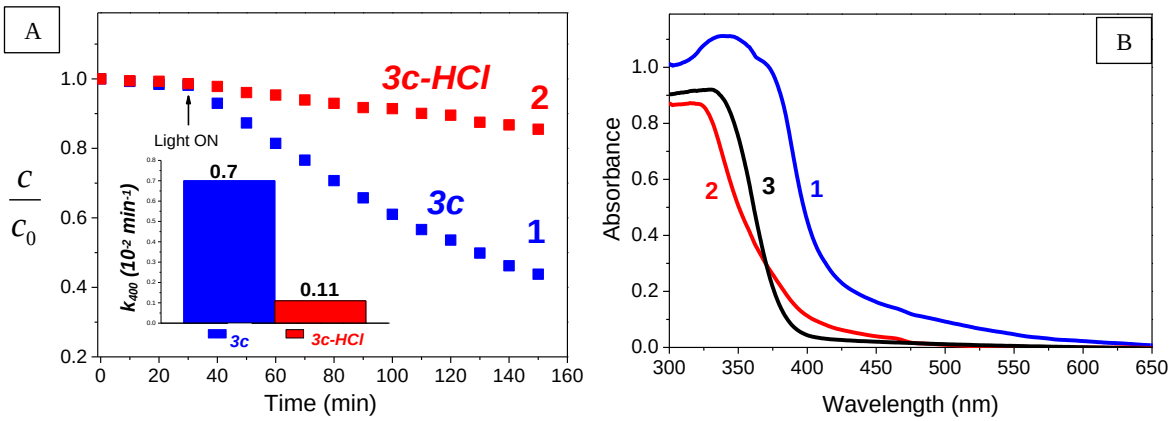

*Figure 72 Photodecolorization of MB with use of the ZnO/TiO_2 composites before (blue scatter 1, **3c**) and after (red scatter 2, **3c-HCl**) dissolution of ZnO-cores in $HCl_{(aq.)}$ (A). Inset A: values of apparent first-order rate constants (k_{400}) calculated for **3c** (blue) and **3c-HCl** (red). Absorption spectra of **3c** (blue curve 1), **3c-HCl** (red curve 2), whereas the black curve 3 corresponds to the spectrum obtained for TiO_2 (B).*

The UV-vis absorption spectrum of the ***3c*** sample (curve 1 in *Figure 72B*) presents two characteristic features: formation of a pronounced 'Urbach tail' in the wavelengths range from 600 nm to 420 nm, absent in the spectrum of TiO_2 powder, and the shift of the absorption threshold towards visible range. Consequently, these two effects may be ascribed to the formation of interfacial states at the ZnO/TiO_2 boundary, with the energy levels localized in the band gap [371]. Hence, the sub-band gap optical transitions become possible as it was discussed more in detail in *Chapter 4.2, paragraph 4.2.1*. However, the treatment with $HCl_{(aq.)}$ leads to the shift of the sample absorption spectrum back towards UV range and to a significant diminution of the absorbance tail. This behavior may be explained by disappearance of the interfacial states due to dissolution of ZnO in $HCl_{(aq.)}$. Since the results presented above supported the key role of ZnO/TiO_2 interface in photocatalytic activity of the composite, an attempt to modify the interfacial

region was undertaken through an additional calcination. For the aim of these studies, two new initial ***3c*** samples were submitted to additional calcination for 3 h at 450 ^{o}C (***3c-Cal)***, whereas only one of them was subsequently treated, as before, with HCl solution (***3c-Cal-HCl***).

The results of MB photocatalytic decolorization (*Figure 73A*) show that the additional calcination leads to the increase of activity of the ZnO/TiO_2 composite (the apparent first-order rate constant increases from $k'_{400} = 0.7 \cdot 10^{-2}$ min^{-1} for ***3c***, to $k''_{400} = 1.0 \cdot 10^{-2}$ min^{-1} for ***3c-Cal***). Considering samples etched in $HCl_{(aq.)}$, it is interesting to note that the photocatalytic activity of the additionally calcined composite (***3c-Cal-HCl***) is remarkably higher (almost three–times) than in the case when such thermal treatment was not applied (***3c-HCl***, *Figure 73B*).

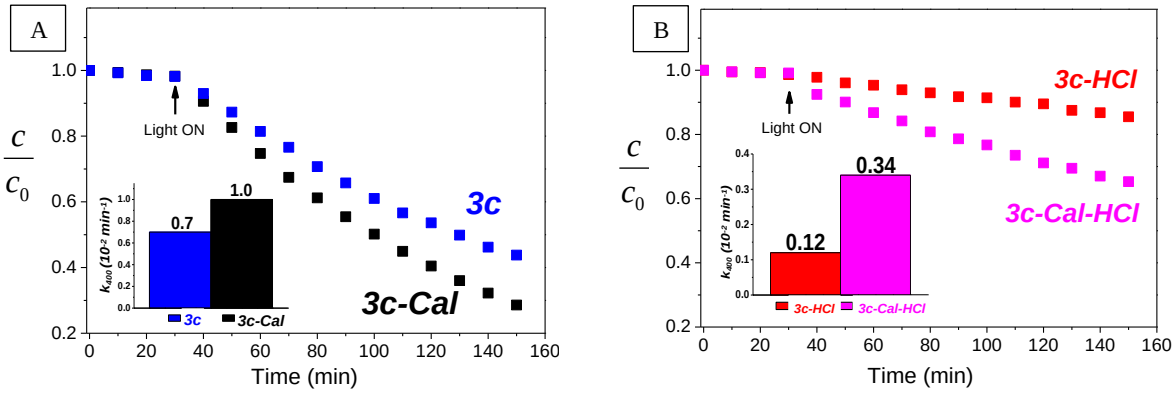

Figure 73 Photodecolorization of MB on the catalysts: ***3c*** *and* ***3c-Cal*** *(A),* ***3c-HCl*** *and* ***3c-Cal-HCl*** *(B).*

The results presented above suggest that the additional calcination significantly modifies the interfacial ZnO/TiO_2 region, and thus influences the photocatalytic activity of the composites. Improvement of the photoactivity by a simple additional calcination is an interesting result and we attempted to understand the origin of this enhancement.

4.3.2. Explanation of improved properties of additionally calcined ZnO/TiO_2

First, we supposed that the enhancement stems from the decrease of the optical band gap and therefore, better absorption in visible range after additional calcination. As visible, in *Figure 74A*, the spectrum of ***3c-Cal*** slightly differs from that of ***3c*** in the visible range, between 420 nm and 600 nm. The calcination leads to diminishing of the 'Urbach tail' and decrease of the absorbance in this range. The optical band gaps determined from the

Tauc plot (inset, *Figure 74A*) indicate that the additional calcination leads to a small increase, from 2.8 eV for ***3c*** to 2.9 eV for ***3c-Cal***. However, the absorbance at 400 nm (at which the photocatalytic tests were performed) of ***3c-Cal*** sample is very similar to that of ***3c***. Thus, the change of the optical properties can hardly explain the observed increase of photocatalytic activity. The similarity of the optical properties of ***3c*** and ***3c-Cal*** samples at 400 nm means that the number of generated electron-holes pairs is similar in both cases. Also, the XRD patterns are very similar for both samples (*Figure 74B*). All peak positions and intensities of ZnO, ITO, and TiO_2-anatase in the XRD patterns, which were previously found in ***3c,*** were not changed after the additional calcination (***3c-Cal***), and neither rutile phase of TiO_2 was formed during this process.

In these conditions the higher photocatalytic activity of ***3c-Cal*** might be related to a lower electron-hole recombination rate in this sample. To check this possibility the composites were characterized by measurements of open-circuit potential (V_{oc}) decay.

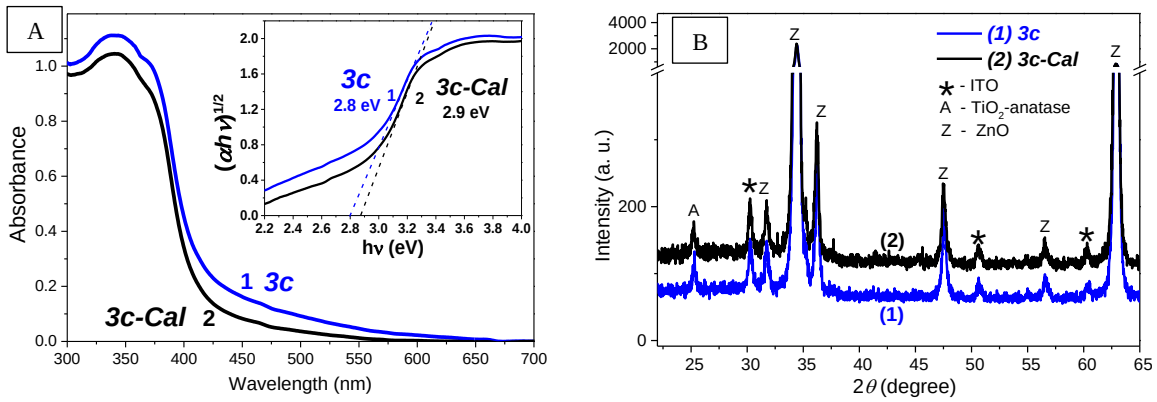

*Figure 74 (A) Optical properties of the ZnO/TiO_2 composites: initial **3c** sample (1, blue curves), and after additional calcination **3c-Cal** (2, black curves). Inset (A): the Tauc plots used for determination of optical band gaps (E_g) of the samples. (B) XRD patterns of the initial **3c** sample and after an additional calcination for 3 h at 450 ^oC (**3c-Cal**).*

The ***3c*** and ***3c-Cal*** samples were illuminated with light of the 400 nm wavelength for 90 s, then the light was switched off and relaxation of the open circuit potential was monitored within 680 s. The results presented in *Figure 75* show that both samples exhibit very similar behavior under illumination and open circuit potential reach the value of –300 mV within several seconds (measured time range: 30 s – 120 s). Regardless of the typical behavior during light-off relaxation (time range 120 s – 800 s) for TiO_2-based electrodes [372,373], a significant difference between the ***3c*** and ***3c-Cal***

was observed in the course of V_{oc} transients during light-off relaxation from the illuminated state to the dark equilibrium.

In the case of the ***3c*** sample, an initial dark value of V_{oc} was reached within 120 s, whereas the relaxation time was much longer (~ 700 s) for the ***3c-Cal***. These results confirm our hypothesis that photogenerated electron-hole pairs in the samples differ in recombination lifetimes. For ZnO and TiO_2 the results of V_{oc} decay can be used to estimate electron lifetime, [374] accordingly to the eq. (20).

Inset in *Figure 75* shows that indeed in the ***3c-Cal*** sample the electron-hole pair recombination process is slower than that in the initial ***3c*** sample. These results allow to ascribe the improved photocatalytic activity of the additionally calcined sample to the prolonged photoelectron and hole lifetime. Thus, the photogenerated charge carriers can be more efficiently utilized in the decomposition of MB.

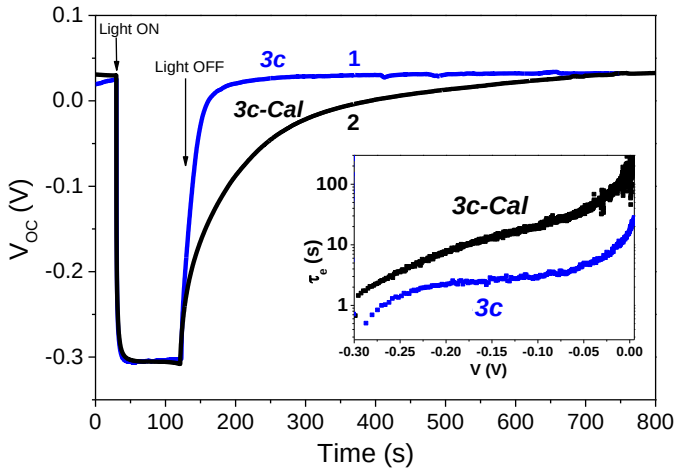

*Figure 75 Open-circuit potential (V_{oc}) decay after switching off the light for the **3c** (1) and **3c-Cal** (2) samples. The V_{oc} measurements were recorded in deareated aqueous solution of 0.2 M KCl in phosphate buffer of pH 6.8. Inset: the plots of lifetime (τ_e) of the photogenerated charge carriers, derived from equation (20) as a function of V_{oc} for **3c** and **3c-Cal**.*

In order to examine how the hindered electron-hole recombination in the ***3c-Cal*** composite influences the photoelectrochemical properties of the system, the investigation of both samples (***3c*** and ***3c-Cal***) in dark and under illumination was performed by linear sweep voltammetry and chronoamperometry. As visible in *Figure 76A*, two-times higher photocurrent was obtained for the ***3c-Cal*** electrode than that for the ***3c*** sample, in a broad range of applied potentials (from 0.4 V to 1.0 V) under illumination at 400 nm (solid

curves 1 and 2), whereas the dark currents for both samples were negligible (dash-dotted curves 3 and 4). The appearance of anodic photocurrent means that the photogenerated holes from valence band take part in oxidation of the surface Ti-O^{-} groups to Ti-O$^{\bullet}$ radicals and/or adsorbed hydroxyl groups to $^{\bullet}$OH radicals [375], as well as in photo-assisted water oxidation [376].

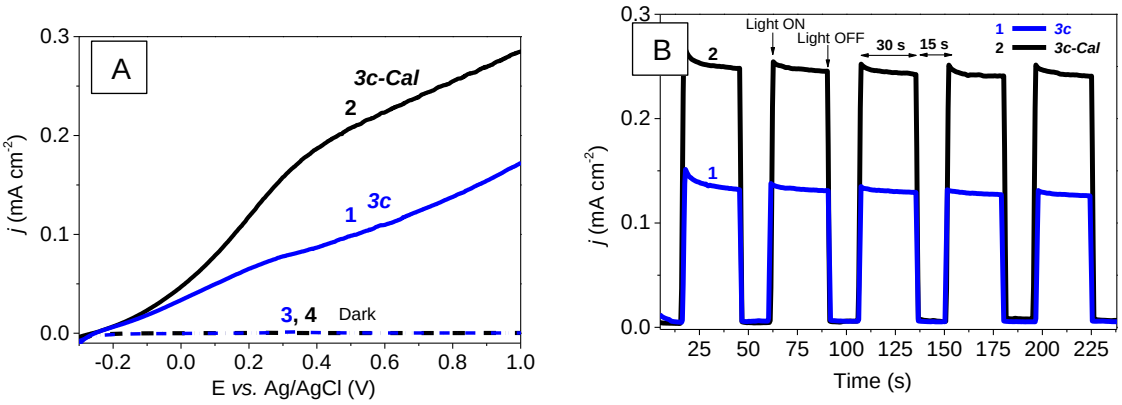

Figure 76 (A) Linear sweep voltammograms for the ***3c*** *(blue curves, 1 and 3) and* ***3c-Cal*** *(black curves, 2 and 4) electrodes in dark (dash-dotted curves) and under illumination (solid curves). LSV taken at a sweep rate of 10 mV s^{-1} in 5 mM Na_2SO_4 aqueous solution, while the photocurrent transients (B) of* ***3c*** *(blue, 1) and* ***3c-Cal*** *(black, 2) were measured at constant potential of 0.8 V vs. $E_{Ag/AgCl}$.*

At the same time the electrons from CB are transported to the ITO substrate and then to the external circuit. The significant increase of photocurrent upon the additional calcination can be explained, as in the case of V_{oc} by prolonged lifetime of the photogenerated charge carriers and increased flux of the electrons to the external circuit. The same conclusions may be derived from the photocurrent transients recorded at constant potential of 0.8 V *vs.* Ag/AgCl, presented in *Figure 76B*, where the photocurrent is almost two times higher for the additionally calcined sample. It is also important to note that after illumination of the electrode the photocurrent stabilizes within several seconds and the response is reproducible in the successive dark and illumination cycles. Such strong positive effect of calcination on the photocatalytic and photoelectrochemical properties of the ZnO/TiO_2 system can be a result of morphological changes, especially at the interface. In order to verify this point we characterized the structural changes occurring during calcination. To this end, XPS and STEM with EDX elemental mapping and line scans were used. The obtained results are described in the next section.

4.3.3. Morphology and structure analysis

HAADF-STEM was used to examine thermal modifications of the ZnO/TiO_2 composites. By means of HAADF-STEM technique it is possible to acquire images in which the signal is proportional not only to the thickness but also to atomic number of the elements (Z-contrast). In HAADF-STEM images presented in *Figure 77*, the external TiO_2 shell, the ZnO core, and so the internal structure of composites can be clearly distinguished. *Figures 77A* and *77B* present, respectively, the results for ZnO nanorods covered with as-deposited amorphous TiO_2 layers (prepared in three subsequent deposition cycles without any calcination after each one) and the same sample after calcination for only 1 h at 450 ^{o}C (the calcination was done after the third deposition cycle).

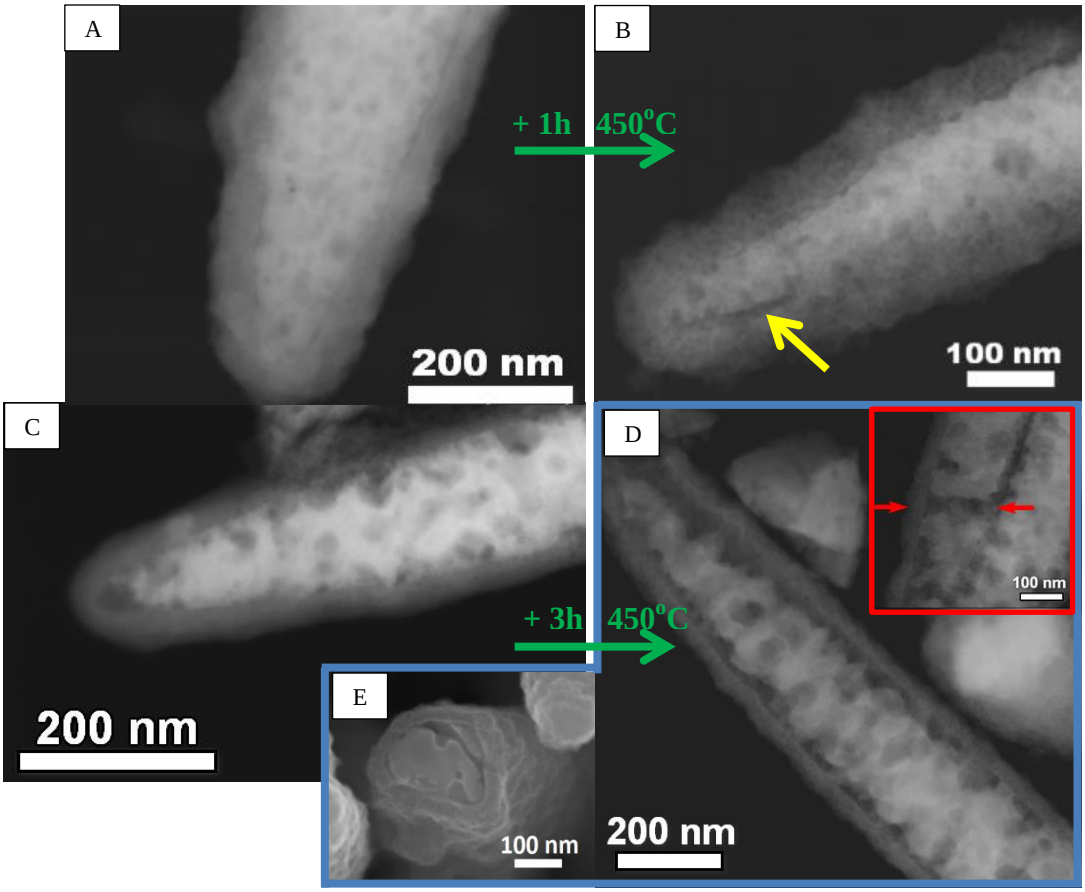

Figure 77 HAADF-STEM images of ZnO nanorods covered with amorphous TiO_2 layer after three deposition cycles without any calcination (A), and the same sample after 1 h of calcination at 450 ^{o}C (B). Yellow arrow on the Figure B depicts initial spot of void enlargement. Images of ZnO/TiO_2 composites: ***3c*** *(C) and* ***3c-Cal*** *(D, E). Inset D, in red frame, shows a hollow channel through the* ***3c-Cal*** *nanorod, whereas SEM image of the same sample, intentionally broken, reveals internal structure seen from the top view.*

As visible, the sample without any calcination possesses continuous bounding between ZnO core and as-deposited amorphous shell. After 1 h of calcination, at the boundary region, some small void spaces were formed (yellow arrow indication *Figure 77B*). The calcination of sample for 1 h at 450 ^{o}C after each deposition cycle (***3c***, *Figure 77C*) gives rise to expansion of void spaces observed at the ZnO/TiO_2 interface. It is worth noting that the additional calcination (3 h at 450 ^{o}C) results in further enlargement of voids at the boundary between ZnO and TiO_2 (***3c-Cal***, *Figure 77D*). At a close inspection, it can be seen that the thickness of the external TiO_2 layer was not changed (~ 35 nm) after the additional calcination (***3c-Cal)*** with respect to thickness observed before (***3c)***, whereas the remaining ZnO-core appeared to be significantly more 'etched'. The hollow spaces in the ZnO-core may even form void channels across the nanorod, as illustrated in the inset in *Figure 77D* and *Figure 77E*. The appearance of voids at the interface between two materials is an indication of the Kirkendall effect [377,378,379,380]. This effect consists in a more rapid diffusion of one of the components during solid-solid reaction. Such preferential diffusion of one solid (ZnO in our case) would lead to formation of voids at the interface between two solids. Therefore, this effect should result in enrichment of TiO_2 with Zn. To verify this fact EDX and XPS studies were carried out.

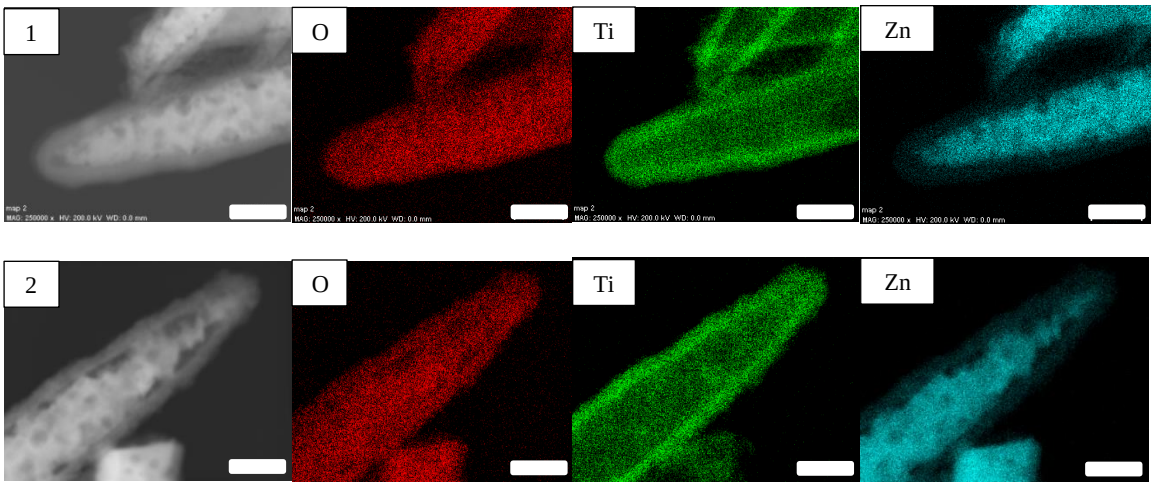

Figure 78 STEM-EDX elemental maps of ***3c*** *(1), and* ***3c-Cal*** *(2). White scale bars length =100 nm.*

EDX-STEM atomic mapping and line scan profiles of the ZnO/TiO_2 systems were acquired to confirm the presence of zinc in the TiO_2 external layer. The maps of elements distribution (*Figure 78*) indicate that zinc is indeed present in the TiO_2 layers of the ***3c*** and ***3c-Cal*** samples, before and after the additional calcination.

EDX-STEM line scan analyses were done along the red lines as indicated in the HAADF-STEM images in *Figure 79*. As visible, the amount of zinc increases in the outer part of TiO_2 layer after additional calcination of ***3c***. These results showed that the process of zinc ions diffusion into the TiO_2 layer took place already in the ***3c*** sample and becomes more pronounced after additional calcination (***3c-Cal)***.

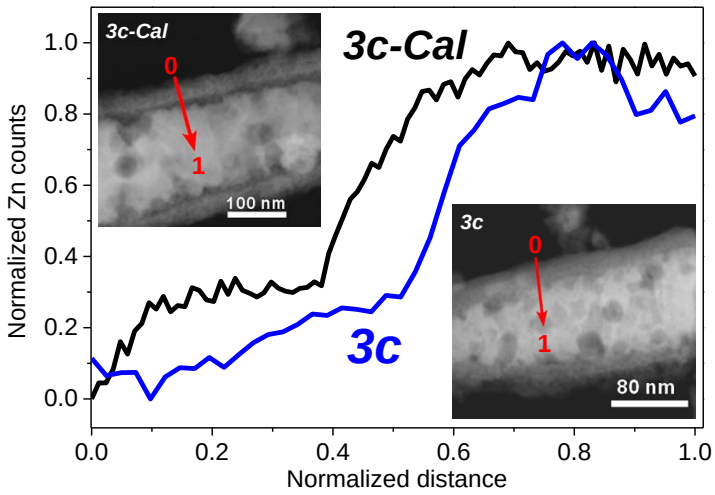

Figure 79 Zinc count profiles obtained from linear EDX-STEM analysis across the ZnO/TiO_2 nanorods: ***3c*** *and* ***3c-Cal****. Insets: HAADF-STEM images of the* ***3c*** *(bottom) and* ***3c-Cal*** *(top) samples with red arrows indicating the line scan direction.*

To confirm the results of EDX analyses, XPS spectra were measured for the ***3c***, ***3c-HCl***, ***3c-Cal***, and ***3c-Cal-HCl*** samples (*Figure 80*). In the XPS spectra of all samples, the position of main Ti ($2p_{1/2}$) signal corresponds to TiO_2, the Zn ($2p_{3/2}$) signal to ZnO, and the O1s signals corresponds to O^{2-} in the lattice of metal oxides and hydroxyl groups [381,382]. The Zn:Ti atomic ratios calculated from the XPS spectra are given in Table 12. The Zn amount in the external TiO_2 layer increases significantly by factor of 2.7 when the ***3c*** sample is additionally calcined (***3c-Cal***). The same tendency is observed when comparing ***3c-HCl*** and ***3c-Cal-HCl*** (factor of increase: 1.8). These results thus confirm that the formation of voids is accompanied by Zn^{2+} diffusion into the TiO_2 layer. Also, STEM images and XPS results ensure that the zinc signal was detected from Zn-modified most external parts TiO_2 layer and not from ZnO-core, due to porosity of TiO_2 layer. The data listed in Table 12 also show that the increase of the Zn/Ti ratio in the outer layer is well correlated with the increase of photocatalytic activity of the samples.

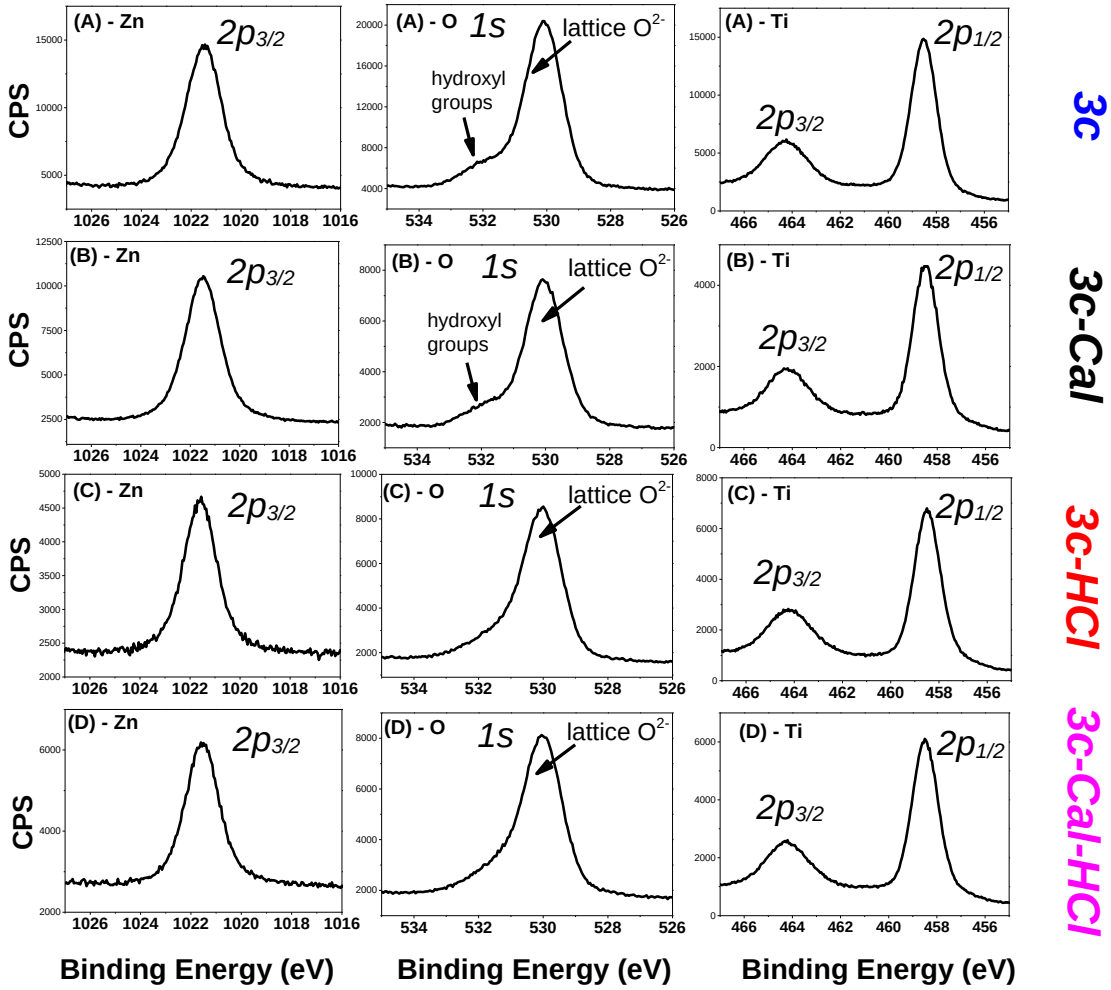

Figure 80 XPS spectra of ZnO/TiO_2 composite systems: ***3c****,* ***3c-Cal****,* ***3c-HCl****, and* ***3c-Cal-HCl****.*

Table 12 The Zn:Ti ratios determined from XPS spectra of ***3c*** *composite,* ***3c*** *composite after additional calcination (****3c-Cal****), and after HCl-treatment (****3c-HCl, 3c-Cal-HCl****). The values of apparent first-order rate constant (k_{400}) of photocatalytic MB decolorization on the samples are also given in the latter column.*

Sample	XPS Zn : Ti atomic %	XPS Zn : Ti atomic ratio	MB decolorization apparent first-order rate constant k_{400} ($\cdot 10^{-2}$ min^{-1})
3c	10 : 20	0.50	0.7
3c-Cal	20.7 : 15.6	1.33	1.0
3c-HCl	4.7 : 21.8	0.22	0.12
3c-Cal-HCl	8.1 : 20.4	0.40	0.34

From the conclusion driven from the enrichment of TiO_2 with zinc a question regarding the nature of the thus formed phase arises. It should be noted that a gradient of Zn concentration exists across the TiO_2 layer and consequently different phases might be formed depending on the distance from ZnO surface. Thus, zinc-rich titanates (Zn_2TiO_4 or $ZnTiO_3$) may exist in the close proximity to ZnO. In contrast, the bulk of TiO_2 layer can accommodate Zn ions in the form of a zinc-poor solid solution. The absence of any peak of zinc titanates in the diffractograms of ***3c-Cal***, *Figure 74B*) does not however allow to exclude their formation but indicates that the main phase is a zinc-containing TiO_2-anatase. This fact points to a possible reason of the increase of the photoexcited electron lifetime observed in the ***3c-Cal*** material. We attribute it to the presence of oxygen vacancies whose formation allows to compensate the charge of Zn^{2+} cations incorporated into the TiO_2-anatase structure. Higher concentration of the oxygen vacancies in the Zn-enriched TiO_2 is confirmed by photoluminescence (PL) spectra of ***3c-HCl*** and ***3c-Cal-HCl*** (*Figure 81*). The intensity of the peak at 510 nm, whose appearance is correlated with formation of oxygen vacancies [383,384,385], increases after additional calcination.

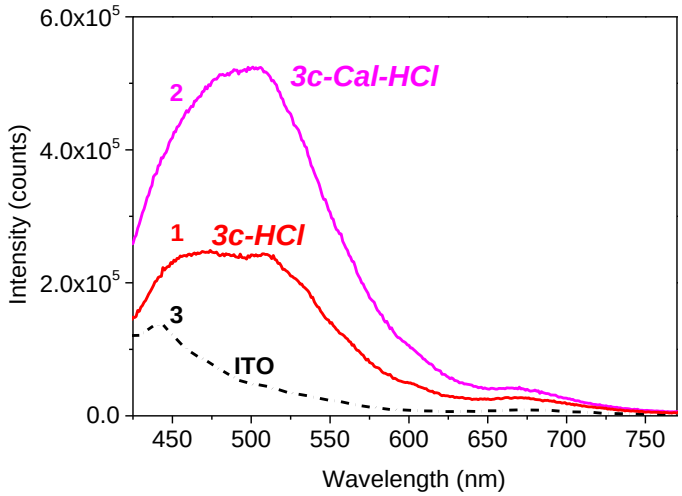

Figure 81 Room-temperature photoluminescence spectra of ***3c-HCl*** *(1),* ***3c-Cal-HCl*** *(2), and ITO-support as reference (3), excited at 400 nm.*

The influence of oxygen vacancies on the photocatalytic properties of TiO_2 is a subject of debates in the literature. While some studies suggest a negative role of these defects, other works describe enhanced properties of the defective samples [386]. This controversy is certainly due to a large number of parameters describing oxygen vacancies which are difficult to determine. Thus, their concentration, charge, spatial distribution, presence or absence of other species in their surrounding can all determine the way how

the oxygen vacancies impact the photocatalytic properties of TiO_2. These parameters appear to be favorable in our case for decreasing the electron-hole recombination rate and consequently for improving photocatalytic and photoelectrochemical properties of the composite.

Our findings about modification of TiO_2 layer in the calcined composite allow to explain the stronger variation of the catalytic activity in MB decolorization observed in the etched samples ($0.12 \cdot 10^{-3}$ min^{-1} for ***3c-HCl*** *vs.* $0.34 \cdot 10^{-3}$ min^{-1} for ***3c-Cal-HCl***) than for the composite ones ($7 \cdot 10^{-3}$ min^{-1} for ***3c*** *vs.* 10^{-2} min^{-1} for ***3c-Cal***).

As it was demonstrated in the *Chapter 4.2. paragraph 4.2.2*, that high photocatalytic activity of ZnO/TiO_2 composites under 400 nm illumination was achieved due to appearance of two effects: i) formation of additional energy levels within the band gap (allowing the sub-band optical transitions) and ii) enhancement of the separation efficiency of photogenerated e^-/h^+ pairs. The additional calcination of the ZnO/TiO_2 composite brings up the third effect – the increase of charge carriers lifetime. The first and the second effects were hence dominantly acting in the pristine ***3c*** sample due to the presence of ZnO/TiO_2 interface. The increase of the lifetime of the charge carriers appearing in ***3c-Cal*** sample seems to be of a lower importance than these two above mentioned effects and therefore, it does not lead to a dramatic increase of its photocatalytic activity in comparison with that of ***3c*** sample. In contrast, in the etched samples (***3c-HCl*** and ***3c-Cal-HCl***) the ZnO/TiO_2 interface was eliminated and for that reason, the related interfacial effects are no longer valid. The only difference between these two samples is a slower electron-hole recombination in ***3c-Cal-HCl*** due to the presence of oxygen vacancies formed upon incorporation of Zn cations into TiO_2. This effect, although 'masked' in the composites, becomes an essential one in the etched samples. This explains why the relative increase of the rate constant upon additional calcination is much larger in case of the HCl-etched samples than for the non-treated ones.

Migration of Zn ions into TiO_2 layer proceeds in our composite at 450 ^oC which is an unusually low temperature for such phenomenon to occur. Thus, in a similar nanostructured (core)ZnO/TiO_2(shell) system the reaction proceeded at 700 °C [387]. The higher reactivity of ZnO in our case is supposed to be related with some particular properties of the surface layer of ZnO nanorods which is in direct contact with the TiO_2

shell. To clarify this point the surface microstructure of as-grown and calcined ZnO nanorods was characterized by HAADF-STEM.

4.3.4. Origin of the modification of the ZnO/TiO_2 interface at moderate temperature

Results of HAADF-STEM imaging of as-synthetized ZnO nanorods, the same nanorods after calcination at 300 ^{o}C, and ZnO nanorods calcined at 450 ^{o}C are presented in *Figures 82A – 82E*. It can be seen that ZnO nanorods after calcination at 300 ^{o}C contain numerous small dark spots on its surface. These extended surface defects designated as 'dents' can be clearly observed on the HAADF-STEM image of ZnO nanorods calcined at elevated temperature at 450 ^{o}C for 1 h (*Figure 82C*). Also, it should be noted that prolongation of calcination time from 1 h to 3 h (*Figure 82D*), or 6 h (*Figure 82E*) have no further influence on ZnO surface morphology. We speculate that these defects may be formed during crystallization of external amorphous layer of zinc (oxo)hydroxide obtained in the hydrothermal synthesis which can be seen as blurred external layer in *Figure 82A*. Crystallization of this layer during calcination at 300 ^{o}C results in its shrinking and formation of a 'dented' surface layer. Such rough surface should be enriched with steps and/or kinks which contain an important number of undercoordinated Zn^{2+} possessing high reactivity. During sol-gel deposition the amorphous Ti-containing species fill up the 'dents' at the ZnO surface and thus come in a close contact with the highly reactive zinc species. This particular configuration would allow for diffusion of Zn^{2+} into TiO_2 already at 450 ^{o}C. We consider that both this specific surface roughness of ZnO nanorods and the used sol-gel deposition method make possible Zn ion diffusion at such moderate temperature.

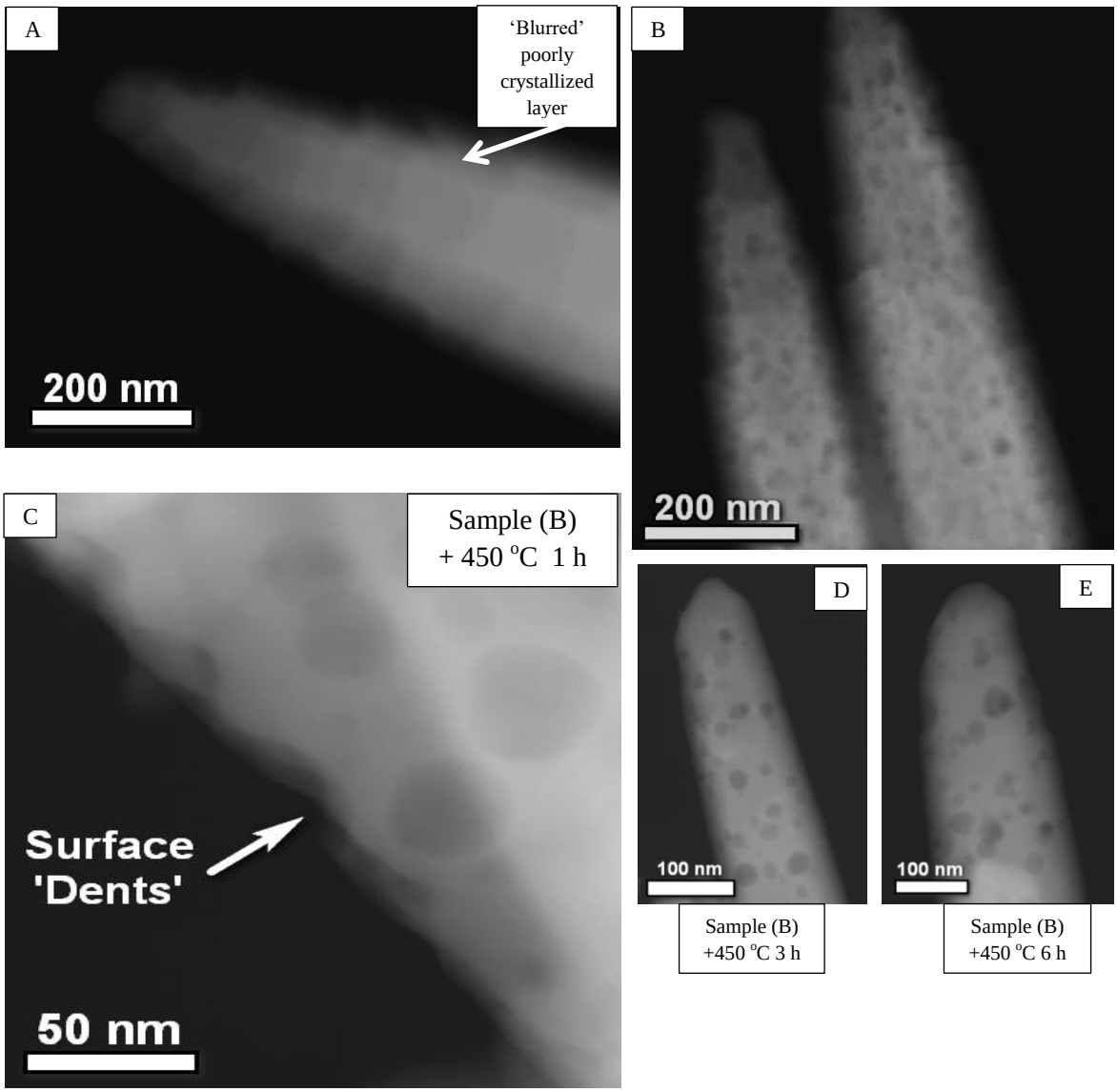

Figure 82 HAADF-STEM images of hydrothermally as-synthesized ZnO nanorods (A), and after their calcination at 300 °C for 1 h (B). Samples B after subsequent their calcination at 450 °C for: 1 h, 3 h, and 6 h are presented on images, C, D, and E, respectively.

A scheme depicting this possible diffusion scenario is presented in *Figure 83*. Hence, improved photocatalytic and photoelectrochemical properties of ZnO/TiO_2 composite can be attributed to the presence of ZnO/TiO_2 interface responsible for improved light absorption and to Zn-modified TiO_2 layers responsible for prolonged electron-hole pair recombination lifetime.

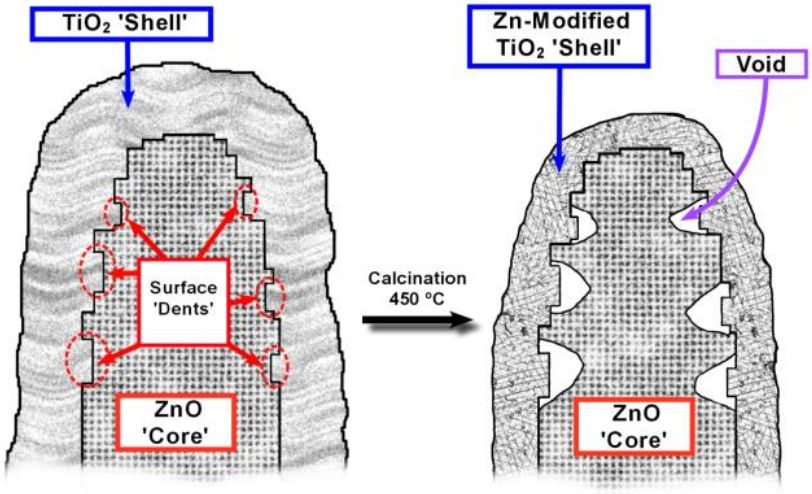

Figure 83 Schematic illustration depicting presumable thermal diffusion process of Zn ions into TiO_2 at the ZnO/TiO_2 interface at 450 ^oC accompanied with formation of 'voids' in ZnO-core.

4.3.5. Conclusions

In this Chapter it was directly proven that presence of both ZnO(core) and TiO_2(shell) is needed for obtaining photoactive composites, which efficiently decolorize MB under 400 nm light irradiation. The origin of this effectiveness was shown to be related to the improved absorption in the visible range due to formation of new electronic mid gap states at the ZnO/TiO_2 interface.

We found that an additional calcination of the ZnO/TiO_2 composite at 450 °C leads to the increase of photocatalytic activity in MB decolorization and remarkable improvement of the photocurrent response of the composite in photoassisted water oxidation. The measurements of open circuit potential transients showed that this effect stems from a lower electron–hole recombination rate in the additionally calcined composite. The observed improvement of the photocatalytic properties was found to be accompanied by a pronounced modification of the microstructure of the ZnO/TiO_2 composite. Despite a moderate value of the used temperature (450 °C), voids appear at ZnO/TiO_2 interface and Zn ions migrate into TiO_2 shell. We suggest that formation of the Zn-enriched TiO_2 shell is responsible for the observed enhancement of the photocatalytic and photoelectrochemical properties. This phenomenon was ascribed to the Kirkendall effect which was observed for the first time at such low temperature due to defective surface structure of ZnO nanorods. Given the importance of ZnO and TiO_2 in photocatalysis

these findings may be useful in designing more efficient photoactive materials, as well as in application of ZnO/TiO_2 composites in degradation of other pollutants.

4.4. Imparting visible light activity to the ZnO/TiO_2 composites

4.4.1 Optimization of N-doping of TiO_2

In order to obtain nitrogen-modified TiO_2 powder the same sol-gel approach was used. Firstly, the weight of TiO_2 powder obtained in a single 30 min cycle was estimated and calculated into molar yield. Addition of nitrogen precursor salt (NH_4Cl) during precipitation was adjusted to this TiO_2 molar yield in a mole ratio of TiO_2:N-atom varying from 1:1 to 1:20. The optical properties of obtained N-doped TiO_2 powders are presented in *Figure 84*. As seen the highest absorption, and improvement of absorption towards visible light was observed for a powder prepared in middle-way conditions, that is with initial molar ratio TiO_2:N 1:10 and. The preparation conditions of such powder were then chosen for our next stage of N-doped TiO_2 covering of ZnO nanostructures.

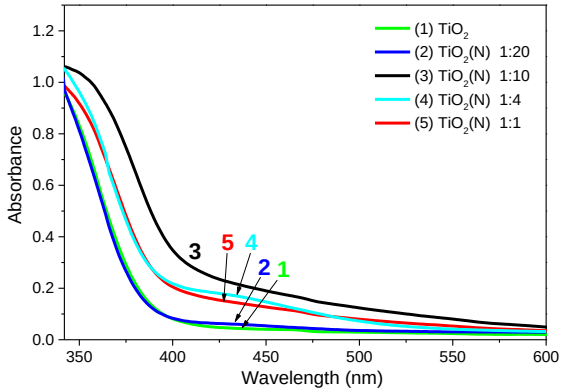

Figure 84 Absorbance spectra of N-modified TiO_2 powders prepared by sol-gel method.

Absorption spectra of the parent materials (ZnO nanorods (NRs) and TiO_2 powder obtained by sol-gel method) and ZnO(core)/TiO_2(shell) composites are compared in *Figure 85A*. As visible, the light absorption in the visible wavelength range (longer than 400 nm) by ZnO and TiO_2 is negligible (curves 1 and 2, respectively), while the formation of ZnO/TiO_2 interface (sample ***1c***) resulted in the red shift of the absorbance spectrum and appearance of so called 'Urbach tail' in the range from 400 nm to 525 nm (curve 3). These features have been ascribed by us to formation of new energy levels localized at the metal oxides boundary. As also presented in *Figure 85A*, the light absorption in the visible range was improved after doping of TiO_2 with nitrogen (curve 4). The shift of the absorption edge of the sample (***3c(N)***) towards longer wavelength may be explained by a presence of nitrogen atoms in the interstitial positions in TiO_2 crystal structure, leading to appearance of N2p interband energy levels in the TiO_2 band

gap just above the upper edge of the valence band [388,389,390]. Consequently, it makes possible to transfer the electrons from the nitrogen midgap state to the conduction band of TiO_2. It is also worth noting that the 'red' shift of the spectrum of the sample ***3c(N)*** is not accompanied with formation of the additional absorption shoulder, thus suggesting a homogeneous distribution of a nitrogen dopant in TiO_2. Following the Tauc equation, the energy of optical band gap (E_g) of semiconductor (or composite) can be determined [391], as it is shown in *Figure 85B*. The ***3c(N)*** composite proved to have lower value of E_g (~ 2.78 eV) in a comparison to that of the ***1c*** sample (E_g ~ 2.90 eV).

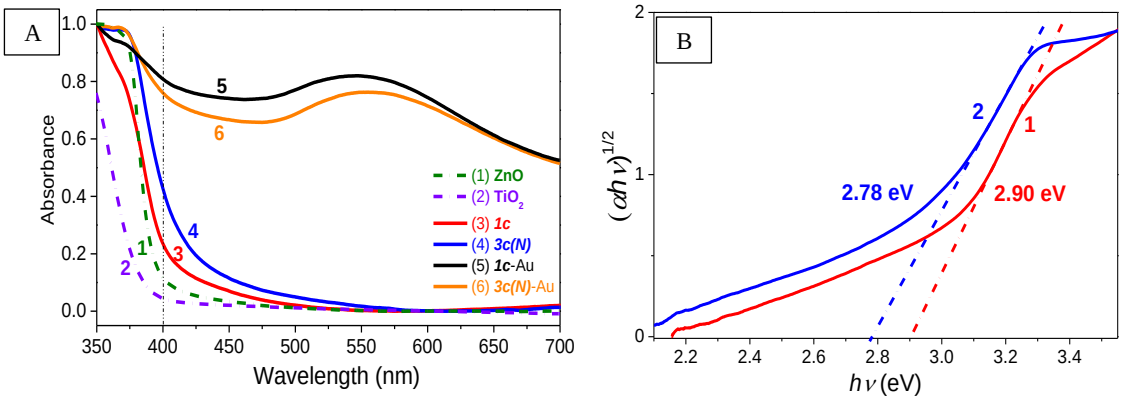

*Figure 85 (A) Comparison of UV-vis absorption spectra of ZnO NRs (curve 1) TiO_2 (curve 2) and composites: ZnO/TiO_2 (**1c**, curve 3), ZnO/TiO_2(N) (**3c(N)**, curve 4), ZnO/TiO_2/Au (**1c-Au**, curve 5) and ZnO/TiO_2(N)/Au (**3c(N)-Au**, curve 6). (B) Determination of optical band-gap energies from the absorption spectra of **1c** (curve 1) and **3c(N)** (curve 2) samples.*

Photodeposition of Au nanoparticles on both samples results in appearance of strong and broad absorption bands with maxima located at approx. 556 nm for ***3c(N)-Au*** and 545 nm for ***1c-Au*** (curves 5 and 6 in *Figure 85A*, respectively). Both peaks may be ascribed to the plasmonic bands of metallic gold nanoparticles [392]. A direct interaction between Au and TiO_2 is responsible for a red shift of the plasmon absorption band compared to that of nanoparticles suspended in the solution (530 nm) and for extended absorption in infrared region [393]. The different position of the plasmonic peaks in ***1c*** and ***3c(N)*** samples is possibly due to the well-known sensitivity of this parameter to the composition of the species being in contact with the plasmonic nanoparticles [394].

4.4.2. Chemical composition

The differences observed in optical absorption spectra of the samples are reflected in their different compositions (Table 13). The chemical composition of the samples was

determined by EDX-SEM analysis. It can be noticed that amount of TiO_2 deposited in the presence of NH_4Cl is smaller than that obtained in salt-free conditions. Indeed, according to our previous results, the Ti/Zn ratio in the sample prepared within three cycles of deposition without NH_4Cl (***3c***) was 0.27, while it was only 0.05 in the ***3c(N)*** sample. Such a strong decrease of the amount of deposited TiO_2 despite the same reaction time can be attributed to the presence of chloride anions which were shown to slow down the hydrolysis of titanium alkoxides [395]. The amount of Au deposited on both samples (1.1 – 1.8 wt. %) is similar to that reported for other Au-loaded photocatalysts [396,397,398]. It is worth noting that the Ti/Au atomic ratios are similar for both gold-containing composites (11.9 and 11.3 for ***1c-Au*** and ***3c(N)-Au***, respectively) which is important for correct comparison of their photocatalytic properties. The same observation holds also for the average sizes of the gold particles estimated from the broadening of 111 peak of metallic gold (located at $2\theta = 38.2^{o}$) in the XRD patterns of the samples (*Figure 86*).

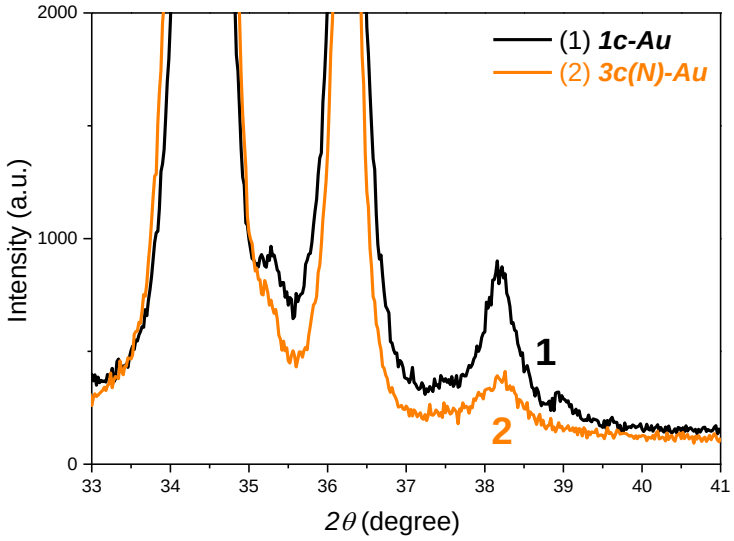

Figure 86 XRD patterns used for the determination of the average sizes of Au NPs from the broadening of 111 peak of metallic gold (located at 2θ = 38.2).

In order to confirm the presence of nitrogen in ***3c(N)*** sample, the XPS measurements were performed. The N1s peak observed in the spectrum presented in *Figure 87A* reveals non-symmetrical shape which is likely a result of overlapping of two different signals. A strong peak located at 400.0 eV (deconvoluted as a blue line) can be attributed to nitrogen bounded either as Ti–O–N or Ti–N–O, characteristic of interstitial N atoms. The second, less pronounced N1s peak (398.0 eV, red) possibly originates from replacement

of oxygen atom with nitrogen in TiO_2 crystal lattice. Such nitrogen incorporation can be presented as Ti–N–Ti and described as substitutional nitrogen [399,400,401].

Table 13 Chemical composition of initial ZnO/TiO_2 as well as N-doped and Au-deposited composites.

Sample	Composition, at. % *(EDX-SEM analysis)*			crystallite size of Au, nm *(XRD)*
	Zn	Ti	Au	
1c	46	4.6	-	-
1c-Au	45	4.4	0.37 (1.8 wt. %)	17
3c(N)	47	2.3	-	-
3c(N)-Au	46	2.6	0.23 (1.1 wt. %)	15

These findings allow to conclude that the used sol-gel procedure resulted in successful doping of TiO_2 layer with nitrogen. Concerning the spectra of Ti and Zn, their positions are 458.2 eV and 464.0 eV for Ti2p, and 1021.6 eV and 1044.6 eV for Zn2p, corresponding to typical binding energies in metal oxides [402,403] (*Figure 87C, 87D, 87E*). In case of the O1s XPS spectrum, the maximum at 529.8 eV assigned to oxygen in metal oxides [404] is followed by a shoulder corresponding to oxygen of the surface adsorbed hydroxyl groups [405].

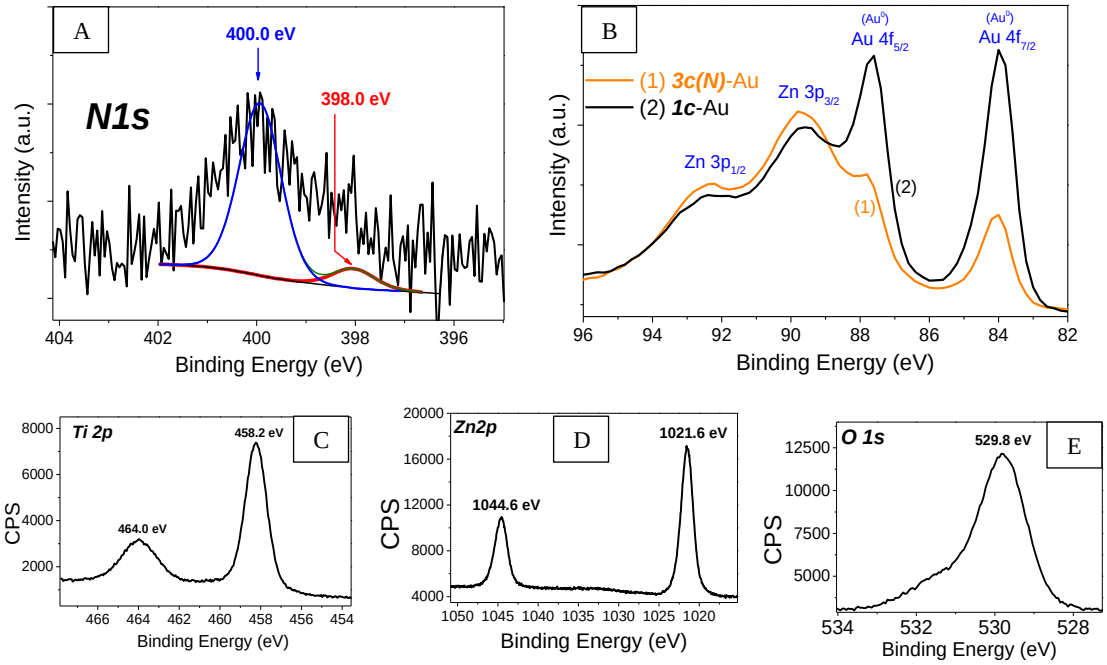

Figure 87 XPS spectra of N1s (A) in nitrogen doped TiO_2 deposited on ZnO, and Zn3p and Au4f in Au-decorated composites (B). XPS spectra of Ti2p (C), Zn2p (D), O1s (E) in nitrogen doped TiO_2 deposited on ZnO.

The XPS spectrum of Au is complex because of its strong overlap with the peaks of Zn (*Figure 87B*). However, in the spectra of both ***1c-Au*** and ***3c(N)-Au*** samples, four peaks can be clearly distinguished. Zn peaks of $3p_{1/2}$ and $3p_{3/2}$ contribute to the overlapped spectra and are located at around 92.3 eV and 89.7 eV, respectively. The Au $4f_{7/2}$ peak located at 84.0 eV is well separated apart from the others, so that its position can be determined precisely. As a consequence of spin-orbital splitting (Δ = 3.6 eV), the second peak ($4f_{5/2}$) is observed at 87.6 eV [406,407]. Comparison of the observed bond energy with the values reported for different Au compounds [408,409] allows to conclude that it corresponds to the metallic gold. Absence of any other peaks in the range 85 eV – 86 eV suggests that in our composites the gold is present only in the metallic state (see also STEM EDX data below).

4.4.3. Microstructure of the composites

*N-modified TiO_2 in ZnO/TiO_2 composite – **3c(N)***

The microstructure of ***1c*** sample was characterized in detail in our previous work. The SEM and HAADF-STEM images of ***3c(N)*** sample are presented in *Figure 88*. They reveal the presence of a continuous and visibly porous layer of TiO_2 anatase of *ca.* 20 nm in thickness (*Figure 88B*). Similarity of microstructure of TiO_2 layer in ***1c*** and ***3c(N)***

samples (see *Chapter 4.2*, *Figure 55*) justifies our choice of ***1c*** as the nitrogen free composite for comparison with ***3c(N)***.

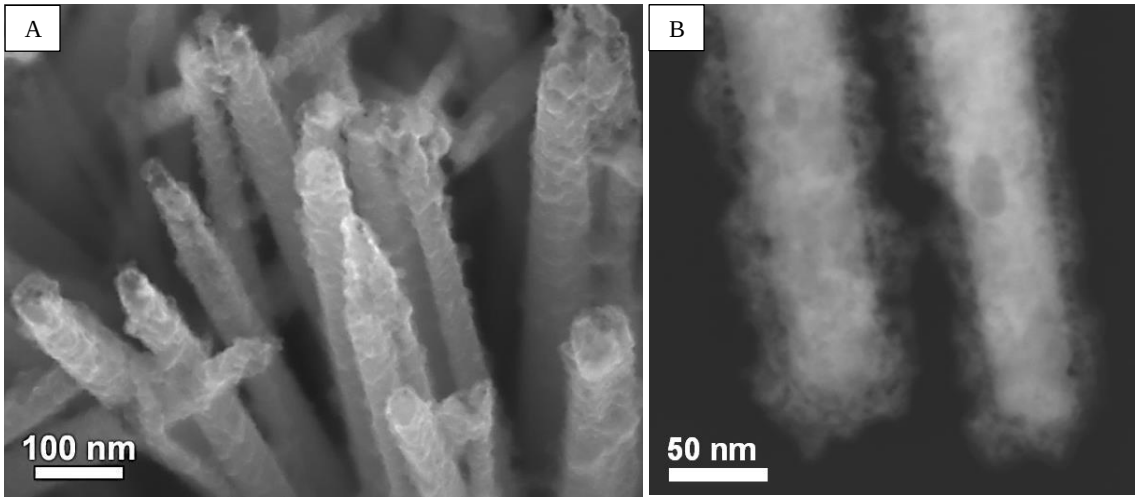

*Figure 88 SEM (A) and HAADF-STEM (B) images of **3c(N)** sample.*

According to our previous results, the photodecolorization rate of MB on ZnO/TiO_2 composite in aqueous solution strongly depends on morphology of TiO_2 layers deposited on ZnO nanorods and accessibility of the solution species to the ZnO/TiO_2 interface. This aspect was also taken into account in selection of the sample for the studies on the influence of nitrogen doping and decoration of the ZnO/TiO_2 surface with Au nanoparticles on photocatalytic and photo-electrochemical properties of the composites.

4.4.4. Au-nanoparticle decorated composites

The gold nanoparticles are easily detected as bright spots in SEM images obtained using the low-angle backscattered electron detection which signal intensity is proportional to atomic number of the analyzed element (*Figure 89*). Therefore, Au nanoparticles can be easily seen in ***1c*** and ***3c(N)*** nanostructures as spots of much brighter contrast than Zn or Ti (in ZnO or TiO_2) (Au nanoparticles are indicated by red circles in the SEM images).

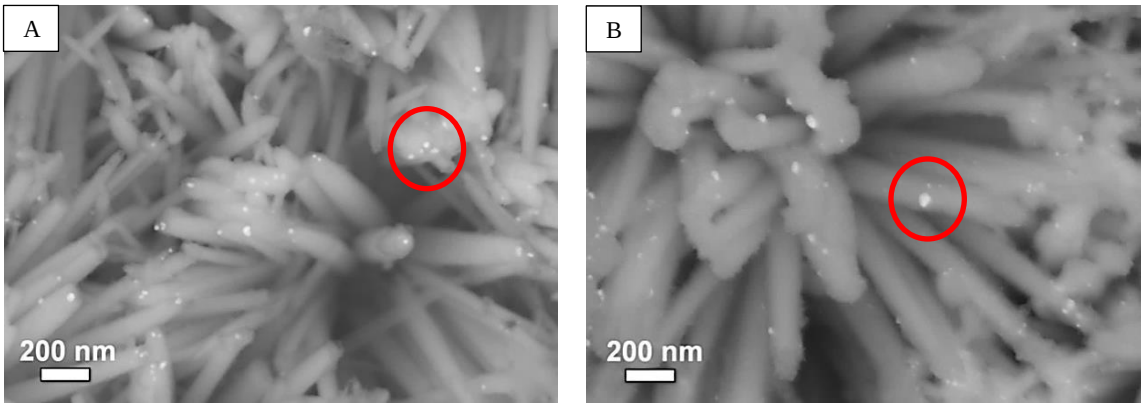

*Figure 89 SEM images of **3c(N)**-Au (A) and **1c**-Au (B) samples in low-angle backscattered electron (LABE) detection mode.*

The spatial resolution of the SEM is however insufficient to determine precisely the size and characterize in detail the morphology of Au nanoparticles. This information was obtained using HR-TEM and HAADF-STEM techniques (*Figure 90*). Analysis of the images shows that despite the presence of large particles (> 30 nm), the size of the most particles lies within the range 7 nm – 25 nm which is in agreement with the average value determined from XRD (Table 13). Such a broad dispersion of the particles size is not surprising since a simple photodeposition was used without addition of any growth-limiting agents. The similarity of the size distribution of gold particles for ***1c-Au*** and ***3c(N)-Au*** shows that the presence of nitrogen in the latter sample does not influence the process of photodeposition. Another important feature of the obtained samples is a high crystallinity of the obtained nanoparticles which is attested by the high resolution images (*Figures 90E* and *90F*).

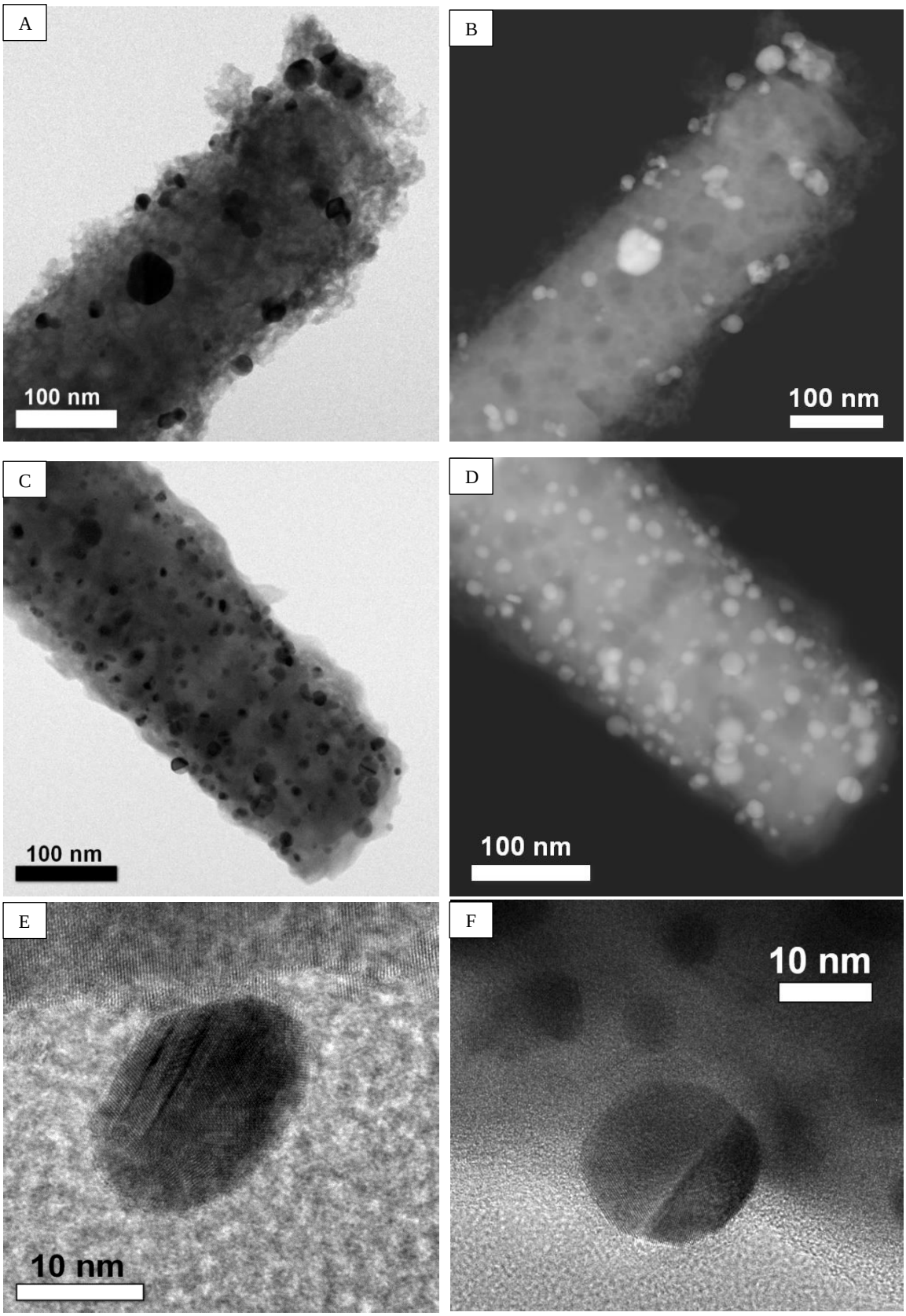

*Figure 90 TEM and HAADF-STEM images of **3c(N)-Au** (A, B), **1c-Au** (C, D) samples and HR-TEM images of Au NPs deposited on **3c(N)-Au** (E), and **1c-Au** (F), respectively.*

The EDX analysis with a high spatial resolution present in HAADF-STEM setup was used also to answer a question concerning the chemical form of gold present in our samples. Given the preparation procedure and short time of photodeposition (20 s) one can suppose that the reduction of gold is incomplete and some fraction may be present in form of ionic species dispersed on the surface of TiO_2. To check this possibility we analyzed by EDX the chemical composition of two different areas: one contained gold nanoparticles (*pt 1*) and another one was free of them (*pt 2*) (*Figure 91*). While the gold is clearly detected in the first area, it is completely absent in the second one. If gold were present in any ionic form it would have been distributed homogeneously and observed everywhere. Its absence in the second area thus strongly supports that gold is present only in the form of nanoparticles.

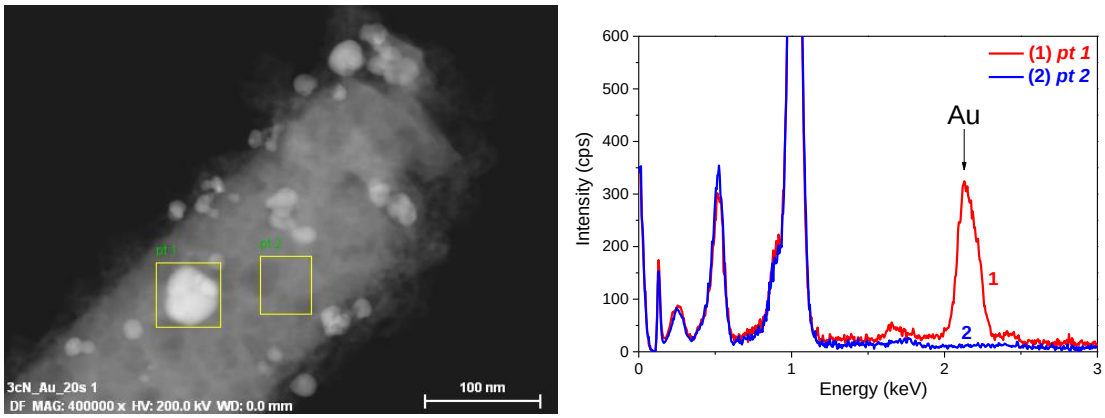

Figure 91 EDX chemical analysis in HAADF-STEM mode on selected areas: with (pt 1) and without Au nanoparticles (pt 2).

4.4.5. Photocatalytic (PC) properties ZnO/TiO_2/Au composites

The photocatalytic activity of the prepared composites was firstly tested in MB decolorization reaction, according to ISO procedure. The decrease of MB concentration under illumination and the plots used for determination of the corresponding apparent first-order rate constants are presented in *Figure 92A* and *92B*, respectively. It follows that ***1c*** and ***3c(N)*** samples have similar activities despite the presence of nitrogen in the latter and its higher absorbance in visible range (*see Figure 85*). For Au-decorated samples a similar effect is observed: k_{vis} value for ***3c(N)-Au*** is even lower than that of ***1c-Au***. The presence of nitrogen, which should have yielded a higher activity, is possibly offset by other features of nitrogen-containing composites such as formation of N-induced states in doped TiO_2 which may promote e^-/h^+ recombination [410]. This explanation is supported by the kinetic analysis of photocurrent transients (see *Chapter*

4.4, paragraph 4.4.6) and by the fact that under external polarization (enhancing e^-/h^+ separation) the N-doped samples show higher activity than their non-doped counterparts.

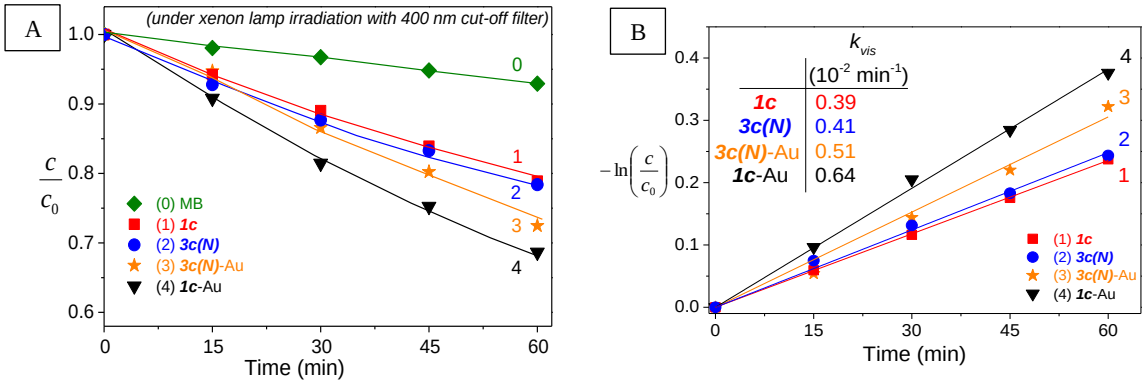

Figure 92 Decolorization of MB under visible light irradiation (Xe lamp with 400 nm cut-off filter) without any catalyst (line 0) and in the presence of composites: ***1c*** *(line 1),* ***3c(N)*** *(line 2),* ***3c(N)-Au*** *(line 3), and* ***1c-Au*** *(line 4) (A) and determination of* $\boldsymbol{k_{vis}}$*-values of the catalysts (B).*

Addition of the Au nanoparticles results in a 36% increase of the rate of MB decolorization for nitrogen-incorporated samples (k_{vis} = 0.41 ·10^{-2} min^{-1} for ***3c(N)***, and k_{vis} = 0.51 ·10^{-2} min^{-1} for ***3c(N)-Au***). On the other hand, the photocatalytic activity of the nitrogen-free composite was more prone to the influence of Au nanoparticles since it resulted in almost 60% enhancement (k_{vis} = 0.39 ·10^{-2} min^{-1} for ***1c***, and k_{vis} = 0.64 ·10^{-2} min^{-1} for ***1c-Au***). It is important to notice that the measurements of TOC showed that MB is not only decolorized but also partially mineralized under used conditions (*Figure 93*).

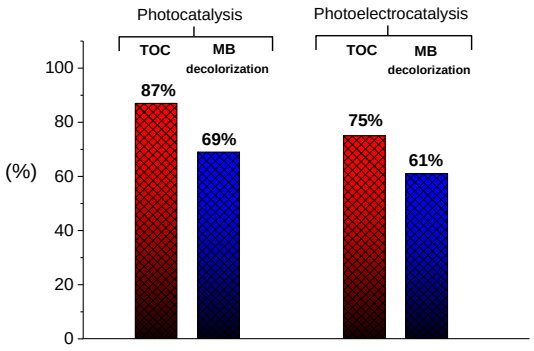

Figure 93 Percentage of mineralization (from TOC measurements) and decolorization (from UV-vis absorption spectra) of MB (initial concentration 10 μM) with the use of ***1c-Au*** *composite, after 60 min of visible light illumination. Photoelectrocatalytic experiments were performed at constant potential of –0.25 V vs. Ag/AgCl in the presence of 5 mM* Na_2SO_4 *supporting electrolyte.*

The slightly lower degree of mineralization than that of decolorization is due to slower kinetics of the former process [97]. The enhancement of the photocatalytic activity of gold-containing samples suggests that the plasmonic excitation in Au nanoparticles enhances the visible light response of ZnO/TiO_2 core/shell composites. One can suppose that this increase of activity should be even greater under bias conditions when the generated e^-/h^+ pairs are separated more efficiently. That is why in the following sections the photoelectrochemical properties of the composites in different reactions were characterized in detail.

4.4.6. Photoelectrocatalytic (PEC) properties ZnO/TiO_2/Au composites

Figure 94 presents a comparison of the linear sweep voltammograms obtained for the non-modified ZnO/TiO_2 composite (sample ***1c***), modified by N-doping (sample ***3c(N)***), and the two other samples additionally decorated with Au nanoparticles (samples ***1c-Au*** and ***3c(N)-Au***, respectively). The voltammograms were recorded in dark and under illumination with visible light ($\lambda > 400$ nm).

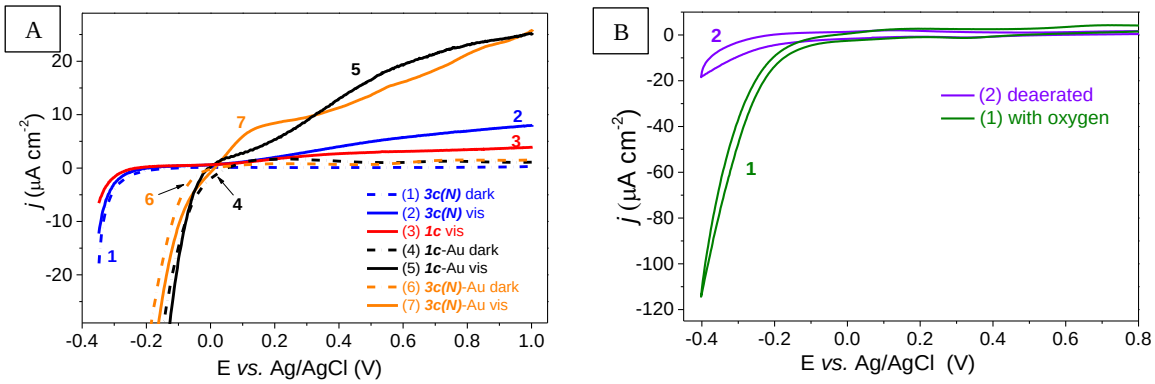

*Figure 94 (A) Linear sweep voltammograms in dark and under visible light irradiation for ZnO/TiO_2 samples: without any modification (**1c**, line 3), N-doped TiO_2 (**3c(N)**, lines 1, 2), decorated with Au (**1c-Au**, lines 4, 5), N-doped TiO_2 and decorated with Au (**3c(N)-Au**, lines 6, 7). (B) Comparison of the cyclic voltammograms obtained for ZnO/TiO_2/Au sample in the solution containing oxygen (line 1) and after deaeration (line 2).*

It is interesting to note, that deposition of the Au nanoparticles on ZnO/TiO_2 composites gives rise to significant increase of the photocurrent in anodic potential range, while the reduction current is strongly enhanced even without illumination (lines 4 – 7 in *Figure 94A*). The possible reason of the latter effect is catalytic electroreduction of dissolved oxygen on Au, which was confirmed by the result of a control experiment

performed on the same electrode in deareated solution. As one can observe in *Figure 94B,* the reduction current was strongly diminished after 30 min of purging of the solution with stream of Ar.

It is well known that catalytic oxygen reduction reaction (ORR) on noble metal electrodes in aqueous solutions proceeds via either a 'direct' four-electron reduction ($E^o(O_2/H_2O)$ = 1.23 V *vs.* NHE) or 'series' of reaction pathways, including two-electron reduction of O_2 to H_2O_2 ($E^o(O_2/H_2O_2)$ = 0.68 V *vs.* NHE) [411]. The overall mechanism of the process is complicated and involves formation of various intermediates, depending on the kind of electrode material, catalyst and electrolyte. One of postulated intermediates in the first reaction step is superoxide radical anion:

$$O_2 + e^- \rightleftarrows O_2^{\bullet -} \tag{70}$$

easily detected in non-aqueous solutions ([412] and references therein). The standard potential of the reaction (70) in aqueous solution is –0.16 V *vs.* NHE, at pH = 7 (i.e. –0.35 V *vs.* Ag/AgCl), while in non-aqueous media its value depends on the solvation properties of the solvent. In aqueous solutions it is difficult to confirm the presence of $O_2^{\bullet -}$ radical due to its rapid protonation and/or disproportionation with water, leading to formation of H_2O_2 or/and $HO_2^{\bullet -}$ and OH^- [413]. Moreover, H_2O_2 created in these reactions may undergo further transformations, leading to formation of radical $^{\bullet}OH$, according to the schemes [414,415]:

$$H_2O_2 + e^- \rightarrow {}^{\bullet}OH + OH^- \tag{71}$$

$$H_2O_2 + O_2^{\bullet -} \rightarrow {}^{\bullet}OH + OH^- + O_2 \tag{72}$$

The ORR is usually investigated in acidic or basic solutions, while only a few reports deal with neutral media [416,417,418]. The formation of $O_2^{\bullet -}$ in the first step of oxygen reduction on Pt thin film electrode in the solution of pH = 11 has been confirmed by Adzic *et al.* [419] by spectroscopic and voltammetric measurements. Recently, the formation of superoxide radical intermediate in reaction of oxygen reduction on Au in neutral and mildly alkaline aqueous solutions has been supported by Scherson *et al.* [420] by means of rotating ring-disc electrode measurements. Regardless of the exact mechanism of oxygen reduction on ZnO/TiO_2/Au composite, formation of active oxygen species ($O_2^{\bullet -}$, H_2O_2 and $^{\bullet}OH$) may influence on photoelectrocatalytic properties of the

system with respect to MB degradation and this aspect will be discussed further in the text (see *Figure 97* and discussion below).

In contrast to the behavior in the negative potential range, the dark current on Au-decorated samples at $E > 0$ V *vs.* Ag/AgCl is practically zero, while after illumination with visible light an anodic current appears due to oxidation of the surface hydroxyl groups and/or water molecules by photogenerated holes. It is also worth noting, that non-zero photocurrent was also recorded for the pristine sample ***1c*** (without N-doping or decoration with Au nanoparticles), in spite of the fact that in the visible light only a small part of photons possesses energy high enough to generate the e^-/h^+ pairs in the wide band-gap semiconductor. Further increase of photocurrent was found after doping of TiO_2 shell with nitrogen (line 2 in *Figure 94A*). The reason of photoactivity of these two samples in visible range was discussed in the *paragraph 4.4.1* and explained by the presence of additional energy levels within the band gap, due to formation of ZnO/TiO_2 interface and incorporation of nitrogen into TiO_2 structure.

A strong improvement of photocurrent in the range of positive potentials was observed after deposition of Au nanoparticles: ***1c-Au*** and ***3c(N)-Au***. Since the shape of the voltammograms presented in *Figure 94A* is not the same for both Au-decorated composites, probably due to some non-stationary processes occurring at the TiO_2/solution interface during polarization of the electrode in a wide potential range, the photoelectrochemical activity of the samples was studied at constant potential. The current transients recorded for all studied electrodes at the potential of 0.8 V *vs.* Ag/AgCl in dark and under illumination are presented in *Figure 95*.

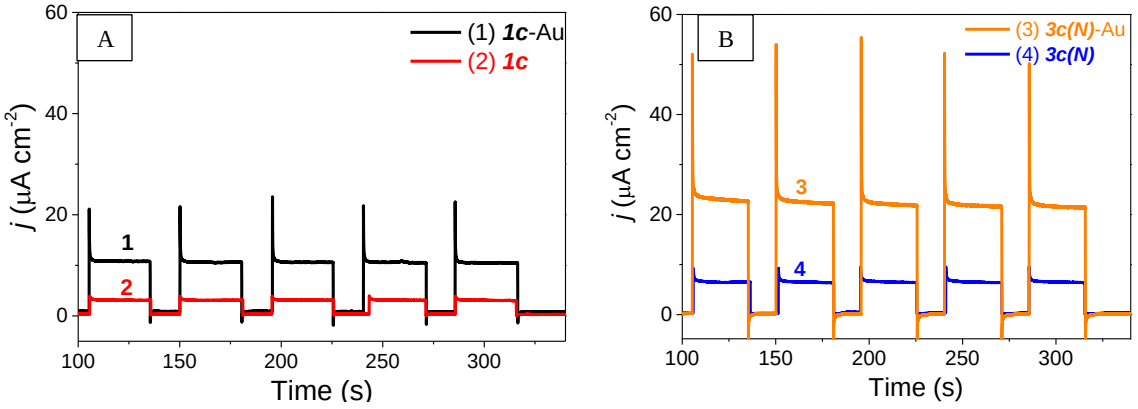

*Figure 95 Comparison of the current transient in dark and under illumination with visible light at constant potential of 0.8 V vs. Ag/AgCl for the samples: (A): **1c-Au** (plot 1) and **1c** (plot 2); (B): **3c(N)-Au** (plot 3) and **3c(N)** (plot 4).*

As visible, all current responses are very reproducible in the subsequent dark-illumination cycles and it was found that the photocurrent was stable even after 50 on/off cycles (*Figure 96*). The steady-state current is similar to that in *Figure 95*, while smaller spikes are a consequence of extension of the interval time due to long time scale of the experiment.

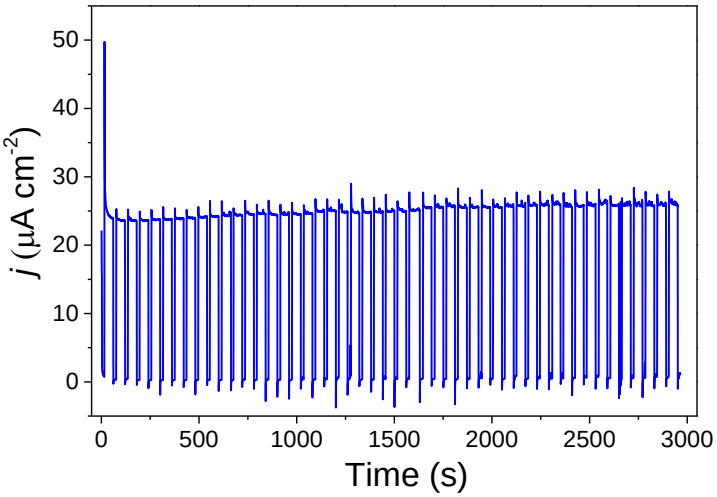

*Figure 96 Long-term chronoamperometric tests for the sample **3c(N)** in dark and underillumination at constant potential of 0.8 V vs. Ag/AgCl.*

The data recorded for the Au-free samples are consistent with the results obtained by the linear sweep voltammetry. Namely, the photocurrent for the sample doped with nitrogen ***3c(N)*** (*Figure 95B*, line 4) is about two times greater than that for non-doped ***1c*** composite (*Figure 95A*, line 2). On the other hand, decoration of ZnO/TiO_2 and ZnO/TiO_2(N) with Au nanoparticles leads in both cases to three-fold increase of

photocurrent with respect to the 'bare' composites, namely from 3.24 μA cm^{-2} to 10.5 μA cm^{-2} for the samples without nitrogen and from 6.5 μA cm^{-2} to 22.3 μA cm^{-2} for N-doped ones. The reason of enhanced visible light activity of TiO_2 loaded with Au nanoparticles is still under debate in the literature. According to the most common approach, the localized surface plasmon resonance (LSPR) induces the collective coherent oscillations of electrons of the metal nanoparticles and transfer of the electrons to conduction band of TiO_2, leaving behind the hole which may be filled by electron from a donor species present in the solution [421]. Alternative explanation is based on the local electric field enhancement due to interaction of oscillating electrons with electromagnetic field of incident light, leading to the formation of excitons in the local TiO_2 regions. The hole after exciton dissociation may be filled, as postulated above, by the electron from the solution species.

Another characteristic features of the transients presented in *Figures 95* are the current spikes just after the switching light on, followed by exponential decays within 1 – 3 seconds to the steady-state values. The current overshoot in opposite direction and decay back to zero was observed after switching light off. These characteristic spikes in the onset regions of photo- and dark currents, are an evidence for e^-/h^+ surface recombination, competing with the light-driven electrode reactions at the semiconductor/solution interface [57]. It is interesting to note, that intensity of the spikes is greater for the process occurring on Au-loaded electrodes, suggesting higher recombination rate. In order to estimate a ratio of the rate constants for charge transfer across the semiconductor/solution interface (k_{tr}) and for e^-/h^+ recombination (k_{rec}), the photocurrent transients *j(t)* were analyzed according to the protocol proposed by Peter's relation (see *Bibliography* section for more details):

$$\frac{j(\infty)}{j(0)} = \frac{k_{tr}}{k_{tr}+k_{rec}} \tag{73}$$

As one can see from the plots presented in *Figure 95* and data listed in Table 14, the doping of TiO_2 with N leads to two opposite effects. On one hand, it results in higher steady-state photocurrents (due to higher amount of electrons and holes photogenerated by visible light) but on the other, the appearance of new N-doping levels in TiO_2 may also act as the trapping states promoting the e^-/h^+ recombination [422]. The latter effect is probably responsible for relatively low performance of N-doped sample in photodecolorization of MB with respect to that of non-doped composites.

Table 14. Ratio of charge transfer and recombination rate constants determined from photocurrent transients.

Sample	k_{tr}/k_{rec}
1c	4.06
1c-Au	1.05
3c(N)	2.45
3c(N)-Au	0.75

The data listed in Table 14 indicate also enhancement of recombination after decoration of both types of the samples (***1c*** and ***3c(N)***) with Au nanoparticles. This may be rationalized taking into account participation in this process of the electrons appeared in the conduction band of TiO_2 owing to plasmonic effect.

On the other hand, one can expect that these extra electrons may be involved in reduction of dissolved oxygen under cathodic polarization of the electrode (reaction (70)). This is thermodynamically possible because the conduction band energy $E_{CB(TiO2)}$ at pH = 7 (–0.5 V *vs.* NHE, i.e. –0.69 V *vs.* Ag/AgCl) is located above the redox standard potential of $O_2/O_2^{\bullet-}$ couple (0.16 V *vs.* NHE, i.e. 0.03 V *vs.* Ag/AgCl). The occurrence of the process is confirmed by the increase of the reduction current, for illuminated ZnO/TiO_2/Au under constant potential of –0.25 V *vs.* Ag/AgCl, as illustrated in *Figure 97A*. In contrast, this effect was not observed for Au-free sample (*Figure 97B*). The same difference was found for N-doping samples with and without Au nanoparticles (see *Figure 97C*).

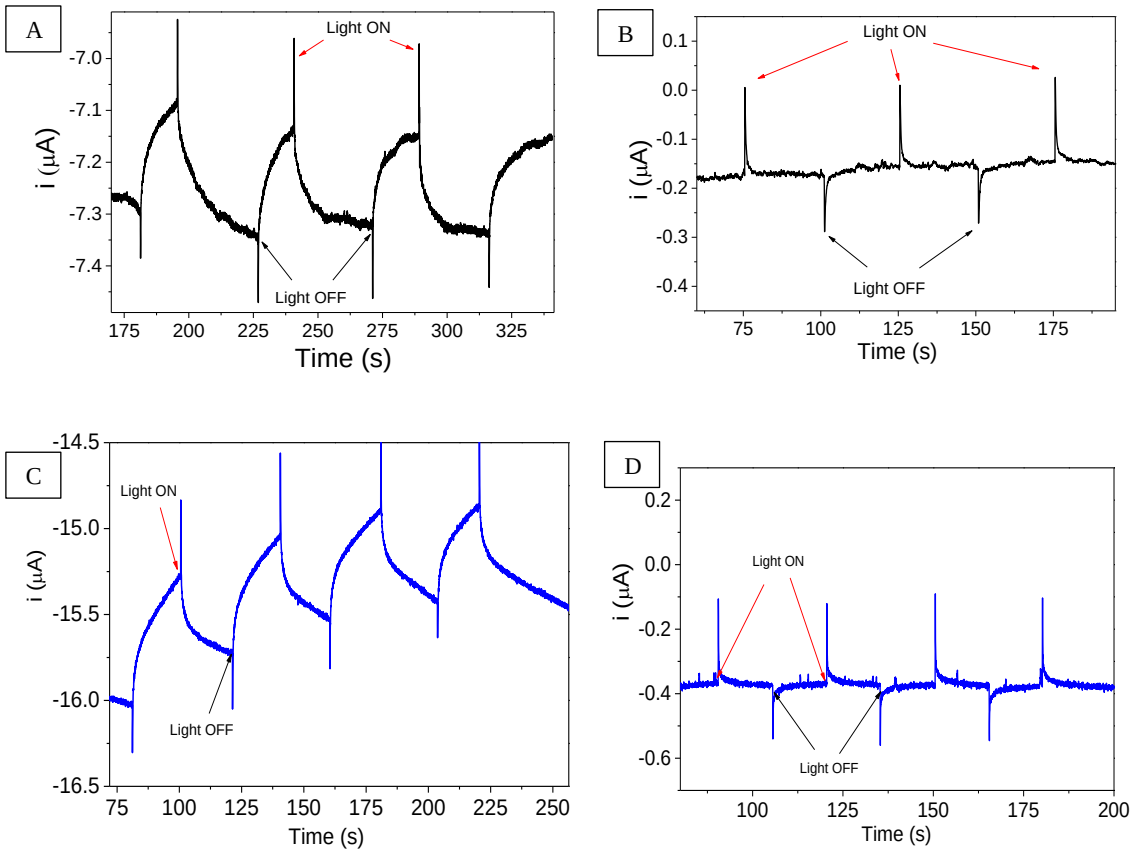

*Figure 97 Current transients recorded during polarization of ZnO/TiO_2/Au electrode (**1c-Au**) (A) and ZnO/TiO_2 (**1c**) (B) in dark and under illumination with visible light in aqueous solution of 5 mM Na_2SO_4 at constant potential of –0.25 V vs. Ag/AgCl. Current transients recorded during polarization of ZnO/TiO_2(N)/Au electrode (**3c(N)-Au**) (C) and ZnO/TiO_2(N) (**3c(N)**) (D) in dark and under illumination with visible light in aqueous the solution containing 5 mM Na_2SO_4 at constant potential of –0.25 V vs. Ag/AgCl.*

According to the literature, photodegradation of organic dyes, such as methylene blue (MB) or methyl orange (MO) at TiO_2 surface occurs mainly *via* highly active hydroxyl radicals formed in oxidation of H_2O or surface hydroxyl groups by photogenerated holes [423]. Moreover, a positive potential applied to the working electrode induces the transport of photo-excited electrons to the counter electrode via an external circuit, preventing the e^-/h^+ recombination [424,425]. Therefore, the photoelectrochemical degradation of these dyes is usually investigated in the positive potential range [426,427]. It has been also postulated that the electrons transferred to the counter electrode may be consumed in oxygen reduction to superoxide and then to hydroxyl radical which is further active in the degradation of dye at the metal electrode but not on semiconductor.

Since the results presented above indicate that the electrochemical reduction of oxygen at Au-decorated electrodes (***1c*-*Au***, ***3c(N)*-*Au***) is enhanced by visible light, we decided to verify if products of O_2 electroreduction may improve photoelectrochemical degradation of methylene blue in the range of negative potentials. At first it was necessary to examine the electrochemical behavior of methylene blue on ZnO/TiO_2 electrodes (***1c***) without Au nanoparticles. The cyclic voltammograms were recorded in the potential range from 0.8 V to –0.4 V *vs*. Ag/AgCl in dark and under visible light illumination in aqueous solution of 10 μM MB, containing 5 mM Na_2SO_4 as the supporting electrolyte. As visible in *Figure 98A*, a quasi-reversible redox behavior with cathodic peak at –0.27 V and its anodic counterpart at –0.18 V is observed in dark, which may be ascribed to reduction of MB to semi-reduced radical $MB^{\bullet-}$ [428] and its reoxidation back to MB. The intensity of the reduction peak increased only slightly under illumination with visible light. In the case of voltammograms performed on the Au-decorated electrode (***1c*-*Au***), the cathodic current related to catalytic oxygen reduction dominates and increases significantly under illumination of the sample with visible light. Thus, if this process leads to production of superoxide radicals and then in the consecutive reactions (71) and (72) to formation of $^{\bullet}OH$, the photoelectrocatalytic degradation of MB at the negative polarization potential should be improved. In order to verify this reasoning, the UV-vis spectra of the MB solution were recorded after every 15 min of electrolysis to determine the change in MB concentration. The measurements were carried out both for pristine (***1c***) and Au-decorated (***1c*-*Au***) electrodes (*Figures 98B-D*. The corresponding apparent rate constants of MB decolorization are summarized in Table 15.

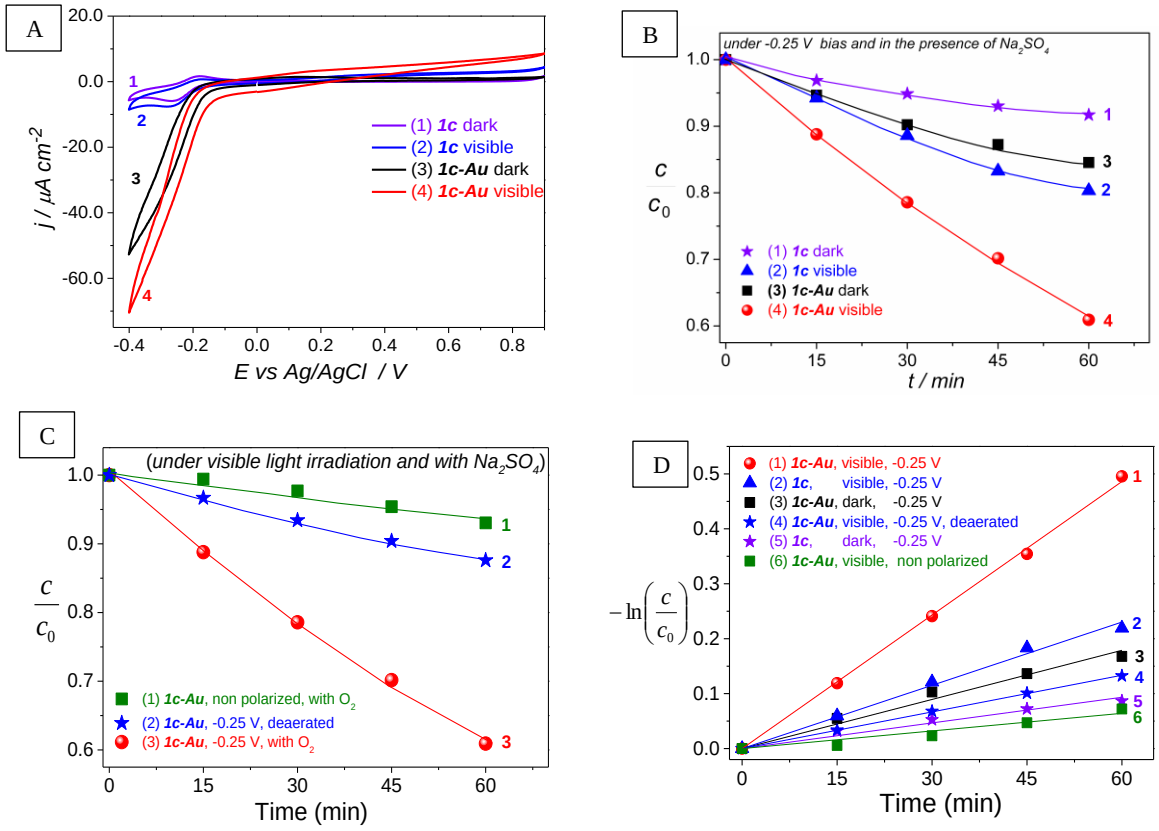

Figure 98 Cyclic voltammograms (A) and relative changes of MB concentration at constant potential of –0.25 V vs. Ag/AgCl (B) in dark and under visible light illumination for samples ***1c*** *(curves 1-dark and 2-vis) and* ***1c-Au*** *(curves 3-dark and 4-vis) in aqueous solution of 5 mM Na_2SO_4 containing 10 μM MB. (C) Influence of oxygen in the solution and application of external cathodic potential (–0.25 V vs. Ag/AgCl) on photoelectrocatalytic decolorization of MB with the use of ZnO/TiO_2/Au composite (**1c-Au**), and determination of* k_{vis}*-values of MB decolorization (D).*

Table 15 The apparent first-order rate constants for MB decolorization at –0.25 V in the presence of 5 mM Na_2SO_4.

Sample	k_{vis} ($\cdot 10^{-2}$ min^{-1})
1c (dark)	0.16
1c (visible)	0.38
1c-Au (dark)	0.30
1c-Au (visible)	0.81
1c-Au (visible) ***deaerated***	0.22
1c-Au (visible) ***non-polarized***	0.11

As visible in *Figure 98B*, polarization of the Au-free sample (***1c***) in dark at the potential of –0.25 V *vs.* Ag/AgCl corresponding to the reduction peak of MB to $MB^{\bullet-}$, results in a slight decolorization of MB. The relative decrease of MB concentration in the solution after 60 min of electrolysis was about 9%. According to the literature, the semi reduced $MB^{\bullet-}$ radical may undergo to disproportionation to MB and colorless *leuco*-methylene blue (LMB).

However, LMB is stable only in anaerobic conditions, while in the presence of oxygen it is regenerated back to MB. The results presented in *Figure 98B* and in Table 15 indicate that the illumination of ***1c*** sample accelerated MB decolorization, resulting in the increase of the rate constant from 0.16 $\cdot 10^{-2}$ min^{-1} to 0.38 $\cdot 10^{-2}$ min^{-1}. Much stronger changes were found when the same experiments were carried out with the use of the Au-decorated ITO/ZnO/TiO_2 electrode. The rate constant of MB decolorization raised from 0.38 $\cdot 10^{-2}$ min^{-1} for ***1c*** to 0.81 $\cdot 10^{-2}$ min^{-1} for ***1c-Au*** sample i.e. to the value higher than that obtained in the photocatalytic tests without polarization (see *Figure 98*).

In order to confirm the crucial role of oxygen reduction in photoelectrochemical degradation of MB, the control experiment was performed with the use of ***1c-Au*** under the same conditions but in deoxygenated solution. As visible in *Figure 98C* and in Table 15, the potential-assisted decolorization rate constant considerably decreased from 0.81 $\cdot 10^{-2}$ min^{-1} in the presence of oxygen to 0.22 $\cdot 10^{-2}$ min^{-1} in deaerated solution. Thus, it is evident that the active oxygen species formed in process of oxygen electroreduction on Au-decorated composites participate in photocatalytic decolorization of MB.

The presence of supporting electrolyte (Na_2SO_4), added to provide a sufficient conductivity of the solution allowed us to observe an unexpected effect of cathodic polarization on the rate of MB decomposition. Indeed, according to the literature, inorganic anions such as SO_4^{2-}, NO_3^-, $H_2PO_4^-$ inhibit the photocatalytic activity of TiO_2 in MB degradation [366,367]. Our experiments show that this negative effect can be strongly attenuated by polarizing ***1c-Au*** composite at –0.25 V (*Figure 98C* and Table 15). We notice that the apparent first-order rate constant of MB decolorization in the presence of Na_2SO_4 increases dramatically when polarization is applied (from 0.11 $\cdot 10^{-2}$ min^{-1} to 0.81 $\cdot 10^{-2}$ min^{-1}). Cathodic polarization of ***1c-Au*** allows thus to suppress the inhibition effect of Na_2SO_4 on the photocatalytic activity of the composite.

It is worth noting that under used conditions MB is not only decolorized but also mineralized, as follows from TOC analysis after illumination for 60 min. The increase of the activity of ***1c-Au*** in the presence on Na_2SO_4 through application of negative bias is probably due to a higher concentration of active species produced from oxygen electrocatalytic reduction on Au^0 nanoparticles. It is not clear if such enhancement can be observed for other dyes and other inorganic salts. The future study involving different substrates would allow to answer this question.

4.4.7. Conclusions

In this chapter it was found that the visible light response of ZnO(core)/TiO_2(shell) composites can be considerably improved through N-doping of TiO_2 shell and its decoration with Au^0 nanoparticles. Both promoters were introduced through simple procedures under mild conditions. N-doping was achieved by precipitation of amorphous titanium precursor in the presence of NH_4Cl. The gold nanoparticles of the size 7 nm – 25 nm were grown by photodeposition for 20 s from $[AuCl_{4-x}(OH)_x]^-$ precursor solution (pH ~ 6.7). Thus obtained nitrogen- and gold-promoted composites showed a significantly higher photocatalytic activity in comparison with that of the non-promoted materials in different test reactions realized under Xe lamp illumination with a 400 nm cut-off filter. It was found that plasmonic effect in Au-decorated ZnO/TiO_2 composite increased the rate of MB decolorization by 60% in comparison with the non-promoted sample. Moreover, due to the presence of Au NPs, a three-fold increase of photocurrent in photoassisted water oxidation was achieved under potential of 0.8 V *vs.* Ag/AgCl.

We also found that the presence of gold in the composite provokes appearance of cathodic current which was shown to originate from the reduction of dissolved O_2. The active species produced by this reaction allow to gain a significant increase of the rate of MB decolorization in the presence of dissolved inorganic salt (Na_2SO_4). The rate at the Au^0-promoted ZnO/TiO_2 core/shell composite polarized at –0.25 V *vs.* Ag/AgCl was found to be seven times higher than that on the same composite but without applied potential. This finding might be important for practical application of the elaborated composites for purification of waste water which usually contain considerable amounts of inorganic salts.

5. General conclusions and perspectives

The particulars results obtained in the present thesis were summarized in the corresponding chapters of the *Results and Discussion* part. The aim of this section is to put our particular findings for ZnO/TiO_2 core/shell composites in a more general context in order to see if they can be useful for other types of nanostructured composites used in the field of heterogeneous photocatalysis.

High potential of wet chemical synthetic methods. Our study showed that simple and easily scalable chemical approaches can be successfully employed to construct rather complex nanostructured systems. Indeed the ZnO nanorods of variable morphology were successfully grown on the seed layer prepared by electrochemical deposition from aqueous solution. The sol-gel method, used to deposit TiO_2 layer, is well established and scalable technique. Despite its simplicity it allowed to obtain the layers of very different microstructure by varying the duration of deposition and number of cycles. Moreover, the same approach made possible N-doping of TiO_2 under similar reaction conditions by adding ammonium salt in the reaction solution. Another important fact to underline is the similarity of the photocatalytic activities of the composites obtained by ALD and CVD and those of the materials prepared by sol-gel approach. This fact shows that wet chemical methods can successfully compete with the complex physical approaches in production of highly active photocatalysts.

Key role of the interface. The results obtained in this thesis clearly show that the interface between the components of composite plays a crucial role in their photocatalytic behavior. In general the performance of composites in photocatalysis is analyzed in terms of electron and hole transfer between two (or more) components having different band structures. Our results show that this analysis should be completed by taking into account the microstructure of the components and of the interface between them. Indeed using the same oxides (ZnO and TiO_2) we were able to construct the composites with considerably different photocatalytic activities by varying two parameters. First, we increased the porosity of the anatase layer and by this we improved the accessibility of the interface. Second, we changed the interface structure through the outward Zn^{2+} diffusion into TiO_2 layer upon additional calcination (the Kirkendall effect). Application of these approaches allowed to improve significantly the activity of the composites in MB degradation and in photoassisted water oxidation. These findings

show that the accessibility of the interface and its microstructure are of crucial importance for the performance of composites and these parameters should therefore be taken into account when developing new materials.

Extension of light absorption into visible range. A serious drawback of ZnO and TiO_2 is the large band gap allowing utilization of the light only with wavelength below 400 nm. One of the major results of our work is the observation of optical absorption at higher wavelength attributed to formation of midgap states at the ZnO/TiO_2 interface. It is worth noting that this unexpected effect has not been systematically observed in ZnO/TiO_2 composites described in literature indicating that its origin must depend on the used preparation method. Even if the exact nature of the midgap states is not known, some observations allowed us to correlate their appearance with the presence of structural defects. In order to further increase the visible light response of our composites, the N-doping of TiO_2 layer was combined with decoration by Au nanoparticles. This approach, well documented for pure TiO_2, has been shown for the first time to be efficient as well for ZnO/TiO_2 composites bringing a significant increase of activity in photoassisted water oxidation under visible light.

Application of external potential. The use of Au-decorated composites permitted us to observe another important effect: small cathodic polarization of material considerably increased the rate of MB degradation in the presence of mineral salts. This effect was shown to be due to increase of production of active species by reduction of dissolved oxygen. Given that waste water subjected to photocatalytic depollution always contains mineral salts, the observed enhancement might be very helpful in development of novel advanced water purification techniques.

The **perspectives** of the present work are related to the aspects described above. Regarding the preparation method, it would be interesting to see if the composites prepared by sol-gel method but having a simple structure (i.e. ZnO/TiO_2 bilayer) possess the high activity found in our materials. This question is important in the context of water purification in which conducting composites are not needed and simpler configuration may be applied. The appearance of optical absorption above 400 nm in our composites is another point worth further investigation. Better understanding of the nature of the formed mid gap states at ZnO/TiO_2 interface would be highly desirable in order to further increase their concentration. The investigation of N-doped and Au-

decorated composites deserves also further development. First of all, other methods of N-doping and Au deposition should be evaluated. Second, composite configurations, e.g. ZnO/Au/N-TiO_2, can be prepared and characterized. Third, the generality of the observed photoelectrocatalytic activity of these samples worth being studied by substrates other than MB, for example phenol and its derivatives.

The results presented in this dissertation could be considered also in a broader context. The knowledge of correlation between synthesis-morphology-properties observed for our ZnO/TiO_2 composites may transferable to other metal oxide composites, may be useful in elaboration of novel visible light-driven photocatalysts.

Appendix 1

List of Selected Conferences

- 9th European Meeting on Solar Chemistry and Photocatalysis: Environmental Applications (SPEA 9), June 2016, Strasbourg (France) – poster presentation (**Award for the Best Presentation)**
- European Materials Research Society (E-MRS) Fall Meeting Scientific/Technical Symposia & Exhibition, Warsaw (Poland) – oral presentation (2014) and poster (2015)
- 17th International French-Polish Seminar on Reactivity of Solids, June-July 2015, Dijon (France) – oral presentation
- 65th Annual Meeting of the International Society of Electrochemistry (ISE), September 2014, Lausanne (Switzerland) – poster presentation
- 2nd Symposium on Progress in Research and Application of Photocatalysts based on TiO_2, July 2014, Szczecin (Poland) – oral presentation
- "From MPD to KNOW" Conference, September 2013, Rawa Mazowiecka (Poland) – poster presentation (**Award for the Best Presentation**)
- 7th Copernican Seminars, June 2013, Toruń (Poland) – oral presentation

Scientific and Industrial experience

- 2016-2013 Main executor of a **Grant Project** funded by National Science Centre - governmental agency (Poland) Title: "*Development and studies of solid state photocatalytic systems based on doped metal-oxide nanostructures with adsorbed semiconductor/noble metal nanoparticles*" DEC 2012/07/B/ST5/02431, Project director: prof Magdalena Skompska
- 2013 Research assistant at the Institute of Material Research and Engineering (**IMRE – A*STAR**), Singapore, Singapore (3 months)
- 2009 Laboratory assistant in the quality control laboratory at **CTS TCT** Company Group (Polish-French industrial company producing plastic composites and chemical products) Sochaczew, Poland (internship)

6. References

[1] N.S. Lewis, *Research opportunities to advance solar energy utilization*, Science 351 (2016) 1920–1(9).

[2] M.G. Walter, E.L. Warren, J.R. McKone, S.W. Boettcher, Q. Mi, E.A. Santori, N.S. Lewis, *Solar water splitting cells*, Chem. Rev. 110 (2010) 6446–6473.

[3] J.R. McKone, N.S. Lewis, H.B. Gray, *Will solar-driven water-splitting devices see the light of day?*, Chem. Mater. 26 (2014) 407–414.

[4] H. Zhou, Y. Qu, T. Zeid, X. Duan, *Towards highly efficient photocatalysts using semiconductor nanoarchitectures*, Energy Environ. Sci. 5 (2012) 6732.

[5] G.V. Buxton, C.L. Greenstock, W.P. Helman, A.B. Ross, *Critical Review of rate constants for reactions of hydrated electrons, hydrogen atoms and hydroxyl radicals (·OH/·O− in Aqueous Solution*, J. Phys. Chem. Ref. Data 17 (1988) 513–535.

[6] M. Pelaez, N.T. Nolan, S.C. Pillai, M.K. Seery, P.Falaras, A.G. Kontos, P.S.M. Dunlop, J.W.J. Hamilton, J.A. Byrne, K. O'Shea, M.H. Entezari, D.D. Dionysiou, *A review on the visible light active titanium dioxide photocatalysts for environmental applications*, App. Catal. B Environ. 125 (2012) 331–349.

[7] S. Linic, P. Christopher, D.B. Ingram, *Plasmonic-metal nanostructures for efficient conversion of solar to chemical energy*, Nature Mat. 10 (2001) 911–921.

[8] S. Sakthivel, M.V. Shankar, M. Palanichamy, B. Arabindoo, D.W. Bahnemann,V. Murugesan, *Enhancement of photocatalytic activity by metal deposition: characterization and photonic efficiency of Pt, Au and Pd deposited on TiO_2 catalyst*, Water Res. 38 (2004) 3001–3008.

[9] P.V. Kamat, *Manipulation of Charge Transfer Across Semiconductor Interface. A Criterion That Cannot Be Ignored in Photocatalyst Design*, J. Phys. Chem. Lett. 3 (2012) 663–672.

[10] D. Robert, *Photosensitization of TiO_2 by M_xO_y and M_xS_y nanoparticles for heterogeneous photocatalysis applications*, Catal. Today 122 (2007) 20–26.

[11] C.X. Kronawitter, L. Vayssieres, S. Shen, L. Guo, D.A. Wheeler, J.Z. Zhang, B. R.Antoun, S.S. Mao, *A perspective on solar-driven water splitting with all-oxide hetero-nanostructures*, Energy Environ. Sci. 4 (2011) 3889–3899.

[12] F.E. Osterloh, *Inorganic nanostructures for photoelectrochemical and photocatalytic water splitting*, Chem. Soc. Rev. 42 (2013) 2294–2320.

[13] A. Janotti, C.G. Van de Walle, *Fundamentals of zinc oxide as a Semiconductor*, Rep. Prog. Phys. 72 (2009) 126501, 1–29.

[14] S.B. Zhang, S.-H. Wei, A. Zunger, *Intrinsic n-type versus p-type doping asymmetry and the defect physics of ZnO*, Phys. Rev. B 63 (2001) 075205 7pp.

[15] B.G. Yacobi, *Semiconductor Materials: an Introduction to Basic Principles*, Kluwer Academic/Plenum Publishers: New York, 2003.

[16] J.M. Coronado, F. Fresno, M.D. Hernández-Alonso, R. Portela, *Design of Advanced Photocatalytic Materials for Energy and Environmental Applications*, Springer, April 2013.

[17] H. Kisch, *Semiconductor Photocatalysis—Mechanistic and Synthetic Aspects*, Angew. Chem. Int. Ed. 52 (2013) 812–847.

[18] S. Schiavello, *Photoelectrochemistry, photocatalysis and photoreactors*, D. Reidel publishing Company, Dordrecht, (1984).

[19] M.R. Hoffmann, S.T. Martin, W. Choi, D.W. Bahnemann, *Environmental Applications of Semiconductor Photocatalysis*, Chem. Rev. 95 (1995) 69–96.

[20] J. Schneider, M. Matsuoka, M. Takeuchi, J. Zhang, Y. Horiuchi, M. Anpo, D.W. Bahnemann, *Understanding TiO_2 Photocatalysis: Mechanisms and Materials*, Chem. Rev. 114 (2014) 9919−9986.

[21] T. Ohno, K. Sarukawa, M. Matsumura, *Photocatalytic activities of pure rutile particles isolated from TiO_2 powder by dissolving the anatase component in HF solution*, J. Phys. Chem. B 105 (2001) 2417–2420.

[22] S. Selçuk, A. Selloni, *Surface Structure and Reactivity of Anatase TiO_2 Crystals with Dominant {001} Facets*, J. Phys. Chem. C 117 (2013) 6358−6362.

[23] B.D. Sosnowchik, H.C. Chiamori, Y. Ding, J.-Y. Ha, Z.L. Wang, L. Lin, *Titanium dioxide nanoswords with highly reactive, photocatalytic facets*, Nanotechnology 21 (2010) 485601, 1–6.

[24] T. Tachikawa, N. Wang, S. Yamashita, S.-C. Cui, T. Majima, *Design of a highly sensitive fluorescent probe for interfacial electron transfer on a TiO_2 surface*, Angew. Chem. Int. Ed. 49 (2010) 8593–8597.

[25] N. Wu, J. Wang, D.N. Tafen, H. Wang, J.-G. Zheng, J.P. Lewis, X. Liu, S.S. Leonard, A. Manivannan, *Shape-enhanced photocatalytic activity of single-crystalline anatase TiO_2(101) nanobelts*, J. Am. Chem. Soc. 132 (2010) 6679–6685.

[26] Y.-F. Li, Z.-P. Liu, *Particle size, shape and activity for photocatalysis on titania anatase nanoparticles in aqueous surroundings*, J. Am. Chem. Soc. 133 (2011) 15743–15752.

[27] N. Roy, Y. Sohn, D. Pradhan, *Synergy of Low-Energy {101} and High-Energy {001} TiO_2 Crystal Facets for Enhanced Photocatalysis*, ACS Nano 7 (2013) 2532 – 2540.

[28] G. Zhao, H. Kozuka, H. Lin, T. Yoko, *Sol-gel preparation of $Ti_{1-x}V_xO_2$ solid solution film electrodes with conspicuous photoresponse in the visible region*, Thin Solid Films 339 (1999) 123–128.

[29] D. Vollath, *Nanoparticles – Nanocomposites – Nanomaterials, An Introduciton for Beginners* (2013) Wiley-VCH, Weinheim, Germany

[30] B.O. Aduda, P. Ravirajan, K.L. Choy, J. Nelson, *Effect of morphology on electron drift mobility in porous TiO_2*, Int. J. Photoenergy 6 (2004) 141–147.

[31] M.L. Hitchman, F. Tian, *Studies of TiO_2 thin films prepared by chemical vapour deposition for photocatalytic and photoelectrocatalytic degradation of 4-chlorophenol*, J. Electroanal. Chem. 538–539 (2002) 165–172.

[32] D.M. Eagles, *Polar modes of lattice vibration and polaron coupling constants in rutile*, Phys. Chem. Solids 25 (1964) 1243–1251.

[33] F. Möllers, H.J. Tolle, and R. Memming, *On the Origin of the Photocatalytic Deposition of Noble Metals on TiO_2*, J. Electrochem. Soc. 121(9) (1974) 1160–1167.

[34] J. Tauc, *Absorption edge and internal electric fields in amorphous semiconductors*, Mater. Res. Bull. 5 (1970) 721–729.

[35] J. Tauc, R. Grigorovivi, A. Vancu, *Optical properties and electronic structure of amorphous germanium*, J. Phys. Soc. Jpn. 21 (1966) 123–126

[36] J.I. Pankove, *Optical Processes in Semiconductors*, Prentience-Hall Inc., Englewood Cliffs, NJ. 1971.

[37] P.K. Gattu, K. Ghule, A.A. Kashale, V.B. Patil, D.M. Phase, R.S. Mane, S.H. Han, R. Sharma, A.V. Ghule, *Bio-green synthesis of Ni-doped tin oxide nanoparticles and its influence on gas sensing properties*, RSC Adv. 5 (2015) 72849.

[38] M. Studenyak, M. Kranjčec, M. Kurik, *Urbach Rule in Solid State Physics*, Int. J. Opt. Appl. 4(3) (2014) 76–83.

[39] R.C. Rai, *Analysis of the Urbach tails in absorption spectra of undoped ZnO thin films*, J. Appl. Phys. 113 (2013) 153508.

[40] R.A. Marcus, *Electron transfer reactions in chemistry: theory and experiment*, Angew. Chem. Int. Ed. Engl. 32 (1993) 1111–1121.

[41] H. Gerischer, *Charge transfer processes at semiconductor-electrolyte interfaces in connection with problem of catalysis*, Surf. Sci. 18 (1969) 97–122.

[42] D. Vanmaekelbergh, *Electron Transfer in Chemistry* (ed. V. Balzani), Wiley-VCH Verlag GmbH, Weinheim, 126–188, 2001.

[43] H. Gerischer, *Fundamentals of Semiconductor Electrochemistry, in Photovoltaic and Photoelectrochemical Solar Energy Conversion*, Eds. F. Cardon, W. P. Gomes, W. Dekeyser, Olenum Press, New York and London (1981).

[44] H. Gerischer, *Solar photoelectrolysis with semiconductor electrodes*, Top. Appl. Phys. 31 (1979) 115–172.

[45] M. Sharon, *The Photoelectrochemistry of Semiconductor/Electrolyte Solar Cells in Encyclopedia of Electrochemistry*, vol 6, *Semiconductor Electrodes and Photoelectrochemistry*, Eds. A.J. Bard, M. Stratmann, D. Licht, Wiley 2002.

[46] S.R. Morrison, *Electrochemistry as Semiconductor and Oxidized Metal Electrodes*, Plenum Press, New York, 1980.

[47] S.R. Memming, *Semiconductor Electrochemistry*, Wiley-VCH Verlag Gmbh, Weinheim 2001.

[48] B. Ohtani, *Photocatalysis A to Z—What we know and what we do not know in a scientific sense*, J Photochem Photobiol C: Photochemi Rev. 11 (2010) 157–178.

[49] N. Philippidis, E. Nikolakaki, S. Sotiropoulos, I. Poulios, *Photoelectrocatalytic inactivation of E. coli XL-1 blue colonies in water*, J. Chem. Technol. Biotechnol. 85 (2010) 1054–1060.

[50] K. Rajeshwar, *Fundamentals of Semiconductor Electrochemistry and Photoelectrochemistry, in Encyclopedia of Electrochemistry*, vol 6, *Semiconductor Electrodes and Photoelectrochemistry*, Eds. A.J. Bard, M. Stratmann, D. Licht, Wiley 2002.

[51] W.W. Gärtner, *Depletion-Layer Photoeffects in Semiconductors*, Phys. Rev. 116 (1959) 84.

[52] G. Rothenberger, D. Fitzmaurice, M. Gräetzel, *Spectroscopy of conduction band electrons in transparent metal oxide semiconductor films: optical determination of the flatband potential of colloidal titanium dioxide films*, J. Phys. Chem. 96 (1992) 5983–5986.

[53] A. Hagfeldt, M. Gräetzel, *Light-induced redox reactions in nanocrystallie systems*, Chem. Rev. (Washington) 95 (1995) 49–68.

[54] G. Hodes, I.D.J. Howell, L.M. Peter, *Nanocrystalline photoelectrochemical cells. A new concept in photovoltaic cells*, J. Electrochem. Soc. 139 (1992) 3136–3140.

[55] R. Solarska, I. Rutkowska, R. Morand, J. Augustyński, *Photoanodic reactions occuring at nanostructured titanium dioxide films*, Electrochim. Acta 51 (2006) 2230–2236.

[56] D. Monllor-Satoca, R. Gomez, *A photoelectrochemical and spectroscopic study of phenol and catechol oxidation on titanium dioxide nanoporous electrodes*, Electrochim. Acta 55 (2010) 4661–4668.

[57] L.M. Peter, *Energetics and kinetics of light-driven oxygen evolution at semiconductor electrodes: the example of hematite*, J. Solid State Electrochem. 17 (2013) 315–326.

[58] H.K. Dunn, J.M. Feckl, A. Müller, D. Fattakhova-Rohlfing, S.G. Morehead, J. Roos, L.M. Peter, C. Scheua, T. Bein, *Tin doping speeds up hole transfer during light-driven water oxidation at hematite photoanodes*, Phys.Chem.Chem.Phys. 16 (2014) 24610.

[59] R. Zhang, L. Gao, Q. Zhang, *Photodegradation of surfactants on the nanosized TiO_2 prepared by hydrolysis of the alkoxide titanium*, Chemosphere 54 (2004) 405–411.

[60] T. Berger, D. Monllor-Satoca, M. Jankulovska, T. Lana-Villarreal, R. Gomez, *The Electrochemistry of Nanostructured Titanium Dioxide Electrodes*, ChemPhysChem 13 (2012) 2824–2875.

[61] A. Ikram, S. Sahai, S. Rai, S. Dass, R. Shrivastav, V.R. Satsangi, *Improved charge transportation at PbS QDs/TiO_2 interface for efficient PEC hydrogen generation*, Phys.Chem.Chem.Phys. 18 (2016) 15815.

[62] M. Quintana, T. Edvinsson, A. Hagfeldt, G. Boschloo, *Comparison of Dye-Sensitized ZnO and TiO_2 Solar Cells: Studies of Charge Transport and Carrier Lifetime*, J. Phys. Chem. C 11 (2007) 1035–1041.

[63] A. Zaban, M. Greenshtein, J. Bisquert, *Determination of the electron lifetime in nanocrystalline dye solar cells by photovoltage decay measurements*, J. Chem. Phys. Chem. 4 (2003) 859–864.

[64] T. Ohnishi, Y. Nakato, H. Tsubomura, *Quantum yield of photolysis of water on titanium dioxide electrodes*, Ber. Bunsen. Ges. 79 (1975) 523–525.

[65] T. Bąk, J. Nowotny, M. Rękas, C.C. Sorrell, *Photo-electrochemical hydrogen generation from water using solar energy. Materials-related aspects*, Int. J. Hydro. Ener. 27 (2002) 991–1022.

[66] A. Nanthakumar, N.R. Amstrong, I. Finklea HO, editor. *Semiconductor electrodes*, Amsterdam: Elsevier (1988) 203–240.

[67] G.G. Bessegato, T.T. Guaraldo, M. Valnice, B. Zanoni, Chapter 10: *Enhancement of Photoelectrocatalysis Efficiency by Using Nanostructured Electrodes, Nanotechnology and Nanomaterials "Modern Electrochemical Methods in Nano, Surface and Corrosion Science"*, book edited by Mahmood Aliofkhazraei, ISBN 978-953-51-1586-1, 2014.

[68] The UV/Oxidation Handbook, Solarchem Environmental Systems Copyright 1994, Chaper 1

[69] H. Kisch, *Semiconductor Photocatalysis—Mechanistic and Synthetic Aspects,* Angew. Chem. Int. Ed. 52 (2013) 812–847.

[70] S. Banerjee, J. Gopal, P. Muraleedharan, A.K. Tyagi, B. Raj, *Physics and chemistry of photocatalytic titanium dioxide: Visualization of bactericidal activity using atomic force microscopy*, Current Sci, 90/10 (2006) 1378 – 1383.

[71] J.-M. Herrmann, *Heterogenous photocatalysis: fundamentals and applications to the removal of various types of aqueous pollutants*, Catal. Today 53 (1999) 115 – 129.

[72] D.M. Blake, P.C. Maness, Z. Huang, E.J. Wolfrum, J. Huang, W.A. Jacoby, *Application of the photocatalytic chemistry of titanium dioxide to disinfection and the killing of cancer cells,* Sep. Purif. Methods 28 (1999) 1–50.

[73] Y. Nosaka, T. Daimon, A.Y. Nosaka, Y. Murakami, *Singlet oxygen formation in photocatalytic TiO_2 aqueous suspension*, Phys. Chem. Chem. Phys. 6 (2004) 2917–2918.

[74] T.A. Konovalova, J. Lawrence, L.D. Kispert, *Generation of superoxide anion and most likely singlet oxygen in irradiated TiO_2 nanoparticles modified by carotenoids*, J. Photochem. Photobiol. A 162 (2004) 1–8.

[75] A.J. Bard, R. Parsons, J. Jordan, *Standard Potentials in Aqueous Solution*, Marcel Dekker, New York 1985.

[76] H. Tang, K. Prasad, R. Sanjincs, P.E. Schmid, F. Levy, *Electrical and optical properties of TiO_2 anatase thin films,* J. Appl. Phys. 75 (1994) 2042.

[77] B. Enright, G. Redmond, D. Fitzmaurice, *Spectroscopic determination of flatband potentials for polycrystalline TiO_2 electrodes in mixed solvents systems*, J. Phys. Chem. 98 (1994) 6195–6200.

[78] J. Cunningham, G. Al-Sayyed, S. Srijaranai, *Adsorption of model pollutants onto TiO_2 particles in relation to photoremediation of contaminated water*, in: G.R. Helz, R.G. Zepp, D.G. Crosby (Eds.), *Aquatic and Surface Photochemistry*, Lewis, Boca Raton (1994) p. 317.

[79] H. Gerischer, A. Heller, *The role of oxygen in photooxidation of organic molecule on semiconductor particles*, J. Phys. Chem. 95 (1991) 5261–5267.

[80] G. Horner , P. Johne, R. Kunneth, G. Twardzik, H. Roth, T. Clark, H. Kisch, *Semiconductor Type A Photocatalysis: Role of Substrate Adsorption and the Nature of Photoreactive Surface Sites in Zinc Sulfide Catalyzed C–C Coupling Reactions*, Chem Eur. J. 5 (1999) 208–217.

[81] E.J. Ruiz, C. Arias, E. Brillas, A. Hernández-Ramírez, J.M. Peralta-Hernández, *Mineralization of Acid Yellow 36 azo dye by electro-Fenton and solarphotoelectro-Fenton processes with a boron-doped diamond anode*, Chemosphere 82 (2011) 495–501.

[82] S.S. Shinde, C.H. Bhosale, K.Y. Rajpure, *Hydroxyl radical's role in the remediation of wastewater*, J. Photochem. Photobio. B: Biol. 116 (2012) 66–74.

[83] T. Fang, L. Liao, X. Xu, J. Peng, Y. Jing, *Removal of COD and color in real pharmaceutical wastewater by photoelectrocatalytic oxidation method*, Environ. Technol. 34 (2013) 779–786.

[84] X. Zhou, Y. Zheng, J. Zhou, S. Zhou, *Degradation kinetics of photoelectrocatalysis on landfill leachate using codoped TiO_2 Tiphotoelectrodes*, J. Nanomater. (2015), ID 810579, 11p.

[85] T. Fang, L. Liao, X. Xu, J. Peng, Y. Jing, *Removal of COD and colour in real pharmaceutical wastewater by photoelectrocatalytic oxidation method*, Environ. Technol. 34 (2013) 779–786.

[86] J.C. Cardoso, G.C. Bessegato, M.V.B. Zanoni, *Efficiency comparison ofozonation photolysis, photocatalysis and photoelectrocatalysis methods inreal textile wastewater decolorization*, Water Res. 98 (2016) 39–46.

[87] ISO 10678:2010(E), *Fine ceramics (advanced ceramics, advanced technical ceramics) — Determination of photocatalytic activity of surfaces in an aqueous medium by degradation of methylene blue* (2010)

[88] A. Mills, *An overview of the methylene blue ISO test for assessing the activities of photocatalytic films,* Appl. Catal. B: Environ. 128 (2012) 144–149.

[89] A. Mills, H. Claire, P.K.J. Robertson, *Overview of the current ISO tests for photocatalytic materials*, J. Photochem. Photobiol. A: Chemistry 237 (2012) 7–23.

[90] A. Mills, J. Wang, *Photobleaching of methylene blue sensitized by TiO_2: an ambiguous system?* J. Photochem. Photobiol. A: Chem. 127 (1999) 123–134.

[91] D. Melgoza, A. Hernandez-Ramırez, J.M. Peralta-Hernandez, *Comparative efficiencies of the decolourisation of Methylene Blue using Fenton's and photo-Fenton's reactions*, Photochem. Photobiol. Sci. 8 (2009) 596 – 599.

[92] K. Patil, R. Pawar, P. Talap, *Self-aggregation of Methylene Blue in aqueous medium and aqueous solutions of Bu4NBr and urea*, Phys. Chem. Chem. Phys. 2 (2000) 4313–4317.

[93] C.A.K. Gouvêa, F. Wypych, S.G. Moraes, N. Durán, N. Nagata, P. Peralta-Zamora, *Semiconductor-assisted photocatalytic degradation of reactive dyes in aqueous solution*, Chemosphere, 40 (2000) 433–440.

[94] H. Park, Y. Park, W. Kim, W. Choi, *Surface modification of TiO_2 photocatalyst for environmental applications*, J. Photochem. Photobiol. C: Photochem. Rev. 15 (2013) 1–20.

[95] T.J. Jacobsson, T. Edvinsson, *Photoelectrochemical Determination of the Absolute Band Edge Positions as a Function of Particle Size for ZnO Quantum Dots*, J. Phys. Chem. C 16 (2012) 15692−15701.

[96] X. Zhou, Y. Zheng, J. Zhou, S. Zhou, *Degradation Kinetics of Photoelectrocatalysis on Landfill Leachate Using Codoped TiO_2/Ti Photoelectrodes*, J. Nanomater. (2015) 11pp.

[97] A. Houas, H. Lachheb, M. Ksibi, E. Elaloui, C.Guillard, J.-M. Herrmann, *Photocatalytic degradation pathway of methylene blue in water*, Appl. Catal. B: Environ. 31 (2001) 145–157.

[98] D.C. Reynolds, D.C. Look, B. Jogai, *Optically pumped ultraviolet lasing from ZnO*, Solid State Commun. 12 (1996) 873–875.

[99] A. Mang, K. Reimann, S. Rübenacke, *Band gaps, crystal-field splitting, spin-orbit coupling, and exciton binding energies in ZnO under hydrostatic pressure*, Solid State Commun. 94 (1995) 251–254.

[100] S.F. Chichibu, T. Onuma, M. Kubota, A. Uedono. Sota. Tsukazaki, A. Ohtomo, M. Kawasaki, *Improvements in quantum efficiency of excitonic emissions in ZnO epilayers by the elimination of point defects*, J. Appl. Phys. 99 (2006) 093505.

[101] D.M. Bagnall, Y.F. Chen, Z. Zhu, T. Yao, S. Koyama, M.Y. Shen, T. Goto, *Optically pumped lasing of ZnO at room temperature*, Appl. Phys. Lett. 70 (1997) 2230–2232.

[102] J.D. Albrecht, P.P. Ruden, S. Limpijumnong, W.R. L. Lambrecht, K.F. Brennan, *High field transport properties of bulk ZnO*, J. Appl. Phys. 86 (1999) 6864.

[103] T.P. Chou, Q. F. Zhang, G. E. Fryxell, G. Z. Cao, *Hierarchically Structured ZnO Film for Dye-Sensitized Solar Cells with Enhanced Energy Conversion Efficiency*, Adv. Mater. 19 (2007) 2588–2592.

[104] I. Gonzalez-Valls, M. Lira-Cantu, *Vertically-aligned nanostructures of ZnO for excitonic solar cells: a review*, Energy Environ. Sci. 2 (2009) 19–34.

[105] Y. Liu, C.R. Gorla, S. Liang, N. Emanetoglu, Y. Lu, H. Shen, M. Wraback, *Ultraviolet detectors based on epitaxial ZnO films grown by MOCVD*, J. Electron. Mater. 29 (2000) 69.

[106] J. Song, S. Baek, S.L. *Effect of hydrothermal reaction conditions on the optical properties of ZnO nanorods*, Physica B 403 (2008) 1960–1963.

[107] M. Skompska, K. Zarębska, *Electrodeposition of ZnO Nanorod Arrays on Transparent Conducting Substrates–a Review*, Electrochim. Acta 127 (2014) 467–488.

[108] T. Yasuda, Y. Obata, M. Sato, *Epitaxial Growth of ZnO by Sol-Gel Method*, J. Kor. Phys. Soc. 53(5) (2008) 2921–2924.

[109] T. Maruo, N. Ueno, S. Ichikawa, N. Nishiyama, Y. Egashira, K. Ueyama, *Transmission electron microscopy study on the growth of zinc oxide crystals under hydrothermal conditions*, Mater. Lett. 63 (2009) 2373–2376.

[110] M. Lannoo, J. Bourgoin, *Point Defects in Semiconductors I: Theoretical Aspects* (Berlin: Springer, 1981), and M. Lannoo, J. Bourgoin, *Point Defects in Semiconductors II: Experimental Aspects* (Berlin: Springer (1983).

[111] S.T. Pantelides, *Deep Centers in Semiconductors: A State-of-the-Art Approach*, 2nd ed. (Yverdon: Gordon and Breach (1992).

[112] J. Han, P.Q. Mantas, A.M.R. Senos, *Defect chemistry and electrical characteristics of undoped and Mn-doped ZnO*, J. Eur. Ceram. Soc. 22 (2002) 49.

[113] Ü. Özgür, Y.I. Alivov, C. Liu, A. Teke, M.A. Reshchikov, S. Doğan, V. Avrutin, S.-J. Cho, H. Morkoç, *A comprehensive review of ZnO materials and devices*, J. Appl. Phys. 98 (2005) 041301.

[114] E.N. Epie, W.K. Chu, *Ionoluminescence study of Zn−and O−implanted ZnO crystals:An additional perspective*, Appl. Surf. Sci. 371 (2016) 28–34.

[115] J. Xua, Q. Panb, Y. Shuna, Z. Tian, *Grain size control and gas sensing properties of ZnO gas sensor* Sens. Actuators B: Chem. 66 (2000) 277–279.

[116] Q. Wan, C.L. Lin, X.B. Yu, T.H. Wang, *Room-temperature hydrogen storage characteristics of ZnO nanowires*, Appl. Phys. Lett. 84 (2004) 1.

[117] M.H. Koch, P.Y. Timbrel1, R.N. Lamb, *The influence of film crystallinity on I the coupling efficiency of ZnO optical modulator waveguides*, Semicond. Sci. Technoi. 10 (1995) 1523–1527.

[118] Q. Zhang, T.P. Chou, B. Russo, S.A. Jenekhe, G. Cao, *Polydisperse Aggregates of ZnO Nanocrystallites: A Method for Energy-Conversion-Efficiency Enhancement in Dye-Sensitized Solar Cells*, Adv. Func. Mater. 18 (2008) 1654–1660.

[119] W.S. Chiua, P.S. Khiewa, M. Clokea, D. Isaa, T.K. Tana, S. Radimanb, R. Abd-Shukorb, M.A. Abd. Hamidb, N.M. Huangc, H.N. Limd, C.H. Chia, *Photocatalytic study of two dimensional ZnO nanopellets in the decomposition of methylene blue*, Chem. Eng. J. 158 (2010) 345–352.

[120] A.J. Hoffman, G. Mills, H. Yee, M.R. Hoffmann, *Q-sized cadmium sulfide: synthesis, characterization, and efficiency of photoinitiation of polymerization of several vinylic monomers*, J. Phys. Chem. 96 (1992) 5546–5552.

[121] B. Kraeutler, C.D. Jaeger, A.J. Bard, *Direct observation of radical intermediates in the photo-Kolbe reaction - heterogeneous photocatalytic radical formation by electron spin resonance*, J. Am. Chem. Soc. 100 (1978) 4903–4905.

[122] T.G. Smijs, S. Pavel, *Titanium dioxide and zinc oxide nanoparticles in sunscreens: focus on their safety and effectiveness*, Nanotechnology, Science and Applications 4 (2011) 95–112.

[123] A.B. Djurišić, A.M.C. Ng, X.Y. Chen, *ZnO nanostructures for optoelectronics: Material properties and device applications*, Progress in Quantum Electronics 34 (2010) 191–259.

[124] J.C. Fan, S.L. Chang, Z. Xie, *ZnO-Based Light-Emitting Diodes Optoelectronics - Advanced Materials and Devices*, Chaper 2, Edited by S.L. Pyshkin, J.M. Ballato, 494 pages, InTech (2013)

[125] D. Vanmaekelbergh, K. Lambert van Vugt, *ZnO nanowire lasers*, Nanoscale 3 (2011) 2783.

[126] T. Luttrell, S. Halpegamage, J. Tao, A. Kramer, E. Sutter, M. Batzill, *Why is anatase a better photocatalyst than rutile? - Model studies on epitaxial TiO_2 films* Sci. Rep. 4 (2014) 4043.

[127] P.J. Huang, H. Chang, C.T. Yeh, C.W. Tsai, *Phase transformation of TiO_2 monitored by Thermo-Raman spectroscopy with TGA/DTA*, Termochim. Acta 297 (1997) 85–92.

[128] W.H. Leng, Z. Zhang, J.Q. Zhang, *Photoelectrocatalytic degradation of anilineover rutile TiO_2/Ti electrode thermally formed at 600 ◦C*, J. Mol. Catal. A: Chem. 206 (2003) 239–252.

[129] P.I. Gouma, M.J. Mills, *Anatase-to-Rutile Transformation in Titania Powders*, J. Am. Ceram. Soc. 84 (2001) 619–622.

[130] T.R. Gordon, M. Cargnello, T. Paik, F. Mangolini, R.T. Weber, P. Fornasiero, C.B. Murray *Nonaqueous Synthesis of TiO_2 Nanocrystals Using TiF4 to Engineer Morphology, Oxygen Vacancy Concentration, and Photocatalytic Activity* J. Am. Chem. Soc. 134 (2012) 6751−6761.

[131] A. Di Paola, M. Bellardita, L. Palmisano, *Brookite, the least known TiO_2 photocatalyst*, Catalysts 3 (2013) 36–73.

[132] T. Luttrell, S. Halpegamage, J. Tao, A. Kramer, E. Sutter, M. Batzill, W*hy isanatase a better photocatalyst than rutile? −Model studies on epitaxial TiO_2 films*, Sci. Rep. 4 (2015) 4043–4050.

[133] S. Sakthivel, H. Kisch, *Photocatalytic and Photoelectrochemical Properties of Nitrogen-Doped Titanium Dioxide*, Chem. Phys. Chem. 4 (2003) 487–490.

[134] B.P. Uberuaga, X.-M. Bai, *Defects in rutile and anatase polymorphs of TiO_2: kinetics and thermodynamics near grain boundaries*, J. Phys.: Condens. Matter 23 (2011) 435004 (11pp).

[135] A.H. Yuwono, B.H. Liu, J.M. Xue, J. Wang, H.I. Elim, W. Ji, Y. Li, T.J. White, *Controlling the crystallinity and nonlinear optical properties of transparent TiO_2–PMMA nanohybrids*, J. Mater. Chem. 14 (2004) 2978–2987.

[136] S. Banerjee, D.D. Dionysiou, S.C. Pillai, *Self-cleaning applications of TiO_2 by photo-induced hydrophilicity and photocatalysis*, Appl. Catal. B: Environ. 176–177 (2015) 396–428.

[137] S. Komornicki, M. Rękas, K. Schneider, J. Wyrwa, *Self-Cleaning Layers of TiO_2 on the Brick Surfaces*, Ceramic Mater. 65 (2013) 130–134.

[138] H.-M. Lin, C.-H. Keng, C.-Y. Tung, *Gas-sensing properties of nanocrystalline TiO_2*, Nanostructured Materials 9 (1997) 747–750.

[139] A. Paul van Hal, M.M. Wienk, J.M. Kroon, W.J.H. Verhees, L.H. Slooff, J.H. Wouter van Gennip, P. Jonkheijm, R.A.J. Janssen, *Photoinduced Electron Transfer and Photovoltaic Response of a MDMO-PPV:TiO_2 Bulk-Heterojunction* Adv. Mater. 15 (2003) 2.

[140] K. Katayama, K. Hasegawa, Y. Takahashi, T. Akiba, *Humidity sensitivity of Nb_2O_5-doped TiO_2 ceramics*, Sensors and Actuators A: Physical 24 (1990) 55–60.

[141] F. Bosc, D. Edwards, N. Keller, V. Keller, A. Ayral, *Mesoporous TiO_2-based photocatalysts for UV and visible light gas-phase toluene degradation*, Thin Solid Films 495 (2006) 272–279.

[142] W. Choi, A. Termin, M.R. Hoffmann, *The Role of Metal Ion Dopants in Quantum-Sized TiO_2: Correlation between Photoreactivity and Charge Carrier Recombination Dynamics*, J. Phys. Chem. 98 (1994) 13669–13679.

[143] D.T. Cromer, K. Herrington, *The Structures of Anatase and Rutile*, J. Am. Chem. Soc. 77 (1955) 4708–4709.

[144] H. Tang, K. Prasad, R. Sanjinbs, P.E. Schmid, F. Levy, *Electrical and optical properties of TiO_2 anatase thin films*, J. Appl. Phys. 75 (1994) 4.

[145] Y. Xu, M.A.A. Schoonen, *The absolute energy positions of conduction and valence bands of selected semiconducting minerals*, American Mineralogist 85 (2000) 543–556.

[146] S. Sato, *Photocatalytic activity of NOx doped TiO_2 in the visible region*, Chem. Phys. Lett. 123(1–2) (1986) 126–128.

[147] C.Z. Wen, Q.H. Hu, Y.N. Guo, X.Q. Gong, S.Z. Qiao, H.G. Yang, *From titanium oxydifluoride ($TiOF_2$) to titania (TiO_2): phase transitioand non-metal doping with enhanced photocatalytic hydrogen (H_2) evolution properties*, Chem. Commun. 47 (2011) 6138–6140.

[148] R. Beranek, B. Neumann, S. Sakthivel et al., *Exploring the electronic structure of nitrogen-modified TiO_2 photo catalysts through photo current and surface photo voltage studies*, Chem. Phys. 339(1–3) (2007) 11–19.

[149] R. Nakamura, T. Tanaka, and Y. Nakato, *Mechanism for Visible Light Responses in Anodic Photocurrents at N-Doped TiO_2 Film Electrodes*, J. Phys. Chem. B 108 (2004) 10617–10620.

[150] C.D. Valentin, G. Pacchioni, A. Selloni, S. Livraghi, E. Giamello, *Characterization of paramagnetic species in N-doped TiO_2 powders by EPR spectroscopy and DFT calculations*, J. Phys. Chem. B 109 (2005) 11414–11419.

[151] S.A. Ansari, M.M. Khan, M.O. Ansaric, M.H. Cho, *Nitrogen-doped titanium dioxide (N-doped TiO_2) for visible light photocatalysis*, New J. Chem. 40 (2016) 3000.

[152] J. Gong, W. Pu, C. Yang, J. Zhang, *A simple electrochemical oxidation method to prepare highly ordered Cr-doped titania nanotube arrays with promoted photoelectrochemical property*, Electrochim. Acta 68 (2012) 178–183.

[153] E. Borgarello, J. Kiwi, M. Gräetzel, E. Pelizzetti, M. Visca, *Visible light induced water cleavage in colloidal solutions of chromium-doped titanium dioxide particles*, J. Am. Chem. Soc. 104 (1982) 2996–3002.

[154] O. Kerkez, I. Boz, *Photo(electro)catalytic activity of Cu^{2+}-modified TiO_2 nanorod array thin films under visible light irradiation*, J. Phys. Chem. Solids 75 (2014) 611–618.

[155] D. Jing, Y. Zhang, L. Guo, *Study on the synthesis of Ni doped mesoporous TiO_2 and its photocatalytic activity for hydrogen evolution in aqueous methanol solution*, Chem. Phys. Lett. 415 (2005) 74–78.

[156] M.A. Khan, S.I. Woo, O.B. Yang, *Hydrothermally stabilized Fe(III) doped titania active under visible light for water splitting reaction*, Int. J. Hydrogen Energy 33 (2008) 5345–5351.

[157] K. Mizushima, M. Tanaka, A. Asai, S. Iida, J.B. Goodenough, *Impurity levels of iron-group ions in TiO_2(II)*, J. Phys. Chem. Solids 40 (1979) 1129–1140.

[158] C.Y. Huang, W.S. You, L.Q. Dang, Z.B. Lei, Z.G. Sun, L.C. Zhang, *Effect of Nd^{3+} Doping on Photocatalytic Activity of TiO_2 Nanoparticles for Water Decomposition to Hydrogen*, Chin. J. Catal. 27 (2006) 203–209.

[159] Y.Q. Wu, G.X. Lu, S.B. Li, *The long-term photocatalytic stability of Co^{2+}-modified P25-TiO_2 powders for the H_2 production from aqueous ethanol solution,* J. Photochem. Photobiol. A 181 (2006) 263–267.

[160] C. Di Valentin, E. Finazzi, G. Pacchioni, A. Selloni, S. Livraghi, M.C. Paganini, E. Giamello, *N-doped TiO_2: Theory and experiment*, Chem. Phys. 339 (2007) 44–56.

[161] K. Siuzdak, M. Abbas, L. Vignau, M. Devynck, G.V. Dubacheva, A. Lisowska-Oleksiak, *Application of non-metal doped titania for inverted polymer solar cells*, J. Appl. Phys. 112 (2012) 123110.

[162] K. Nishijima, T. Kamai, N. Murakami, T. Tsubota, and T. Ohno, *Photocatalytic hydrogen or oxygen evolution from water over S- or N-doped TiO_2 under visible light*, Int. J. Photoenergy Article ID 173943 (2008) 1–7.

[163] A. Lisowska-Oleksiak, K. Szybowska, V. Jasulaitiené, *Preparation and characterisation of visible light responsive iodine doped TiO_2 electrodes*, Electrochim. Acta 55 (2010) 5881–5885.

[164] M. Szkoda, K. Siuzdak, A. Lisowska-Oleksiak, *Non-metal doped TiO_2 nanotube arrays for high efficiency photocatalytic decomposition of organic species in water*, Physica E 84 (2016) 141–145.

[165] M.V. Dozzi, C. D'Andrea, B. Ohtani, G. Valentini, E. Selli, *Fluorine-Doped TiO2 Materials: Photocatalytic Activity vs Time-Resolved Photoluminescence*, J. Phys. Chem. C 117 (2013) 25586−25595.

[166] C. Sotelo-Vazquez, N. Noor, A. Kafizas, R. Quesada-Cabrera, D.O. Scanlon, A. Taylor, J.R. Durrant, I.P. Parkin, *Multifunctional P-Doped TiO_2 Films: A New Approach to Self- Cleaning, Transparent Conducting Oxide Materials*, Chem. Mater. 27 (2015) 3234−3242.

[167] M. Quesada-González, N.D. Boscher, C.J. Carmalt, I.P. Parkin, *Interstitial Boron-Doped TiO_2 Thin Films: The Significant Effect of Boron on TiO_2 Coatings Grown by Atmospheric Pressure Chemical Vapor Deposition*, ACS Appl. Mater. Interfaces 8 (2016) 25024−25029.

[168] K. Siuzdak, M. Szkoda, A. Lisowska-Oleksiak, K. Grochowska, J. Karczewski, J. Ryl, *Thin layer of ordered boron-doped TiO_2 nanotubes fabricated in a novel type of electrolyte and characterized by remarkably improved photoactivity*, Appl. Surf. Sci. 357 (2015) 942–950.

[169] U. Pal, S. Ghosh, D. Chatterjee, *Effect of sacrificial electron donors on hydrogen generation over visible light–irradiated nonmetal-doped TiO_2 photocatalysts*, Transition Met. Chem. 37 (2012) 93–96.

[170] J. Fang, F.C. Shi, J. Bu, J.J. Ding, S.T. Xu, J. Bao, Y.S. Ma, Z.Q. Jiang, W.P. Zhang, C. Gao, W.X. Huang, *One-Step Synthesis of Bifunctional TiO_2 Catalysts and Their Photocatalytic Activity*, J. Phys. Chem. C 114 (2010) 7940–7948.

[171] X. Sun, H. Liu, J. Dong, J. Wei, Y. Zhang, *Preparation and Characterization of Ce/N-Codoped TiO_2 Particles for Production of H_2 by Photocatalytic Splitting Water Under Visible Light,* Catal. Lett. 135 (2010) 219–225.

[172] M.Z. Selcuk, M.S. Boroglu, I. Boz, *Hydrogen production by photocatalytic water-splitting using nitrogen and metal co-doped TiO_2 powder photocatalyst*, Reac. Kinet. Mech. Catal. 106 (2012) 313–324.

[173] T. Cottineau, N. Bealu, P.-A. Gross, S.N. Pronkin, N. Keller, E.R. Savinova, V. Keller, *One step synthesis of niobium doped titania nanotube arrays to form (N,Nb) co-doped TiO2 with high visible light photoelectrochemical activity*, J. Mater. Chem. A 1 (2013) 2151.

[174] R. Asahi, T. Morikawa, T. Ohwaki, K. Aoki, Y. Taga, *Visible-Light Photocatalysis in Nitrogen-Doped Titanium Oxides*, Science 293 (2001).

[175] M. Mrowetz, W. Balcerski, A.J. Colussi, M.R. Hoffmann, *Oxidative Power of Nitrogen-Doped TiO_2 Photocatalysts under Visible Illumination*, J. Phys. Chem. B 108 (2004) 45.

[176] H.M. Yates, M.G. Nolan, D.W. Sheel, M.E. Pemble, *The role of nitrogen doping on the development of visible light-induced photocatalytic activity in thin TiO_2 films grown on glass by chemical vapor deposition*, J. Photochem. Photobiol. A: Chemistry 179 (2006) 213–223.

[177] T. Ihara, M. Miyoshi, Y. Iriyama, O. Matsumoto, and S. Sugihara, *Visible-light-active titanium oxide photocatalyst realized by an oxygen-deficient structure and by nitrogen doping*, Appl. Catal. B 42 (2003) 403–409.

[178] B. Viswanathan, K.R. Krishanmurthy, N*itrogen Incorporation in TiO_2: Does It Make a Visible Light Photo-Active Material?* Int. J. Photoenergy (2012) 10 pages.

[179] C. Kusumawardani, K. Indiana, Narsito, *Synthesis of nanocrystalline N-doped TiO_2 and its application on high efficiency of dye-sensitized solar cells*, Science Journal UBU 1(1) (2010) 1–8.

[180] S. Livraghi, M.C. Paganini, E. Giamello, A. Selloni, C. Di Valentin, G. Pacchioni, *Origin of photoactivity of nitrogen-doped titanium dioxide under visible light*, J. Am. Chem. Soc. 49 (2006) 15666–15671.

[181] C. Di Valentin, E. Finazzi, G. Pacchioni, A. Selloni, S. Livraghi, M.C. Paganin, E. Giamello, *N-doped TiO_2: Theory and experiment* Chem. Phys. 339 (2007) 44–56.

[182] T. Sreethawong, S. Laehsalee, S. Chavadej, *Use of Pt/N-doped mesoporous-assembled nanocrystalline TiO_2 for photocatalytic H_2 production under visible light irradiation*, Catal. Commun. 10 (2009) 538–543.

[183] M. Gartner, P. Osiceanu, M. Anastasescu et al., *Investigation on the nitrogen doping of multilayered, porous TiO_2 thin films*, Thin Solid Films, 22 (2008) 8184–8189.

[184] X.-B. Li, X.-Y. Jiang, J.-H. Huang, X.-J. Wang, *Photocatalytic Activity for Water Decomposition to Hydrogen over Nitrogen-doped TiO_2 Nanoparticle*, Chin. J. Chem. 26 (2008) 2161–2164.

[185] S. Buzby, M.A. Barakat, H. Lin et al., *Visible light photocatalysis with nitrogen-doped titanium dioxide nanoparticles prepared by plasma assisted chemical vapor deposition*, J. Vacuum Science and Technology B 3 (2006) 1210–1214.

[186] K. Siuzdak, M. Szkoda, M. Sawczak, A. Lisowska-Oleksiak, *Novel nitrogen precursors for electrochemically driven doping of titania nanotubes exhibiting enhanced photoactivity*, New J. Chem. 39 (2015) 2741–2751.

[187] D. Chen, Z. Jiang, J. Geng, Q. Wang, and D. Yang, *Carbon and nitrogen co-doped TiO_2 with enhanced visible-light photocatalytic activity*, Industrial & Engineering Chemistry Research 9 (2007) 2741–2746.

[188] Z. Zhao, J. Fan, J. Wang, R. Li, *Effect of heating temperature on photocatalytic reduction of CO_2 by N–TiO_2 nanotube catalyst*, Catal. Commun. 21 (2012) 32–37.

[189] Q.D. Truong, T.H. Le, J.-Y. Liu, C.-C. Chung, Y.-C. Ling, *Synthesis of TiO_2 nanoparticles using novel titanium oxalate complex towards visible light-driven photocatalytic reduction of CO_2 to CH_3OH*, Appl. Catal. A 28 (2012) 437−438.

[190] C. Chen, H. Bai, S.M. Chang, C. Chang, W. Den, *Preparation of N-doped TiO_2 photocatalyst by atmospheric pressure plasma process for VOCs decomposition under UV and visible light sources*, J. Nanoparticle Research, 3 (2007) 365–375.

[191] O. Diwald, T.L. Thompson, T. Zubkov, E.G. Goralski, S.D. Walck, J.T. Yates, *Photochemical activity of nitrogen doped rutile TiO_2(110) in visible light*, J. Phys. Chem. B 19 (2004) 6004–6008.

[192] R. Asahi, T. Morikawa, T. Ohwaki, K. Aoki, Y. Taga, *Visible-light photocatalysis in nitrogen-doped titanium oxides*, Science 293 (269–271) 2001.

[193] C. Cardinaud, G. Lemperiere, M.C. Peignon, P.Y. Jouan, *Characterisation of TiN coatings and of TiN/Si interface by x-ray photoelectron spectroscopy and Auger electron spectroscopy*, Appl. Surf. Sci. 68 (1993) 595–603.

[194] A.P. Bhirud, S.D. Sathaye, R.P. Waichal, J.D. Ambekar, C.-J. Park, B.B. Kale, *In-situ preparation of N-TiO_2/grapheme nanocomposite and its enhanced photocatalytic hydrogen production by H_2S splitting under solar light*, Nanoscale 7 (2015) 5023–5034.

[195] N.C. Saha, H.G. Tompkins, *Titanium nitride oxidation chemistry: an X-ray photoelectron spectroscopy study*, J. Appl. Phys. 7 (1992) 3072–3079.

[196] C.D. Valentin, G. Pacchioni, A. Selloni, *Theory of carbon doping of titanium dioxide, Chemistry of Materials*, 26 (2005) 6656–6665.

[197] C.D. Valentin, G. Pacchioni, A. Selloni, S. Livraghi, E. Giamello, *Characterization of paramagnetic species in N-doped TiO_2 powders by EPR spectroscopy and DFT calculations*, J. Phys. Chem. B 23 (2005) 11414–11419.

[198] D. Valentin, E. Finazzi, G. Pacchioni et al., *N-doped TiO_2: theory and experiment*, Chem. Phys. 339 (2007) 44–56.

[199] J. Wang, D.N. Tafen, J.P. Lewis, Z.L. Hong, A. Manivannan, M.J. Zhi, M. Li, N.Q. Wu, *Origin of Photocatalytic Activity of Nitrogen-Doped TiO_2 Nanobelts*, J. Am. Chem. Soc. 131 (2009) 12290–12297.

[200] T. Ihara, M. Miyoshi, Y. Iriyama, O. Matsumoto, S. Sugihara, *Visible-light-active titanium oxide photocatalyst realized by an oxygen-deficient structure and by nitrogen doping*, Appl. Catal. B: Environ. 42 (2003) 403–409.

[201] S. Livraghi, M.C. Paganini, E. Giamello, A. Selloni, C. Di Valentin, G. Pacchioni, *Origin of Photoactivity of Nitrogen-Doped Titanium Dioxide under Visible Light*, J. Am. Chem. Soc. 49 (2006) 15666–15671.

[202] D. Valentin, E. Finazzi, G. Pacchioni et al., *N-doped TiO_2: theory and experiment*, Chem. Phys. 339 (2007) 44–56.

[203] R. Asahi, T. Morikawa, T. Ohwaki, K. Aoki, Y. Taga, *Visible-Light Photocatalysis in Nitrogen-Doped Titanium Oxides*, Science 293 (2001) 269–271.

[204] S.K. Cushing, N. Wu, *Progress and Perspectives of Plasmon-Enhanced Solar Energy Conversion*, J. Phys. Chem. Lett. 7 (2016) 666−675.

[205] X. Zhou, G. Liu, J. Yu, W. Fan, *Surface plasmon resonance-mediated photocatalysis by noble metal-based composites under visible light*, J. Mater. Chem. 22 (2012) 21337.

[206] M. Xiao, R. Jiang, F. Wang, C. Fang, J. Wang, J.C. Yu, *Plasmon-enhanced chemical reactions* J. Mater. Chem. A 1 (2013) 5790.

[207] X. Zhou, G. Liu, J. Yu, W. Fan, *Surface plasmon resonance-mediated photocatalysis by noble metal-based composites under visible light* J. Mater. Chem. 22 (2012) 21337.

[208] C. Clavero, Pl*asmon-induced hot-electron generation at nanoparticle/metal-oxide interfaces for photovoltaic and photocatalytic devices*, Nature Photonics 8 (2014) 95–103.

[209] Z. Liu, W. Hou, P. Pavaskar, M. Aykol, B.S. Cronin, *Plasmon Resonant Enhancement of Photocatalytic Water Splitting Under Visible Illumination*, Nano Lett. 11 (2011) 1111–1116.

[210] D.B. Ingram, P. Christopher, J.L. Bauer, S. Linic, *Predictive Model for the Design of Plasmonic Metal/Semiconductor Composite Photocatalysts* ACS Catal. 1 (2011) 1441–1447.

[211] S.C. Warren, E. Thimsen, *Plasmonic solar water splitting*, Energy Environ. Sci. 5 (2012) 5133.

[212] J.Y. Lan, X.M. Zhou, G.Liu, J.G. Yu, J.C. Zhang, L.J. Zhi, G.J. Nie, *Enhancing photocatalytic activity of one-dimensional KNbO3 nanowires by Au nanoparticles under ultraviolet and visible-light*, Nanoscale 3 (2011) 5161.

[213] C.G. Silva, R. Juarez, T. Marino, R. Molinari, H. Garcia, *Influence of Excitation Wavelength (UV or Visible Light) on the Photocatalytic Activity of Titania Containing Gold Nanoparticles for the Generation of Hydrogen or Oxygen from Water*, J. Am. Chem. Soc. 133 (2011) 595.

[214] S.C. Chan, M.A. Barteau, *Preparation of Highly Uniform Ag/TiO_2 and Au/TiO_2 Supported Nanoparticle Catalysts by Photodeposition*, Langmuir, 21(12) (2005) 5588–5595.

[215] P.A. Gross, S.N. Pronkin, T. Cottineau, N. Keller, V. Keller, E.R. Savinova, *Effect of deposition of Ag nanoparticles on photoelectrocatalytic activity of, vertically aligned TiO_2 nanotubes*, Catal. Today 189 (2012) 93–100

[216] H. Kominami, A. Tanaka and K. Hashimoto, *Gold nanoparticles supported on cerium(IV) oxide powder for mineralization of organic acids in aqueous suspensions under irradiation of visible light of $\lambda = 530$ nm*, Appl. Catal. A 397 (2011) 121.

[217] H. Zhu, X. Ke, X. Yang, S. Sarina, H. Liu, *Reduction of nitroaromatic compounds on supported gold nanoparticles by visible and ultraviolet light*, Angew. Chem., Int. Ed. 49 (2010) 9657–9661.

[218] W. Hou, Z. Liu, P. Pavaskar, W. H. Hung and S. B. Cronin, *Plasmonic enhancement of photocatalytic decomposition of methyl orange under visible light*, J. Catal. 277 (2011) 149.

[219] H. F. Cheng, B. B. Huang, P. Wang, Z. Y. Wang, Z. Z. Lou, J. P. Wang, X. Y. Qin, X. Y. Zhang and Y. Dai, *In situ ion exchange synthesis of the novel Ag/AgBr/BiOBr hybrid with highly efficient decontamination of pollutants*, Chem. Commun. 47 (2011) 7054.

[220] H. Tada, K. Teranishi, Y. Inubushi, S. Ito, *Ag nanocluster loading effect on TiO_2 photocatalytic reduction of Bis(2-dipyridyl)disulfide to 2-mercaptopyridine by H_2O*, Langmuir, 16 (2000) 3304–3309.

[221] J. Chen, D.F. Ollis, W.H. Rulkens, H. Bruning, *Photocatalyzed oxidation of alcohols and organochlorides in the presence of native TiO_2 and metallized TiO_2 suspensions. Part (i): photocatalytic activity and pH influence*, Water Res. 33 (1999) 661–668.

[222] D.B. Ingram, S. Linic, *Water Splitting on Composite Plasmonic-Metal/Semiconductor Photoelectrodes: Evidence for Selective Plasmon-Induced Formation of Charge Carriers near the Semiconductor Surface*, J. Am. Chem. Soc. 133 (2011) 5202–5205.

[223] Z. Liu, W. Hou, P. Pavaskar, M. Aykol, S.B. *Cronin Plasmon Resonant Enhancement of Photocatalytic Water Splitting Under Visible Illumination*, Nano Lett. 11 (2011) 1111–1116.

[224] O. Rosseler, M.V. Shankar, M. Karkmaz-Le Du, L. Schmidlin, N. Keller, V. Keller, *Solar light photocatalytic hydrogen production from water over Pt and Au/TiO_2(anatase/rutile) photocatalysts: Influence of noble metal and porogen*, J. Catal. 269 (2010) 179–190.

[225] K. Awazu, M. Fujimaki, C. Rockstuhl, J. Tominaga, H. Murakami, Y. Ohki, N. Yoshida, T. Watanabe *A Plasmonic Photocatalyst Consisting of Silver Nanoparticles Embedded in Titanium Dioxide*, J. Am. Chem. Soc. 130 (2008) 1676–1680.

[226] S.T. Kochuveedu, D.-P. Kim, D.H. Kim, *Surface-Plasmon-Induced Visible Light Photocatalytic Activity of TiO_2 Nanospheres Decorated by Au Nanoparticles with Controlled Configuration*, J. Phys. Chem. C 116 (2012) 2500–2506.

[227] P. Christopher, D.B. Ingram, S. Linic, *Enhancing Photochemical Activity of Semiconductor Nanoparticles with Optically Active Ag Nanostructures: Photochemistry Mediated by Ag Surface Plasmons*, J. Phys. Chem. C 114 (2010) 9173–9177.

[228] M. Logar, B. Jancar, S. Sturm, D. Suvorov, *Weak Polyion Multilayer-Assisted in Situ Synthesis as a Route toward a Plasmonic Ag/TiO_2 Photocatalyst*, Langmuir 26(14) (2010) 12215–12224.

[229] E. Kowalska, R. Abe, B. Ohtani, *Visible light-induced photocatalytic reaction of gold-modified titanium(IV) oxide particles: action spectrum analysis*, Chem. Commun. (2009) 241–243.

[230] Z. Zheng, B. Huang, X. Qin, X. Zhang, Y. Dai, M.-H. Whangbo, *Facile in situ synthesis of visible-light plasmonic photocatalysts M@TiO_2 (M = Au, Pt, Ag) and evaluation of their photocatalytic oxidation of benzene to phenol*, J. Mater. Chem. 21 (2011) 9079.

[231] X .Z. Li, F.B. Li, Study of Au/Au^{3+}-TiO_2 Photocatalysts toward Visible Photooxidation for Water and Wastewater Treatment, Environ. Sci. Technol. 35 (2001) 2381–2387.

[232] N. Zhang, S. Liu, X. Fu, Y.-J. Xu, *Synthesis of M@TiO_2 (M = Au, Pd, Pt) Core Shell Nanocomposites with Tunable Photoreactivity*, J. Phys. Chem. C 115 (2011) 9136–9145.

[233] N. Chandrasekharan, P.V. Kamat, *Improving the Photoelectrochemical Performance of Nanostructured TiO_2 Films by Adsorption of Gold Nanoparticles*, J. Phys. Chem. B 104 (2000) 10851–10857.

[234] A.A. Melvin, K. Illath, T. Das, T. Raja, S. Bhattacharyy, C.S. Gopinath, *M–Au/TiO_2 (M = Ag, Pd, and Pt) nanophotocatalyst for overall solar water splitting: role of interfaces*, Nanoscale 7 (2015) 13477.

[235] L. Wu, F. Li, Y. Xu, J.W. Zhang, D. Zhang, G. Li, H. Li, *Plasmon-induced photoelectrocatalytic activity of Au nanoparticles enhanced TiO_2 nanotube arrays electrodes for environmental remediation* Appl. Catal. B: Environ. 164 (2015) 217–224.

[236] Z.W. Seh, S. Liu, M. Low, S.-Y. Zhang, Z. Liu, A. Mlayah, M.-Y. Han, *Janus Au-TiO_2 Photocatalysts with Strong Localization of Plasmonic Near-Fields for Efficient Visible-Light Hydrogen Generation*, Adv. Mater. 24 (2012) 2310–2314.

[237] D.Y Leung, X. Fu, C. Wang, M. Ni, M.K. Leung, X. Wang, X. Fu, *Hydrogen production over titania-based photocatalysts* ,ChemSusChem 3 (2010) 681–694.

[238] T. Hirai, K. Suzuki, I.J. Komasawa, *Preparation and Photocatalytic Properties of Composite CdS Nanoparticles–Titanium Dioxide Particles*, Colloid Interface Sci. 244 (2001) 262–265.

[239] J.S. Jang, H.G. Kim, P.H. Borse, J.S. Lee, *Simultaneous hydrogen production and decomposition of H_2S dissolved in alkaline water over CdS-TiO_2 composite photocatalysts under visible light irradiation*, Int. J. Hydrogen Energy 32 (2007) 4786–4791.

[240] J.S. Jang, S.M. Ji, S.W. Bae, H.C. Son, J.S. Lee, *Optimization of CdS/TiO_2 nano-bulk composite photocatalysts for hydrogen production from Na2S/Na2SO3 aqueous electrolyte solution under visible light ($\lambda \geq 420$ nm)*, J. Photochem. Photobiol. A 188 (2007) 112–119.

[241] X.-Y. Zhang, H.-P. Li, X.-L. Cui, Y. Lin, *Graphene/TiO_2 nanocomposites: synthesis, characterization and application in hydrogen evolution from water photocatalytic splitting*, J. Mater. Chem. 20 (2010) 2801–2806.

[242] Q.J. Xiang, J.G. Yu, M. Jaroniec, *Synergetic Effect of MoS_2 and Graphene as Cocatalysts for Enhanced Photocatalytic H_2 Production Activity of TiO_2 Nanoparticles*, J. Am. Chem. Soc. 134 (2012) 6575–6578.

[243] G. Li, K.A. Gray, *The solid-soild interface: explaining the high and unique photocatalytic reactivity of TiO_2-based nanocomposite materials*, Chem. Phys. 339 (2007) 173–187.

[244] C. Su, B.Y. Hong, C.M. Tseng, *Sol–gel preparation and photocatalysis of titanium dioxide*, Catal. Today 96 (2004) 119–126.

[245] K.L. Schulte, P.A. DeSario, K.A. Gray, *Effect of crystal phase composition on the reductive and oxidative abilities of TiO_2 nanotubes under UV and visible light*, Appl. Catal. B 97 (2010) 354–360.

[246] U. Shaislamov, B.L. Yang, *CdS-sensitized single-crystalline TiO_2 nanorods and polycrystalline nanotubes for solar hydrogen generation*, J. Mater. Res. 28 (2013) 905–906.

[247] J.S. Jang, S.H. Choi, H. Park, W. Choi, J.S. Lee, *A composite photocatalyst of CdS nanoparticles deposited on TiO_2 nanosheets*, J. Nanosci. Nanotechnol. 6 (2006) 3642–3646.

[248] L. Jiang, W. Zhang, Y. Yu, J. Wang, *Preparation and charge transfer properties of carbon nanotubes supported CdS/ZnO-NWs shell/core heterojunction*, Electrochem. Commun. 13 (2011) 627–630.

[249] M. Law , L.E. Greene , A. Radenovic , T. Kuykendall , J. Liphardt, P. Yang, *$ZnO-Al_2O_3$ and $ZnO-TiO_2$ Core−Shell Nanowire Dye-Sensitized Solar Cells*, J. Phys. Chem. B 110 (2006) 22652–22663.

[250] L. Wu, J. Xing, Y. Hou, F.Y. Xiao, Z. Li, H. G. Yang, *Fabrication of Regular ZnO/TiO_2 Heterojunctions with Enhanced Photocatalytic Properties*, Chem. Eur. J. 19 (2013) 8393–8396.

[251] A. Hamrouni, N. Moussa, F. Parrino, A. Di Paola, A. Houas, L. Palmisano, *Sol–gel synthesis and photocatalytic activity of ZnO–SnO_2 nanocomposites*, J. Molecular Catal. A: Chemical 390 (2014) 133–141.

[252] Y. Wang, B. Li, C. Zhang, L. Cui, S. Kang, X. Li, L. Zhou, *Ordered mesoporous CeO_2-TiO_2 composites: Highly efficient photocatalysts for the reduction of CO_2 with H_2O under simulated solar irradiation*, Appl. Catal. B 130 (2013) 277–284.

[253] J. Yu, S. Zhuang, X. Xu, W. Zhu, B. Feng, J. Hu, *Photogenerated electron reservoir in hetero-p–n CuO–ZnO nanocomposite device for visible-light-driven photocatalytic reduction of aqueous Cr(VI)*, J. Mater. Chem. A 3 (2015) 1199–1207.

[254] Y. Bessekhouad, D. Robert, J.-V. Weber, *Photocatalytic activity of Cu_2O/TiO_2, Bi_2O_3/TiO_2 and $ZnMn_2O_4/TiO_2$ heterojunctions*, Catal. Today 101 (2005) 315–321.

[255] P. Wu, H. Zhang, N. Du, L. Ruan, D. Yang, *A Versatile Approach for the Synthesis of ZnO Nanorod Based Hybrid Nanomaterials via Layer-by-Layer Assembly*, J. Phys. Chem. C 119 (2009) 8147–8151.

[256] G. Yang, Z. Yan, T. Xiao, *Preparation and characterization of $SnO_2/ZnO/TiO_2$ composite semiconductor with enhanced photocatalytic activity*, Appl. Surf. Sci. 258 (2012) 8704–8712.

[257] W. Liao, T. Zheng, P. Wang, S. Tu, W. Pan, *Efficient microwave-assisted photocatalytic degradation of endocrine disruptor dimethyl phthalate over composite catalyst ZrOx/ZnO*, J. Environ. Sci. 22(11) 2010 1800–1806.

[258] M. Miyauchi, A. Nakajima, T. Watanabe, K. Hashimoto, *Photoinduced hydrophilic conversion of TiO_2/WO_3 layered thin films*, Chem. Mater. 14 (2002) 4714–4720.

[259] A. Srinivasan, M. Miyauchi, *Chemically Stable WO_3 Based Thin-Film for Visible-Light Induced Oxidation and Superhydrophilicity*, J. Phys. Chem. C 116 (2012) 15421–15426.

[260] M. Grandcolas, T. Cottineau, A. Louvet, N. Keller, V. Keller, *Solar light-activated photocatalytic degradation of gas phase diethylsulfide on WO_3-modified TiO_2 nanotubes*, Appl. Catal. B 138 (2013) 128–140.

[261] M.W. Murphy, P.S.G. Kim, X. Zhou, J. Zhou, M. Coulliard, G.A. Botton, T.-K. Sham, *Biaxial ZnO-ZnS Nanoribbon Heterostructures*, J. Phys. Chem. C 113 (2009) 12.

[262] N. Siedl, M.J. Elser, J. Bernardi, O. Diwald, *Functional Interfaces in Pure and Blended Oxide Nanoparticle Networks: Recombination versus Separation of Photogenerated Charges*, J. Phys. Chem. C 113 (2009) 15792–15795.

[263] A. Kambur, G.S. Pozan, I. Boz, *Preparation, characterization and photocatalytic activity of TiO_2–ZrO_2 binary oxide nanoparticles*, Appl. Catal. B 115 (2012) 149–158.

[264] Z. Wang, Y. Liu, D.J. Martin, W. Wang, J. Tang, W. Huang, *CuOx–TiO_2 junction: what is the active component for photocatalytic H_2 production?* Phys. Chem. Chem. Phys. 15 (2013) 14956–14960.

[265] M. Zhang, T. An, X. Liu, X. Hu, G. Sheng, J. Fu, *Preparation of a high-activity ZnO/TiO_2 photocatalyst via homogeneous hydrolysis method with low temperature crystallization*, Mater. Lett. 64 (2010) 1883–1886.

[266] G.S. Pozan, A. Kambur, *Significant enhancement of photocatalytic activity over bifunctional ZnO–TiO_2 catalysts for 4-chlorophenol degradation*, Chemosphere 105 (2014) 152–159.

[267] R. Liu, H. Ye, X. Xiong, H. Liu, *Fabrication of TiO_2/ZnO composite nanofibers by electrospinning and their photocatalytic property*, Mater. Chem. Phys. 121 (2010) 432–439.

[268] H.R. Pant, C.H. Park, B. Pant, L.D. Tijing, H.Y. Kim, C.S. Kim, *Synthesis, characterization, and photocatalytic properties of ZnO nano-flower containing TiO_2 NPs*, Ceram. Int. 38 (2012) 2943–2950.

[269] M. Agrawal, S. Gupta, A. Pich, N.E. Zafeiropoulos, M. Stamm, *A Facile Approach to Fabrication of ZnO-TiO_2 Hollow Spheres*, Chem. Mater. 21 (2009) 5343–5348.

[270] L. Wu, J. Xing, Y. Hou, F.Y. Xiao, Z. Li, H.G. Yang, *Fabrication of Regular ZnO/TiO_2 Heterojunctions with Enhanced Photocatalytic Properties*, Chem. Eur. J. 19 (2013) 8393 – 8396.

[271] G. Marci, V. Augugliaro, M.J. Lopez-Munoz, C. Martin, L. Palmisano, V. Rives, M. Schiavello, R.J.D. Tilley, A.M. Venezia, *Preparation Characterization and Photocatalytic Activity of Polycrystalline*

ZnO/TiO_2 Systems. 2. Surface, Bulk Characterization, and 4-Nitrophenol Photodegradation in Liquid-Solid Regime, J. Phys. Chem. B 105 (2001) 1033–1040.

[272] C. Cheng, A. Amini, C. Zhu, Z. Xu, H. Song, N, Wang, *Enhanced photocatalytic performance of TiO_2-ZnO hybrid nanostructures*, Sci Rep. 4:4181 (2014) 1–5.

[273] S. Yuan, J. Mu, R. Mao, Y. Li, Q. Zhang, H. Wang, *All-Nanoparticle Self-assembly ZnO/TiO_2 Heterojunction Thin Films with Remarkably Enhanced Photoelectrochemical Activity*, ACS Appl. Mater. Interfaces 6 (2014) 5719−5725.

[274] T.J. Athauda, J.G. Neff, L. Sutherlin, U. Butt, R.R. Ozer, *Systematic Study of the Structure−Property Relationships of Branched Hierarchical TiO_2/ZnO Nanostructures*, ACS Appl. Mater. Interfaces 4 (2012) 6917−6926.

[275] S. Hernández, V. Cauda, D. Hidalgo, V.F. Rivera, D. Manfredi, A. Chiodoni, F.C. Pirri, *Fast and low-cost synthesis of 1D ZnO–TiO_2 core–shell nanoarrays: Characterization and enhanced photo-electrochemical performance for water splitting*, J. Alloys Compd. 615 (2014) 530–537.

[276] S. Panigrahi, D. Basak, Core–shell TiO_2@ZnO nanorods for efficient ultraviolet photodetection, Nanoscale 3 (2011) 2336.

[277] Y-L. Xie, Z.-X. Li, Z.-G. Xu, H.-L. Zhang, *Preparation of coaxial TiO2/ZnO nanotube arrays for high efficiency photo-energy conversion applications*, Electrochem. Comm. 13 (2011) 788–791.

[278] I.A. Ji, M.-J. Park, J.-Y. Jung, M.J. Choi, Y.-W. Lee, J.-H. Lee, J.H. Bang, *One-Dimensional Core/Shell Structured TiO_2/ZnO Heterojunction for Improved Photoelectrochemical Performance*, Bull. Korean Chem. Soc. 33 (2012) 7.

[279] S. Hua, B. Wang, M. Zhu, Y. Ma, Z. Lu, H. Wang, *High-performance 1D type-II TiO_2@ZnO core-shell nanorods arrays photoanodes for photoelectrochemical solar fuel production*, Appl. Surf. Sci. 403 (2017) 126–132.

[280] S. Yuan, J. Mu, R. Mao, Y. Li, Q. Zhang, H. Wang, *All-Nanoparticle Self-assembly ZnO/TiO_2 Heterojunction Thin Films with Remarkably Enhanced Photoelectrochemical Activity*, ACS Appl. Mater. Interfaces 6 (2014) 5719−5725.

[281] F.-X. Xiao, *Construction of Highly Ordered ZnO−TiO_2 Nanotube Arrays (ZnO/TNTs) Heterostructure for Photocatalytic Application*, ACS Appl. Mater. Interfaces 4 (2012) 7055−7063.

[282] S. Siuleimana, N. Kanevaa, A. Bojinovaa, K. Papazova, A. Apostolov, D. Dimitrov, *Photodegradation of Orange II by ZnO and TiO_2 powders and nanowire ZnO and ZnO/TiO_2 thin films*, Colloids Surf. A: Physicochem. Eng. Aspects 460 (2014) 408–413.

[283] L. Zhao, M. Xia, Y. Liu, B. Zheng, Q. Jiang, J. Lian, *Structure and Photocatalysis of TiO_2/ZnO Double-Layer Film Prepared by Pulsed Laser Deposition Materials Transactions*, 53(3) (2012) pp. 463–468

[284] K. Pan, Y. Dong, W. Zhou, Q. Pan, Y. Xie, T. Xie, G. Tian, G. Wang, *Facile Fabrication of Hierarchical TiO_2 Nanobelt/ZnO Nanorod Heterogeneous Nanostructure: An Efficient Photoanode for Water Splitting* ACS Appl. Mater. Interfaces 5 (2013) 8314−8320.

[285] C.W. Zou, W. Gao, *Fabrication, Optoelectronic and Photocatalytic Properties of Some Composite Oxide Nanostructures*, Ttans. Electr. Electron. Mater. 11(1) (2010) pp. 1–10.

[286] Y. Huanga, Y. Wei, J. Wu, C. Guo, M. Wang, S. Yin, T. Sato, *Low temperature synthesis and photocatalytic properties of highly oriented ZnO/$TiO_{2-x}N_y$ coupled photocatalysts*, Appl. Catal. B: Environ. 123–124 (2012) 9–17.

[287] S. Mukhopadhyay, D. Maiti, S. Chatterjee, P.S. Devi, G.S. Kumar, *Design and application of Au decorated ZnO/TiO_2 as a stable photocatalyst for wide spectral coverage* Phys.Chem.Chem.Phys. 18 (2016) 31622.

[288] P. Zhang, C. Shao, X. Li, M. Zhang, X. Zhang, Y. Sun, Y. Liu, *In situ assembly of well-dispersed Au nanoparticles on TiO_2/ZnO nanofibers: A three-way synergistic heterostructure with enhanced photocatalytic activity*, J. Hazard. Mater. 237 (2012) 331–338.

[289] D.M. Fouad, M.B. Mohamed, *Studies on the photo-catalytic activity of semiconductor nanostructures and their gold core–shell on the photodegradation of malathion*, Nanotechnology 22 (2011) 455705–455713.

[290] P.C.J. Turkevich, J.H. Stevenson, *A study of the nucleation and growth processes in the synthesis of colloidal gold*, Discuss Faraday Soc. 11 (1951) 55–75.

[291] R.M. Pasquarelli, D.S. Ginley, R. O'Hayre, *Solution processing of transparent conductors: from flask to film*, Chem. Soc. Rev. 40 (2011) 5406–5441.

[292] X.-D. Gao, F. Peng, X.-M. Li, W.-D. Yu, J.-J. Qiu, *Growth of highly oriented ZnO films by the two-step electrodeposition technique*, J. Mater. Sci. 42 (2007) 9638–9644.

[293] K. Zarębska, M. Kwiatkowski, M. Gniadek, M. Skompska, *Electrodeposition of $Zn(OH)_2$, ZnO thin films and nanosheet-like Zn seed layers and influence of their morphology on the growth of ZnO nanorods*, Electrochim. Acta 98 (2013) 255–262.

[294] R. Savu, R. Parra, E. Joanni, B. Jancar, S.A. Eliziario, R. Camargo, P.R. Bueno, J.A. Varela, E. Longo, M.A. Zaghet, *The effect of cooling rate during hydrothermal synthesis of ZnO nanorods*, J. Cryst. Growth 311 (2009) 4102–4108.

[295] J.J. Richardson, F.F. Lange, *Controlling Low Temperature Aqueous Synthesis of ZnO. 1. Thermodynamic Analysis*, Cryst. Growth Des. 9(6) (2009) 2570-2575.

[296] H. Tada, T. Mitsui, T. Kiyonaga, T. Akita, K. Tanaka, *All-solid-state Z-scheme in CdS–Au–TiO_2 three-component nanojunction system*, Nat. Mater. Lett. 5 (2006) 782–786.

[297] J. Goldstein, D.E. Newbury, D.C. Joy, P. Echlin, C.E. Lyman, E. Lifshin, *Scanning electron microscopy and X-ray microanalysis*, USA: Springer; 2003.

[298] K. Kanaya, S. Okayama, *Penetration and energy-loss theory of electrons in solid targets*, J. Phys. Appl. Phys. 5 (1972) 43–58.

[299] C.S. Schwandt, *Characterizing Nanometer-Scale. Materials Using a low-angle backscattered electron detector*, Technical Article, American Laboratory November/December (2010) 13–17.

[300] M. Suga, S. Asahina, Y. Sakuda, H. Kazumori, H. Nishiyama, T. Nokuo, V. Alfredsson, T. Kjellman, S.M. Stevens, H.S. Cho, M. Cho, L. Han, S. Che, M.W. Anderson, F. Schüth, H. Deng, O.M. Yaghi, Z. Liu, H.Y. Jeong, A. Stein, K. Sakamoto, R. Ryoo, O. Terasaki, *Recent progress in scanning electron microscopy for the characterization of fine structural details of nano materials*, Prog. Solid State Chem. 42 (2014) 1–21.

[301] C.S. Schwandt, *Characterizing Nanometer-Scale. Materials Using a low-angle backscattered electron detector*, Technical Article, American Laboratory November/December (2010) 13–17.

[302] D.B. Williams, C.B. Carter, *Transmission Electron Microscopy*, Plenum Press, New York (1996).

[303] P.D. Nellist, *The Principles of STEM Imaging* S.J. Pennycook, P.D. Nellist (eds.), *Scanning Transmission Electron Microscopy*, 91 Springer Science and Business Media, LLC (2011)

[304] G.P. Joshi, N.S. Saxena, R. Mangal, A. Mishra, T.P. Sharma, *Band gap determination of Ni-Zn ferrites*, Bull. Mater. Sci. 26 (2003) 387–389.

[305] J. Wanga, E. Elamurugua, V. Sallet, F. Jomard, A. Lusson, A.M. Botelho do Regoc, P. Barquinha, G. Gonc, R. Martins, E. Fortunato, *Effect of annealing on the properties of N-doped ZnO films deposited by RF magnetron sputtering*, Appl. Surf. Sci. 254 (2008) 7178–7182.

[306] D. Reyes-Coronado, G. Rodriguez-Gattorno, M.E. Espinosa-Pesqueira, C. Cab, R. de Coss, G. Oskam, *Phase-pure TiO_2 nanoparticles: anatase, brookite and rutile*, Nanotechnology 19 (2008) 145605.

[307] S. Sen, S. Mahanty, S. Roy, O. Heintz, S. Bourgeois, D. Chaumont, *Investigation on sol–gel synthesized Ag-doped TiO_2 cermet thin films*, Thin Solid Films, 474 (2005) 245–249.

[308] D. Monllor-Satoca, R. Gomez, M. González-Hidalgo, P. Salvador, *The "Direct–Indirect" model: An alternative kinetic approach in heterogeneous photocatalysis based on the degree of interaction of dissolved pollutant species with the semiconductor surface*, Catal. Today 129 (2007) 247–255.

[309] J. Torrent, V. Barrón, *Diffuse Reflectance Spectroscopy Chapter 13 Methods of Soil Analysis. Part 5. Mineralogical Methods*. Soil Science Society of America (2008) 367–385.

[310] V. Kumar, N. Singh, V. Kumar, L.P. Purohit, A. Kapoor, O.M. Ntwaeaborwa, H.C. Swart, *Doped zinc oxide window layers for dye sensitized solar cells*, J. Appl. Phys. 114 (2013) 134506.

[311] X. Guo, W. Di, C. Chen, C Liu, X. Wang, W. Qin, *Enhanced near-infrared photocatalysis of NaYF4:Yb, Tm/CdS/TiO_2 composites*, Dalton Trans. 43 (2014) 1048.

[312] C.D. Wagner, W.M. Riggs, L.E. Davis, J.F. Moulder, G.E. Muilenberg, *Handbook of X-ray Photoelectron Spectroscopy*, Perkin-Elmer Corporation, Physical Electronics Division (1979)

[313] S. Marciniak, *Photoelectron Spectroscopy*, IFM Surface Physics and Chemistry (2004)

[314] B. Valeur, M. Nuno, B. Santos, *Molecular Fluorescence: Principles and Applications*, Second Edition., Wiley-VCH Verlag GmbH & Co. KGaA (2013).

[315] P. Gabbott, *Principles and Applications of Thermal Analysis*, Blackwell Publishing Ltd, Oxford, UK (2008).

[316] D. Scheid, C. Lederle, S. Vowinkel, C.G. Schäfer, B. Stühnb, M. Gallei, *Redox- and mechano-chromic response of metallopolymer-based elastomeric colloidal crystal films*, J. Mater. Chem. C 2 (2014) 2583.

[317] S. Prahl, Oregon Medical Laser Center, http://omlc.ogi.edu/spectra/mb

[318] Z. Liu, J. Ya, E. Lei, *Effects of substrates and seed layers on solution growing ZnO nanorods*, J. Solid State Electrochem 14 (2010) 957.

[319] E. Hosono, S. Fujihara, T. Kimura, H. Imai, *Growth of layered basic zinc acetate in methanolic solutions and its pyrolytic transformation into porous zinc oxide films*, Journal of Colloid and Interface Science 272 (2004) 391.

[320] K. Govender, D.S. Boyle, P.B. Kenway, P. O'Brien, *Understanding the factors that govern the deposition and morphology of thin films of ZnO from aqueous solution*, Journal of Materials Chemistry 14 (2004) 2575.

[321] R.D. Armstrong, M. Fleischmann, H.R. Thirsk, *The anodic behaviour of mercury in hydroxide ion solutions*, J. Electroanal. Chem. 11 (1966) 208.

[322] S. Ullah, A. Badshah, F. Ahmed, R. Raza, A.A. Altaf, R. Hussain, *Electrodeposited zinc electrodes for high current Zn/AgO bipolar batteries*, International Journal of Electrochemical Science 6 (2011) 3801.

[323] J. Yu, H. Yang, X. Ai, Y. Chen, *Effects of anions on the zinc electrodeposition onto glassy-carbon electrode*, Russian Journal of Electrochemistry 38 (2002) 321.

[324] M.R. Mahmoudian, W.J. Basirun, Y. Alias, M. Ebadi, *Facile fabrication of* $Zn/Zn_5(OH)_8Cl_2{\cdot}H_2O$ *flower-like nanostructure on the surface of Zn coated with poly (N-methyl pyrrole)*, Appl. Surf. Sci. 257 (2011) 10539.

[325] S. Inoue, S. Fujihara, *Liquid–liquid biphasic synthesis of layered zinc hydroxides intercalated with long-chain carboxylate ions and their conversion into ZnO nanostructures*, Inorganic Chemistry 50 (2011) 3605.

[326] Y.-C. Zhu, Y. Bando, *Large scale preparation of zinc nanosheets by thermochemical reduction of ZnS powders*, Chemical Physics Letters 372 (2003) 640.

[327] J.-H. Lin, Y.-J. Huang, Y.-P. Su, C.-A. Liu, R.S. Devan, C.-H. Ho, Y.-P. Wang, H.-W. Lee, C.-M. Chang, Y. Liou, Y.-R. Ma, *Room-temperature wide-range photoluminescence and semiconducting characteristics of two-dimensional pure metallic Zn nanoplates*, RSC Advances 2 (2012) 2123.

[328] J.O'M. Bockris, K. Uosaki, *The Stability of Photoelectrodes*, J. Electrochem. Soc. 124 (1977) 98–99.

[329] H.R. Oswald, R. Asper, in: R.M.A. Lieth (Ed.), *Preparation and Crystal Growth of Materials with Layered Structures*, Reidel, Dordrecht, 1977, p. 122.

[330] A. Moezzi, A. McDonagh, A. Dowd, M. Cortie, *Zinc Hydroxyacetate and Its Transformation to Nanocrystalline Zinc Oxide*, Inorg. Chem. 52 (2013) 95−102.

[331] P.X. Gao, C.S. Lao, Y. Ding, Z.L. Wang, *Metal/Semiconductor Core/Shell Nanodisks and Nanotubes*, Adv. Fuct. Mater. 16 (2006) 53–62.

[332] J. Liu, X. Huang, *A low-temperature synthesis of ultraviolet-light-emitting ZnO nanotubes and tubular whiskers*, J. Solid State Chem. 179 (2006) 843–848.

[333] M. Kwiatkowski, Master's thesis: *Hydrothermal synthesis of vertically aligned ZnO nanostructures on transparent conducting substrate* (2012)

[334] D.-M. Tang, G. Liu, F. Li, J. Tan, C. Liu, G.Q. Lu, H.-M. Cheng, *Synthesis and Photoelectrochemical Property of Urchin-like Zn/ZnO Core-Shell Structures*, J. Phys. Chem. C 113 (2009) 11035–11040.

[335] B. Ohtani, Y. Ogawa, S. Nishimoto, *Photocatalytic Activity of Amorphous−Anatase Mixture of Titanium(IV) Oxide Particles Suspended in Aqueous Solutions*, J. Phys. Chem. B 101 (1997) 3746–3752.

[336] S. Songa, T. Yanga, J. Liua, Y. Xin, Y. Li, S. Han, *Rapid thermal annealing of ITO films*, Appl. Surf. Sci. 257 (2011) 7061–7064.

[337] J.J. Valenzuela-Jauregui, R. Quintero-Gonzalez, J. Hernandez-Torres, A. Mendoza-Galvan, R. Ramirez-Bon, *Characterization of SnO_2, In_2O_3, and ITO films prepared by thermal oxidation of DC-sputtered Sn, In and In–Sn films*, Vacuum 76 (2004) 177–180.

[338] Y. Yin, R.M. Rioux, C.K. Erdonmez, S. Hughes, G.A. Somorjai, A.P. Alivisatos, *Formation of hollow nanocrystals through the nanoscale Kirkendall effect*, Science 304 (2004) 711–714.

[339] D. Gumy, C. Morais, P. Bowen, C. Pulgarin, S. Giraldo, R. Hajdu, J. Kiwi, *Catalytic activity of commercial of TiO_2 powders for the abatement of the bacteria (E. coli) under solar simulated light: Influence of the isoelectric point*, Appl. Catal. B: Environ. 63 (2006) 76–84.

[340] J.O. Carneiro, S. Azevedo, F. Fernandes, E. Freitas, M. Pereira, C.J. Tavares, S. Lanceros-Mendez, V. *Teixeira Synthesis of iron-doped TiO2 nanoparticles by ball-milling process: the influence of process parameters on the structural, optical, magnetic, and photocatalytic properties*, J. Mater. Sci. 49 (2014) 7476–7488.

[341] B.F. Dzhurinskii, D. Gati, N.P. Sergushin, V.I. Nefedov, Y.A. V. Salyn, *Simple and coordination compounds*, Russ. J. InorgChem+ 20 (1975) 2307-2314.

[342] C.D. Wagner, J.F. Moulder, L.E. Davis, W.M. Riggs, *Perkin-Elmer Corporation, Physical Electronics Division*.

[343] A. Casagrande, A. Glisenti, E. Lanzoni, E. Tondello, L. Mirenghi, M. Casarin, R. Bertoncello, *Tin, Tic and Ti(C, N) film characterization and its relationship to tribological behaviour*, Surf. Interface Anal. 18 (1992) 525-531.

[344] A.E. Miller, C. Ernsberger, D. Banks, J. Nickerson, T. Smith, J. Vac. Sci. Technol. A (1986) 2784-2788.

[345] N.J. Nicholas, G.V. Franks, W.A. Ducker, *The mechanism for hydrothermal growth of zinc oxide*, Cryst. Eng. Comm. 14 (2012) 1232-1240.

[346] J. Li, H.C. Zeng, *Preparation of Monodisperse Au/TiO2 Nanocatalysts via Self-Assembly*, Chem. Mater. 18 (2006) 4270-4277.

[347] C.R. Clayton, Y.C. Lu, *A Bipolar Model of the Passivity of Stainless Steel: The Role of Mo Addition*, J. Electrochem. Soc. 133 (1986) 2465-2473.

[348] D. Briggs, M.P. Seah, John Willey & Sons, 1993, 2nd edition.

[349] equation proposed by prof. Sven Tougraad, founder of the QUASES software

[350] G.H. Li, L. Yang, Y.X. Jin, L.D. Zhang, *Structural and optical properties of TiO_2 thin film and TiO_2+2 wt.% ZnFe2O4 composite film prepared by r.f. sputtering*, Thin Solid Films 368 (2000) 163–167.

[351] C. Ye, S.S. Pan, X.M. Teng, H.T. Fan, G.H. Li, *Preparation and optical properties of nanocrystalline thin films in the ZnO-TiO2 system*, Appl. Phys. A 90 (2008) 375-378.

[352] C. Ye, Y. Wang, Y. Ye, J. Zhang, G.H. Li, *Preparation and photoluminescence of undoped ZnTiO3ZnTiO3 thin films*, J. Appl. Phys. 106 (2009) 033520.

[353] H.J. Fan, U. Gösele, M. Zacharias, *Formation of Nanotubes and Hollow NanoparticlesBased on Kirkendall and Diffusion Processes: A Review*, Small 3 (2007) 1660–1671.

[354] M.D. McCluskey, S.J. Jokela, *Defects in ZnO*, J. Appl. Phys. 106 (2009) 071101.

[355] A.L. Linsebigler, G. Lu, J.T. Yates, *Photocatalysis on TiO2 Surfaces: Principles, Mechanisms, and Selected Results*, Chem. Rev. 95 (1995) 735–758.

[356] R.M. Navarro, F. del Valle, J.L. G. Fierro, *Photocatalytic hydrogen evolution from CdS–ZnO–CdO systems under visible light irradiation: Effect of thermal treatment and presence of Pt and Ru cocatalysts*, Int. J. Hydrogen. Energy 33 (2008) 4265–4273.

[357] A. Mills, J. Wang, *Photobleaching of methylene blue sensitised by TiO_2: an ambiguous system?*, J. Photochem. Photobiol. A: Chem. 127 (1999) 123–134.

[358] C. Baiocchi, M.C. Brussino, E. Pramauro, A.B. Prevot, L. Palmisano, G. Marc, *Characterization of methyl orange and its photocatalytic degradation products by HPLC/UV–VIS diode array and atmospheric pressure ionization quadrupole ion trap mass spectrometry*, Int. J. Mass Spectro. 214 (2002) 247–256.

[359] M.R. Prairie, L.R. Evans, B.M. Stange, S.L. Martinez, *An investigation of titanium dioxide photocatalysis for the treatment of water contaminated with metals and organic chemicals*, Environ. Sci. Technol. 27 (1993) 1776-1782.

[360] C. Valentin, D. Fittipaldi, *Hole Scavenging by Organic Adsorbates on the TiO2 Surface: A DFT Model Study*, J. Phys. Chem. Lett. 4 (2013)1901−1906.

[361] M. Muuronen, S.M. Parker, E. Berardo, A. Le, M.A. Zwijnenburg, F. Furche, *Mechanism of photocatalytic water oxidation on small TiO_2 nanoparticles*, Chem. Sci. 8 (2017) 2179-2183.

[362] H. Gerischer, S*olar photoelectrolysis with semiconductor electrodes, in Solar Energy Conversion*, Ed. B. O. Seraphin, Springer, Berlin, 1979.

[363] K. Rejeshwar, *Fundamentals of Semiconductor Electrochemistry and Photoelectrochemistry, in Encyclopedia of Electrochemistry*, Vol. 6, Eds A.J. Bard, M. Stratmann, Wiley –VCH, Weinheim, 2002.

[364] A.J. Bard, L.R. Faulkner, *Electrochemical Methods: Fundamentals and Applications*, John Wiley & Sons, New York, 1980.

[365] R. Beranek, *(Photo)electrochemical Methods for the Determination of the Band Edge Positions of TiO_2-Based Nanomaterials*, Adv. Phys. Chem. (2011) 786759 p.20.

[366] C. Guillard, H. Lachheb, A. Houas, M. Ksibi, E. Elaloui, J.-M. Herrmann, *Influence of chemical structure of dyes, of pH and of inorganic salts on their photocatalytic degradation by TiO_2 comparison of the efficiency of powder and supported TiO_2*, J. Photochem. Photobiol. A: Chem. 158 (2003) 27–36.

[367] C. Guillard, E. Puzenat, H. Lachheb, A. Houas, J.-M. Herrmann, *Why inorganic salts decrease the TiO_2 photocatalytic efficiency*, Int. J. Photoenergy 7 (2005) 1–9.

[368] K.E. Kim, S.-R. Jang, J. Park, R. Vittal, K.-J. Kim, *Enhancement in the performance of dye-sensitized solar cells containing ZnO-covered TiO_2 electrodes prepared by thermal chemical vapor deposition*, Solar Energy Materials & Solar Cells 91 (2007) 366–370.

[369] G. Torrisi, A. Di Mauro, M. Scuderi, G. Nicotra, G. Impellizzeri, *Atomic layer deposition of ZnO/TiO2 multilayers: towards the understanding of Ti-doping in ZnO thin films*, RSC Adv. 6 (2016) 88886–88895.

[370] C.W. Zou, X.D. Yan, R.Q. Chen, A. Alyamani, Z.Y. Wu, W. Gao, *The Annealing Effect on the Microstructures and Phase Transformation of the TiO_2 Layer in ZnO/TiO_2 Core-Shell Nanostructures*, Crystal Growth & Design 11(2) (2011) 367–371.

[371] A. Sarkar, A.K. Singh, G.G. Khan, D. Sarkar, K. Mandal, *TiO_2/ZnO core/shell nano-heterostructure arrays as photo-electrodes with enhanced visible light photoelectrochemical performance*, RSC Adv. 4 (2014) 55629.

[372] D. Monllor-Satoca, R. Gómez, *Electrochemical Method for Studying the Kinetics of Electron Recombination and Transfer Reactions in Heterogeneous Photocatalysis: The Effect of Fluorination on TiO_2 Nanoporous Layers*, J. Phys. Chem. C 112 (2008) 139–147.

[373] L. Straka, Y. Yagodzinskyy, H. Kawakami, J. Romu, R. Ilola, H. Hänninen, Open-circuit potential as an indicator of damage of atomic layer deposited TiO_2 on AISI 304 stainless steel, Thin Solid Films, 517 (2008) 641–647.

[374] M. Quintana, T. Edvinsson, A. Hagfeldt, G. Boschloo, *Comparison of Dye-Sensitized ZnO and TiO_2 Solar Cells: Studies of Charge Transport and Carrier Lifetime*, J. Phys. Chem. C, 11 (2007) 1035-1041.

[375] A. Fujishima, X. Zhang, D.A. Tryk, *TiO_2 photocatalysis and related surface phenomena*, Surf. Sci. Rep. 63 (2008) 515–582.

[376] T. Bak, W. Li, J. Nowotny, A.J. Atanacio, J. Davis, *Photocatalytic Properties of TiO_2: Evidence of the Key Role of Surface Active Sites in Water Oxidation*, J. Phys. Chem. A 119 (2015) 9465−9473.

[377] A.D. Smigelskas, E.O. Kirkendall, *Zinc Diffusion in Alpha Brass*, Trans. AIME, 171 (1947) 130-142.

[378] E.O. Kirkendall, *Diffusion of Zinc in Alpha Brass*, Trans. AIME, 147 (1942) 104—110.

[379] E.O. Kirkendall, L. Thomassen, C. Upthegrove, *Rates of Diffusion of Copper and Zinc in Alpha Brass*, Trans. AIME, 133 (1939) 186-203.

[380] H.J. Fan, U. Gösele, M. Zacharias, *Formation of Nanotubes and Hollow Nanoparticles Based on Kirkendall and Diffusion Processes: A Review*, Small 3(10) (2007) 1660–1671.

[381] B. Schumacher, V. Plzak, J. Cai, R.J. Behm, *Reproducibility of highly active Au/TiO_2 catalyst preparation and conditioning*, Catal. Lett. 101 (2005) 215–224.

[382] H.M. Liu, W.S. Yang, Y. Ma, Y. Cao, N.J. Yao, J. Zhang, T.D. Hu, *Synthesis and Characterization of Titania Prepared by Using a Photoassisted Sol−Gel Method*, Langmuir, 19 (2003) 3001–3005.

[383] Y. Lei, L.D. Zhang, G.W. Meng, G.H. Li, X.Y. Zhang, C.H. Liang, W. Chen, S.X. Wang, *Preparation and photoluminescence of highly ordered TiO_2 nanowire arrays*, Appl. Phys. Lett. 78 (2001) 1125–1127.

[384] F.J. Knorr, J.L. McHale, *Spectroelectrochemical Photoluminescence of Trap States of Nanocrystalline TiO_2 in Aqueous Media*, J. Phys. Chem. C 117 (2013) 13654−13662.

[385] J. Shi, J. Chen, Z. Feng, T. Chen, Y. Lian, X. Wang, C. Li, *Photoluminescence Characteristics of TiO_2 and Their Relationship to the Photoassisted Reaction of Water/Methanol Mixture*, J. Phys. Chem. C 111 (2007) 693–699.

[386] X. Pan, M.-Q. Yang, X. Fu, N. Zhang, Y.-J. Xu, *Defective TiO_2 with oxygen vacancies: synthesis, properties and photocatalytic applications*, Nanoscale 5 (2013) 3601-3614.

[387] Y. Yang, R. Scholz, H. J. Fan, D. Hesse, U. Gösele, M. Zacharias, *Multitwinned Spinel Nanowires by Assembly of Nanobricks via Oriented Attachment: A Case Study of Zn_2TiO_4,* ASC Nano 3(3) (2009) 555–562.

[388] H. Irie, Y. Watanabe, K. Hashimoto, *Nitrogen-Concentration Dependence on Photocatalytic Activity of $TiO_{2-x}N_x$ Powders*, J. Phys. Chem. B 107 (2003) 5483–5486.

[389] C. Di Valentin, G. Pacchioni, A. Selloni, *Origin of the different photoactivity of N-doped anatase and rutile TiO_2*, Phys. Rev. B 70 (2004), 085116/1–4.

[390] C. Di Valentin, G. Pacchioni, *Trends in non-metal doping of anatase TiO_2: B, C, N and F*, Catal. Today 206 (2013) 12–18.

[391] G.P. Joshi, N.S. Saxena, R. Mangal, A. Mishra, T.P. Sharma, *Band gap determination of Ni-Zn ferrites*, Bull. Mater. Sci. 26 (2003) 387–389.

[392] Y. Tian, T. Tatsuma, *Plasmon-induced photoelectrochemistry at metal nanoparticles supported on nanoporous TiO_2*, Chem. Commun. (2004) 1810–1811.

[393] V. Subramanian, E. Wolf, P.V. Kamat, *Semiconductor-Metal Composite Nanostructures. To What Extent Do Metal Nanoparticles Improve the Photocatalytic Activity of TiO_2 Films?*, J. Phys. Chem. B 105 (2001) 11439–11446.

[394] S. Zeng, D. Baillargeat, H.-P. Ho, K.-T. Yong, *Nanomaterials enhanced surface plasmon resonance for biological and chemical sensing applications*, Chem. Soc. Rev. 43 (2014) 3426–3452.

[395] J. Livage, M. Henry, C. Sanchez, *Sol-Gel Chemistry of Transition Metal Oxides*, Progress in Solid State Chemistry 18 (1988) 259–342.

[396] C.G. Silva, R. Juárez, T. Marino, R. Molinari, H. García, *Influence of Excitation Wavelength (UV or Visible Light) on the Photocatalytic Activity of Titania Containing Gold Nanoparticles for the Generation of Hydrogen or Oxygen from Water*, J. Am. Chem. Soc. 133 (2011) 595–602.

[397] E. Kowalska, O. Omar, P. Mahaney, R. Abea, B. Ohtani, *Visible-light-induced photocatalysis through surface plasmon excitation of gold on titania surfaces*, Phys. Chem. Chem. Phys. 12 (2010) 2344–2355.

[398] R. Reichert, Z. Jusys, R.J. Behm, *Au/TiO_2 Photo(electro)catalysis: The Role of the Au Cocatalyst in Photoelectrochemical Water Splitting and Photocatalytic H_2 Evolution*, J. Phys. Chem. C 119 (2015) 24750−24759.

[399] C. Cardinaud, G. Lemperiere, M.C. Peignon, P.Y. Jouan, *Characterisation of TiN coatings and of TiN/Si interface by x-ray photoelectron spectroscopy and Auger electron spectroscopy*, Appl. Surf. Sci. 68 (1993) 595–603.

[400] A.P. Bhirud, S.D. Sathaye, R.P. Waichal, J.D. Ambekar, C.-J. Park, B.B. Kale, *In-situ preparation of N-TiO_2/grapheme nanocomposite and its enhanced photocatalytic hydrogen production by H_2S splitting under solar light*, Nanoscale 7 (2015) 5023–5034.

[401] M. Sathish, B. Viswanathan, R.P. Viswanath, C.S. Gopinath, *Synthesis, Characterization, Electronic Structure, and Photocatalytic Activity of Nitrogen-Doped TiO_2 Nanocatalyst*, Chem. Mater. 17 (2005) 6349–6353.

[402] A. Casagrande, A. Glisenti, E. Lanzoni, E. Tondello, L. Mirenghi, M. Casarin, R. Bertoncello, *TiN, TiC and Ti(C, N) film characterization and its relationship to tribological behavior*, Surf. Interface Anal. 18 (1992) 525–531.

[403] B.F. Dzhurinskii, D. Gati, N.P. Sergushin, V.I. Nefedov, Y.A.V. Salyn, *Simple and coordination compounds*, Russ. J. InorgChem, 20 (1975) 2307–2314.

[404] N.J. Nicholas, G.V. Franks, W.A. Ducker, *The mechanism for hydrothermal growth of zinc oxide*, Cryst. Eng. Comm. 14 (2012) 1232–1240.

[405] C.R. Clayton, Y.C. Lu, *A Bipolar Model of the Passivity of Stainless Steel: The Role of Mo Addition*, J. Electrochem. Soc. 133 (1986) 2465–2473.

[406] A.L. Luna, E. Novoseltceva, E. Louarn, P. Beaunier, E. Kowalska, B. Ohtani, M.A. Valenzuel, H. Remita, C. Colbeau-Justin, *Synergetic effect of Ni and Au nanoparticles synthesized on titaniaparticles for efficient photocatalytic hydrogen production*, Appl. Catal. B: Environ. 191 (2016) 18–28.

[407] P. Tripathy, A. Mishra, S. Ram, H.-J. Fecht, J. Bansmann, R.J. Behm, *X-ray photoelectron spectrum in surface interfacing of gold nanoparticles with polymer molecules in a hybrid nanocomposite structure* Nanotechnology 20 (2009) 075701 (10pp).

[408] M. C. Hidalgo, J.J. Murcia, J.A. Navío, G. Colón, *Photodeposition of gold on titanium dioxide for photocatalytic phenol oxidation*, Appl. Catal. A: General 397 (2011) 112–120.

[409] L.A. Calzada, S.E. Collins, C.W. Han, V. Ortalan, R. Zanella, *Synergetic effect of bimetallic Au-Ru/TiO_2 catalysts for complete oxidation of methanol*, Appl. Catal. B: Environ. 207 (2017) 79–92.

[410] G. R. Torres, T. Lindgren, J. Lu, C.-G. Granqvist, S.-E. Lindquist, *Photoelectrochemical Study of Nitrogen-Doped Titanium Dioxide for Water Oxidation*, J. Phys. Chem. B 108 (2004) 5995-6003.

[411] N.M. Markovic, P.N. Ross, *Surface science studies of model fuel cell electrocatalysts*, Surf. Sci. Rep. 45 (2002) 117–229.

[412] M. Hayyan, M.A. Hashim, I.M. Al Nashef, *Superoxide Ion: Generation and Chemical Implications*, Chem. Rev. 116 (2016) 3029−3085.

[413] D.T. Sawyer, J.S. Valentine, *How super is superoxide?*, Acc. Chem. Res. 14 (1981) 393–400.

[414] R. Gao, J. Stark, D.W. Bahnemann, J. Rabani, *Quantum yields of hydroxyl radicals in illuminated TiO_2 nanocrystallite layers*, J. Photochem. Photobiol. A: Chem. 148 (2002) 387–391.

[415] M.R. Hoffmann, S.T. Martin, W. Choi, D.W. Bahnemann, *Environmental Applications of Semiconductor Photocatalysis*, Chem. Rev. 95 (1995) 69–96.

[416] C.R. Raj, A.I. Abdelrahman, T. Ohsaka, *Gold nanoparticle assisted electroreduction of oxygen*. Electrochem. Commun. 7 (2005) 888–893.

[417] J.H. Shim, J. Kim, C. Lee, Y. Lee, *Electrocatalytic Activity of Gold and Gold Nanoparticles Improved by Electrochemical Pretreatment*, J. Phys. Chem. C 115 (2011) 305–309.

[418] G. Gotti, K. Fajerwerg, D. Evrard, P. Gros, *Electrodeposited gold nanoparticles on glassy carbon: Correlation between nanoparticles characteristics and oxygen reduction kinetics in neutral media*, Electrochim. Acta 128 (2014) 412–419.

[419] M. Shao, P. Liu, R. Adzic, *Superoxide Anion is the Intermediate in the Oxygen Reduction Reaction on Platinum Electrodes*, J. Am. Chem. Soc. 128 (2006) 7408–7409.

[420] Z. Feng, N.S. Georgescu, D.A. Scherson, *Rotating Ring-Disk Electrode Method for the Detection of Solution Phase Superoxide as a Reaction Intermediate of Oxygen Reduction in Neutral Aqueous Solutions*, Anal. Chem. 88 (2016) 1088−1091.

[421] K.L. Kelly, E. Coronado, L.L. Zhao, G.C. Schatz, *The Optical Properties of Metal Nanoparticles: The Influence of Size, Shape, and Dielectric Environment*, J. Phys. Chem. B 107 (2003) 668–677.

[422] K. Yamanaka, T. Morikawa, *Charge-Carrier Dynamics in Nitrogen-Doped TiO_2 Powder Studied by Femtosecond Time-Resolved Diffuse Reflectance Spectroscopy*, J. Phys. Chem.C 116 (2012) 1286-1292

[423] S. Sakthivel, B. Neppolian, M.V. Shankar, B. Arabindoo, M. Palanichamy, V. Murugesan, *Solar photocatalytic degradation of azo dye: comparison of photocatalytic efficiency of ZnO and TiO_2*, Sol. Energ. Mat. Sol. Cells 77 (2003) 65–82.

[424] L. Wu, F. Li, Y. Xu, J.W. Zhang, D. Zhang, G. Li, H. Li, *Plasmon-induced photoelectrocatalytic activity of Au nanoparticles enhanced TiO_2 nanotube arrays electrodes for environmental remediation*, Appl. Catal. B: Environ. 164 (2015) 217–224.

[425] T.A. Egerton, *Does photoelectrocatalysis by TiO_2 work?*, J. Chem. Technol. Biotechnol. 86 (2011) 1024–1031.

[426] L.C. Almeida, M.V.B. Zanoni, *Decoration of Ti/TiO_2 Nanotubes with Pt Nanoparticles for Enhanced UV-vis Light Absorption in Photoelectrocatalytic Process*, J. Braz. Chem. Soc. 25 (2014) 579–588.

[427] H. Zhou, J. Ge, M. Zhang, S. Yuan, *Photoelectrocatalytic properties of TiO_2/ATO composite films*, Res. Chem. Intermed. 42 (2016) 1929–1941.